

UC Riverside

UC Riverside Electronic Theses and Dissertations

Title

Performance Optimization of Metallic Iron and Iron Oxide Nanomaterials for Treatment of Impaired Water Supplies

Permalink

<https://escholarship.org/uc/item/7bv3r7zx>

Author

Xie, Yang

Publication Date

2011

Peer reviewed|Thesis/dissertation

UNIVERSITY OF CALIFORNIA
RIVERSIDE

Performance Optimization of Metallic Iron and Iron Oxide Nanomaterials for
Treatment of Impaired Water Supplies

A Dissertation submitted in partial satisfaction
of the requirements for the degree of

Doctor of Philosophy

in

Chemical and Environmental Engineering

by

Yang Xie

December 2011

Dissertation Committee:

Dr. David M. Cwiertny, Co-Chairperson
Dr. Mark R. Matsumoto, Co-Chairperson
Dr. Nosang V. Myung

Copyright by
Yang Xie
2011

The Dissertation of Yang Xie is approved:

Committee Chairperson

University of California, Riverside

Acknowledgements

Foremost, my utmost gratitude must go to my research advisor and mentor, Dr. David M. Cwiertny, without the endless support from whom, this thesis work would not have been finished with satisfactory. He exhibits to me, by setting up a shining example in person, how to conduct and execute research in a professional manner, how to present scientific findings in a logical and plain way, and more importantly, how to comprehend and interpret laboratory factsheets into sounding conclusions. He constantly motivates me in the right direction, to pursue and to achieve a higher degree of performance. He encourages me in front of bottleneck, never gives up even at the worst moments of my research. It is my best fortune and a lifetime benefit, to have chosen him as my PhD advisor and mentor.

I would also like to express my sincere thankfulness to my reading committee members: Dr. Mark R. Matsumoto, Dr. Nosang V. Myung and my candidacy committee members: Dr. Sharon L. Walker and Dr. David R. Parker. They provided me with tons of insightful comments and constructive suggestions, which facilitated to overcome the challenges and fruitful the whole research.

I am also indebted to my colleagues: Shen Qu, Caylyn Lanzl, Rebekah Oulton, Edgard Verdugo and Michael Nalbandian. We shared sweets and bitters through our research process and it made my four years at University of California, Riverside like an eyewink with their accompanies. I am especially grateful to my closest friends: Na Li, Liyan Jin, Yue Wang, Qing Sun, Ji Luo and Qianqian Wang, who always gave me new

inspirations on my research. The support from them kept me enthusiastic and optimistic at frustrated moments. My thanks goes to Yan Lin as well, the experience cooperating with him is unforgettable.

I must acknowledge Stephen McDaniel in the Central Facility for Advanced Microscopy and Microanalysis (CFFAM) at University of California, Riverside for his kindest assistance with TEM training; Dr. Pingyung Feng in the department of Chemistry for the assistant with XRD training; Drs. Michelle M. Scherer and Christopher Gorski in the University of Iowa for their assistance with Mossbauer Analysis; Dr. D. Howard Fairbrother and Kevin Wepasnick at Johns Hopkins University for their assistance with XPS Analysis.

Last but not the least, I owe my loving thanks to my family: my mom Yuzhen Huang, who gives me unconditional love and limitless support to any interest and dream I am pursuing; my dad Shian Xie, who has always been my role model in both career and daily life. And finally, my boyfriend, Wei He who consistently supports me throughout the work and life, constructing me a peaceful spiritual castle to pursue my dream.

ABSTRACT OF THE DISSERTATION

Performance Optimization of Metallic Iron and Iron Oxide Nanomaterials for Treatment of Impaired Water Supplies

by

Yang Xie

Doctor of Philosophy, Graduate Program in Chemical and Environmental Engineering
University of California, Riverside, December 2011
Dr. David M. Cwiertny, Co-Chairperson
Dr. Mark R. Matsumoto, Co-Chairperson

Iron nanomaterials including nanoscale zero valent iron (NZVI), NZVI-based bimetallic reductants (e.g., Pd/NZVI) and naturally occurring nanoscale iron mineral phases represent promising treatment tools for impaired water supplies. However, questions pertaining to fundamental and practical aspects of their reactivity may limit their performance during applications.

For NZVI treatment of pollutant source zones, a major hurdle is its limited reactive lifetime. In Chapter 2, we report the longevity of NZVI towards 1,1,1,2-tetrachloroethane (1,1,1,2-TeCA) and hexavalent chromium [Cr(VI)] in oxygen-free systems with various anionic co-solutes (e.g., Cl^- , SO_4^{2-} , ClO_4^- , HCO_3^- , NO_3^-). Trends in

longevity provide evidence that surface-associated Fe(II) species are responsible for Cr(VI) reduction, whereas 1,1,1,2-TeCA reduction depends on the accessibility of Fe(0) at the NZVI particle surface.

In Chapter 3, we show that dithionite, previously utilized for *in situ* redox manipulation, can restore the reducing capacity of passivated NZVI treatment systems. Air oxidation of NZVI at $\text{pH} \geq 8$ quickly exhausted reactivity despite a significant fraction of Fe(0) persisting in the particle core. Reduction of this passive layer by low dithionite concentrations restored suspension reactivity to levels of unaged NZVI, with multiple dithionite additions further improving pollutant removal.

In Chapter 4, measurements of solvent kinetic isotope effects reveals that optimal Pd/NZVI reactivity results from accumulation of atomic hydrogen, which only occurs in NZVI-based systems due to their higher rates of corrosion. However, atomic hydrogen formation only occurs in aged Pd/NZVI suspensions for ~ 2 weeks, after which any reactivity enhancement likely results from galvanic corrosion of Fe(0).

Finally, the activity of hybrid nanostructures consisting of multi-walled carbon nanotubes decorated with hematite nanoparticles ($\alpha\text{-Fe}_2\text{O}_3/\text{MWCNT}$) is explored in Chapter 5. Sorption of Cu(II) and Cr(VI) is enhanced in hybrid nanostructure systems beyond what would be expected from simple additive sorption capacities of their building blocks. The enhanced sorption capacity is in part derived from the greater surface area of hematite nanoparticles immobilized on MWCNTs relative to aggregated hematite suspensions. The hybrid $\alpha\text{-Fe}_2\text{O}_3/\text{MWCNT}$ may also exhibit unique surface chemistry, as

supported by the tunable values of zeta potential measured as a function of the mass of α - Fe_2O_3 deposited on the MWCNTs.

Table of Contents

Acknowledgements	iv
Abstract	vi
List of Figures	xii
Chapter 1: Introduction	1
1.1. Use of iron-based materials for environmental treatment	1
1.2. Granular iron PRBs for groundwater treatment	4
1.3. Nanoscale zero-valent iron as an innovative treatment alternative to granular iron PRBs	7
1.4. Bimetallic reductants for enhancing zero-valent iron reactivity	13
1.5. Formation and activity of nanoscale iron oxides and their role in environmental quality control	17
1.6. Thesis organization	20
1.7. Literature Cited	24
Chapter 2: Influence of Anionic Co-Solutes and pH on Nanoscale Zero-Valent Iron Longevity: Timescales and Mechanisms of Reactivity Loss Toward 1,1,1,2-Tetrachloroethane and Cr(VI)	39
2. 1. Abstract	39
2. 2. Introduction	40
2. 3. Experimental Section	44
2. 4. Results and Discussion	51
2. 5. Environmental Implications	80
2. 6. Acknowledgements	81
2. 7. Literature Cited	82
Chapter 3: Use of Dithionite to Extend the Reactive	87

Lifetime of Nanoscale Zero-Valent Iron Treatment Systems

3. 1.	Abstract	87
3. 2.	Introduction	88
3. 3.	Experimental Methods	92
3. 4.	Results and Discussion	101
3. 5.	Environmental Implications	124
3. 6.	Acknowledgements	129
3. 7.	Literature Cited	129

Chapter 4: Chlorinated Solvent Transformation in Palladized Zero-Valent Iron Systems: New Insights from Rate Dependence on Reductant Loading and Solvent Kinetic Isotope Effects **134**

4. 1.	Abstract	134
4. 2.	Introduction	135
4. 3.	Experimental Section	139
4. 4.	Results and Discussion	145
4. 5.	Implications for Pd/NZVI Applications	172
4. 6.	Literature Cited	177

Chapter 5: Hybrid hematite/multi-walled carbon nanotube (α -Fe₂O₃/MWCNT) nanostructures as sorbents for Cu(II) and Cr(VI) **180**

5. 1.	Abstract	180
5. 2.	Introduction	181
5. 3.	Experimental Section	184
5. 4.	Results and Discussion	192
5. 5.	Environmental Significance	213
5. 6.	Acknowledgements	214
5. 7.	Literature Cited	215

Chapter 6 : Conclusion **221**

6. 1.	Predicting nanoscale zero-valent iron longevity in complex geochemical environments	221
6. 2.	Extending nanoscale zero-valent iron longevity via chemical regeneration	225
6. 3.	Enhancing zero-valent iron reactivity through the use of noble metal	227

	surface additives	
6. 4.	Improving performance of iron-based nanomaterial sorbents through immobilization on carbon nanotube supports	230
6. 5.	Future work	232
6. 6.	Literature Cited	237
	Curriculum Vitae	239

List of Figures

Chapter 1

- Figure 1-1:** Conceptualization of an Fe(0) PRB for treatment of contaminated groundwater. 4
- Figure 1-2:** Conceptualization of NZVI *in situ* treatment for contaminant source zone. 9
- Figure 1-3:** Comparison of common Fe(0)-based bimetals for the reduction of 1,1,1-trichloroethane. 15

Chapter 2

- Figure 2-1:** Change in the k_{obs} values for 1,1,1,2-TeCA reduction over time in the presence of Cl^- , SO_4^{2-} , ClO_4^- , HCO_3^- and NO_3^- at pH 8 (a) at 5 mN and (b) at 25 mN concentration. 55
- Figure 2-2:** Reduction of nitrate and production of nitrite in suspensions of (a) 5 mN and (b) 25 mN nitrate at pH 7 and 8. 56
- Figure 2-3:** Change in k_{obs} values for 1,1,1,2-TeCA reduction as a function of NZVI aging time in pH 7 and pH 8 suspensions with 5, 25 and 100 mN concentrations of Cl^- , SO_4^{2-} and ClO_4^- . 57
- Figure 2-4:** Change in the k_{obs} values for 1,1,1,2-TeCA reduction over time in pH 7 suspensions of Cl^- , SO_4^{2-} , ClO_4^- , HCO_3^- and NO_3^- (a) at 5 mN and (b) at 25 mN concentration. 58
- Figure 2-5:** Change in Cr(VI) removal capacity (in mg of Cr/g NZVI) as a function of aging time in 5 and 25 mN suspensions of sulfate, chloride, perchlorate, carbonate and nitrate at pH 7 and 8. 61

Figure 2-6: Reactivity loss in (a) 25 mN chloride, (b) 5 mN bicarbonate and (c) 25 mN bicarbonate system at pH 7 and 8.	62
Figure 2-7: (a) TEM images and (b) XRD patterns collected as a function of aging time for NZVI particles aged in pH 7 suspensions with 25 mM NO_3^- .	66
Figure 2-8: (a) TEM images collected as a function of time for NZVI suspensions aged in 25 mN Cl^- at pH 8. Corresponding XRD patterns (b) are shown as a function of aging time for 25 mN Cl^- suspensions aged at pH 7 and pH 8.	67
Figure 2-9: TEM images and X-ray diffraction patterns collected as a function of aging time in pH 7 suspensions of (a) 5 mN Cl^- , (b) 25 mN SO_4^{2-} , and (c) 25 mN ClO_4^- .	68
Figure 2-10: Comparison of corrosion production formation in aged suspensions of (a) 5 mN HCO_3^- and (b) 25 mN HCO_3^- at pH 7 and pH 8 as shown in TEM images.	69
Figure 2-11: Development of corrosion products for NZVI suspension at pH 8 in 5 and 25 mN HCO_3^- suspensions as shown in TEM images.	70
Figure 2-12: Values of oxidation-reduction potential (ORP) measured as a function of aging time for NZVI suspensions containing Cl^- , SO_4^{2-} , ClO_4^- , HCO_3^- and NO_3^- .	75
Figure 2-13: Cr(VI) removal capacity plotted as a function of Fe(II) production rate with data categorized as a function of a) anion identity and concentration where open symbols represent 5 mN suspensions and solid symbols represent 25 mN suspensions and b) suspension pH.	76
Figure 2-14: Production of aqueous Fe(II) as a function of time in 1 g/L suspensions of NZVI containing (a) 25 mN Cl^- at pH 7 and (b) 5 mM NO_3^- system at pH 7.	77
Figure 2-15: Correlation between total Cr(VI) removal capacity and Fe(II) production rate when data from all anion systems is categorized based on the extent of suspension aging.	78
Figure 2-16: Plot of k_{obs} values for 1,1,1,2-TeCA reduction as a function of Fe(II) production rate when data is categorized based upon (a) anion identity and (b) pH condition and anion concentration.	79

Chapter 3

Figure 3-1: (a) Scanning electron microscopy, (b) transmission electron microscopy, (c) powder X-ray diffraction and (d) ^{57}Fe Mössbauer spectroscopy analysis of NZVI from Nanostructured and Amorphous Materials. 93

Figure 3-2: Appearance of NZVI suspensions (a) aged for 3 days in air at pH 6, 7 and 8 or (b) aged for 60 days at pH 7 and 8 within an anaerobic chamber (95% N_2 and 5% H_2). 103

Figure 3-3: (a) X-ray diffraction patterns for NZVI suspensions aged in air for 3 days at pH 6 before and after reaction with various dithionite solutions. (b) Total Cr(VI) removal exhibited by products of the reaction between dithionite and NZVI suspensions aged in air for 3 d at pH 6. 104

Figure 3-4: (a) ^{57}Fe Mössbauer spectra for fresh (as received) NZVI, and NZVI aged in a suspension exposed to air for 3 d at pH 6 and 8. Corresponding TEM images of the products of NZVI aging at (b) pH 6 and (c) pH 8 are also shown. 105

Figure 3-5: (a) X-ray diffraction patterns for NZVI suspensions aged in air for 3 days at pH 8 before and after reaction with various dithionite solutions. Measured reactivity of the products of the reaction between dithionite and NZVI suspensions aged in air for 3 d at pH 8 shown (b) as values of k_{obs} for 1,1,1,2-TeCA reduction and (c) as values of total Cr(VI) removal. 106

Figure 3-6: Concentration profiles for 1,1,1,2-TeCA in NZVI suspensions (2 g/L) aged in air (a) at pH 7 and (b) at pH 8. 107

Figure 3-7: Change in initial k_{obs} values for the reduction of 1,1,1,2-TeCA with respect to the aging time of NZVI suspensions within an anaerobic chamber. 110

Figure 3-8: (a) X-ray diffraction patterns for NZVI suspensions (2 g/L) aged inside an anaerobic chamber (95% N_2 , 5% H_2) for 30 and 60 days at pH 7 (50 mM HEPES) and pH 8 (50 mM Tris). (b) Corresponding TEM images of NZVI aged for 60 days in aqueous suspensions at pH 7 and pH 8. 111

Figure 3-9: Change in dithionite concentration over time during reaction with air-aged NZVI (a) at pH 6 and 7 and (b) at pH 8. 114

Figure 3-10: X-ray photoelectron spectra of air-aged NZVI suspensions (2 g/L) after reaction with dithionite. Shown are spectra for NZVI suspensions aged in air at pH 6 (a, b) and pH 8 (c, d) after reaction with 0.9 and 3.6 g dithionite/g NZVI. 115

Figure 3-11: Change in nitrobenzene concentration over time in suspensions of air-aged NZVI particles after reaction with the concentrations of dithionite noted.	116
Figure 3-12: Inhibitory influence of dithionite on the reactivity toward 1,1,1,2-TeCA of NZVI suspensions (2 g/L) aged at pH 7 (50 mM HEPES) within an anaerobic chamber for (a) 14 d and (b) 30 d.	121
Figure 3-13: Change in 1,1,1,2-TeCA concentration as a function of time in fresh NZVI suspensions, NZVI suspensions aged 30 d inside an anaerobic chamber, and products of the reaction between 0.02 g dithionite/g NZVI and the 30 d aged NZVI suspension.	125
Figure 3-14: Cumulative Cr(VI) removal as a result of multiple, sequential reactions of passivated NZVI suspensions with 0.7 g dithionite/g NZVI.	126
Figure 3-15: X-ray diffraction (XRD) patterns for NZVI suspensions (a) passivated by reaction with excess Cr(VI) in the absence of oxygen and (b) passivated by exposure to air for 3d. Suspensions (2 g/L) were prepared at pH 8 (50 mM Tris).	127
 Chapter 4	
Figure 4-1: Change in the k_{obs} values for 1,1,1,2-TeCA reduction as a function of solid loading (ρ_m values) in systems with (a) ZVI and 1% Pd/ZVI and (b) NZVI, 0.05% Pd/NZVI and 0.35% Pd/NZVI.	149
Figure 4-2: Change in the $k_{obs}(1,1,1,2\text{-TeCA})$ values over time for NZVI at pH 6 and 8.	150
Figure 4-3: Change in mass-normalized rate constants for 1,1,1,2-TeCA reduction [$k_m(1,1,1,2\text{-TeCA})$ values] as a function of the molar ratio of the initial 1,1,1,2-TeCA concentration and iron-based reductant in NZVI, 0.05% Pd/NZVI and 0.35% Pd/NZVI systems.	151
Figure 4-4: Change in Fe(II) production rate for NZVI and 0.35% Pd/NZVI as a function of ρ_m value.	155
Figure 4-5: Change in normalized 1,1,1,2-TeCA concentration as a function of time in NZVI, 0.05% Pd/NZVI, and 0.35% Pd/NZVI suspensions. Data are	156

shown for an initial 1,1,1,2-TeCA concentration of (a) 30 μM and (b) 330 μM .

Figure 4-6: Semi-log plots of 1,1,1,2-TeCA concentration versus time for (a) NZVI, (b) 0.05% Pd/NZVI, and (c) 0.35% Pd/NZVI. 160

Figure 4-7: Correlation between solvent kinetics isotope effect [$k_{\text{obs}}(\text{H}_2\text{O})/k_{\text{obs}}(\text{D}_2\text{O})$] and reactivity enhancement factor [$k_{\text{obs}}(\text{Pd}/\text{Fe})/k_{\text{obs}}(\text{Fe})$] for (a) the reduction of 1,1,1,2-TeCA and (b) the reduction of *cis*-DCE. 161

Figure 4-8 : Representative TEM images of (a) NZVI, (b) 0.05% Pd/NZVI, and (c) 0.35% Pd/NZVI. 162

Figure 4-9: Plot of $k_{\text{obs}}(1,1,1,2\text{-TeCA})$ as a function of Fe(II) production rate for NZVI and 0.35% Pd/NZVI shown on (a) linear and (b) logarithmic scales. 163

Figure 4-10: Concentration profiles for 1,1,1,2-TeCA decay and formation of 1,1-dichloroethylene (1,1-DCE) are shown for (a) NZVI and (b) 0.35% Pd/NZVI at pH 8 and a ρ_m value of 0.22 g/L. 164

Figure 4-11: Plots of the natural log of *cis*-DCE concentration as a function of time in NZVI suspensions of H_2O and D_2O . Experiments were conducted at 0.6 g/L NZVI with initial *cis*-DCE concentration of 176 μM in 25 mM HEPES/25 mM NaCl solutions at pH 8. 168

Figure 4-12: Semi-log plots of *cis*-DCE concentration versus time for (a) 0.05% Pd/NZVI and (b) 0.35% Pd/NZVI. 169

Figure 4-13: Change in 1,1,1,2-TeCA concentration as a function of time in suspensions of (a) ZVI and (b) 1% Pd/ZVI. 170

Figure 4-14: Natural log of *cis*-DCE concentration as a function of time for 1% Pd/ZVI prepared in H_2O and D_2O suspensions of 5.7 g/L. 171

Figure 4-15: Change in the k_{obs} values for 1,1,1,2-TeCA reduction over time for bare NZVI and 0.35% Pd/NZVI in the presence of H_2O and D_2O during anaerobic aging. 175

Figure 4-16: Schematic of the dominant reaction pathway responsible for organohalide (RX) reduction in Pd/NZVI systems (a) At relatively low Pd loadings and low ρ_m values, (b) At high Pd loadings and high ρ_m values. 176

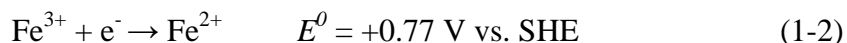
Chapter 5

- Figure 5-1:** TEM images of (a) oxidized MWCNTs at high magnification and (b) aggregated hematite ($\alpha\text{-Fe}_2\text{O}_3$) nanoparticles synthesized from the hydrolysis of ferric nitrate. 194
- Figure 5-2:** TEM images for 0.07 and 0.5 g/g $\alpha\text{-Fe}_2\text{O}_3$ /MWCNT at low (a and b, respectively) and high (c and d, respectively) magnifications. Also shown for each material (e and f, respectively) are dark field images which reveal contrast based on elemental mass. 195
- Figure 5-3:** Zeta potential values measured as a function of pH for suspensions of $\alpha\text{-Fe}_2\text{O}_3$ nanoparticles, 0.07 and 0.5 g/g $\alpha\text{-Fe}_2\text{O}_3$ /MWCNT and oxidized MWCNTs. 198
- Figure 5-4:** Sedimentation results for suspensions of oxidized MWCNTs, 0.5 g/g $\alpha\text{-Fe}_2\text{O}_3$ /MWCNT and $\alpha\text{-Fe}_2\text{O}_3$ nanoparticles. 201
- Figure 5-5:** Adsorption of Cu(II) as a function of pH in suspensions of oxidized MWCNTs, $\alpha\text{-Fe}_2\text{O}_3$ nanoparticles and 0.5 g/g $\alpha\text{-Fe}_2\text{O}_3$ /MWCNT hybrid nanostructures. Adsorbed concentrations of Cu(II) are presented after normalization by the total mass of (a) MWCNT and (b) $\alpha\text{-Fe}_2\text{O}_3$ in suspension. 202
- Figure 5-6:** Data from pH edge adsorption experiments presented on a log-log scale for adsorbed concentrations of Cu(II) normalized by the total mass of (a) MWCNT and (b) $\alpha\text{-Fe}_2\text{O}_3$ in suspension. 205
- Figure 5-7:** Cu(II) adsorption isotherms at pH 6.0 in suspensions of oxidized MWCNTs, $\alpha\text{-Fe}_2\text{O}_3$ nanoparticles and 0.07 and 0.5 g/g $\alpha\text{-Fe}_2\text{O}_3$ /MWCNT hybrid nanostructures. Adsorbed concentrations of Cu(II) are presented after normalization by the total mass of (a) MWCNT and (b) $\alpha\text{-Fe}_2\text{O}_3$ in suspension. 207
- Figure 5-8:** Adsorption of CrO_4^{2-} as a function of pH in suspensions of $\alpha\text{-Fe}_2\text{O}_3$ nanoparticles and 0.5 g/g $\alpha\text{-Fe}_2\text{O}_3$ /MWCNT hybrid nanostructures. 211
- Figure 5-9:** CrO_4^{2-} adsorption isotherms at (a) pH 2.0 and (b) pH 6.0 in suspensions of oxidized $\alpha\text{-Fe}_2\text{O}_3$ nanoparticles and 0.5 g/g $\alpha\text{-Fe}_2\text{O}_3$ /MWCNT hybrid nanostructures. 212

1. Introduction

1.1. *Use of iron-based materials for environmental treatment*

Iron is a versatile, naturally abundant element that plays critical roles in governing the environmental fate of pollutants in both natural and engineered systems. Occurring predominantly in three oxidation states [i.e., Fe(0), Fe(II) and Fe(III)], reduced forms including metallic [Fe(0)] and ferrous [Fe(II)] iron are recognized electron donors (i.e., reductants; see equations 1-1 and 1-2) that are capable of reducing many oxidized pollutant classes.



For example, over the past 15 years granular forms of Fe(0) have been utilized in engineered treatment strategies for groundwater contaminated with halogenated organic compounds [1], heavy metals including arsenic [2] and chromium [3, 4], and radionuclides such as uranium [5]. Fe(0) is a moderately strong reductant [6] (eq 1-1) that provides more reducing equivalents relative to Fe(II), and thus has been broadly applied in the form of permeable reactive barriers (PRBs) [7, 8] and, through recent innovations in the area of engineered nanomaterials, through the subsurface delivery of Fe(0) nanoparticles [9].

Although Fe(0) is limited entirely to engineered treatment applications, the value of Fe(II) as a reductant (eq 1-2) is enhanced from its natural abundance in the subsurface, generated through biogeochemical processes. Specifically, dissimilatory iron reducing

bacteria (DIRB) [10] utilize insoluble ferric (oxyhydr)oxides as terminal electron acceptors during oxidation of organic matter, in turn producing a variety of Fe(II) species including dissolved and complexed forms of soluble Fe(II) and ferrous iron-containing solids including green rusts, siderite (FeCO_3), mackinawite (FeS), and magnetite (Fe_3O_4) that are typically more potent reductants than aqueous Fe(II). Many of these Fe(II)-containing phases have been demonstrated to reduce oxidized pollutant classes including chlorinated solvents [11, 12] and heavy metals [13, 14], although typically at a rate that is slower than Fe(0). Accordingly, several instances also exist where manipulation of subsurface redox conditions has been engineered (e.g., *in situ* redox manipulation with dithionite [15] or biostimulation of DIRB coupled with addition of ferrous sulfate [16]) to increase the abundance of Fe(II) phases in the subsurface in hopes of promoting pollutant transformation in these enriched zones.

Ferric iron [Fe(III)] has no readily available electrons to serve as a reductant, and it also exhibits sparingly limited solubility in most environmentally relevant (i.e., circumneutral) pH systems. As such, it commonly exists as iron (oxyhydr)oxides including amorphous ferric hydroxide or ferrihydrite, or crystalline phases including lepidocrocite ($\gamma\text{-FeOOH}$), goethite ($\alpha\text{-FeOOH}$) and hematite ($\alpha\text{-Fe}_2\text{O}_3$) [17]. These phases will hereafter collectively be referred to as iron oxides.

Aside from their critical role as a source for Fe(II) production via their reductive dissolution, the value of these Fe(III) phases with respect to pollutant fate and transport is derived from their role as sorbents. Most naturally occurring iron oxides exhibit a zero-point of charge around pH 7 or 8 [18], making them capable sorbents for both cationic

and anionic species over the range of environmentally pH values. For example, Parfitt observed the adsorption of phosphate on iron oxides from natural soils [19], and Zhang *et al.* demonstrated the capacity of natural iron ores for As(V) removal [20]. Given their recognized role as sorbents in natural systems, engineered applications of Fe(III) oxides also exist that try to exploit their sorbent activity for water treatment. For example, granular ferric hydroxide (GFH® Media) is commercially available through Siemens Water [21] and marketed for the sequestration of arsenic during water treatment. A variety of support materials including activated carbon [22], clay [23], sand [24] and polymers [25] have also been proposed for the manufacturing of composites with high surface area iron oxides for use as sorbents in water treatment.

Work presented in this thesis demonstrates the application of each of the aforementioned iron oxidation states for the treatment of impaired water supplies (e.g., groundwater and drinking water). A general theme for the Fe(0), Fe(II)-containing solids phases, or Fe(III) oxides considered herein is how their reactivity can be optimized to enhance pollutant removal in engineered treatment systems. This includes research on approaches to better predict, enhance and extend the reactivity of nanoscale and granular Fe(0) particles, particularly through manipulation of their surface chemistry and the Fe(II)-containing phases generated via Fe(0) corrosion, as well as development of innovative application platforms for nanoscale Fe(III) oxides as high surface area sorbents for heavy metals in water.

1.2. Granular iron PRBs for groundwater treatment

Over past two decades, Fe(0) has been widely applied to treat contaminated groundwater in the form of a permeable reactive barrier (or PRB) (Figure 1-1) [8, 26-29]. In this technology, a trench is dug down gradient from a contaminant plume, and it is subsequently filled with filings of granular Fe(0), typically on the order of several millimeters in grain size. This produces a permeable barrier in the subsurface that allows contaminated groundwater to pass through via its natural flow gradient. Within the barrier, the Fe(0) particles generate a highly reducing environment that chemically transforms and/or immobilizes many classes of oxidized pollutants, ideally producing more environmentally benign products. The treatment process thereby yields treated groundwater down gradient of the PRB installation.

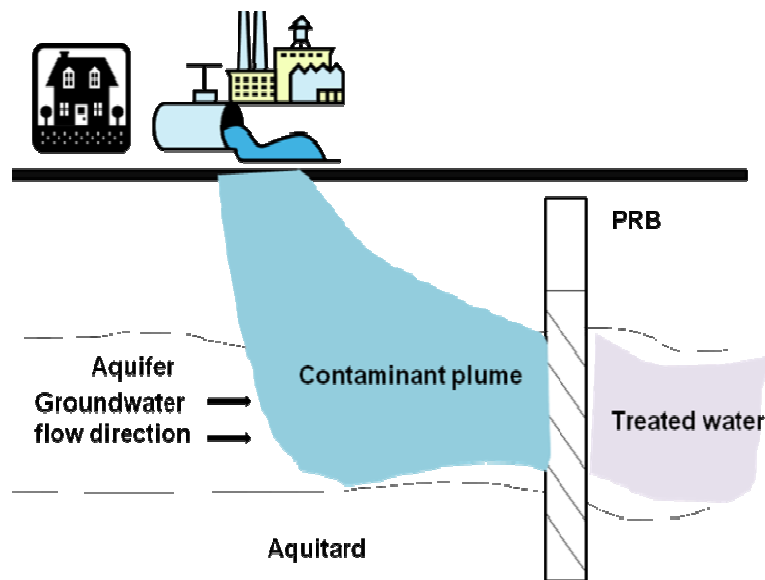


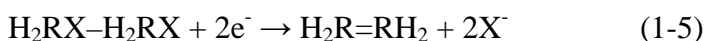
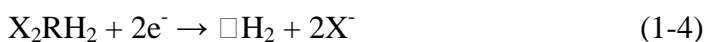
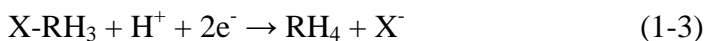
Figure 1-1. Conceptualization of an Fe(0) PRB for treatment of contaminated groundwater.

Generally, Fe(0) PRBs are highly effective technologies for passive, *in situ* groundwater treatment with low capital and routine operation and maintenance expenditures [30]. These favorable attributes have resulted in more than 100 PRB installations sites worldwide [31]. For example, at an installation in Elizabeth City, North Carolina, effluent concentrations of Cr(VI), TCE and *cis*-1,2-dichloroethylene (*cis*-DCE) were maintained below Environmental Protection Agency (EPA) established maximum contaminant levels (MCL) for several years after PRB installation [3].

Among PRB applications, chlorinated organic solvents represent the primary treatment target [7]. Chlorinated solvents are ubiquitous groundwater contaminants due to their extensive use and ultimate mishandling and disposal during industrial applications as metal degreasers, dry cleaning solvents and adhesives [32]. As a result of their greater density than water and their sparing aqueous solubility, they frequently exist in the subsurface as a separate, pure organic phase, which can persist over long timescales because they are relatively chemically inert and slow to biodegrade [32].

Chlorinated solvent degradation in PRBs occurs via a process in which Fe(0) serves as the primary electron donor (eq 1-1), while the organohalide solvents are chemically reduced to products with a lower degree of halogenations (i.e., dehalogenation). In addition, it is possible that other redox active species generated as byproducts of Fe(0) corrosion can also act as reductants in PRBs [33]. These species include Fe(II)-containing corrosion products such as magnetite [34] or surface-associated atomic hydrogen species [35], which are intermediates in the formation of molecular hydrogen gas [$H_2(g)$] during Fe(0) corrosion in oxygen-free environments.

Two major reductive dehalogenation pathways are commonly observed for chlorinated solvents. These are (i) hydrogenolysis, where a halogen substituent is replaced by hydrogen via a net two-electron transfer (eq 1-3); and (ii) reductive elimination in which two halide ions are liberated via a net two-electron transfer. Reductive elimination can proceed via either α -elimination, in which two halogen substituents are lost from the same carbon center to yield a carbene intermediate [36] (eq 1-4), or β -elimination, where two halides are lost from adjacent carbon centers, thereby increasing the carbon-carbon bond order (eq 1-5). Vinyl [37] and alkyl polyhalides [38, 39] with halogen substituents on adjacent carbon centers undergo exclusive reductive β -elimination, whereas α -elimination and hydrogenolysis occur in parallel for species that only possess multiple halogens on the same carbon center.



Another frequent target of Fe(0) PRBs is hexavalent chromium [Cr(VI)]. Cr(VI) compounds such as chromate (CrO_4^{2-} , HCrO_4^-) and dichromate ($\text{Cr}_2\text{O}_7^{2-}$) are used extensively in industrial processes, and when discharged into the environment are highly soluble and mobile in water. Permeable reactive barriers minimize the mobility of Cr(VI) by reducing it to Cr(III), which is sparingly soluble in water and will persist as insoluble Cr(III) oxides. Notably, both Fe(0) and Fe(II) are functional reductants for Cr(VI). Reduction of Cr(VI) has been demonstrated for both granular [40] and nanoscale [41]

Fe(0), and Cr(VI) reduction has also been observed with aqueous Fe(II) [42] and several Fe(II)-containing solids including siderite [43], pyrite [44], green rust [14, 45, 46], magnetite [13], and iron sulfide [47]. In fact, the reactivity of Fe(II) toward Cr(VI) has frequently been exploited for applications of *in situ* redox manipulation. For example, Ludwig *et al.* [48] applied a combination of ferrous sulfate and sodium dithionite at a field site to immobilize a dissolved Cr(VI) plume, observing 98% removal of the initial 4-8 mg/L of Cr(VI) over 1000 days.

1.3. *Nanoscale zero-valent iron as an innovative treatment alternative to granular iron PRBs*

Despite the success of Fe(0) PRBs, there are key shortcomings that limit their application. Over time, Fe(0) corrosion products including magnetite, maghemite, various green rusts and siderite (FeCO₃) can accumulate within the PRB [49-52], causing reduction in hydraulic conductivity and reactivity loss by inhibiting electron transfer from the underlying Fe(0) [8, 53, 54]. For example, an Fe(0) PRB constructed in Ohio for TCE remediation ceased operation after only 6 months due to clogging [55]. Another limitation is that PRB application is restricted to shallow, subsurface zones where barriers can be easily constructed. This prevents their use for plumes located deep in the subsurface and diffuse pollutant plumes. It also prohibits their application to stationary pollutant source zones, which require treatment options that can be delivered specifically to the location of contamination in the subsurface.

In recent years, zero-valent iron nanoparticles (typically 10-100 nm in diameter) have shown much promise for groundwater treatment and source zone control [9, 56, 57]. Relative to traditional granular iron particles (typically 0.3-3 mm in particle diameter), nanoscale zero valent iron (or NZVI) exhibits comparable or greater removal efficiencies for the broad spectrum of chemical contaminants reduced by Fe(0) [2, 9, 41, 58-60]. Their enhanced reactivity is often attributed to their larger specific surface area (40-60 m²/g) relative to granular Fe(0) (typically < 1 m²/g) and the potential for greater inherent reactivity due to material and size-dependent reactive properties. Furthermore, their nanoscale dimensions can potentially overcome many of the practical shortcomings commonly associated with traditional granular iron PRBs; unlike larger granular iron, slurries of NZVI can be directly delivered into the subsurface at the point of contamination, thereby enabling treatment of deep DNAPL plumes and source zones (Figure 1-2). As of 2005, there were 25 field-scale applications (6 full-scale, 19 pilot-scale) of NZVI for groundwater and soil remediation [61].

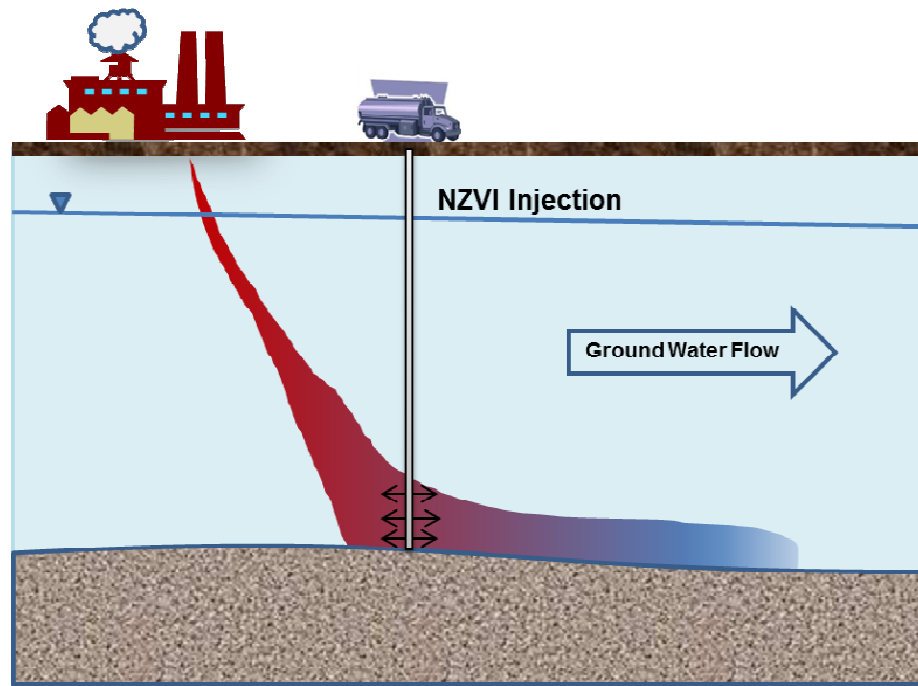


Figure 1-2. Conceptualization of NZVI *in situ* treatment for contaminant source zone.

Although early returns on NZVI field-scale performance have been encouraging [62-65], it is a developing technology and several questions persist that may hinder its growth into a mature treatment strategy. To date, most attention has focused on preventing the aggregation of NZVI particles during application, which limits its delivery in the subsurface [66]. To address this problem, surface modifiers such as triblock copolymers [67], poly(styrene sulfonate), polyaspartate and surfactant sodium dodecyl benzene sulfonate [68] have been used to stabilize NZVI particles. This keeps the particles well-dispersed and improves subsurface delivery [67-69], while only resulting in a modest decline in particle reactivity [70].

A concern that has received far less focus is the reactive lifetime or longevity of NZVI in the subsurface. Due to its high reactivity, NZVI exhibits a low degree of selectivity and will react readily with dissolved oxygen and water during subsurface application [9, 27]. These side reactions consume reducing equivalents and hasten formation of passivating Fe(III) oxides that ultimately shorten NZVI longevity.

Despite several field scale installations [61-65], data on the long-term performance of NZVI (i.e., pollutant removal over periods longer than several weeks) remains limited. Elliott and Zhang [64] observed that the reactivity of NZVI towards TCE, tetrachloroethene (PCE), and *cis*-dichloroethene (*cis*-DCE) was maintained for 4 weeks, although ORP (oxidation reduction potential) continuously increased over this duration from -360 mv to -100 mv at the injection location. Besides this field assessment, Zhang and co-workers [56] also conducted batch studies suggesting NZVI lifetimes of 6-8 weeks based on repeated spiking of reaction slurries with TCE. Longevity also has been estimated by measuring changes in the Fe(0) content within NZVI particles in aqueous suspensions over time. Fe(0) content dropped from 70% to 20% over 200 days in a concentrated, alkaline slurry (pH 10.6) under anaerobic conditions [71]. In a similar investigation, Fe(0) persisted as 30% of the particle composition after 6 months of aging in an aerobic slurry, with the aged particles displaying weak reactivity towards carbon tetrachloride [72]. Another complementary study observed ~40% Fe(0) was preserved after 6 month of exposure to anaerobic water in suspensions of 10 g/L NZVI particles, although Fe(0) content was rapidly consumed via exposure to O₂-saturated water for 24 h (~2 % Fe(0) remaining) [73].

These works estimate that NZVI has a reactive lifetime anywhere between 2-6 months in oxygen-free aqueous systems, a value that is considerably shorter than lifetimes reported or estimated for Fe(0) PRBs (with typical longevities from years to decades [74]). However, these reported longevities for NZVI likely represent the best case scenario; longevity studies to date have largely been conducted under strict anaerobic conditions and at relative high pH values that likely do not reflect the variability of subsurface environments. Furthermore, laboratory longevity studies to date have used solution conditions that do not reflect the geochemical complexity of subsurface systems. Specifically, studies have yet to consider how geochemical conditions (e.g., anionic co-solutes) affect the corrosion products generated on the surface of NZVI particles and the implications of these corrosion products on NZVI performance and longevity.

For granular Fe(0) applications, the nature of the oxide layer initially present on the particle surface and how it evolves over time is recognized to define system reducing capacity [6]. If the film is passive, it inhibits the access of electrons to target contaminants in solution, acting as a barrier between the underlying Fe(0) and aqueous phase targets. If the iron in the film is fully oxidized (i.e., typically found to contain passive Fe(III) oxides such as maghemite [17, 34, 75, 76]), the reducing capacity of the particle will be lost entirely, and electron transfer will only occur if localized defects (e.g., cracks or pits) exist in the passive layer [77]. If Fe(II) centers are present via incorporation into mixed-valent oxides (i.e., magnetite), the resistivity of the oxide film decreases, improving conduction of electrons from the Fe(0) particle core to the

pollutants at the particle water interface. For instance, Stratmann and Muller [78] suggested that the kinetics of electron transfer in Fe(0) systems is highly dependent on the ratio of Fe(II)-to-Fe(III) in overlying oxide layer.

Based on this established behavior for granular Fe(0), the composition of the oxide film that evolves on the NZVI surface will influence particle reactivity and longevity. However, very little remains known about how the corrosion products generated in NZVI systems evolve over time, vary in response to solution phase chemistry, and ultimately impact the reactivity of NZVI toward a broad spectrum of pollutants. In a noteworthy study, Liu *et al.* [79] investigated the effect of dissolved groundwater constituents on NZVI reactivity toward TCE, observing the following reactivity trend (from least inhibitory to most inhibitory): $\text{Cl}^- < \text{SO}_4^{2-} < \text{HCO}_3^- < \text{HPO}_4^{2-}$. However, the types of corrosion products generated as a result of changes in solution chemistry and the effect of these anions on NZVI lifetime were not determined. In a follow-up study by Reinsch *et al.* [73], corrosion products formed in the presence of selected anions were identified in NZVI suspensions aged over 180 days. However, characterization over time focused on loss of Fe(0), and corrosion products were not presented for all solution chemistries (e.g., products formed in the presence of carbonate were not presented). Moreover, complementary reactivity data toward a model pollutant were not collected by Reinsch *et al.* [73], preventing any correlation between their observed changes in NZVI oxidation and NZVI reactivity.

Ultimately, in the event of complete reactivity loss, current approaches for NZVI application would require multiple injections of NZVI to the subsurface to sustain

reactivity [9], which would be expensive and will negatively impact hydraulic conductivity. There are also growing concerns over potential adverse implications of engineered nanomaterials in the environment [80, 81]. Thus, the high levels of NZVI introduced into the subsurface to sustain reactivity may also be undesirable from the perspective of human and ecosystem health. To improve the field-scale performance of NZVI, broaden the range of sites amenable to treatment and mitigate concerns over material cost and the fate of engineered nanomaterials, strategies must be developed to sustain the reactivity of NZVI *in situ* treatment zones and increase the extent of pollutant removal per unit mass of NZVI applied in the field.

1.4. *Bimetallic reductants for enhancing zero-valent iron reactivity*

Over the course of Fe(0) technology development, it has been noted that certain environmental contaminants including polychlorinated biphenyls (PCBs) [82], halogenated phenols [83], and most mono- and di-substituted methyl and alkyl polychlorides (e.g., dichloromethane and 1,2-dichloroethane) [38] appear recalcitrant. Furthermore, some pollutants may undergo only partial dehalogenation, which can result in the accumulation of more persistent byproducts, as is the case for chloroform [33] and 1,1-dichloroethane [36] production from the reduction of carbon tetrachloride and 1,1,1,-trichloroethane, respectively. A popular alternative to Fe(0) that can overcome some of these shortcomings is so-called bimetallic reductants. Iron-based bimetallic reductants are generated by the deposition of a noble metal additive onto the Fe(0) particle surface,

which is typically accomplished using a plating reaction between Fe(0) and a metal salt of the additive (e.g., Pd, Pt, Ag, and Cu). Numerous studies have shown that bimetallic reductants exhibit greater reactivity than Fe(0) (see Figure 1-3) [82, 84-88], while evidence also suggests that bimetallic reductants alter product yields to favor more completely dehalogenated daughter products [84, 86, 89, 90]. The promise of enhanced reactivity and more environmentally benign transformation products has resulted in multiple field-scale applications of Fe(0)-based bimetallic reductants for treatment of contaminated groundwater and pollutant source zones [62, 64, 65, 91, 92].

Several factors are known to influence the reactivity of Fe(0)-based bimetallic reductants. These include the identity of the additive [84, 85, 88], the amount of additive deposited on Fe(0) [84, 87, 93-95], the nature (e.g., alkyl versus vinyl polyhalides) [96] and concentration [97] of the target pollutant, and relevant reaction conditions such as solution pH [94, 98], temperature [87, 94, 97] and the extent of particle aging [99, 100]. For example, reactivity of bimetallic systems typically increases with additive loading, ultimately reaching a point where reactivity either plateaus at some maximum value [84] or drops [87]. Chun *et al.* [95] found incorporation of metal additives into the Fe(0) particle as an alloy resulted in lower reactivity relative to Fe(0) particles with additives deposited on the surface, consistent with dechlorination occurring at the metal additive surface. Consistent with such a scenario, in another study [99] Pd/Fe particles exhibited an 80% decrease in reactivity toward trichloroethene over 24 h, over which time Pd islands on the Fe(0) surface became completely buried underneath extensive iron oxides that accumulated during aging.

Despite great progress in the study of Fe(0)-based bimetallic reductants, several fundamental questions about their reactivity and practical questions about their performance remain, which may ultimately limit their field-scale application. For example, Pd/Fe is perhaps the most popular Fe(0)-based bimetal because it typically exhibits the greatest reactivity. However, a close examination of the wealth of prior

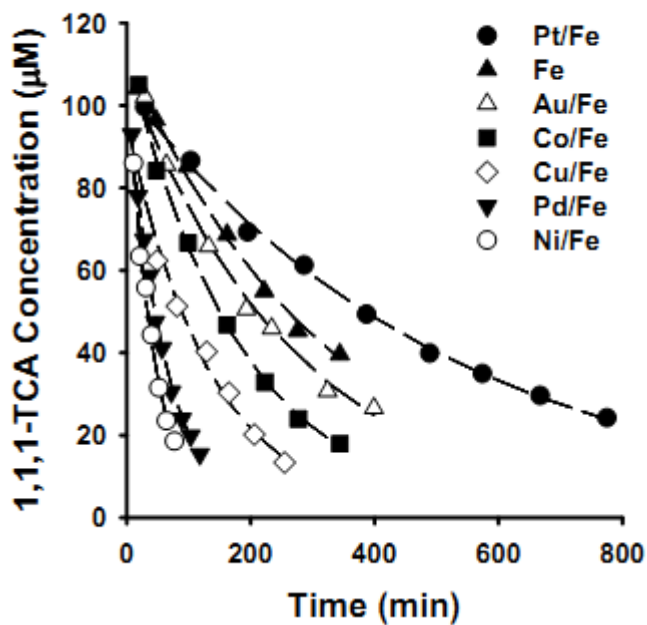


Figure 1-3. Comparison of common Fe(0)-based bimetals for the reduction of 1,1,1-trichloroethane. All reductants had a deposited additive mass of $\sim 13 \mu\text{moles/g Fe}$. Data for unamended Fe(0) is shown for comparison. From Cwiertny *et al.* [86].

results available for Pd/Fe reveals vast differences in reactivity. Specifically, reports of the magnitude by which Pd/Fe enhances reactivity relative to Fe(0) widely range from 2-fold [84] to more than 1000-fold [96], and the source of such variation is not known. Another question pertains to the type of Fe(0) used to generate bimetallic materials;

there has yet to be a systematic study demonstrating the impact of Fe(0) particle size on resulting bimetal reactivity.

From a more fundamental perspective, the molecular-level processes responsible for the enhanced reactivity displayed by bimetallic reductants remain poorly understood. One hypothesis [101, 102] attributes the enhanced reactivity of bimetallic reductants to the formation of a galvanic couple between Fe(0) and the noble metal surface additive. In the couple, Fe(0) functions as the anode whereas the noble metal surface deposit serves as the cathode at which pollutant reduction occurs. In this scenario, Fe(0) becomes preferentially oxidized, facilitating electron transfer to the solution interface through the metal additive, in turn yielding higher reduction rates. Others [35, 84, 88, 102-104] have postulated that the metal additives function as a catalyst for hydrogenation, and that adsorbed or absorbed atomic hydrogen species associated with the additive surface are the reactive entity responsible for pollutant transformation. To support such a mechanism of rate enhancement, a prior study [84] reported a strong correlation between rates of 1,1,1-trichloroethane reduction in various bimetallic systems and measures of atomic hydrogen solubility in the additives. In another study [102], a relatively large solvent kinetic isotope effect (defined as the rate of reaction in H₂O normalized to the rate of reaction in D₂O) for TCE reduction by Ni/Fe was interpreted as evidence for the involvement of some form of atomic hydrogen.

1.5. Formation and activity of nanoscale iron oxides and their role in environmental quality control

Different types of nanoscale iron oxides including hematite (α -Fe₂O₃) and goethite (α -FeOOH) can be produced naturally in soils and surface waters through mineral weathering, oxidation of ferrous iron [Fe(II)] and, in the case of Fe(II)-containing solids such as magnetite (Fe₃O₄), chemical and/or biological reduction of naturally occurring ferric iron [Fe(III)] oxides [105]. Nanoscale iron oxides, with at least one dimension less than 100 nm, possess large surface area-to-volume ratios. Thus, although they may not comprise a large mass fraction of a natural system, they may still represent important phases for interfacial reactions occurring in the subsurface or surface waters [105]. Because of their nanoscale dimensions, there is also the potential for unique surface activity relative to their larger scale analogues.

Notably, Fe(II)-containing phases (e.g., iron sulfides) and iron oxides with mixed-valent oxidation states (i.e., Fe(II)- and Fe(III)-containing phases) represent a route for the natural attenuation and remediation of groundwater contaminants in subsurface environments with low dissolved oxygen. Previous work has shown that Fe(II)-containing and mixed-valent iron oxides represent functional electron donors for highly oxidized chlorinated solvents such as trichloroethylene and tetrachloroethylene [11], carbon tetrachloride [106] and hexachloroethane [12], nitroaromatic compounds including chloronitrobenzene [12], and heavy metals such as hexavalent chromium [13]. Also, Fe(II) associated with the surface of Fe(III) oxides or soluble Fe(II) complexes can exhibit reducing capacity towards many compounds including polyhalogenated methanes

[107], pesticides such as oxamyl and methomyl [108], RDX (hexahydro-1,3,5-trinitro-1,3,5-triazine) [109] and nitroaromatic compounds [110]. For example, Klausen *et al.* observed Fe(II) associated with goethite and lepidocrocite were able to reduce nitrobenzene to aniline, while aqueous Fe(II) phases or Fe(III) oxides alone remained unreactive [111]. In addition, Amonette *et al.* [112] observed that Fe(II) sorbed to the surface of goethite actively dechlorinated carbon tetrachloride to chloroform under anoxic conditions.

With the advent of Fe(0)-based treatment technologies, it has become clear that in addition to the natural routes of iron oxide formation discussed above, a variety of redox active iron phase can be produced at the Fe(0) particle-water interface via corrosion. Trends in corrosion product formation in granular iron systems are well established, and work on their production in NZVI systems is growing. Notably, as nanoscale corrosion products have been observed for granular Fe(0) [50], it is highly likely that corrosion products of NZVI will also be of nanoscale dimensions. Harnessing the reactivity of high surface area, Fe(II)-containing products of NZVI corrosion may, therefore, represent a viable route to sustaining the redox activity of *in situ* treatment zones long after Fe(0) is lost from the system. These Fe(II)-containing phases will be produced in large quantities in NZVI systems due to the high corrosion rate exhibited by NZVI [113], and their lower reactivity relative to Fe(0) should make them persist longer through slower rates of reaction with non-target species in the subsurface such as water and oxygen.

Another promising application of nanoscale iron oxides arising from their high surface area is as adsorbents, particularly towards regulated metals such as chromium

[114-116] and arsenic [117, 118], for which iron oxides are recognized to be efficient sorbents. However, a common challenge encountered during the application of high surface area nanoparticles relates to their instability in suspensions at environmentally relevant pH values, which results in nanoparticle aggregation that constrains available surface area [119] and limits mass transport and surface activity [120]. To overcome this shortcoming, a promising application route for iron oxide nanoparticles is through their integration and immobilization on support structures. Traditional supports considered for Fe(III) oxides include activated carbon [22] and clays [23].

A promising support material that has yet to garner much interest for environmental treatment applications is carbon nanotubes. Carbon nanotubes (CNTs) exhibit several favorable properties as support structures including their high external surface area and their mechanical strength, which should make them stable in extreme chemical environments. Most importantly, several routes are available for the synthesis of hybrid nanostructures of CNTs decorated with metal or metal oxide nanoparticles [121-123]. CNTs have been widely utilized as supports in catalysis for metals including Sn [124], Au [125], Pt [126], Ag [127]. These nanocomposites were synthesized through established approaches such as an incipient wetness impregnation procedure [128], sol-gel technique [129], chemical vapor deposition [130], ball milling [131] and electron beam evaporation [132]. For iron oxides nanoparticles, magnetite has been most extensively explored for growth on CNT surfaces [133-135].

A potential benefit of using CNT-supported iron oxides as sorbents is that the distribution and size of the deposited oxides can be tuned during synthesis and post-

processing, which allows unique control over the specific surface area and sorption capacity of the hybrid nanomaterial sorbent. Furthermore, the use of CNTs as a support allows for various application platforms that are more ideal for large scale water treatment than traditional sorbent particles suspensions. The ability to immobilize CNTs on membrane supports [136, 137] allows application in which a fixed bed of hybridized CNTs sorbents can treat high flow rates of water while minimizing nanoparticle release into the treated product. Nevertheless, despite the great promise of hybrid iron oxide-CNT nanostructures as sorbent materials for environmental quality control, there is little work available on their synthesis, optimization and performance during water treatment.

1.6. Thesis organization

This work contains four chapters of original research investigating routes to optimize the application of NZVI, Fe(0)-based bimetallic reductants (e.g., Pd/Fe), and nanoscale iron oxides for treatment of impaired water supplies. The overall objective of this work is to increase the application and performance of Fe(0) and iron oxide nanoparticles for treatment of contaminated groundwater and surface water. Specific objectives are detailed below for each chapter, which utilize a general experimental approach that couples reactivity studies with materials characterization to develop insights into the properties of iron-based nanomaterials most responsible for their chemical activity.

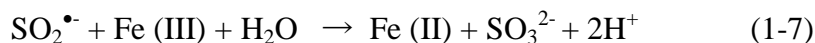
The work in Chapter 2 aims to better predict the lifetime of NZVI over a range of geochemical conditions representative of *in situ* treatment zones. Over one month,

reactivity studies measured 1,1,1,2-tetrachloroethane (1,1,1,2-TeCA) degradation rates, hexavalent chromium [Cr(VI)] removal capacities, values of oxidation-reduction potential (ORP) and rates of Fe(II) production from NZVI corrosion. The suspensions of NZVI used in reactivity studies were aged under different geochemical conditions (e.g., various co-solutes, pH values, redox environments), and changes in reactivity over time were related to the evolving mineralogy of suspensions via characterization with transmission electron microscopy (TEM) and X-ray diffraction (XRD).

The co-solutes investigated in Chapter 2 were nitrate, carbonate, sulfate, chloride and perchlorate, which were chosen because of their environmental relevance and their different degree of interaction with Fe(0) based upon trends established for larger scale granular iron. Nitrate can be reduced by Fe(0) [138-140], whereas carbonate, depending on its concentration, is reported to either enhance or inhibit Fe(0) reactivity through formation of redox-active carbonate green rust species [14] or passivating siderite [FeCO₃(s)] [53, 141-143], respectively. Chloride and sulfate are corrosion promoters that can also favor the formation of redox-active green rust species [77, 144-147]. Perchlorate was used as a control, as it is widely considered to interact minimally with Fe(0) surfaces [148, 149]. Solution pH also plays a significant role in Fe(0) reactivity, with several studies observing that the reactivity of micron-sized Fe(0) decreases with increasing pH, behavior that is likely linked to precipitation of passive iron oxides that block reactive sites [150]. In Chapter 2, pH was maintained using pH buffers at environmentally relevant values (pH 7 and 8), improving upon other studies that have not

stabilized pH and, in turn, achieved suspension pH values unrealistic for field-scale treatment applications (pH ~10) during aging.

Chapter 3 explores simple, cost-effective chemical amendments that can be used in tandem with NZVI to enhance the longevity of *in situ* treatment zones by transforming passive corrosion products into Fe(II)-containing phases that represent functional reductants for several common groundwater contaminants. The reductant utilized in Chapter 3 is dithionite, a strong reductant ($E^0 = -1.12$ V) and a sulfur-containing oxyanion ($S_2O_4^{2-}$) that has previously been used for groundwater remediation [15, 151] via *in situ* redox manipulation. During application dithionite decomposes to two highly reactive sulfoxyl radicals (eq 1-6) that can reduce Fe(III) to yield various forms of soluble, complexed and solid-phase Fe(II) (eq 1-7).



In Chapter 3, suspensions of NZVI were aged under a variety of aqueous conditions, including in the presence and absence of oxygen over a range of environmentally relevant pH values. Reactivity loss over time was monitored toward 1,1,1,2-TeCA and Cr(VI), and upon complete reactivity loss, passive NZVI suspensions were reacted with various amounts of dithionite in an attempt to restore the reducing capacity of the suspension. Reactivity studies with 1,1,1,2-TeCA and Cr(VI) were once again conducted to assess the efficiency of dithionite in restoring reactivity to the passivated suspensions, whereas materials characterization on the suspension both before

and after reaction with dithionite was used to determine the reactive phases produced via the regeneration reaction that were responsible for the restored redox capacity.

The potential benefits of the work in Chapter 3 are great. Using dithionite as a chemical regenerant of passivated NZVI treatment zones, site longevity can be extended, allowing lower amounts of NZVI to obtain clean-up goals. Furthermore, the ability to sustain NZVI longevity may also facilitate a wider range of applications, including the use of NZVI injection at polluted environments that are not strictly anaerobic.

Chapter 4 aims to identify the optimal conditions for the field-scale application of Pd/Fe bimetallic reductants, while also exploring the underlying mechanism responsible for the enhanced reactivity of Pd/Fe relative to unamended Fe(0). Experiments examined the reactivity enhancement afforded by Pd/Fe relative to Fe(0) over a range of Pd loadings, Pd/Fe reductant loading or concentration (in g/L), initial concentration of the target chlorinated solvents (1,1,1,2-TeCA and *cis*-DCE), anaerobic aging timescales (up to one month), and solution pH. This work also represents the first to systematically compare the reactivity of Pd/Fe generated from NZVI relative to larger, micron-sized Fe(0) particles, attempting to identify the impact of the Fe(0) substrate in the overall reactivity of the Pd/Fe reductant.

For mechanistic insights, the origin of reactivity enhancement in the Pd/Fe systems was explored through measurement of solvent kinetics isotope effects (hereafter referred to as SKIEs), defined as the rate constant for pollutant transformation in water normalized to the rate constant in a corresponding system with D₂O [$k_{\text{obs}}(\text{H}_2\text{O})/k_{\text{obs}}(\text{D}_2\text{O})$]. SKIEs were quantified as a function of Pd loading and Pd/Fe concentration,

and significant SKIEs were interpreted as evidence for the involvement of surface associated atomic hydrogen in pollutant transformation reactions. Practical implications for these mechanistic insights are presented in the form of SKIEs measured for Pd/NZVI reductants that were aged over one month in anaerobic suspensions so as to simulate field-scale application.

Finally, Chapter 5 develops novel hematite-coated multi-walled carbon nanotubes (α -Fe₂O₃/MWCNT) and applies these hybrid nanostructures as high-surface area sorbents for heavy metals during water treatment. Hybrid α -Fe₂O₃/MWCNT nanostructures were prepared through the surface-assisted forced hydrolysis of ferric nitrate in the presence of MWCNTs. The amount of deposited α -Fe₂O₃, which influences the nanoparticle size and coverage density, was tuned during synthesis and the sorption capacity of the resulting nanomaterials was examined toward Cu(II) and Cr(VI) as a function of pH and metal concentration. Sorption properties of the hybrid nanostructures were then compared to metal uptake in systems with the individual material components (e.g., dispersions of nanoscale hematite particles or MWCNTs) and observed sorption trends were related to material properties obtained through complementary materials characterization (e.g., TEM with selected area diffraction, total deposited iron through acid digestion, suspensions sedimentation rates and zeta potential analysis).

1.7. Literature Cited

1. Gillham, R.W.; O'Hannesin, S.F., Enhanced Degradation of Halogenated Aliphatics by Zero-Valent Iron. *Ground Water* **1994**, 32, 958-967.

2. Kanel, S.R.; Manning, B.; Charlet, L.; Choi, H., Removal of Arsenic(III) from Groundwater by Nanoscale Zero-Valent Iron. *Environ. Sci. Technol.* **2005**, 39, 1291-1298.
3. Puls, R.W.; Blowes, D.W.; Gillham, R.W., Long-Term Performance Monitoring for a Permeable Reactive Barrier at the U.S. Coast Guard Support Center, Elizabeth City, North Carolina. *J. Haz. Mater.* **1999**, 68, 109-124.
4. Wilkin, R.T.; Su, C.; Ford, R.G.; Paul, C.J., Chromium-Removal Processes During Groundwater Remediation by a Zerovalent Iron Permeable Reactive Barrier. *Environ. Sci. Technol.* **2005**, 39, 4599-4605.
5. Wang, Y.; Salvage, K., Immobilization of Uranium in the Presence of Fe(0)(s): Model Development and Simulation of Contrasting Experimental Conditions. *Appl. Geochem.* **2005**, 20, 1268-1283.
6. Scherer, M.M.; Balko, B.; Tratnyek, P., The Role of Oxides in Reduction Reactions at the Metal-Water Interface. In *Kinetics and Mechanism of Reactions at the Mineral/Water Interface*, American Chemical Society: Washington, DC, 1999; pp 301-322.
7. U.S. Environmental Protection Agency. *Field Applications of in Situ Remediation Technologies: Permeable Reactive Barriers*; U.S. EPA, Office of Solid Waste and Emergency Response, Technology Innovation Office: Washington, DC, 2002.
8. Henderson, A.D.; Demond, A.H., Long-Term Performance of Zero-Valent Iron Permeable Reactive Barriers: A Critical Review. *Environ. Eng. Sci.* **2007**, 24.
9. Tratnyek, P.G.; Johnson, R.L., Nanotechnologies for Environmental Cleanup. *Nano Today* **2006**, 1, 44-48.
10. Lovley, D.R., Microbial Fe(III) Reduction in Subsurface Environments. *FEMS Microbiol. Rev.* **1997**, 20, 305-313.
11. Butler, E.C.; Hayes, K.F., Kinetics of the Transformation of Trichloroethylene and Tetrachloroethylene by Iron Sulfide. *Environ. Sci. Technol.* **1999**, 33, 2021-2027.
12. Elsner, M.; Schwarzenbach, R.P.; Haderlein, S.B., Reactivity of Fe(II)-Bearing Minerals toward Reductive Transformation of Organic Contaminants. *Environ. Sci. Technol.* **2004**, 38, 799-807.

13. Peterson, M.L.; White, A.F.; Brown, G.E.; Parks, G.A., Surface Passivation of Magnetite by Reaction with Aqueous Cr(VI): XAFS and TEM Results. *Environ. Sci. Technol.* **1997**, 31, 1573-1576.
14. Williams, A.G.B.; Scherer, M.M., Kinetics of Cr(VI) Reduction by Carbonate Green Rust. *Environ. Sci. Technol.* **2001**, 35, 3488-3494.
15. Amonette, J.E.; Szecsody, J.E.; Schaef, H.T.; Templeton, J.C.; Gorby, Y.A.; Fruchter, J.S., Abiotic Reduction of Aquifer Materials by Dithionite: A Promising In-Situ Remediation Technology. In *In Situ Remediation: Scientific Basis for Current and Future Technologies*, Gee, G. W.; Wing, N. R., Eds. Battelle Press: Columbus, OH, 1994; pp 851-881.
16. Zwiernik, M.J.; Quensen, J.F.; Boyd, S.A., FeSO₄ Amendments Stimulate Extensive Anaerobic PCB Dechlorination. *Environ. Sci. Technol.* **1998**, 32, 3360-3365.
17. Cornell, R.M.; Schwertmann, U., *The Iron Oxides: Structure, Properties, Reactions, Occurrences and Uses* 2nd ed.; Wiley-VCH: Weinheim, Germany, 2003; p 664.
18. Stumm, W.; Morgan, J.J., *Aquatic Chemistry: Chemical Equilibria and Rates in Natural Waters*. John Wiley and Sons: New York, 1981.
19. Parfitt, R.L., Phosphate Reactions with Natural Allophane, Ferrihydrite and Goethite. *J. Soil Sci.* **1989**, 40, 359-369.
20. Zhang, W.; Singh, P.; Paling, E.; Delides, S., Arsenic Removal from Contaminated Water by Natural Iron Ores. *Miner. Eng.* **2004**, 17, 517-524.
21. Siemens, GFH® Media for Arsenic Removal, http://www.water.siemens.com/sitecollectiondocuments/product_lines/general_filter_products/brochures/gf-gfh-br-0709.29.pdf; accessed October 25, 2011.
22. Oliveira, L.C.A.; Rios, R.V.R.A.; Fabris, J.D.; Garg, V.; Sapag, K.; Lago, R.M., Activated Carbon/Iron Oxide Magnetic Composites for the Adsorption of Contaminants in Water. *Carbon* **2002**, 40, 2177-2183.
23. Oliveira, L.C.A.; Rios, R.V.R.A.; Fabris, J.D.; Sapag, K.; Garg, V.K.; Lago, R.M., Clay Iron Oxide Magnetic Composites for the Adsorption of Contaminants in Water. *Appl. Clay Sci.* **2003**, 22, 169-177.
24. Benjamin, M.M.; Sletten, R.S.; Bailey, R.P.; Bennett, T., Sorption and Filtration of Metals Using Iron-Oxide-Coated Sand. *Water Res.* **1996**, 30, 2609-2620.

25. Katsoyiannis, I.A.; Zouboulis, A.I., Removal of Arsenic from Contaminated Water Sources by Sorption onto Iron-Oxide-Coated Polymeric Materials. *Water Res.* **2002**, 36, 5141-5155.
26. U.S. Environmental Protection Agency, *Field Applications of In Situ Remediation Technologies: Permeable Reactive Barriers*. US EPA, Office of Solid Waste and Emergency Response, Technology Innovation Office: EPA-68-W-00-084, Washington, DC, 2002.
27. Gillham, R.W., Factors in the Long-Term Performance of Granular Iron PRBs. *Ground Water Monitoring and Remediation* **2001**, 23.
28. Thiruvengkatachari, R.; Vigneswaran, S.; Naidu, R., Permeable Reactive Barrier for Groundwater Remediation. *J. Ind. Eng. Chem.* **2008**, 14, 145-156.
29. U.S. Environmental Protection Agency, *Permeable Reactive Barrier Technologies for Contaminant Remediation*; EPA-600-R-98-125; U.S. Environmental Protection Agency, Office of Research and Development and Office of Solid Waste and Emergency Response: Washington, D.C., 1998.
30. Powell, R.M.; Powell, P.D.; Puls, R.W. *Economic Analysis of the Implementation of Permeable Reactive Barriers for Remediation of Contaminated Ground Water*; EPA/600/R-02/034; United States Environmental Protection Agency, National Risk Management Research Laboratory, Subsurface Protection and Remediation Division: 2002.
31. EnvironMetals Technologies (an Adventus company); <http://www.eti.ca>; accessed October 20, 2011.
32. Pankow, J.F.; Cherry, J.A., Dense Chlorinated Solvents and Other Dnaps in Groundwater. Waterloo Press: 1996; p 525.
33. Matheson, L.J.; Tratnyek, P.G., Reductive Dehalogenation of Chlorinated Methanes by Iron Metal. *Environ. Sci. Technol.* **1994**, 28, 2045-2053.
34. Ritter, K.; Odziemkowski, M.S.; Gillham, R.W., An In Situ Study of the Role of Surface Films on Granular Iron in the Permeable Iron Wall Technology. *J. Contam. Hydrol.* **2002**, 55, 87-111.
35. Li, T.; Farrell, J., Reductive Dechlorination of Trichloroethene and Carbon Tetrachloride Using Iron and Palladized-Iron Cathodes. *Environ. Sci. Technol.* **2000**, 34, 173-179.

36. Fennelly, J.P.; Roberts, A.L., Reaction of 1,1,1-Trichloroethane with Zero-Valent Metals and Bimetallic Reductants. *Environ. Sci. Technol.* **1998**, 32, 1980-1988.
37. Arnold, W.A.; Roberts, A.L., Pathways and Kinetics of Chlorinated Ethylene and Chlorinated Acetylene Reaction with Fe(0) Particles. *Environ. Sci. Technol.* **2000**, 34, 1794-1805.
38. Cwiertny, D.M.; Arnold, W.A.; Kohn, T.; Rodenburg, L.A.; Roberts, A.L., Reactivity of Alkyl Polyhalides toward Granular Iron: Development of Qsars and Reactivity Cross Correlations for Reductive Dehalogenation. *Environ. Sci. Technol.* **2010**, 44, 7928-7936.
39. Cwiertny, D.M.; Roberts, A.L., On the Nonlinear Relationship between k_{obs} and Reductant Mass Loading in Iron Batch Systems. *Environ. Sci. Technol.* **2005**, 39, 8948-8957.
40. Kaplan, D.; Gilmore, T., Zero-Valent Iron Removal Rates of Aqueous Cr(VI) Measured under Flow Conditions. *Water Air Soil Poll.* **2004**, 155, 21-33.
41. Li, X.-Q.; Cao, J.; Zhang, W.-X., Stoichiometry of Cr(VI) Immobilization Using Nanoscale Zerovalent Iron (NZVI): A Study with High-Resolution X-Ray Photoelectron Spectroscopy (HR-XPS). *Ind. Eng. Chem. Res.* **2008**, 47, 2131-2139.
42. Fendorf, S.E.; Li, G., Kinetics of Chromate Reduction by Ferrous Iron. *Environ. Sci. Technol.* **1996**, 30, 1614-1617.
43. Erdem, M.; Gr, F.; Tmen, F., Cr(VI) Reduction in Aqueous Solutions by Siderite. *J. Haz. Mater.* **2004**, 113, 217-222.
44. Blowes, D.W.; Ptacek, C.J.; Jambor, J.L., In-Situ Remediation of Cr(VI)-Contaminated Groundwater Using Permeable Reactive Walls: Laboratory Studies. *Environ. Sci. Technol.* **1997**, 31, 3348-3357.
45. Loyaux-Lawniczak, S.; Refait, P.; Ehrhardt, J.-J.; Lecomte, P.; Genin, J.-M.R., Trapping of Cr by Formation of Ferrihydrite During the Reduction of Chromate Ions by Fe(II)-Fe(III) Hydroxysalt Green Rusts. *Environ. Sci. Technol.* **1999**, 34, 438-443.
46. Skovbjerg, L.L.; Stipp, S.L.S.; Utsunomiya, S.; Ewing, R.C., The Mechanisms of Reduction of Hexavalent Chromium by Green Rust Sodium Sulphate: Formation of Cr-Goethite. *Geochim. Cosmochim. Acta* **2006**, 70, 3582-3592.

47. Patterson, R.R.; Fendorf, S.; Fendorf, M., Reduction of Hexavalent Chromium by Amorphous Iron Sulfide. *Environ. Sci. Technol.* **1997**, 31, 2039-2044.
48. Ludwig, R.D.; Su, C.; Lee, T.R.; Wilkin, R.T.; Acree, S.D.; Ross, R.R.; Keeley, A., In Situ Chemical Reduction of Cr(VI) in Groundwater Using a Combination of Ferrous Sulfate and Sodium Dithionite: A Field Investigation. *Environ. Sci. Technol.* **2007**, 41, 5299-5305.
49. Furukawa, Y.; Kim, J.-w.; Watkins, J.; Wilkin, R.T., Formation of Ferrihydrite and Associated Iron Corrosion Products in Permeable Reactive Barriers of Zero-Valent Iron. *Environ. Sci. Technol.* **2002**, 36, 5469-5475.
50. Kohn, T.; Livi, K.J.T.; Roberts, A.L.; Vikesland, P.J., Longevity of Granular Iron in Groundwater Treatment Processes: Corrosion Product Development. *Environ. Sci. Technol.* **2005**, 39, 2867-2879.
51. Phillips, D.H.; Gu, B.; Watson, D.B.; Roh, Y.; Liang, L.; Lee, S.Y., Performance Evaluation of a Zerovalent Iron Reactive Barrier: Mineralogical Characteristics. *Environ. Sci. Technol.* **2000**, 34, 4169-4176.
52. Roh, Y.; Lee, S.Y.; Elless, M.P., Characterization of Corrosion Products in the Permeable Reactive Barriers. *Environ. Geol.* **2000**, 40, 184-194.
53. Mackenzie, P.D.; Horney, D.P.; Sivavec, T.M., Mineral Precipitation and Porosity Losses in Granular Iron Columns. *J. Haz. Mater.* **1999**, 68, 1-17.
54. Kober, R.; Schlicker, O.; Ebert, M.; Dahmke, A., Degradation of Chlorinated Ethylenes by Fe(0): Inhibition Processes and Mineral Precipitation. *Environ. Geol.* **2002**, 41, 644-652.
55. Liang, L.Y.; Korte, N.; Gu, B.H.; Puls, R.; Reeter, C., Geochemical and Microbial Reactions Affecting the Long-Term Performance of in Situ "Iron Barriers". *Adv. Environ. Res.* **2000**, 4, 273-286.
56. Zhang, W.-X., Nanoscale Iron Particles for Environmental Remediation: An Overview. *J. Nanopart. Res.* **2003**, 5, 323-332.
57. Li, X.-Q.; Elliott, D.W.; Zhang, W.-X., Zero-Valent Iron Nanoparticles for Abatement of Environmental Pollutants: Materials and Engineering Aspects. *Sol. State Mater. Sci.* **2006**, 31, 111-122.
58. Choe, S.; Lee, S.-H.; Chang, Y.-Y.; Hwang, K.-Y.; Khim, J., Rapid Reductive Destruction of Hazardous Organic Compounds by Nanoscale Fe(0). *Chemosphere* **2001**, 42, 367-372.

59. Song, H.; Carraway, E.R., Reduction of Chlorinated Methanes by Nano-Sized Zero-Valent Iron. Kinetics, Pathways, and Effect of Reaction Conditions. *Environ. Eng. Sci.* **2006**, 23, 13.
60. Nurmi, J.T.; Tratnyek, P.G.; Sarathy, V.; Baer, D.R.; Amonette, J.E.; Pecher, K.; Wang, C.; Linehan, J.C.; Matson, D.W.; Penn, R.L.; Driessen, M.D., Characterization and Properties of Metallic Iron Nanoparticles: Spectroscopy, Electrochemistry, and Kinetics. *Environ. Sci. Technol.* **2005**, 39, 1221-1230.
61. Watlington, K. *Emerging Nanotechnologies for Site Remediation and Wastewater Treatment*. U.S. EPA ,Office of Solid Waste and Emergency Response, Office of Superfund Remediation and Technology Innovation, Technology and Field Services Division: Washington, DC, 2005.
62. He, F.; Zhao, D.; Paul, C., Field Assessment of Carboxymethyl Cellulose Stabilized Iron Nanoparticles for *In Situ* Destruction of Chlorinated Solvents in Source Zones. *Water Res.* **2010**, 44, 2360-2370.
63. Henn, K.W.; Waddill, D.W., Utilization of Nanoscale Zero-Valent Iron for Source Remediation- A Case Study. *Remediation Journal* **2006**, 16, 57-77.
64. Elliott, D.W.; Zhang, W.-X., Field Assessment of Nanoscale Bimetallic Particles for Groundwater Treatment. *Environ. Sci. Technol.* **2001**, 35, 4922-4926.
65. Wei, Y.-T.; Wu, S.-C.; Chou, C.-M.; Che, C.-H.; Tsai, S.-M.; Lien, H.-L., Influence of Nanoscale Zero-Valent Iron on Geochemical Properties of Groundwater and Vinyl Chloride Degradation: A Field Case Study. *Water Res.* **2010**, 44, 131-140.
66. Phenrat, T.; Saleh, N.; Sirk, K.; Tilton, R.D.; Lowry, G.V., Aggregation and Sedimentation of Aqueous Nanoscale Zerovalent Iron Dispersions. *Environ. Sci. Technol.* **2006**, 41, 284-290.
67. Saleh, N.; Phenrat, T.; Sirk, K.; Dufour, B.; Ok, J.; Sarbu, T.; Matyjaszewski, K.; Tilton, R.D.; Lowry, G.V., Adsorbed Triblock Copolymers Deliver Reactive Iron Nanoparticles to the Oil/Water Interface. *Nano Lett.* **2005**, 5, 2489-2494.
68. Saleh, N.; Kim, H.-J.; Phenrat, T.; Matyjaszewski, K.; Tilton, R.D.; Lowry, G.V., Ionic Strength and Composition Affect the Mobility of Surface-Modified Fe⁰ Nanoparticles in Water-Saturated Sand Columns. *Environ. Sci. Technol.* **2008**, 42, 3349-3355.

69. Phenrat, T.; Kim, H.-J.; Fagerlund, F.; Illangasekare, T.; Tilton, R.D.; Lowry, G.V., Particle Size Distribution, Concentration, and Magnetic Attraction Affect Transport of Polymer-Modified Fe(0) Nanoparticles in Sand Columns. *Environ. Sci. Technol.* **2009**, 43, 5079-5085.
70. Phenrat, T.; Liu, Y.; Tilton, R.D.; Lowry, G.V., Adsorbed Polyelectrolyte Coatings Decrease Fe(0) Nanoparticle Reactivity with Tce in Water: Conceptual Model and Mechanisms. *Environ. Sci. Technol.* **2009**, 43, 1507-1514.
71. Liu, Y.; Lowry, G.V., Effect of Particle Age (Fe(0) Content) and Solution pH on NZVI Reactivity: H₂ Evolution and TCE Dechlorination. *Environ. Sci. Technol.* **2006**, 40, 6085-6090.
72. Sarathy, V.; Tratnyek, P.G.; Nurmi, J.T.; Baer, D.R.; Amonette, J.E.; Chun, C.L.; Penn, R.L.; Reardon, E.J., Aging of Iron Nanoparticles in Aqueous Solution: Effects on Structure and Reactivity. *J. Phys. Chem. C.* **2008**, 112, 2286-2293.
73. Reinsch, B.C.; Forsberg, B.; Penn, R.L.; Kim, C.S.; Lowry, G.V., Chemical Transformations During Aging of Zerovalent Iron Nanoparticles in the Presence of Common Groundwater Dissolved Constituents. *Environ. Sci. Technol.* **2010**, 44, 3455-3461.
74. Blowes, D.W.; Ptacek, C.J.; Benner, S.G.; McRae, C.W.T.; Bennett, T.A.; Puls, R.W., Treatment of Inorganic Contaminants Using Permeable Reactive Barriers. *J. Contam. Hydrol.* **2000**, 45, 123-137.
75. Farrell, J.; Wang, J.; O'Day, P.; Conklin, M., Electrochemical and Spectroscopic Study of Arsenate Removal from Water Using Zero-Valent Iron Media. *Environ. Sci. Technol.* **2001**, 35, 2026-2032.
76. Jolivet, J.-P.; Tronc, E., Interfacial Electron Transfer in Colloidal Spinel Iron Oxide. Conversion of Fe₃O₄-Fe₂O₃ in Aqueous Medium. *J. Coll. Inter. Sci.* **1988**, 125, 688-701.
77. Gotpagar, J.; Lyuksyutov, S.; Cohn, R.; Grulke, E.; Bhattacharyya, D., Reductive Dehalogenation of Trichloroethylene with Zero-Valent Iron: Surface Profiling Microscopy and Rate Enhancement Studies. *Langmuir* **1999**, 15, 8412-8420.
78. Stratmann, M.; Muller, J., The Mechanism of the Oxygen Reduction on Rust-Covered Metal Substrates. *Corros. Sci.* **1994**, 36, 327-359.
79. Liu, Y.; Phenrat, T.; Lowry, G.V., Effect of TCE Concentration and Dissolved Groundwater Solutes on NZVI-Promoted TCE Dechlorination and H₂ Evolution. *Environ. Sci. Technol.* **2007**, 41, 7881-7887.

80. Wiesner, M.R.; Lowry, G.V.; Alvarez, P.; Dionysiou, D.; Biswas, P., Assessing the Risks of Manufactured Nanomaterials. *Environ. Sci. Technol.* **2006**, 40, 4336-4345.
81. Lowry, G.V.; Casman, E.A., Nanomaterial Transport, Transformation, and Fate in the Environment: A Risk-Based Perspective on Research Needs. In *Risk, Uncertainty and Decision Analysis for Nanomaterials: Environmental Risks and Benefits and Emerging Consumer Products*, Linkov, I.; Steevens, J., Eds. Springer Amsterdam, Netherlands, 2009; pp 125-137.
82. Wang, C.-B.; Zhang, W.-X., Synthesizing Nanoscale Iron Particles for Rapid and Complete Dechlorination of TCE and PCBs. *Environ. Sci. Technol.* **1997**, 31, 2154-2156.
83. Kim, Y.-H.; Carraway, E.R., Dechlorination of Pentachlorophenol by Zero Valent Iron and Modified Zero Valent Irons. *Environ. Sci. Technol.* **2000**, 34, 2014-2017.
84. Cwiertny, D.M.; Bransfield, S.J.; Livi, K.J.T.; Fairbrother, D.H.; Roberts, A.L., Exploring the Influence of Granular Iron Additives on 1,1,1-Trichloroethane Reduction. *Environ. Sci. Technol.* **2006**, 40, 6837-6843.
85. Kim, Y.-H.; Carraway, E.R., Reductive Dechlorination of TCE by Zero Valent Bimetals. *Environ. Technol.* **2003**, 24, 69-75(7).
86. Lien, H.-L.; Zhang, W.-X., Nanoscale Iron Particles for Complete Reduction of Chlorinated Ethenes. *Coll. Surf. A* **2001**, 191, 97-105.
87. Lien, H.-L.; Zhang, W.-X., Nanoscale Pd/Fe Bimetallic Particles: Catalytic Effects of Palladium on Hydrodechlorination. *Appl. Catal. B. Environ.* **2007**, 77, 110-116.
88. Lin, C.J.; Lo, S.L.; Liou, Y.H., Dechlorination of Trichloroethylene in Aqueous Solution by Noble Metal-Modified Iron. *J. Haz. Mater.* **2004**, 116, 219-228.
89. Muftikian, R.; Fernando, Q.; Korte, N., A Method for the Rapid Dechlorination of Low Molecular Weight Chlorinated Hydrocarbons in Water. *Water Res.* **1995**, 29, 2434-2439.
90. Zhang, W.-X.; Wang, C.-B.; Lien, H.-L., Treatment of Chlorinated Organic Contaminants with Nanoscale Bimetallic Particles. *Catal. Today* **1998**, 40, 387-395.

91. U.S. Environmental Protection Agency, Selected Sites Using or Testing Nanoparticles for Remediation (www.clu-in.org/download/remed/nano-site-list.pdf) Office of Solid Waste and Emergency Response, 2008.
92. Korte, N.E.; Zutman, J.L.; Schlosser, R.M.; Liang, L.; Gu, B.; Fernando, Q., Field Application of Palladized Iron for the Dechlorination of Trichloroethene. *Waste Management* **2000**, 20, 687-694.
93. Bransfield, S.J.; Cwiertny, D.M.; Roberts, A.L.; Fairbrother, D.H., Influence of Copper Loading and Surface Coverage on the Reactivity of Granular Iron toward 1,1,1-Trichloroethane. *Environ. Sci. Technol.* **2006**, 40, 1485-1490.
94. Wei, J.; Xu, X.; Liu, Y.; Wang, D., Catalytic Hydrodechlorination of 2,4-Dichlorophenol over Nanoscale Pd/Fe: Reaction Pathway and Some Experimental Parameters. *Water Res.* **2006**, 40, 348-354.
95. Chun, C.L.; Baer, D.R.; Matson, D.W.; Amonette, J.E.; Penn, R.L., Characterization and Reactivity of Iron Nanoparticles Prepared with Added Cu, Pd, and Ni. *Environ. Sci. Technol.* **2010**, 44, 5079-5085.
96. Cwiertny, D.M.; Bransfield, S.J.; Roberts, A.L., Influence of the Oxidizing Species on the Reactivity of Iron-Based Bimetallic Reductants. *Environ. Sci. Technol.* **2007**, 41, 3734-3740.
97. Fang, Y.; Al-Abed, S.R., Dechlorination Kinetics of Monochlorobiphenyls by Fe/Pd: Effects of Solvent, Temperature, and PCB Concentration. *Appl. Catal. B. Environ.* **2008**, 78, 371-380.
98. Fang, Y.; Al-Abed, S.R., Correlation of 2-Chlorobiphenyl Dechlorination by Fe/Pd with Iron Corrosion at Different pH. *Environ. Sci. Technol.* **2008**, 42, 6942-6948.
99. Yan, W.; Herzing, A.A.; Li, X.-Q.; Kiely, C.J.; Zhang, W.-X., Structural Evolution of Pd-Doped Nanoscale Zero-Valent Iron (NZVI) in Aqueous Media and Implications for Particle Aging and Reactivity. *Environ. Sci. Technol.* **2010**, 44, 4288-4294.
100. Zhu, B.-W.; Lim, T.-T., Catalytic Reduction of Chlorobenzenes with Pd/Fe Nanoparticles: Reactive Sites, Catalyst Stability, Particle Aging, and Regeneration. *Environ. Sci. Technol.* **2007**, 41, 7523-7529.
101. Xu, Y.; Zhang, W.-X., Subcolloidal Fe/Ag Particles for Reductive Dehalogenation of Chlorinated Benzenes. *Ind. Eng. Chem. Res.* **2000**, 39, 2238-2244.

102. Schrick, B.; Blough, J.L.; Jones, A.D.; Mallouk, T.E., Hydrodechlorination of Trichloroethylene to Hydrocarbons Using Bimetallic Nickel Iron Nanoparticles. *Chem. Mater.* **2002**, 14, 5140-5147.
103. Bryden, K.J.; Ying, J.Y., Pulsed Electrodeposition Synthesis and Hydrogen Absorption Properties of Nanostructured Palladium-Iron Alloy Films. *J. Electrochem. Soc.* **1998**, 145, 3339-3346.
104. Cheng, I.F.; Fernando, Q.; Korte, N., Electrochemical Dechlorination of 4-Chlorophenol to Phenol. *Environ. Sci. Technol.* **1997**, 31, 2443-2443.
105. Waychunas, G.A.; Kim, C.S.; Banfield, J.F., Nanoparticulate Iron Oxide Minerals in Soils and Sediments: Unique Properties and Contaminant Scavenging Mechanisms. *J. Nanopart. Res.* **2005**, 7, 409-433.
106. McCormick, M.L.; Bouwer, E.J.; Adriaens, P., Carbon Tetrachloride Transformation in a Model Iron-Reducing Culture: Relative Kinetics of Biotic and Abiotic Reactions. *Environ. Sci. Technol.* **2002**, 36, 403-410.
107. Pecher, K.; Haderlein, S.B.; Schwarzenbach, R.P., Reduction of Polyhalogenated Methanes by Surface-Bound Fe(II) in Aqueous Suspensions of Iron Oxides. *Environ. Sci. Technol.* **2002**, 36, 1734-1741.
108. Strathmann, T.J.; Stone, A.T., Reduction of the Pesticides Oxamyl and Methomyl by Fe(II): Effect of pH and Inorganic Ligands. *Environ. Sci. Technol.* **2002**, 36, 653-661.
109. Gregory, K.B.; Larese-Casanova, P.; Parkin, G.F.; Scherer, M.M., Abiotic Transformation of Hexahydro-1,3,5-Trinitro-1,3,5-Triazine by Fe(II) Bound to Magnetite. *Environ. Sci. Technol.* **2004**, 38, 1408-1414.
110. Hofstetter, T.B.; Neumann, A.; Schwarzenbach, R.P., Reduction of Nitroaromatic Compounds by Fe(II) Species Associated with Iron-Rich Smectites. *Environ. Sci. Technol.* **2005**, 40, 235-242.
111. Klausen, J.; Troeber, S.P.; Haderlein, S.B.; Schwarzenbach, R.P., Reduction of Substituted Nitrobenzenes by Fe(II) in Aqueous Mineral Suspensions. *Environ. Sci. Technol.* **1995**, 29, 2396-2404.
112. Amonette, J.E.; Workman, D.J.; Kennedy, D.W.; Fruchter, J.S.; Gorby, Y.A., Dechlorination of Carbon Tetrachloride by Fe(II) Associated with Goethite. *Environ. Sci. Technol.* **2000**, 34, 4606-4613.

113. Reardon, E.J.; Fagan, R.; Vogan, J.L.; Przepiora, A., Anaerobic Corrosion Reaction Kinetics of Nanosized Iron. *Environ. Sci. Technol.* **2008**, 42, 2420-2425.
114. Hu, J.; Chen, G.; Lo, I.M.C., Removal and Recovery of Cr(VI) from Wastewater by Maghemite Nanoparticles. *Water Res.* **2005**, 39, 4528-4536.
115. Hu, J.; Lo, M.C.; Chen, G.H., Adsorption of Cr(VI) by Magnetite Nanoparticles. *Water Sci. Technol.* **2004**, 50, 139-146.
116. Wang, P.; Lo, I.M.C., Synthesis of Mesoporous Magnetic γ -Fe₂O₃ and its Application to Cr(VI) Removal from Contaminated Water. *Water Res.* **2009**, 43, 3727-3734.
117. Mayo, J.T.; Yavuz, C.; Yean, S.; Cong, L.; Shipley, H.; Yu, W.; Falkner, J.; Kan, A.; Tomson, M.; Colvin, V.L., The Effect of Nanocrystalline Magnetite Size on Arsenic Removal. *Sci. Technol. Adv. Mater.* **2007**, 8, 71-75.
118. Shipley, H.J.; Yean, S.; Kan, A.T.; Tomson, M.B., Adsorption of Arsenic to Magnetite Nanoparticles: Effect of Particle Concentration, pH, Ionic Strength, and Temperature. *Environ. Toxicol. Chem.* **2009**, 28, 509-515.
119. Yean, S.; Cong, L., Effect of Magnetite Particle Size on Adsorption and Desorption of Arsenite and Arsenate. *J. Mater. Res.* **2005**, 20, 3255-3264.
120. Vikesland, P.J.; Heathcock, A.M.; Rebodos, R.L.; Makus, K.E., Particle Size and Aggregation Effects on Magnetite Reactivity toward Carbon Tetrachloride. *Environ. Sci. Technol.* **2007**, 41, 5277-5283.
121. Georgakilas, V.; Gournis, D.; Tzitzios, V.; Pasquato, L.; Guldi, D.M.; Prato, M., Decorating Carbon Nanotubes with Metal or Semiconductor Nanoparticles. *J. Mater. Chem.* **2007**, 17, 2679-2694.
122. Hu, X.; Dong, S., Metal Nanomaterials and Carbon Nanotubes-Synthesis, Functionalization and Potential Applications towards Electrochemistry. *J. Mater. Chem.* **2008**, 18, 1279-1295.
123. Peng, X.; Chen, J.; Misewich, J.A.; Wong, S., Carbon Nanotube-Nanocrystal Heterostructures. *Chem. Soc. Rev.* **2009**, 38, 1076-1098.
124. Wang, Y.; Wu, M.; Jiao, Z.; Lee, J.Y., Sn@CNT and Sn@C@CNT Nanostructures for Superior Reversible Lithium Ion Storage. *Chem. Mater.* **2009**, 21, 3210-3215.

125. Velamakanni, A.; Magnuson, C.W.; Ganesh, K.J.; Zhu, Y.; An, J.; Ferreira, P.J.; Ruoff, R.S., Site-Specific Deposition of Au Nanoparticles in CNT Films by Chemical Bonding. *ACS Nano* **2010**, 4, 4962-4962.
126. Xu, L.; Zhu, Y.; Tang, L.; Yang, X.; Li, C., Biosensor Based on Self-Assembling Glucose Oxidase and Dendrimer-Encapsulated Pt Nanoparticles on Carbon Nanotubes for Glucose Detection. *Electroanalysis* **2007**, 19, 717-722.
127. Jung, J.H.; Hwang, G.B.; Lee, J.E.; Bae, G.N., Preparation of Airborne Ag/CNT Hybrid Nanoparticles Using an Aerosol Process and Their Application to Antimicrobial Air Filtration. *Langmuir* **2010**, 27, 10256-10264.
128. Kim, H.-S.; Lee, H.; Han, K.-S.; Kim, J.-H.; Song, M.-S.; Park, M.-S.; Lee, J.-Y.; Kang, J.-K., Hydrogen Storage in Ni Nanoparticle-Dispersed Multiwalled Carbon Nanotubes. *J. Phys. Chem. B* **2005**, 109, 8983-8986.
129. Yoon, B.; Wai, C.M., Microemulsion-Templated Synthesis of Carbon Nanotube-Supported Pd and Rh Nanoparticles for Catalytic Applications. *J. Am. Chem. Soc.* **2005**, 127, 17174-17175.
130. Zhu, Y.; Elim, H.I.; Foo, Y.L.; Yu, T.; Liu, Y.; Ji, W.; Lee, J.Y.; Shen, Z.; Wee, A.T.S.; Thong, J.T.L.; Sow, C.H., Multiwalled Carbon Nanotubes Beaded with ZnO Nanoparticles for Ultrafast Nonlinear Optical Switching. *Adv. Mater.* **2006**, 18, 587-592.
131. An, J.W.; You, D.H.; Lim, D.S., Tribological Properties of Hot-Pressed Alumina-CNT Composites. *Wear* **2003**, 255, 677-681.
132. Zhang, Y.; Franklin, N.W.; Chen, R.J.; Dai, H., Metal Coating on Suspended Carbon Nanotubes and Its Implication to Metal-Tube Interaction. *Chem. Phys. Lett.* **2000**, 331, 35-41.
133. Wan, J.; Cai, W.; Feng, J.; Meng, X.; Liu, E., In Situ Decoration of Carbon Nanotubes with Nearly Monodisperse Magnetite Nanoparticles in Liquid Polyols. *J. Mater. Chem.* **2007**, 17, 1188-1192.
134. Wang, X.; Zhao, Z.; Qu, J.; Wang, Z.; Qiu, J., Fabrication and Characterization of Magnetic Fe₃O₄-CNT Composites. *J. Phys. Chem. Sol.* **2010**, 71, 673-676.
135. Zhang, Q.; Zhu, M.; Zhang, Q.; Li, Y.; Wang, H., The Formation of Magnetite Nanoparticles on the Sidewalls of Multi-Walled Carbon Nanotubes. *Composites Sci. Technol.* **2009**, 69, 633-638.

136. Sae-Khow, O.; Mitra, S., Fabrication and Characterization of Carbon Nanotubes Immobilized in Porous Polymeric Membranes. *J. Mater. Chem.* **2009**, *19*, 3713-3718.
137. Ismail, A.F.; Goh, P.S.; Sanip, S.M.; Aziz, M., Transport and Separation Properties of Carbon Nanotube-Mixed Matrix Membrane. *Separation and Purification Technology* **2009**, *70*, 12-26.
138. Cheng, I.F.; Muftikian, R.; Fernando, Q.; Korte, N., Reduction of Nitrate to Ammonia by Zero-Valent Iron. *Chemosphere* **1997**, *35*, 2689-2695.
139. Ritter, K.; Odziemkowski, M.S.; Simpgraga, R.; Gillham, R.W.; Irish, D.E., An In Situ Study of the Effect of Nitrate on the Reduction of Trichloroethylene by Granular Iron. *J. Contam. Hydrol.* **2003**, *65*, 121-136.
140. Hao, Z.-W.; Xu, X.-H.; Jin, J.; He, P.; Liu, Y.; Wang, D.-H., Simultaneous Removal of Nitrate and Heavy Metals by Iron Metal. *Journal of Zhejiang University Science* **2005**, *6*, 307-310.
141. King, D.W., Role of Carbonate Speciation on the Oxidation Rate of Fe(II) in Aquatic Systems. *Environ. Sci. Technol.* **1998**, *32*, 2997-3003.
142. Agrawal, A.; Tratnyek, P.G., Reduction of Nitro Aromatic Compounds by Zero-Valent Iron Metal. *Environ. Sci. Technol.* **1995**, *30*, 153-160.
143. Agrawal, A.; Ferguson, W.J.; Gardner, B.O.; Christ, J.A.; Bandstra, J.Z.; Tratnyek, P.G., Effects of Carbonate Species on the Kinetics of Dechlorination of 1,1,1-Trichloroethane by Zero-Valent Iron. *Environ. Sci. Technol.* **2002**, *36*, 4326-4333.
144. Erbs, M.; Bruun Hansen, H.C.; Olsen, C.E., Reductive Dechlorination of Carbon Tetrachloride Using Iron(II) Iron(III) Hydroxide Sulfate (Green Rust). *Environ. Sci. Technol.* **1998**, *33*, 307-311.
145. Klausen, J.; Ranke, J.; Schwarzenbach, R.P., Influence of Solution Composition and Column Aging on the Reduction of Nitroaromatic Compounds by Zero-Valent Iron. *Chemosphere* **2001**, *44*, 511-517.
146. Refait, P.H.; Abdelmoula, M.; Gein, J.M.R., Mechanisms of Formation and Structure of Green Rust One in Aqueous Corrosion of Iron in the Presence of Chloride Ions. *Corrosion Sci.* **1998**, *40*, 1547-1560.
147. Lipczynska-Kochany, E.; Harms, S.; Milburn, R.; Sprah, G.; Nadarajah, N., Degradation of Carbon Tetrachloride in the Presence of Iron and Sulphur Containing Compounds. *Chemosphere* **1994**, *29*, 1477-1489.

148. Cao, J.; Elliott, D.W.; Zhang, W.-X., Perchlorate Reduction by Nanoscale Iron Particles. *J. Nanopart. Res.* **2005**, *7*, 499-506.
149. Moore, A.M.; De Leon, C.H.; Young, T.M., Rate and Extent of Aqueous Perchlorate Removal by Iron Surfaces. *Environ. Sci. Technol.* **2003**, *37*, 3189-3198.
150. Tamara, M.L.; Butler, E.C., Effects of Iron Purity and Groundwater Characteristics on Rates and Products in the Degradation of Carbon Tetrachloride by Iron Metal. *Environ. Sci. Technol.* **2004**, *38*, 1866-1876.
151. Williams, M.D.; Vermeul, V.R.; Szecsody, J.E.; Fruchter, J.S. *100-D Area in Situ Redox Treatability Test for Chromate-Contaminated Groundwater* PNNL-13349; Pacific Northwest National Laboratory: Richland Washington, 2000.

2. Influence of Anionic Co-Solutes and pH on Nanoscale Zero-Valent Iron Longevity: Timescales and Mechanisms of Reactivity Loss Toward 1,1,1,2-Tetrachloroethane and Cr(VI)¹

2.1. Abstract

Nanoscale zero-valent iron (NZVI) was aged over 30 days in aqueous suspensions with different anions (chloride, perchlorate, sulfate, carbonate and nitrate), anion concentrations (5, 25, and 100 mN), and pH (7 and 8). During aging, suspension samples were reacted periodically with two model pollutants, 1,1,1,2-tetrachloroethane (1,1,1,2-TeCA) and Cr(VI), to determine the timescales and primary mode of NZVI reactivity loss. Rate constants for 1,1,1,2-TeCA reduction in Cl^- , SO_4^{2-} and ClO_4^- suspensions were essentially equivalent up to 100 mN and independent of pH, decreasing by 95% over 1 month. In contrast, longevity toward 1,1,1,2-TeCA was concentration-dependent for NO_3^- and HCO_3^- , with complete reactivity loss over 1 and 14 days, respectively, in 25 mN suspensions. X-ray diffraction suggests that reactivity loss toward 1,1,1,2-TeCA results from Fe(0) conversion into magnetite in NO_3^- , Cl^- , SO_4^{2-} and ClO_4^- systems, whereas formation of iron carbonate hydroxide is responsible in HCO_3^- suspensions. Markedly different trends in Cr(VI) removal capacity were observed during aging, exhibiting a pronounced pH-dependence and longevity that was generally independent of anion concentration. A strong correlation was observed between Cr(VI)

¹ An abbreviated version of this chapter has been submitted for publication in Environmental Science and Technology. Y. Xie and D.M. Cwiertny, Influence of Anionic Co-solutes and pH on Nanoscale Zero-Valent Iron Longevity: Timescales and Mechanisms of Reactivity Loss Toward 1,1,1,2-Tetrachloroethane and Cr(VI)

removal capacities and rates of Fe(II) production measured in the absence of Cr(VI). While Fe(0) availability dictates longevity toward 1,1,1,2-TeCA, this correlation suggests different entities, specifically surface-associated forms of Fe(II), are primarily responsible for Cr(VI) reduction.

2.2. Introduction

Although nanoscale zero valent iron (NZVI) treatment zones are becoming a popular alternative to permeable reactive barriers (PRBs) [1-4], questions surround the reactive lifetime of NZVI during application. To date, available field-scale monitoring data [5-8] are limited, and laboratory aging studies [9-11] have yet to examine NZVI reactivity loss in geochemically complex systems representative of contaminated subsurface environments. While generally accepted that the longevity of NZVI treatment zones will be shorter than that of PRBs (operative from several years to decades [12]), establishing timescales of NZVI reactivity loss in response to geochemical conditions will help to identify the optimal condition for application.

From established behavior of granular iron [13-18], the identity and concentration of anionic co-solutes are expected to dictate NZVI longevity because of their influence on the nature and stability of oxide layers at the particle-water interface. Chloride [13, 15, 19] and sulfate [13, 20], corrosion promoters capable of destabilizing passive surface films [21], have been reported to enhance granular iron reactivity. The influence of (bi)carbonate has been extensively investigated in laboratory and field-scale investigations [13, 22-27] [28, 29], typically revealing effects on granular iron reactivity

that depend on (bi)carbonate concentration and exposure time. In a recent work by Bi *et al.* [30], enhanced reactivity toward 4-chloronitrobenzene was observed at low carbonate concentrations, where it was hypothesized that amorphous $\text{Fe}(\text{OH})_2$ precipitates preferentially relative to passive FeCO_3 (siderite), allowing free CO_3^{2-} to promote $\text{Fe}(0)$ corrosion. Klausen *et al.* [27] observed reactivity toward organohalides and nitroaromatics in column studies that was initially enhanced (over 90 days) at a high bicarbonate concentration (20 mM), but ultimately resulted in inhibited activity due to formation of passive iron carbonate precipitates [31]. Unlike these other anions, nitrate is reducible by zero-valent iron [14, 32, 33], which promotes formation of passive ferric iron ($\text{Fe}(\text{III})$) (oxyhydr)oxides that dampen reactivity and shorten longevity [13, 17, 18].

While the roles of anions as inhibitors or promoters should not change in NZVI systems, NZVI performance is likely to be far more sensitive to their presence due to its greater corrosion rate. Reardon *et al.* observed the corrosion rate for commercially available NZVI ($\sim 2 \text{ mol kg}^{-1}\text{d}^{-1}$) [34] to be orders of magnitude greater than that of commercially available granular iron samples ($1.4 - 31.3 \times 10^{-4} \text{ mol kg}^{-1}\text{d}^{-1}$) and electrolytic iron powder ($7.9 \times 10^{-2} \text{ mol kg}^{-1}\text{d}^{-1}$) [35, 36]. At such markedly higher corrosion rates, solubility limits for passive phases (e.g., siderite in HCO_3^- systems) will be achieved more readily, in turn accelerating NZVI reactivity loss. For corrosion promoters (e.g., Cl^- and SO_4^{2-}), enhanced corrosion rates may also shorten longevity by increasing electron transfer to non-targets such as oxygen and water. In this case, the anions' influence on surface oxide formation will be critical for longevity because this

layer will regulate the rate of electron transfer from the metallic particle core to pollutants at the particle-water interface [37, 38].

To date, timescales of NZVI reactivity loss toward model pollutants have only been examined in idealized systems, not allowing to the influence anionic co-solutes to be quantified. Multiple studies conducted in unbuffered, deionized water systems indicate that NZVI maintains reactivity toward common chlorinated solvents (e.g., carbon tetrachloride and trichloroethylene) over 100-200 days [9, 10]. Because the pH in unbuffered systems can increase to values not representative of the subsurface, we recently aged NZVI in buffered suspensions at near-neutral pH [11]. At pH 7 and 8, we observed NZVI longevity to be considerably less, with measureable activity toward 1,1,1,2-tetrachlorethane (1,1,1,2-TeCA) for only 1 to 2 months.

In a noteworthy series of studies, Liu and Lowry reported the following reactivity trend (from most enhanced to most inhibited) toward trichloroethene (TCE) in NZVI suspensions with 5 mN concentration of different anions: $\text{Cl}^- > \text{SO}_4^{2-} > \text{HCO}_3^- > \text{HPO}_4^{2-} > \text{NO}_3^-$ [39]. However, this trend reflects pseudo-first-order rate constants for TCE reduction measured over relatively short periods of time (6 d). As such, it only reflects the immediate impact of these anions on NZVI reactivity while providing little indication of how long the enhanced or diminished reactivity is sustained in each solution. A follow-up study [40] characterized the NZVI corrosion products generated over 6 months in anaerobic, unbuffered suspensions with either 10 mN Cl^- , NO_3^- , SO_4^{2-} , HPO_4^- or HCO_3^- . After one month, the following trend in NZVI oxidation was observed based upon the Fe(0) remaining in the particle as determined by EXAFS (from most to least

oxidized): $\text{NO}_3^- > \text{Cl}^- > \text{SO}_4^{2-} > \text{HPO}_4^- > \text{HCO}_3^-$. However, the reactivity of these aged NZVI suspensions toward a model pollutant target such as TCE was not simultaneously measured. Because these same authors previously showed TCE reduction rates to be independent of Fe(0) content in aged NZVI [9], it is not possible to relate the changes in Fe(0) content to effective treatment lifetime.

Here, we simultaneously monitor changes in reactivity and material properties for NZVI suspensions aged up to one month in solutions of Cl^- , HCO_3^- , NO_3^- , SO_4^{2-} , and ClO_4^- over a range of concentrations (5, 25 and 100 mN) and buffered at environmentally relevant pH values (pH 7 and 8). Over time, reactivity loss in aged suspensions was quantified via multiple metrics including rates of aqueous Fe(II) production, the pseudo-first order rate constant for reduction (k_{obs} values) of 1,1,1,2-TeCA, hexavalent chromium (Cr(VI)) removal capacity (in mg of Cr/g NZVI), and measurement of oxidation-reduction potential (ORP), which is often used to monitor NZVI performance at field-scale installations [5, 8]. Inclusion of 1,1,1,2-TeCA and Cr(VI) as model pollutant targets allows the total reducing capacity available in aged NZVI suspensions to be evaluated; from our prior work [11], 1,1,1,2-TeCA is only degraded over short timescales by Fe(0), whereas Cr(VI) can be reduced both by Fe(0) and forms of aqueous and solid phase Fe(II). Thus, differences in suspension reactivity toward 1,1,1,2-TeCA and Cr(VI) provide an indirect measure of the relative amount of reducing equivalents available as Fe(0) and Fe(II) in aged NZVI particles. Finally, aged particles were characterized over time using transmission electron microscopy (TEM) and X-ray diffraction (XRD) to relate measured reactivity loss to changes in corrosion products generated during aging.

2.3. Experimental Section

Reagents

NZVI was purchased from Nanostructured and Amorphous Materials, Inc. (Houston, TX). The nanoparticles are provided as a dry powder packaged under N₂ that is synthesized from the reduction of iron oxides by H₂. Although stabilized via partial oxidation under 10% O₂, the material remained highly reactive and ignited upon exposure to air. The vendor reports an average particle size of 25 nm and a BET surface area of 40-60 m²/g. Characterization of this material in our previous work [1] suggests the particles consist of roughly 80% Fe(0) and 20% magnetite. Because of slight batch to batch reactivity in the product supplied by the vendor, unless otherwise noted, aging experiments were conducted with the same lot of NZVI powder.

For aging, NZVI suspensions were prepared in HEPES buffer (Sigma-Aldrich; 99.5%) with sodium chloride (NaCl, Aldrich, ≥ 99.0%), sodium sulfate (NaSO₄, Aldrich, ≥ 99.0%), sodium perchlorate (NaClO₄, Acros, 99+%,), sodium bicarbonate (NaHCO₃, Sigma, > 99.5%) or sodium nitrate (NaNO₃, Aldrich, ACS reagent). All solutions were prepared using deionized water (Milipore, Q-Grad 2) and were deoxygenated by sparging with compressed nitrogen for at least 1 hr/L. Model pollutants used in reactivity studies include Cr(VI) prepared from potassium chromate (K₂CrO₄, reagent grade, Fisher chemical) and 1,1,1,2-TeCA (~99%, Aldrich). Reagents used in colorimetric analysis of aqueous Fe(II) include 1,10-phenanthroline (Aldrich, 99+%), ammonium acetate (Sigma-Aldrich, ≥ 98%), glacial acetic acid (Fisher, certified ACS plus) and hydrochloric acid

(Fisher, trace metal grade). Reagents used in Cr(VI) analysis include sulfuric acid (Fisher, certified ACS plus) and S-diphenyl carbazide (Fisher; certified ACS).

Aging Protocol for NZVI Suspensions

Within an anaerobic chamber (97% N₂, 3% H₂), 2 g/L suspensions of NZVI were prepared by weighing 400 mg NZVI into a 250 mL Kimax bottle and combining it with 200 mL of 50 mM HEPES buffer with an appropriate ionic composition. The anion concentrations were 5, 25 and 100 mN for Cl⁻, SO₄²⁻ and ClO₄⁻ and 5 and 25 mN for HCO₃⁻ and NO₃⁻, and sodium salts of all anions were used. ClO₄⁻ was included because although it has previously been assumed to interact minimally with the granular iron surface [13], it is also known to be a weak oxidant for NZVI [41] and granular iron [42]. Thus, the extent of its influence on NZVI longevity remains largely unknown. HEPES buffer (pK_a value of 7.55) provided reasonable buffering capacity at both pH 7 and 8. As detailed in our prior work [11], suspension pH was not stable over time in the absence of buffer, rapidly increasing due to water reduction.

After preparing the suspensions, the bottles were screw-capped, the cap was wrapped in Parafilm, and the sealed bottle was briefly removed from the anaerobic chamber for sonication (~10 s) to disperse the NZVI powder. The bottles then were returned to the glovebox where they aged for 30 d while sealed. During aging, suspensions did not contain a model pollutant, with water reduction (i.e., corrosion) representing the only aging process. The suspensions were vigorously mixed by hand daily, and when necessary, small amounts of 5 N HCl were added to maintain a relatively

constant pH of 7.0 (± 0.2) or 8.0 (± 0.2). Notably, HCl was used to maintain the pH of all suspensions, even those with anions other than Cl^- , because it achieved the necessary pH adjustment with addition of relatively small volumes. In all cases, the HCl required to maintain suspension pH resulted in the addition of less than 1 mM of Cl^- over the duration of aging.

Evaluation of NZVI Reactivity during Aging

The reactivity of aged NZVI suspensions was evaluated via measurement of k_{obs} values for 1,1,1,2-TeCA reduction and the removal capacity of Cr(VI) (in mg of Cr/g NZVI) according to procedures summarized in the SI and detailed in our previous work [11]. Reactivity studies were conducted with samples of suspensions periodically withdrawn during aging. To remove any reactivity contribution from the aqueous Fe(II) that accumulated in suspension over time, these samples were centrifuged (8000 RPM for 5 min), and the supernatant was decanted inside anaerobic chamber. The aged particles were then washed twice with deoxygenated, deionized water prior to being re-suspended to the desired solid loading (typically 2 g/L) in the appropriate buffer for reactivity studies. To monitor how the redox character of the suspension changed over time, oxidation-reduction potential (ORP) was also measured periodically using a single-junction ORP electrode (Oakton Instruments).

For reaction with 1,1,1,2-TeCA, 22 mL of the aged NZVI slurry (2 g/L) was directly added to a serum bottle and sealed with a Teflon-lined butyl rubber septa. This volume resulted in no headspace within the reactor. After construction, reactors were

removed from the glovebox and the reaction with 1,1,1,2-TeCA was initiated immediately. To initiate the reaction, 70 μL of a 55.56 mM solution of 1,1,1,2-TeCA in methanol was added to the reactor, producing an initial concentration of $\sim 175 \mu\text{M}$. Reactors were then placed on a Roto-torque rotator (Cole-Parmer), which mixed the reactors end over end at 60 rpm. During experiments, 100-200 μL of aqueous sample was extracted using a glass microliter syringe, and the reaction was quenched by extracting 1,1,1,2-TeCA (extraction efficiencies were essentially 100%) with 1 mL of n-hexane (Fisher Scientific; GC Grade). We note that no difference in reactivity was observed when reactors were conducted within or outside the anaerobic chamber. NZVI free controls were conducted in a manner identical to that described above.

Removal capacities of Cr(VI) were quantified through repeated addition of Cr(VI) to a sample of aged suspension (with an equivalent of 1 g/L of NZVI) until Cr(VI) removal was no longer observed. Because aqueous Fe(II), which accumulated over time during suspension aging, also represents a capable reductant for Cr(VI) [2, 3], samples of the aged NZVI suspension were processed to remove Fe(II) prior to reaction. Specifically, 8 mL of NZVI slurry was removed from the well-mixed aged suspension, transferred to a centrifuge tube that was screw-capped and wrapped with Parafilm, and then centrifuged (8000 RPM for 5 minutes using an Eppendorf 5840R Centrifuge) to separate the aged particles from the aqueous supernatant. The aged NZVI particles were then resuspended in 16 mL of fresh buffer with the same pH value and anionic composition of the solution used to age the NZVI, producing a 1 g/L NZVI suspension. To initiate reaction, 150 μL of a 50 mM potassium chromate solution was added to the

NZVI suspension, producing an initial concentration of ~0.5 mM and a distinguishable yellow color in the suspension. The reactor was then placed on a roto-torque rotator (Cole-Parmer), which mixed the reactors end over end at 60 rpm. Upon color loss, which occurred relatively rapidly (typically on the order of 2 minutes), another Cr(VI) spike was added to the suspension. This respiking procedure continued until Cr(VI) removal was no longer measurable. Although reactors were assembled within the anaerobic chamber, all reactions with 1,1,1,2-TeCA and Cr(VI) were conducted outside of the glovebox. No difference was observed in suspension activity for experiments conducted inside versus outside of the anaerobic chamber.

Experiments measuring Fe(II) production were conducted in a similar fashion to experiments with Cr(VI). Samples of aged suspension were pretreated via centrifugation and washing to remove accumulated Fe(II) and then resuspended in an appropriate buffer and anion solution to yield a 1 g/L suspension of aged particles. The reactor was placed on a rotator and mixed end over end inside an anaerobic chamber to avoid oxidation of aqueous Fe(II) during sample collection. Samples were periodically withdrawn over the first 15 minutes of reaction so as to capture the initial rate of Fe(II) production. Samples were passed through a 0.2 μm nylon syringe driven filter (Xpertek) to remove the aged NZVI particles from suspensions. First-order rate constants for Fe(II) production ($k_{\text{Fe(II)}}$) were then determined via linear regression analysis of the concentration versus time data.

Analytical Methods

Dissolved Fe(II) was quantified using the 1,10-phenanthroline method [4, 5]. Within the anaerobic chamber, 1 mL of reactor solution was passed through a 0.2 μm syringe filter (PTFE) and added to 40 μL 5 M HCl to preserve the samples for iron analysis. Samples were removed from glovebox and diluted as appropriate with deionized water. For colorimetric analysis, 200 μL of 1 g/L phenanthroline solution and 200 μL of a 100 g/L ammonium acetate buffer solution were added to the sample, and the samples were allowed to sit in the dark for \sim 30 min prior to analysis. Absorbance measurements were then performed on a Shimadzu UV-visible spectrophotometer (at $\lambda=510$ nm). Standards for Fe(II) were prepared from anhydrous beads of ferrous chloride (FeCl_2 , 99.9%, Sigma-Aldrich).

Dissolved concentrations of Cr(VI) were determined colorimetrically with the reagent diphenylcarbazide [6]. Briefly, 80 μL of filtered sample was diluted with 1 mL of deionized water and then combined with 40 μL 5N sulfuric acid and 40 μL of a solution prepared by dissolving 250 mg of diphenylcarbazide in 50 mL acetone. The mixture was allowed to react for 30 minutes in the dark, over which time a pink color developed if Cr(VI) was present above the detection limits (\sim 35.86 $\mu\text{g/L}$). The solutions were analyzed on a Shimadzu UV/visible spectrophotometer at ($\lambda = 540$ nm). Standards of Cr(VI) were made from potassium chromate and were prepared for UV/vis analysis in a manner identical to the experimental samples.

The concentration of 1,1,1,2-TeCA and its sole reduction product 1,1-dichloroethylene (1,1-DCE) were determined via gas chromatography with electron capture detection (GC/ECD). During batch experiments, 100-200 μL of aqueous sample

was extracted with 1 mL of n-hexane (Fisher Scientific; GC Resolv.) followed by subsequent dilutions in hexane. Diluted extracts were analyzed using an Agilent 7890A GC with micro-ECD that was equipped with an Rtx-1 column (30 m, 0.32 mm ID, 5.00 μm film thickness, Restek) and autosampler (CTC Analytics, CombiPal). The temperature program involved holding at the initial temperature of 45 °C for 0.5 min, increase at a rate of 15°C/min to 150 °C, then increase at 15°C/min to 250 °C followed by a hold for 2 min. Standards of all analytes were prepared in hexane and were analyzed in a manner identical to the experimental samples.

A small number of studies examined the fate of nitrate in NZVI systems. Nitrate and nitrite, a likely reduction product, were analyzed using an IonPac AS14 column on a DIONEX 1000 ion chromatography. The DIONEX IC requires samples to be passed through a 0.1 micron filter prior to injection to prevent organic matter buildup in the column. Samples were automatically injected using an AS 40 liquid autosampler. The method utilized an eluent of 3.5 mM Na_2CO_3 /1.0 mM NaHCO_3 with a flow rate of 1 mL/min. The method detection limit was 200 $\mu\text{g/L}$ for nitrate (as N) or nitrite (as N).

ORP measurements were made by placing the electrode into a well-mixed suspension of 2 g/L NZVI with at least 25 mL of total volume. Stable readings were typically achieved after 1 minute. The probe was calibrated with saturated solutions of quinhydrone at pH 4 and 7 according to procedures recommended by the manufacturer.

Materials Characterization

Changes in NZVI mineralogy during aging were investigated with powder X-ray diffraction (XRD) using a Bruker D8 Advance Diffractometer with Cu K α radiation ($\lambda = 1.54 \text{ \AA}$). The tube current was 40mA with tube voltage of 40 kV. 2θ ranged from 5° to 80° with a scanning rate of 0.5 min/step and a step size of 0.02° . As in our prior work [11], samples of aged suspensions for XRD analysis were deposited on a standard microscope slide and allowed to dry overnight within the anaerobic chamber prior to analysis. Dried samples were then analyzed immediately, with a typical analysis time of 30 min. Notably, the effect of oxidation during XRD analysis was found to be negligible, with analysis of select samples prepared in 10-50% glycerol by volume, which inhibits oxidation, yielded identical diffraction patterns to the same samples prepared without glycerol. As sample size was often limited for XRD analysis, the majority of samples were conducted without added glycerol so as to optimize the diffraction signal during analysis.

The morphology of materials was examined using transmission electron microscopy (TEM; FEI Tecnai 12 G2 equipped with a LaB6 electron gun) operated at 120 kV. Prior to characterization, materials suspensions were centrifuged to separate the solids from the supernatant and then resuspended in DI water (for XRD) or methanol (for TEM). This procedure limited interference from buffers and salts present in suspension during analysis. For TEM, a drop of diluted sample was dried on a carbon-coated Cu grid (300 mesh). All samples were stored in glovebox until analysis.

2.4. Results and Discussion

Trends in Reactivity Loss toward 1,1,1,2-TeCA

Figure 2-1 illustrates the changes in k_{obs} values for 1,1,1,2-TeCA reduction ($k_{\text{obs}}(1,1,1,2\text{-TeCA})$) as a function of suspension aging time in the presence of 5 mN (Figure 2-1a) and 25 mN (Figure 2-1b) anionic co-solutes at pH 8. Data are presented from at least duplicate aged suspensions. In all systems, 1,1,1,2-TeCA concentrations exhibited exponential decay, thus $k_{\text{obs}}(1,1,1,2\text{-TeCA})$ values were obtained from the slopes of semi-log plots of 1,1,1,2-TeCA concentration versus time. Minor 1,1,1,2-TeCA losses occurred in NZVI-free controls, attributable to sorption on the septa used to seal reactors. The loss coefficient measured in these controls is represented by the dashed horizontal line in Figure 2-1. Aged NZVI was assumed to possess no further reducing capacity toward 1,1,1,2-TeCA when $k_{\text{obs}}(1,1,1,2\text{-TeCA})$ values were equivalent to the value measured in controls (representing >99% loss relative to the maximum k_{obs} value). When 1,1,1,2-TeCA loss exceeded that in controls, 1,1,1,2-TeCA transformation occurred via reductive dechlorination; 1,1-dichloroethylene was the only detectable reaction product and sorption-corrected carbon mass balances were greater than 90%.

In all 5 mN suspensions (Figure 2-1a), reactivity increased by roughly 2- to 3-fold over the first two days of aging. Previous studies [10, 39] have attributed such behavior to autoreduction of the passivating oxide layer initially present on the particle surface. Another notable feature is the very modest reactivity differences observed during aging in most 5 mN anion suspensions. Suspensions of Cl^- , ClO_4^- , and HCO_3^- yielded essentially equivalent $k_{\text{obs}}(1,1,1,2\text{-TeCA})$ values, whereas SO_4^{2-} exhibited slightly depressed reactivity during moderate aging times (5-14 days) relative to these other anions. Nitrate-containing suspensions exhibited appreciably lower reactivity than other systems, with 5

mN NO_3^- immediately dampening NZVI reactivity and yielding a k_{obs} value roughly an order of magnitude less than other systems. The reactivity in NO_3^- systems slowly rebounded over the first 5 days, increasing by roughly a factor of 5 attributable in part to autoreduction. Reduction of NO_3^- occurred readily in these systems (Figure 2-2). Thus the reactivity enhancement may also reflect consumption of NO_3^- over time, thereby increasing the reducing equivalents available for 1,1,1,2-TeCA. Exposure to 5 mN NO_3^- ultimately shortened NZVI longevity, with complete reactivity loss observed by 30 d at pH 8. All other anion suspensions, including HCO_3^- , maintained measurable reactivity over this period, with 1,1,1,2-TeCA loss greater than that in controls, although the extent of reactivity loss was substantial (~95%).

For 25 mN suspensions at pH 8 (Figure 2-1b), Cl^- , SO_4^{2-} and ClO_4^- revealed the same relative reactivity as at 5 mN, where k_{obs} (1,1,1,2-TeCA values) for Cl^- and ClO_4^- were equivalent, while comparatively SO_4^{2-} was slightly less reactive. Also for Cl^- , SO_4^{2-} and ClO_4^- , k_{obs} (1,1,1,2-TeCA) values were approximately equal to those measured in 5 mN suspensions, exhibiting roughly 95% reactivity loss over 30 d. Additional experiments revealed that trends in NZVI reactivity and longevity toward 1,1,1,2-TeCA were unaffected by concentrations up to 100 mN for these anions (Figure 2-3). The comparable reactivity of ClO_4^- suspensions to Cl^- and SO_4^{2-} at all concentrations suggests minimal reduction by NZVI occurred; notably, NZVI loadings used herein (2 g/L) are considerably less than those found to achieve 60% ClO_4^- reduction over 28 days (20 g/L) [41].

At 25 mN, NZVI longevity was shortened considerably in both HCO_3^- and NO_3^- systems. After an initial increase in reactivity over 2 days from autoreduction, values of $k_{\text{obs}}(1,1,1,2\text{-TeCA})$ in 25 mN HCO_3^- suspensions decreased suddenly, with reduction of 1,1,1,2-TeCA not observed beyond 21 days. Reactivity loss occurred most rapidly in 25 mN NO_3^- systems, in which there was no increase in k_{obs} values from autoreduction and 1,1,1,2-TeCA loss attributable to reduction ceased after 1 d. Only ~20% of available NO_3^- was reduced by NZVI prior to complete reactivity loss (Figure 2-2), suggesting consumption of reducing equivalents by excess NO_3^- limited activity toward 1,1,1,2-TeCA.

Values of $k_{\text{obs}}(1,1,1,2\text{-TeCA})$ as a function of aging time at pH 7 are shown in Figure 2-4. At 5 mN, a minimal pH effect was observed over the duration of aging for all anions, although in a few instances the peak $k_{\text{obs}}(1,1,1,2\text{-TeCA})$ value achieved after autoreduction was notably higher at pH 7. This behavior is most noticeable for NO_3^- systems, but also observed for Cl^- and ClO_4^- suspensions, suggesting the rate and extent of autoreduction reaction is pH dependent. At 25 mN, there also was little, if any, discernible pH effect in SO_4^{2-} , HCO_3^- , and NO_3^- . For 25 mN Cl^- and ClO_4^- , on the other hand, $k_{\text{obs}}(1,1,1,2\text{-TeCA})$ values over the aging period were smaller at pH 7. This pH-dependence is counter to that commonly observed for NZVI [11] and granular iron reductants [46], and as a result led to slightly greater rates of reactivity loss in 25 mN Cl^- and ClO_4^- systems relative to pH 8.

Despite these few notable differences observed between pH 7 and pH 8 suspensions, most observable pH effects exerted little impact on the relative longevity of

different anionic suspensions of NZVI toward 1,1,1,2-TeCA. In comparing Figure 2-1 and 2-4, reactivity loss generally occurred to the same extent over comparable timescales in all systems, except high concentration HCO_3^- and NO_3^- systems.

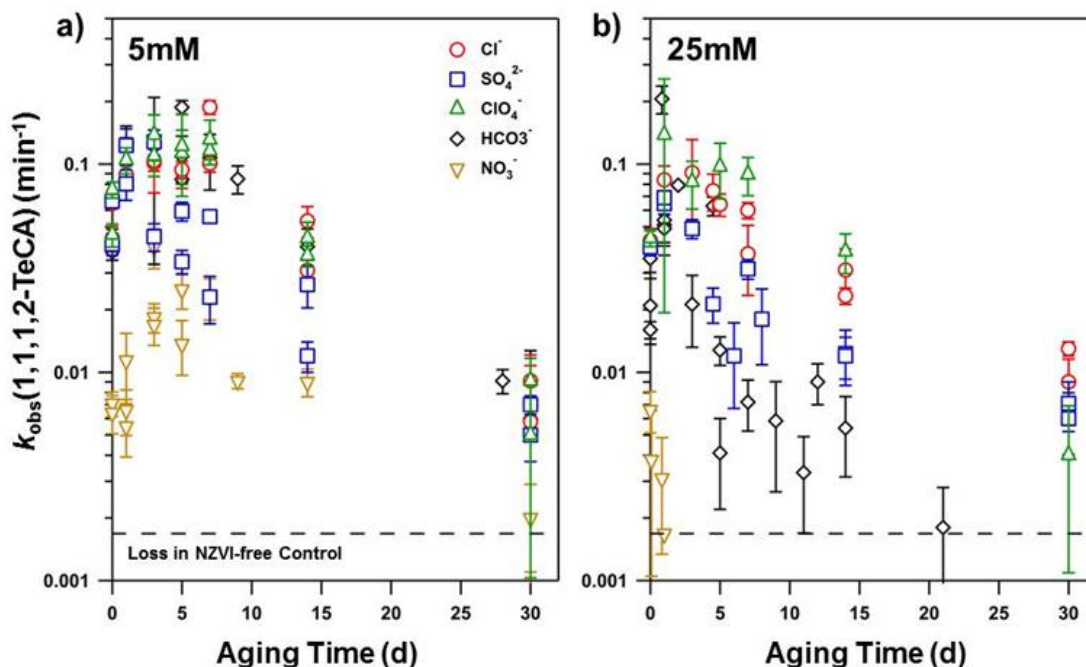


Figure 2-1. Change in the k_{obs} values for 1,1,1,2-TeCA reduction over time in the presence of Cl^- , SO_4^{2-} , ClO_4^- , HCO_3^- and NO_3^- at pH 8 (a) at 5 mM and (b) at 25 mM concentration. Comparable reactivity trends and timescales for reactivity loss were observed at pH 7 (see Figure 2-4). Dashed line represents the rate constant corresponding to the extent of 1,1,1,2-TeCA loss in NZVI-free controls, as described in the text. Uncertainties represent 95% confidence intervals from regression analyses performed on semi-log plots of 1,1,1,2-TeCA concentration as a function of time, the slopes of which were used to obtain the k_{obs} values shown.

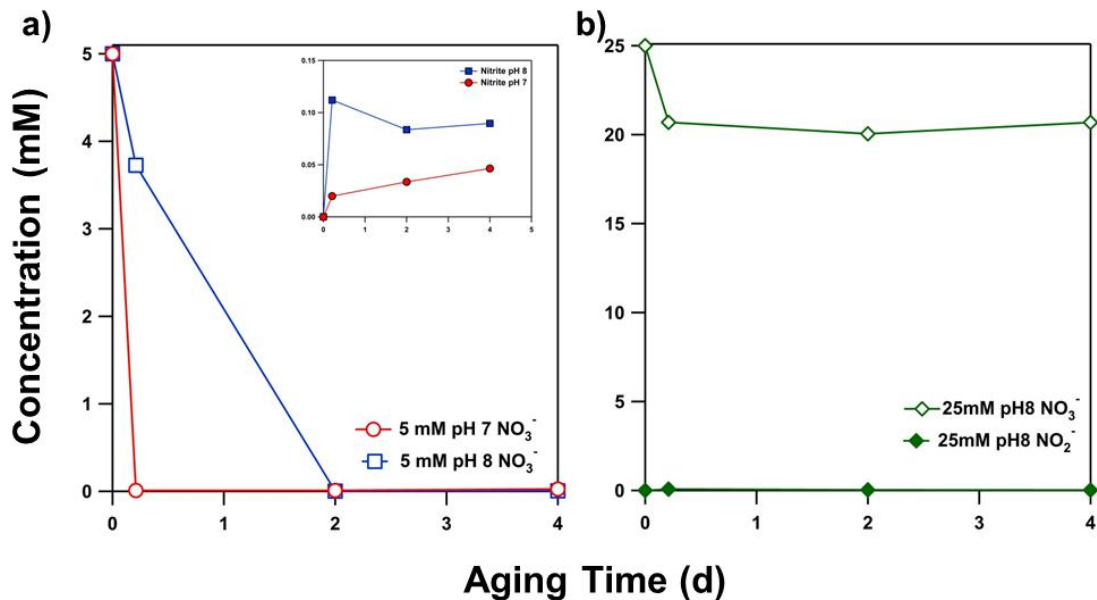


Figure 2-2. Reduction of nitrate and production of nitrite in suspensions of (a) 5 mN and (b) 25 mN nitrate at pH 7 and 8. In 5 mN suspensions, production of nitrite is shown as an inset, whereas nitrite in 25 mN nitrate suspensions, while observed, was at or near the limit of analytical detection with our ion chromatography method. Experiments were conducted in a manner analogous to the reactions with 1,1,1,2-TeCA using a fresh NZVI suspension of 2 g/L in 25 mM HEPES buffer at the appropriate pH and initial nitrate concentration.

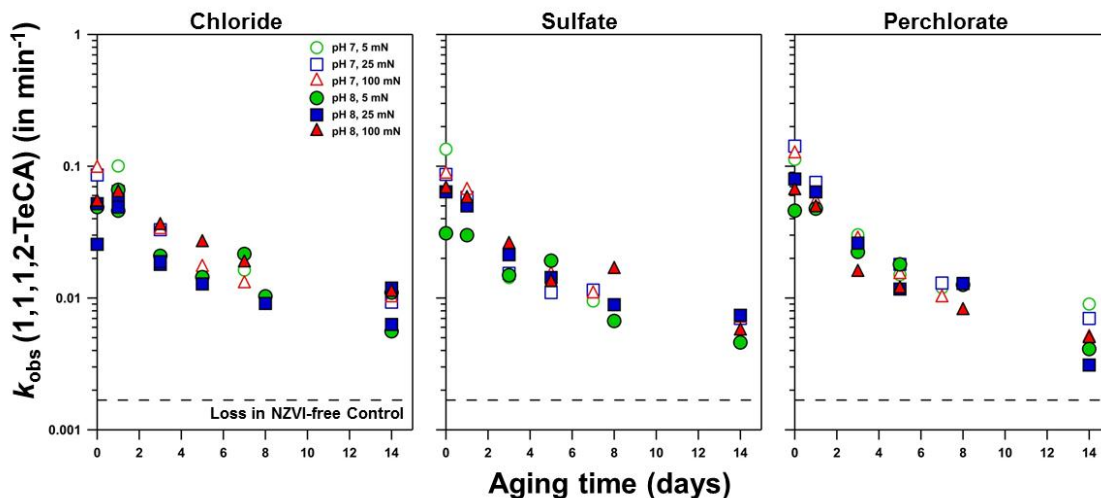


Figure 2-3. Change in k_{obs} values for 1,1,1,2-TeCA reduction as a function of NZVI aging time in pH 7 and pH 8 suspensions with 5, 25 and 100 mN concentrations of Cl^- , SO_4^{2-} and ClO_4^- . As noted in the main text, the dashed line represents the rate constant observed for 1,1,1,2-TeCA loss in NZVI-free controls, in which a small amount of 1,1,1,2-TeCA loss was observed as a result of sorption to the septa used to seal the reactors. Experiments were conducted in suspensions with an equivalent of 2 g/L of fresh NZVI in 25 mM HEPES and the appropriate anion composition. We note that these experiments examining NZVI reactivity loss at 100 mN anion concentrations were conducted with a new lot of NZVI powder from Nanostructured and Amorphous Materials because the original lot was consumed during the aging studies presented in Figures 2-1 and 2-4. Notably, this newer lot exhibited initial reactivity toward 1,1,1,2-TeCA that was less than the lot of NZVI used in the majority of the experiments presented herein. Moreover, this newer lot also exhibited slightly elevated rates of reactivity loss toward 1,1,1,2-TeCA. As data from 100 mN systems were not directly comparable to data previously presented at 5 and 25 mN concentrations in Figure 2-1 and 2-4, additional experiments with the new NZVI lot at 5 and 25 mN were conducted and are the data shown. As is clearly evident from the results with the new NZVI lot, there was not obvious change in the rate of reactivity loss toward 1,1,1,2-TeCA over the entire range of anion concentrations considered.

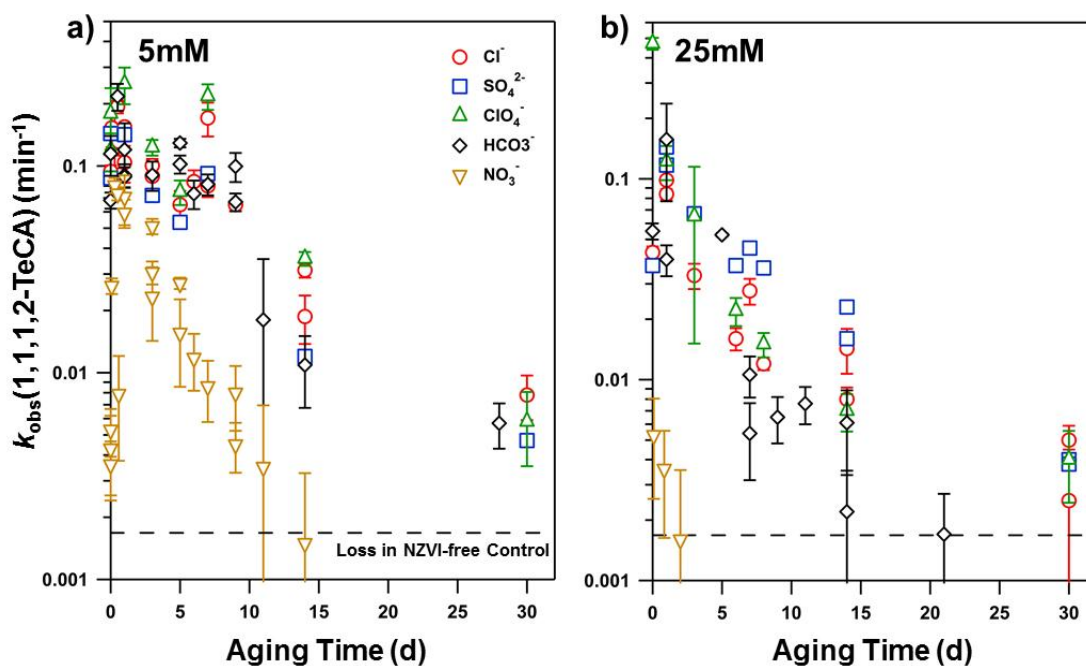


Figure 2-4. Change in the k_{obs} values for 1,1,1,2-TeCA reduction over time in pH 7 suspensions of Cl^- , SO_4^{2-} , ClO_4^- , HCO_3^- and NO_3^- (a) at 5 mM and (b) at 25 mM concentration. The dashed line indicates the rate constant for the amount of 1,1,1,2-TeCA loss observed in NZVI-free controls, in which a small amount of loss was observed as a result of sorption to septa used to seal the reactors. Reactors contained a reduction loading equivalent to 2 g/L of fresh NZVI, 25 mM HEPES buffer to stabilize pH at 7.0 ± 0.2 , and the appropriate anion composition. As is our previous work [1], decay of 1,1,1,2-TeCA was consistent with reductive β -elimination to produce 1,1-dichloroethylene (1,1-DCE) in all systems. Reduction of 1,1,1,2-TeCA followed exponential decay, and thus for this system we report pseudo-first-order rate constants (k_{obs} values) for 1,1,1,2-TeCA reduction as a function of aging time for each suspension

Trends in Reactivity Loss toward Cr(VI)

Measured Cr(VI) removal capacities (in mg of Cr(VI) per g of NZVI) as a function of aging time for 5 and 25 mN anionic suspensions at pH 7 and 8 are shown in Figure 2-5. In Figure 2-5, y-axes share the same range to facilitate comparison between different systems. Based on evidence presented in our earlier work [11], reduction represented the primary mechanism of Cr(VI) loss in our systems.

Unlike $k_{\text{obs}}(1,1,1,2\text{-TeCA})$ values, Cr(VI) removal capacities exhibited a much clearer pH-dependence. Generally, suspensions aged at pH 7 exhibited considerably more removal than those aged at pH 8, behavior most easily observed for SO_4^{2-} and HCO_3^- suspensions. Rates of reactivity loss toward Cr(VI) were also different from those observed for 1,1,1,2-TeCA. First, no influence of autoredox was observed, as removal capacities either were constant or decreased slightly during initial periods of aging. Another key difference from 1,1,1,2-TeCA was that removal of Cr(VI) was measurable in nearly all suspensions over the entire duration of aging. Notably, 25 mN HCO_3^- suspensions that were passive toward 1,1,1,2-TeCA after two weeks maintained relatively high reactivity toward Cr(VI) over 30 d.

Trends in Cr(VI) removal were also far less sensitive to anion concentration. In SO_4^{2-} and HCO_3^- systems, for example, no appreciable differences were observed between 5 and 25 mN at either pH, and Cr(VI) removal remained roughly constant over time. While the concentration of Cl^- did not affect Cr(VI) removal, the rate of reactivity loss was greater at pH 7 relative to pH 8. As the exceptions, anion concentration influenced NZVI performance in ClO_4^- - and NO_3^- -containing systems. For ClO_4^- , higher

concentration hastened reactivity loss in pH 7 suspensions, yet exerted no influence at pH 8. Although removal of Cr(VI) was generally suppressed in all NO_3^- suspensions (near 10-15 mg of Cr/g NZVI), complete reactivity loss was only observed in the 25 mN at pH 8 after 5 d.

Because of the numerous differences exhibited between aged suspensions of each anion, it is difficult to develop generalizable trends for NZVI reactivity and longevity toward Cr(VI). However, the generally disparate behavior observed toward Cr(VI) and 1,1,1,2-TeCA (Figure 2-6) support unique reductants for each species in aged NZVI suspensions. Notably, our data suggest that the species primarily responsible for Cr(VI) removal persists over longer timescales and exhibits a greater sensitivity to solution pH.

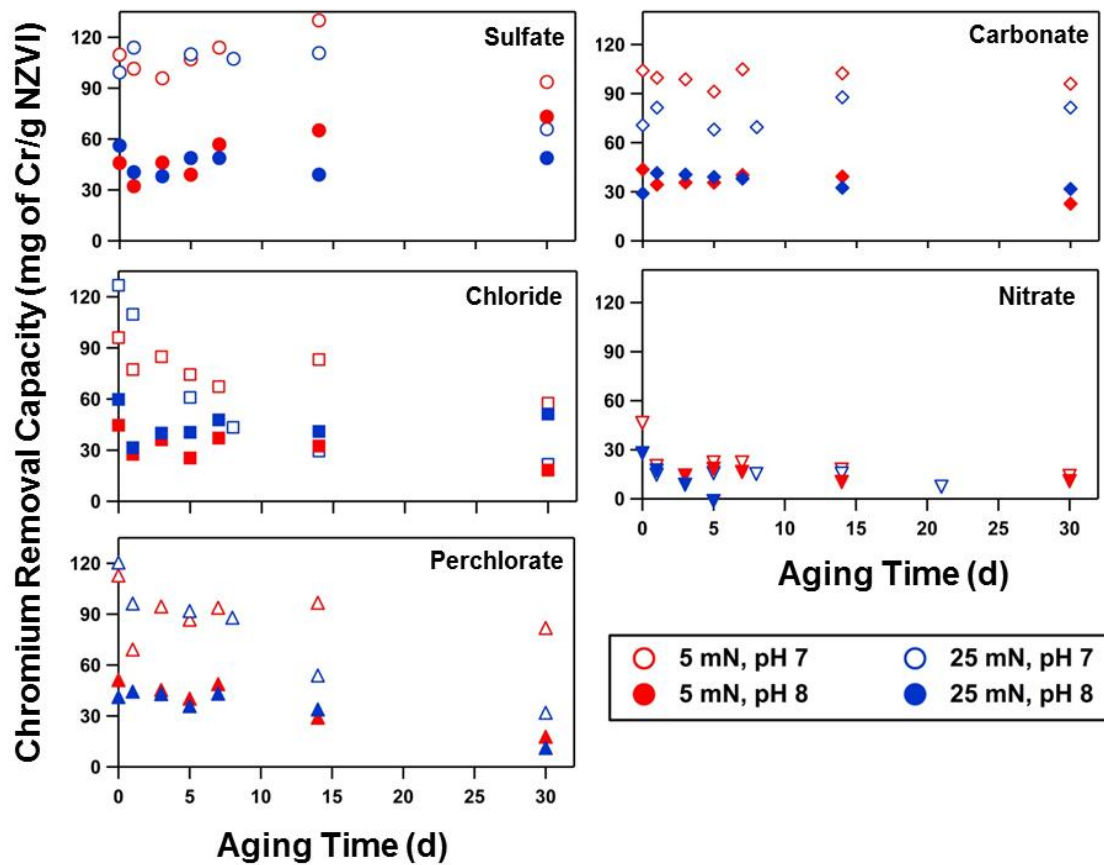


Figure 2-5. Change in Cr(VI) removal capacity (in mg of Cr/g NZVI) as a function of aging time in 5 and 25 mN suspensions of sulfate, chloride, perchlorate, carbonate and nitrate at pH 7 and 8. Data are shown on the same y-axis scale for the purpose of comparison.

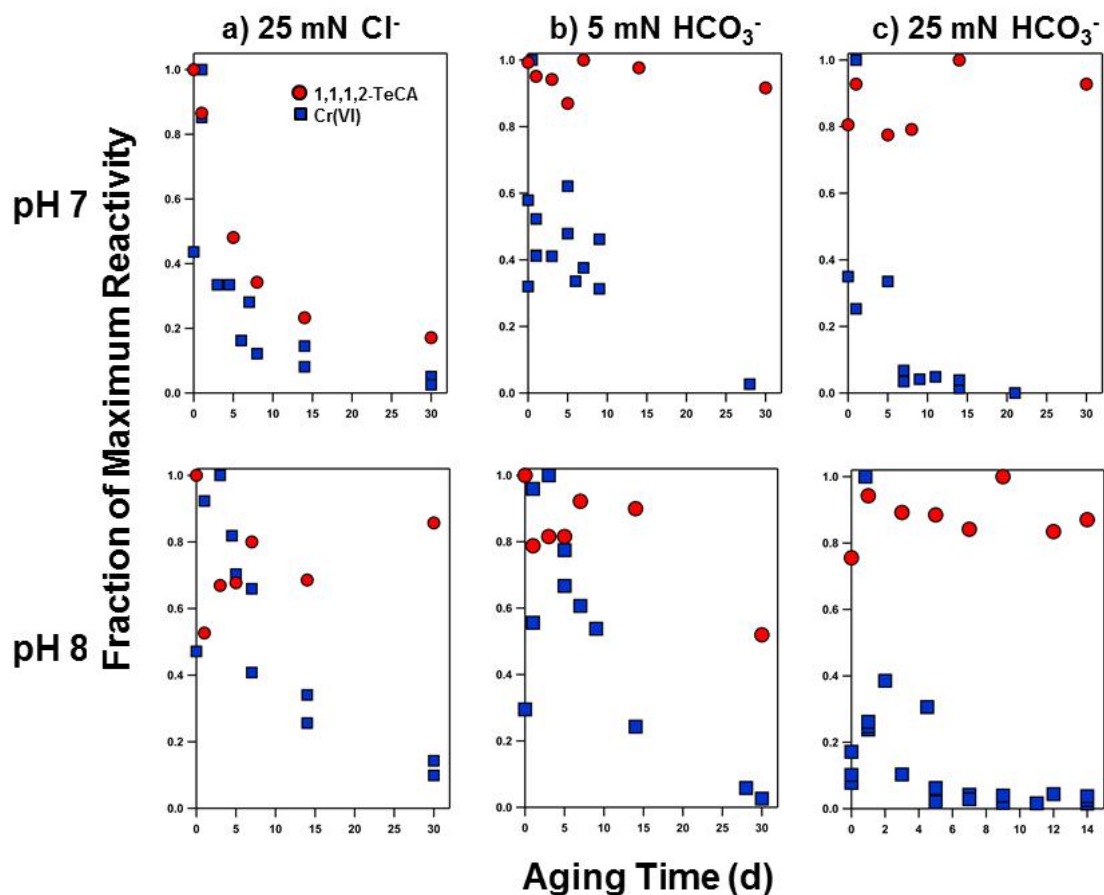


Figure 2-6. Reactivity loss in (a) 25 mN chloride, (b) 5 mN bicarbonate and (c) 25 mM bicarbonate system at pH 7 and 8. Rather than showing absolute k_{obs} values for 1,1,1,2-TeCA reduction and Cr(VI) removal capacities (as presented in Figures 2-1 and 2-4, and Figure 2-5, respectively), reactivity data are presented as fraction of the maximum reactivity measured toward each target compound. For 1,1,1,2-TeCA, all k_{obs} values were normalized the maximum k_{obs} value measured, which typically was measured after 1 or 2 days of aging due to the autoreduction reaction. In contrast, the maximum removal capacity for Cr(VI) was sometimes observed early in the aging process (e.g., 25 mN Cl⁻ at pH 8), but in other instances maximum removal capacities were measured after several days of aging (e.g., 25 mN HCO₃⁻ systems at pH 7 and pH 8). While there are certain instances where rates of reactivity loss were comparable in systems with 1,1,1,2-TeCA and Cr(VI), for the overwhelming majority of systems reactivity loss was more rapid and extensive toward 1,1,1,2-TeCA. This is particularly evident in the carbonate systems shown, where fractional reactivity loss toward Cr(VI) was in most instances minimal relative to 1,1,1,2-TeCA.

Role of Corrosion Products in Reactivity Loss Toward 1,1,1,2-TeCA

Trends in corrosion product formation most readily explain reactivity loss observed toward 1,1,1,2-TeCA. For example, characterization results of NZVI aged in 25 mN NO_3^- at pH 7 are shown in Figure 2-7. Diffraction patterns (Figure 2-7b) revealed rapid loss of Fe(0) accompanied by magnetite formation over 2 h, yet consistent with other reports [26], TEM images (Figure 2-7a) revealed no significant morphological changes over 30 d. For 25 mN NO_3^- suspensions, timescales associated with Fe(0) consumption closely parallel reactivity loss toward 1,1,1,2-TeCA (see Figures 2-1b and 2-4b), suggesting that 1,1,1,2-TeCA reduction is closely linked to the availability of Fe(0) in suspension. Thickening of the magnetite surface layer, promoted by nitrate's role as an oxidant, depresses reactivity toward 1,1,1,2-TeCA until the near-complete consumption of Fe(0) ultimately entirely suppresses 1,1,1,2-TeCA reduction.

Conversion of Fe(0) to magnetite also appears to be the primary mechanism for reactivity loss toward 1,1,1,2-TeCA in Cl^- , SO_4^{2-} and ClO_4^- suspensions. Characterization results for 25 mM Cl^- suspensions at pH 7 and 8 are shown in Figure 2-8, and aging products in pH 7 suspensions of Cl^- , SO_4^{2-} and ClO_4^- are compared in Figure 2-9. In all instances, diffraction patterns show loss of Fe(0) and predominance of magnetite over time. Notably, an Fe(0) signal was apparent in XRD characterization of Cl^- suspensions aged for 30 d at pH 8 but not at pH 7 (Figure 2-8), likely due to the greater rate of Fe(0) corrosion at lower pH values. TEM images reveal that while aged NZVI particles largely retain their initial morphology during aging, secondary phases with hexagonal plate morphologies consistent of green rust [47] are observable after 30-40 d (Figure 2-9).

Although the rate of Fe(0) consumption appears to explain reactivity loss in Cl^- , SO_4^{2-} and ClO_4^- suspensions, in our previous work [11] air-oxidized NZVI suspensions retained a significant portion of Fe(0) but were unreactive toward 1,1,1,2-TeCA because of a passive ferric oxide coating formed during air oxidation. Thus, for transformation of 1,1,1,2-TeCA, Fe(0) must not only be present in the particle core, but its reducing equivalents must also be accessible to solution via a conductive oxide surface layer such as the magnetite observed in suspensions of Cl^- , SO_4^{2-} and ClO_4^- .

For HCO_3^- suspensions, the formation rate and nature of corrosion products were essentially independent of pH (see Figure 2-10) but were strongly influenced by bicarbonate concentration. At 5 mN, TEM images (Figure 2-11a) collected over the first week reveal small amounts of a secondary mineral phase associated with NZVI aggregates that has the characteristic hexagonal plate morphology of carbonate green rust [47]. This phase was not present at sufficient quantities to observe via XRD, with magnetite and residual Fe(0) representing the only detectable phases (Figure 2-11b). After 30 d, TEM images show the formation of another secondary phase with a sheet- or plate-like morphology. The XRD pattern for this new phase is most consistent with iron carbonate hydroxide, which possesses a distinct diffraction pattern relative to other iron-carbonates including green rust and siderite [31]. Iron carbonate hydroxide ((ICH; $[\text{Fe}_3(\text{OH})_{2.2}\text{CO}_3]$) has previously been observed in field-scale PRBs [48] and in laboratory column studies with Master Builder granular iron [31]. In the latter work, SEM imaging of particle cross-sections revealed a surface-associated phase with needle-like or thin platelet morphology consistent with the phase identified with TEM in Figure

2-11. At 25 mM HCO_3^- , TEM (Figure 2-11c) and diffraction patterns (Figure 2-11d) indicate that ICH formed more extensively and over shorter timescales. As seen in TEM images, ICH phase tends to generate in close proximity to NZVI aggregates, with most NZVI aggregates being enveloped by the sheet-like morphology of ICH.

These characterization results provide evidence that ICH formation is primarily responsible for shortening the longevity of NZVI towards 1,1,1,2-TeCA in suspensions of HCO_3^- . Suspensions of 5 mM HCO_3^- were largely free of detectable ICH over 30 d and exhibited comparable reactivity to ClO_4^- , SO_4^{2-} and Cl^- systems. In contrast, the extensive ICH formation over two weeks in 25 mM suspensions coincides with reactivity loss toward 1,1,1,2-TeCA. Given the manner in which ICH grows on and around NZVI particle aggregates, a probable mechanism for reactivity loss toward 1,1,1,2-TeCA is steric blocking, in which the relatively large ICH crystals limit access to reactive sites on the NZVI surface.

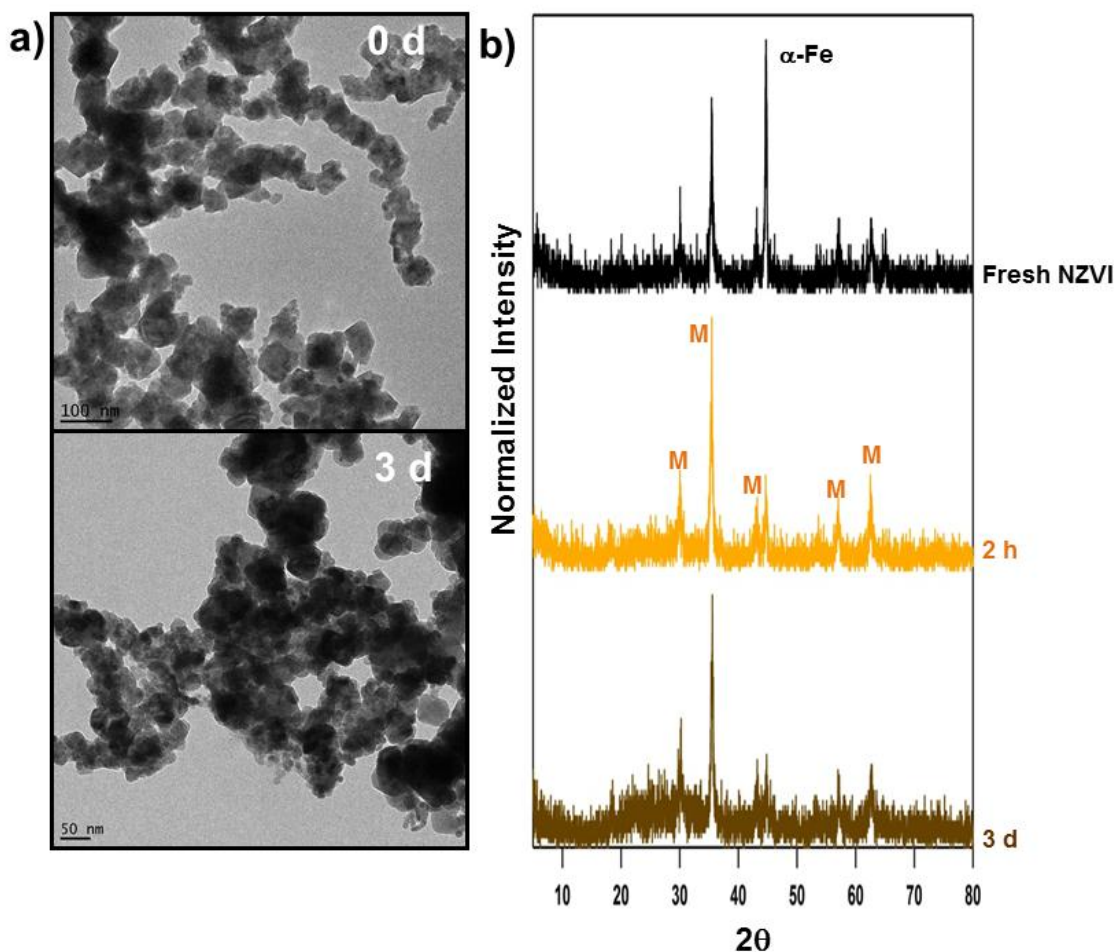


Figure 2-7. (a) TEM images and (b) XRD patterns collected as a function of aging time for NZVI particles aged in pH 7 suspensions with 25 mM NO_3^- . While TEM images revealed no clear changes in particle structure or morphology over the first 3 days of aging, XRD patterns reveal that the signal for $\alpha\text{-Fe}(0)$ is lost over this same timescale while the signal for magnetite (Fe_3O_4 characteristic diffraction lines are noted by “M”) persists. No other iron-containing phases were observed via XRD. Notably, over this same timescale of 3 d, reactivity toward 1,1,1,2-TeCA is entirely lost. However, these aged materials exhibit measurable, albeit inhibited, removal capacities for Cr(VI) (~15 mg of Cr(VI) per gram of NZVI) for up to 30 days of aging. The measurable removal of Cr(VI) suggests that oxidation products produced in nitrate-containing suspensions of NZVI must be of possess redox activity, as would be expected from the persistence of mixed valence magnetite observed with XRD.

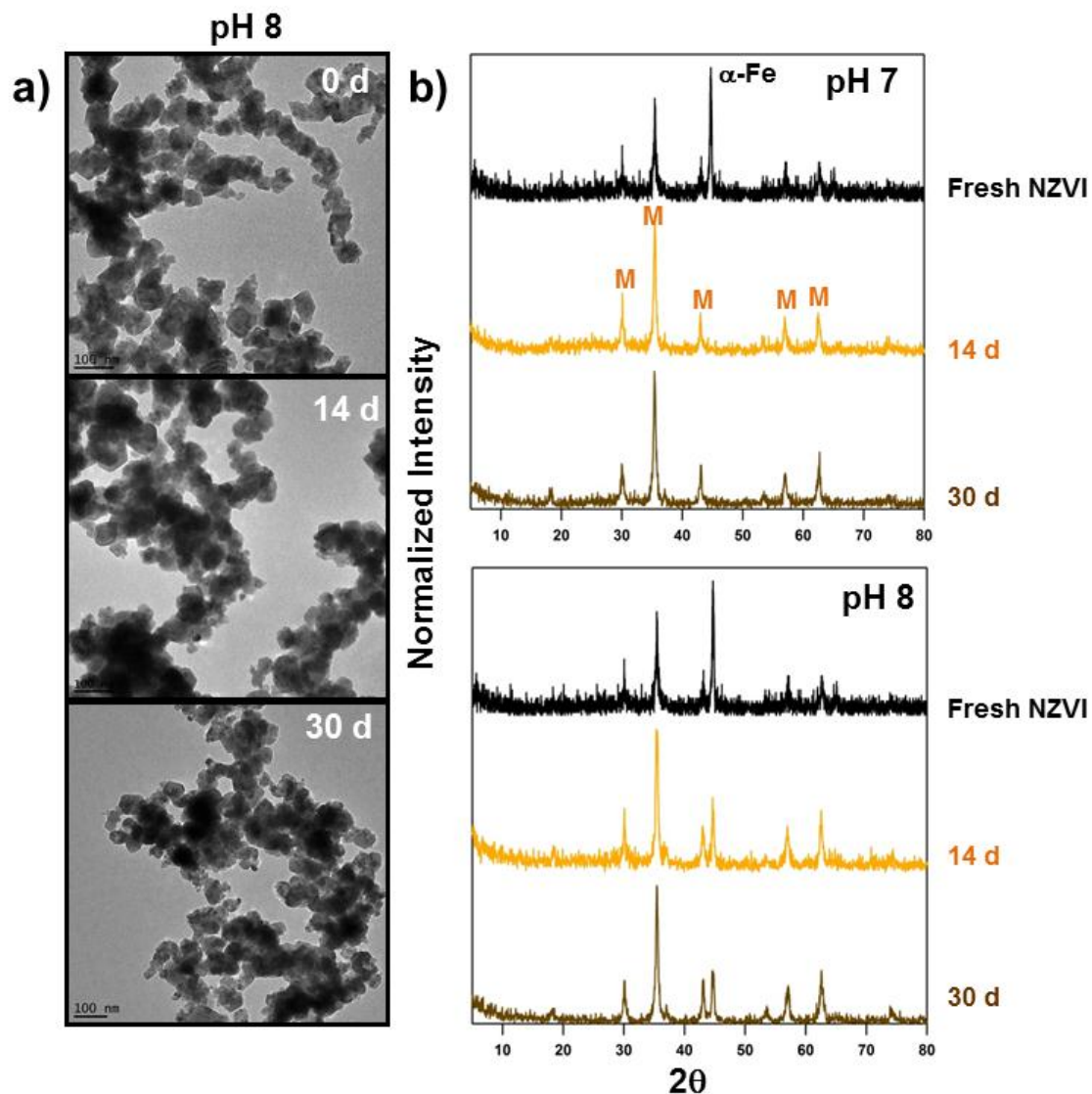


Figure 2-8. (a) TEM images collected as a function of time for NZVI suspensions aged in 25 mM Cl^- at pH 8. Corresponding XRD patterns (b) are shown as a function of aging time for 25 mM Cl^- suspensions aged at pH 7 and pH 8. Relative modest changes in particle morphology were observed over time with TEM images, while XRD patterns are consistent with magnetite (indicated by “M”) as the dominant corrosion product formed in NZVI suspension aged in the presence of Cl^- . Notably, a the characteristic diffraction line for $\alpha\text{-Fe}(0)$ persisted over the entire 30 d aging period at pH 8, whereas a signal for $\alpha\text{-Fe}(0)$ was not detectable at pH 7 over the same timescales. The persistence of $\alpha\text{-Fe}(0)$ at pH 8 likely results from the lower $\text{Fe}(0)$ corrosion rate at this higher pH value, in combination with the less reactive magnetite surface layer, thereby slowing rates of $\text{Fe}(0)$ consumption in the NZVI particle core.

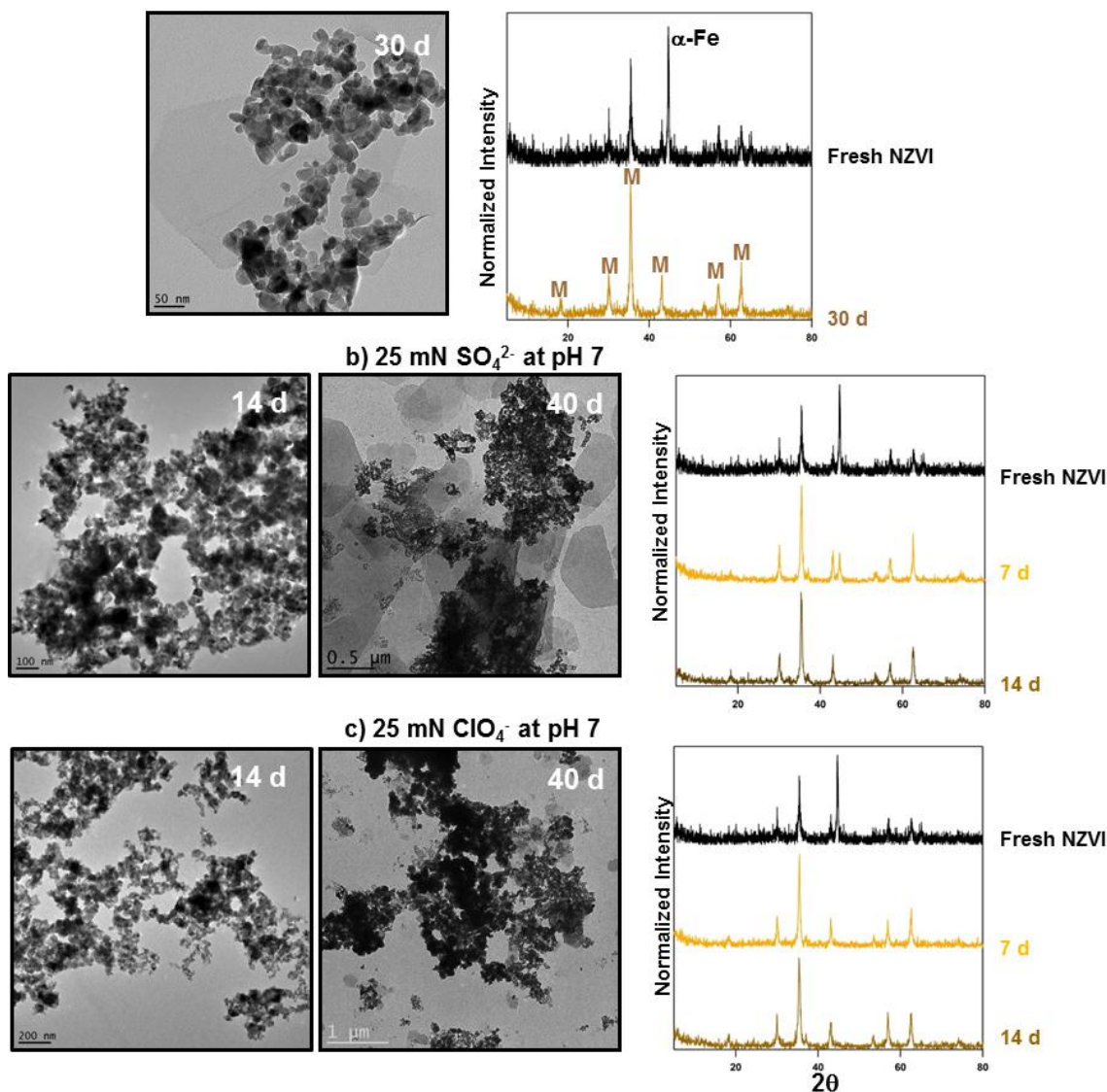


Figure 2-9. TEM images and X-ray diffraction patterns collected as a function of aging time in pH 7 suspensions of (a) 5 mN Cl⁻, (b) 25 mN SO₄²⁻, and (c) 25 mN ClO₄⁻. Generally, comparable time-dependent trends in corrosion product formation are observed for these anions. In all instances, TEM images show clear evidence for the formation of secondary mineral precipitates. Notably, the observation of large, hexagonal platelets is consistent with green rust formation in all suspensions, although green rust was not detectable with XRD. Rather, XRD patterns indicate magnetite (indicated by “M”) is the dominant corrosion product formed in all systems. The similarities of aged Cl⁻, SO₄²⁻, and ClO₄⁻ suspensions is consistent with their near equivalent reactivity toward 1,1,1,2-TeCA, which we proposed is reduced via electron transfer from available Fe(0) at or near the particle-solution interface.

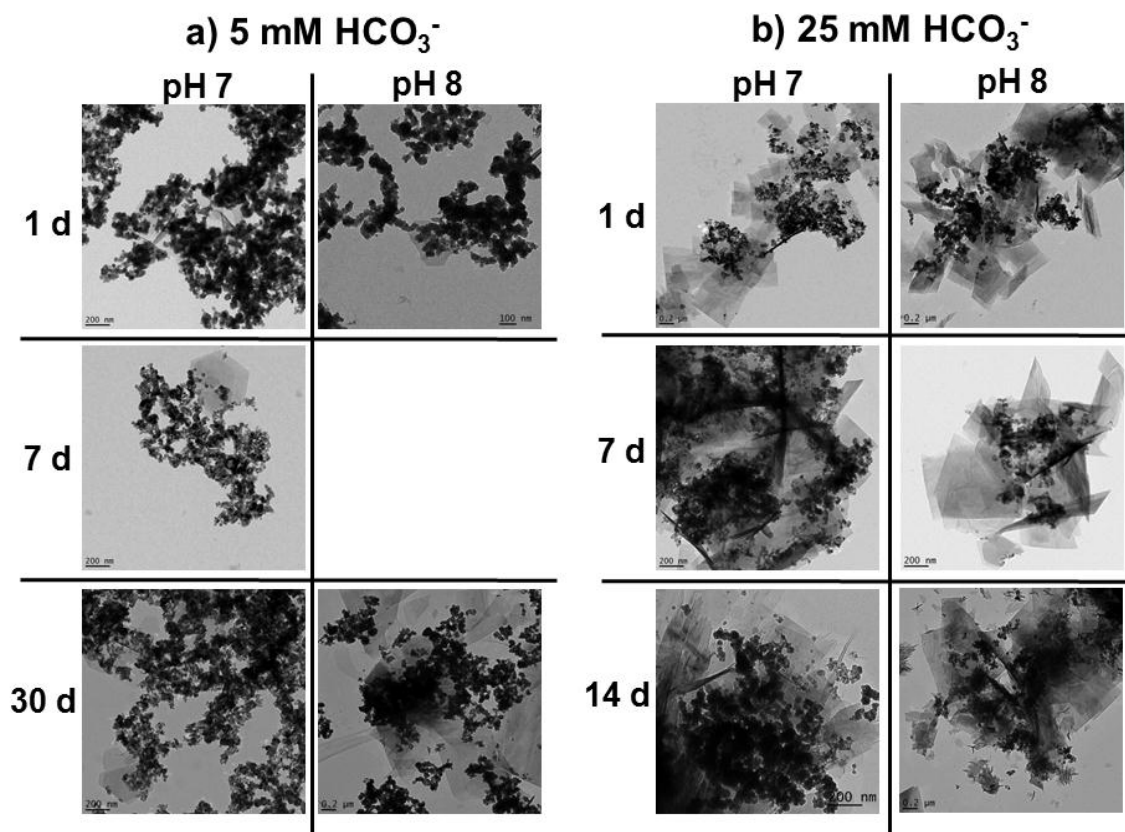


Figure 2-10. Comparison of corrosion product formation in aged suspensions of (a) 5 mM HCO_3^- and (b) 25 mM HCO_3^- at pH 7 and pH 8. As shown in TEM images and supported by XRD analysis, the formation rate and nature of corrosion products in carbonate systems were essentially independent of pH but strongly influenced by carbonate concentration; with the formation iron carbonate hydroxide (ICH) occurring more extensively and over shorter timescales in 25 mM suspensions. As shown in the TEM images, this phase tends to generate in close proximity of NZVI aggregates, with NZVI aggregates being enveloped by the sheet-like ICH morphology. The formation of this secondary mineral phase in 25 mM suspensions coincided with loss of NZVI reactivity toward 1,1,1,2-TeCA but not Cr(VI). Thus, the phase must be redox active but not sufficiently so as to facilitate electron transfer from the Fe(0) particle core to 1,1,1,2-TeCA at the particle-solution interface. Given the manner in which ICH grows on and around NZVI particle aggregates, a possible mechanism responsible for reactivity loss toward 1,1,1,2-TeCA is via steric blocking of reactive sites on NZVI particles, in which the relatively large ICH crystals generated during aging limit access of 1,1,1,2-TeCA to the NZVI surface. Notably, in 5 mM suspensions that remained active toward 1,1,1,2-TeCA over the duration of aging, ICH formation is largely absent in 5 mM concentrations until day 30.

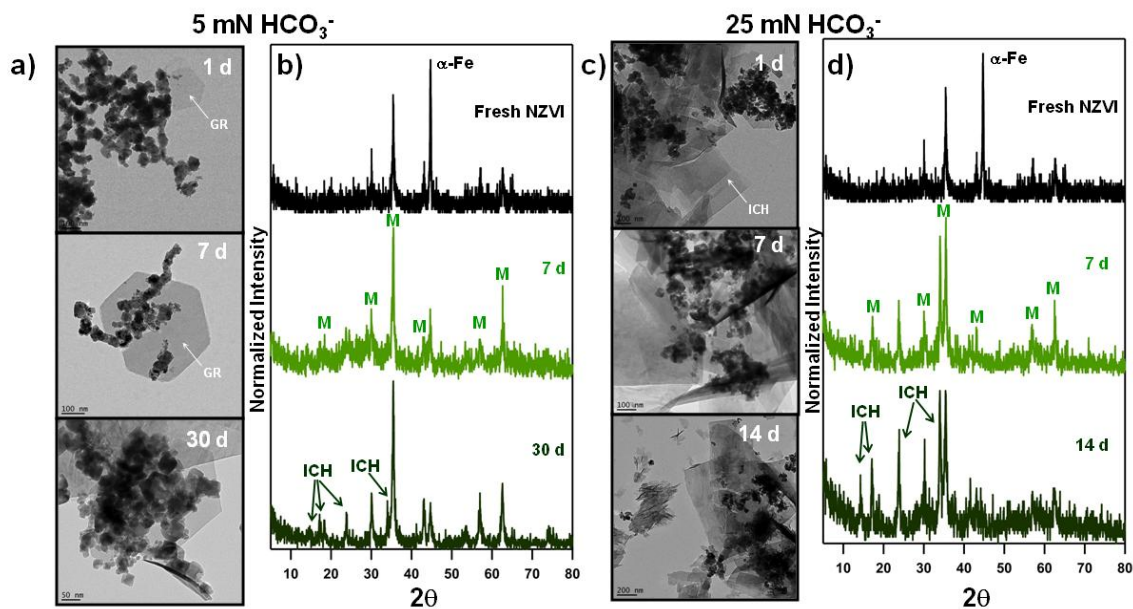


Figure 2-11: Development of corrosion products for NZVI suspension at pH 8 in 5 and 25 mM HCO_3^- suspensions. For each respective concentration, TEM images (a and c, respectively) and XRD patterns (b and d, respectively) are shown as a function of aging timescales. In XRD patterns diffraction lines associated with specific phases are identified, and select phases are indicated by arrows in TEM images. These include $\alpha\text{-Fe}$ for Fe(0), M for magnetite, and ICH for iron carbonate hydroxide. Diffraction lines were identified based upon comparison to d-spacings and 2θ values provided by Kohn *et al.* [31] and references therein.

Influence of Corrosion Products on Longevity Toward Cr(VI)

Unlike longevity toward 1,1,1,2-TeCA, the nature of corrosion products cannot explain the trends in Cr(VI) removal capacity observed for aged NZVI suspensions. In HCO_3^- systems, for example, the timescales and nature of corrosion product formation were independent of pH, yet Cr(VI) removal capacity was almost two times greater at pH 7 than pH 8 (Figure 2-5). Also, despite rather considerable differences in the rates and extent of ICH formation in 5 and 25 mM HCO_3^- suspensions, Cr(VI) removal capacity

was essentially constant over time and did not vary with HCO_3^- concentration (Figure 2-5). Trends in Cr(VI) removal, therefore, provide new insight into the nature of ICH as a redox active phase; although it does not facilitate electron transfer from the Fe(0) particle core to 1,1,1,2-TeCA, it is sufficiently redox active to sustain Cr(VI) removal. The comparable corrosion products observed in Cl^- , SO_4^{2-} and ClO_4^- systems also fail to explain the unique differences in Cr(VI) removal capacity, rates of reactivity loss toward Cr(VI), and pH dependence for Cr(VI) removal in these systems. In the context of Cr(VI) removal, therefore, characterization results further support a scenario in which the source of reactivity and pathways responsible for reactivity loss differ substantially from 1,1,1,2-TeCA.

Correlation of NZVI Reactivity with ORP and Fe(II) Production Rates

ORP proved to be a poor indicator of suspension reactivity toward 1,1,1,2-TeCA and Cr(VI) (Figure 2-12). For nearly all anions and aquatic conditions, ORP values remained between -600 and -700 mV over the duration of aging. Over time, significant changes in ORP were only observed in 25 mN NO_3^- suspensions, which achieved more positive ORP values (roughly -200 mV at pH 7 and -400 mV at pH 8) after 30 d of aging. Generally, the relative insensitivity of ORP in suspensions with anions other than nitrate may reflect the measurement conditions; recent work by Shi *et al.*[49] found that above NZVI concentrations of 200 mg/L, particle attachment to the electrode lessens sensitivity to changes in solution chemistry.

A strong indicator of NZVI reactivity toward Cr(VI) was the rate of Fe(II) production; plots of Cr(VI) removal capacity as a function of measured Fe(II) production rate produced a positive, linear relationship (Figure 2-13). We reiterate that Fe(II) production rates were measured in the absence of 1,1,1,2-TeCA and Cr(VI) using NZVI particles that were water-washed to remove any Fe(II) accumulated during aging. Thus, this relationship in no way reflects the reactivity of Fe(II) that accumulated in the suspension during aging. We note that Fe(II) was not measurable in reactivity studies with Cr(VI), which we attribute to the ability of soluble Fe(II) to reduce Cr(VI) directly [30]. Also in Figure 2-13, Cr(VI) removal data in NO_3^- systems are shown along the y-axis (i.e., corresponding to a Fe(II) production rate of zero) because rates of Fe(II) production were not measurable in these suspensions. While most systems showed the anticipated initially linear increase in Fe(II) concentration over time (Figure 2-14a), soluble Fe(II) concentrations in 5 mN NO_3^- were essentially constant over time (Figure 2-14b), while in 25 mN NO_3^- system aqueous Fe(II) was below detection in all samples, which we attribute to its consumption via reaction with either NO_3^- or its reduction products (e.g., nitrite) [27].

Upon examination, this linear relationship is independent of anion identity and concentration, as data from all anion systems are distributed randomly over the range of Cr(VI) removal capacities and Fe(II) production rates reported (Figure 2-13a). This is also the case when data is categorized based upon the extent of aging (Figure 2-15), which also produces a random distribution. In contrast, the key suspension variable governing Cr(VI) removal by NZVI is pH; when Cr(VI) removal data are classified by

suspension pH (Figure 2-13b), clear clusters in the relationship with Fe(II) production rate are observed. Low pH values correspond to the highest rates of Fe(II) production and the greatest Cr(VI) removal capacities, and vice versa. Additional Cr(VI) removal studies spanning a broader range of suspensions pH values (suspensions of Cl^- and SO_4^{2-} aged over 7 days at pH 6 and 9) also followed this relationship. Thus, regardless of the anion identity, anion concentration, and the duration of aging, Cr(VI) removal by NZVI can be predicted entirely from the rate of Fe(II) production, which is a metric of Fe(0) corrosion.

In Figure 2-13, a noteworthy feature is the y-axis intercept. Excluding nitrate suspensions, this corresponds to a Cr(VI) removal capacity of ~ 25 mg Cr(VI)/g Fe when Fe(II) production was not measurable, as was typical for suspensions aged at high pH. We hypothesize that this lower limit of Cr(VI) removal reflects the available density of Fe(0) sites initially exposed at or near the NZVI particle surface. When exposed to solution at corrosion pits, cracks or defects in the surface oxide layer, Fe(0) can either reduce water to generate soluble Fe(II) or transfer electrons directly to Cr(VI). At high pH where Fe(II) production is slow, Cr(VI) receives the majority of reducing equivalents, but subsequent precipitation of Cr(III)-Fe(III) hydroxides blocks these sites and prevents further Cr(VI) removal. At low pH values, in contrast, these surface sites produce relatively high concentrations of ferrous iron species that are also capable of reducing Cr(VI) directly. Because soluble Fe(II) was never measurable in the presence of Cr(VI), these reactive forms of ferrous iron must exist entirely in the near-surface region of the NZVI particle. Although the exact nature of these ferrous iron species is not known, they

appear to be the dominant entity responsible for Cr(VI) reduction in NZVI suspensions at pH values less than or equal to 8.

Finally, values of $k_{\text{obs}}(1,1,1,2\text{-TeCA})$ revealed no relationship with Fe(II) production rate (Figure 2-16), regardless of whether data were evaluated as a function of the anion identity, anion concentration, system pH or duration of aging. Thus, we propose that while Cr(VI) reduction is largely dominated by Fe(II) species generated from corrosion, 1,1,1,2-TeCA reduction is controlled by the availability of Fe(0) at the NZVI particle surface. This scenario would explain why Cl^- , SO_4^{2-} , ClO_4^- and even low concentrations of HCO_3^- all exhibited essentially equal reactivity toward 1,1,1,2-TeCA but divergent reactivity toward Cr(VI). Cr(VI) removal will be sensitive to the nature of the Fe(II) species produced on the NZVI surface during aging, whereas 1,1,1,2-TeCA reduction will only be affected by the ability of these phases to block Fe(0) surface sites. The latter scenario is consistent with increases in $k_{\text{obs}}(1,1,1,2\text{-TeCA})$ values observed in response to autoreduction, during which thinning of the overlying surface oxide makes reducing equivalents from Fe(0) more accessible to solution.

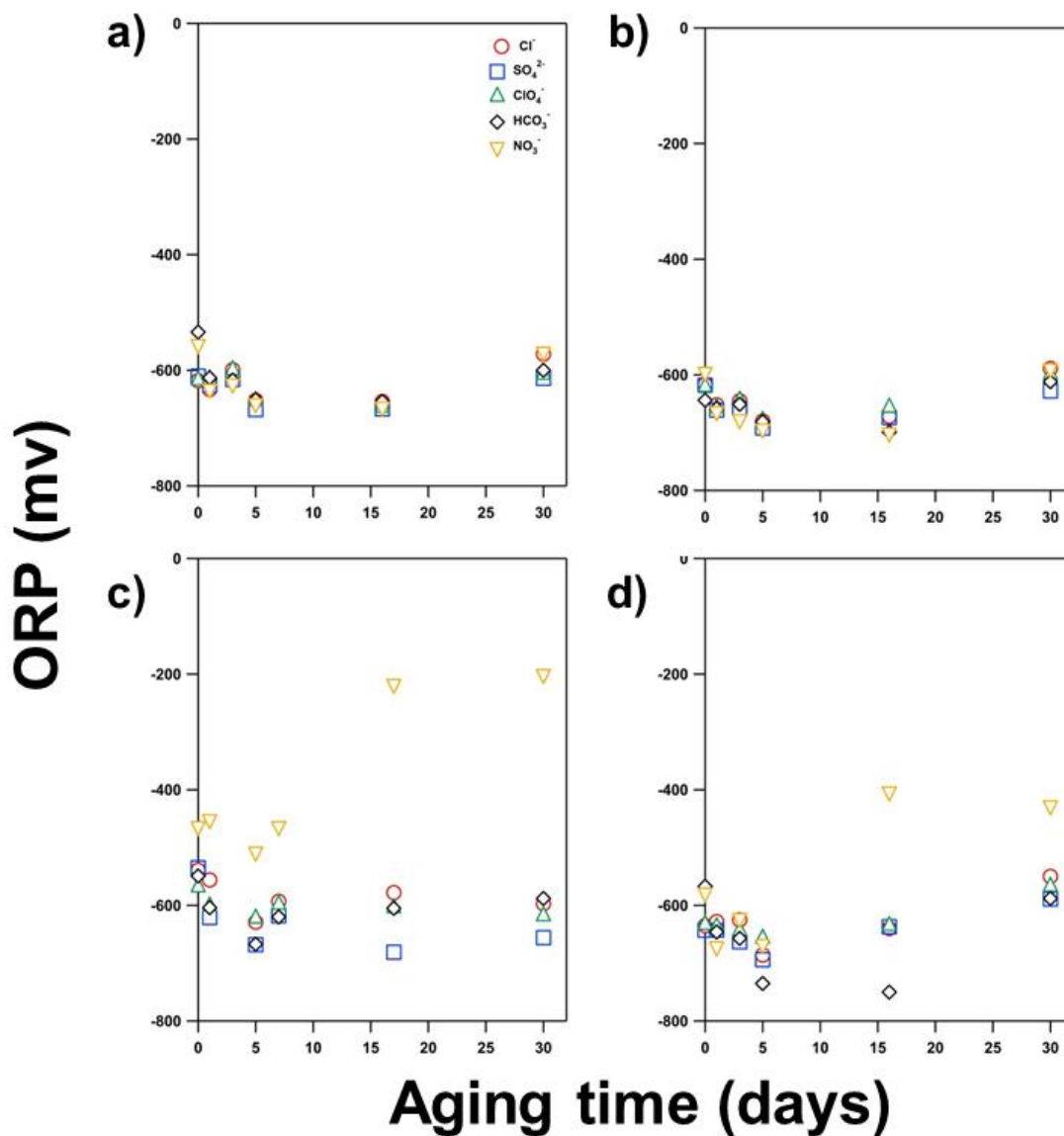


Figure 2-12. Values of oxidation-reduction potential (ORP) measured as a function of aging time for NZVI suspensions containing Cl⁻, SO₄²⁻, ClO₄⁻, HCO₃⁻ and NO₃⁻. ORP values are shown for suspensions with the respective anion concentration and pH values of (a) 5 mN and pH 7; (b) 5 mN and pH 8; (c) 25 mN and pH 7; and (d) 25 mN and pH 8. ORP measurements were made with a commercially available ORP electrode for well-mixed suspensions of 2 g/L NZVI with at least 25 mL of total volume. Generally, ORP values were insensitive to the extent of aging in nearly all anion systems. Clear differences in ORP over time were only measured for 25 mN nitrate systems, in with ORP increased to less negative values over the 30 day aging period. Given the relative insensitivity of suspension ORP to suspensions aging time, ORP proved to be a poor descriptor or predictor of reactivity loss toward 1,1,1,2-TeCA and Cr(VI).

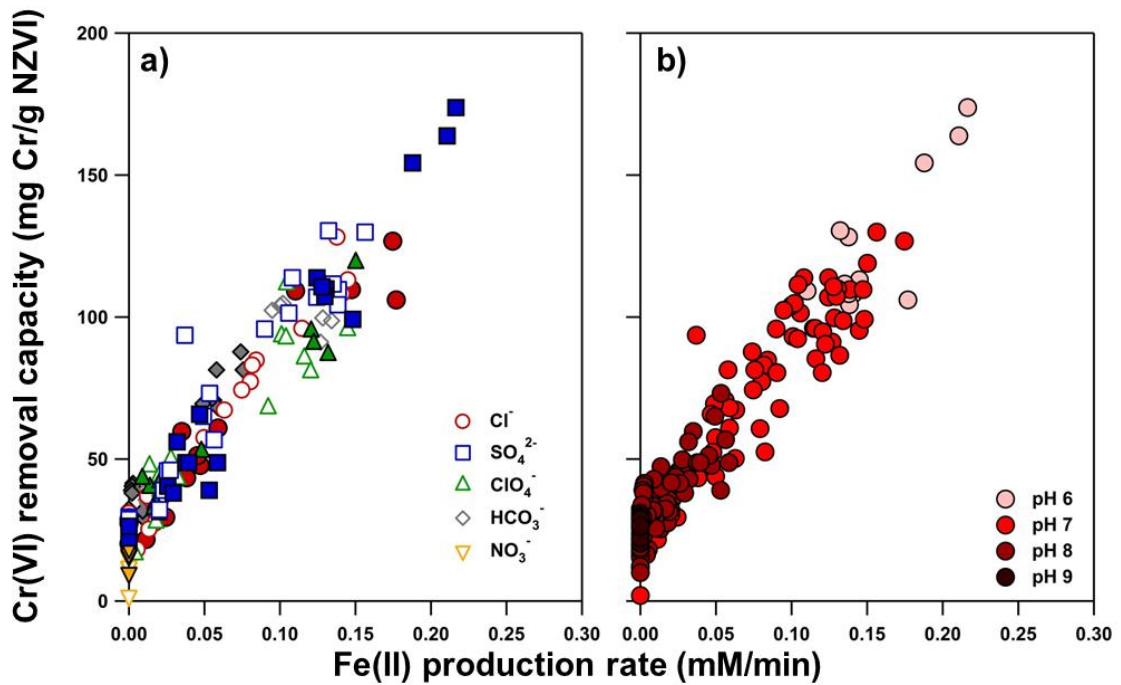


Figure 2-13. Cr(VI) removal capacity plotted as a function of Fe(II) production rate with data categorized as a function of a) anion identity and concentration where open symbols represent 5 mN suspensions and solid symbols represent 25 mN suspensions and b) suspension pH. Figure 2-15 shows a similar plot for data evaluated based on the extent of suspension aging.

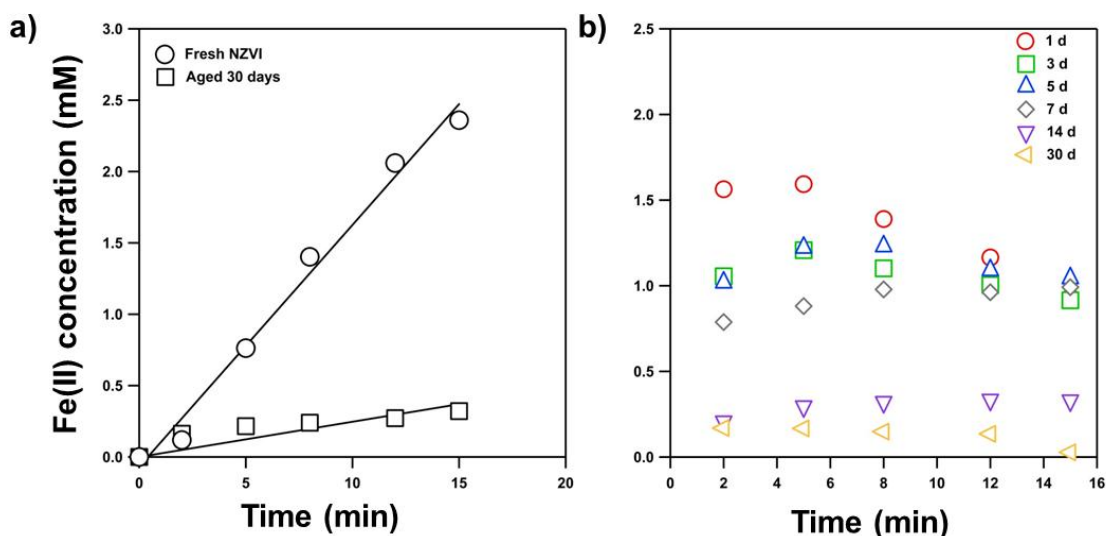


Figure 2-14. Production of aqueous Fe(II) as a function of time in 1 g/L suspensions of NZVI containing (a) 25 mM Cl^- at pH 7 and (b) 5 mM NO_3^- system at pH 7. In each case, data are shown as a function of duration of aging. As shown for chloride-containing suspensions, concentration profiles for Fe(II) in chloride, sulfate, perchlorate and carbonate-containing systems followed expected initially linear behavior over all aging timescales, thereby allowing the rate of Fe(II) production to be determined by linear regression (typical linear regression fits are shown in (a)). In contrast for 5 mM nitrate suspensions, Fe(II) concentrations over time did not follow expected dissolution behavior. Rather, as shown in (b), Fe(II) concentration was initially relative high at early aging timescales, and subsequently decreased with time. Over longer periods of aging, the amount of Fe(II) produced initially decreased, and Fe(II) concentration remained relatively constant or slightly decreased over time. We believe that the unexpected Fe(II) concentration profiles in 5 mM nitrate systems reflect the ability of aqueous and surface-associated Fe(II) to reduce nitrate and/or the products of nitrate reduction by NZVI (e.g., nitrite, which was detected in nitrate-containing NZVI suspensions; see Figure 2-2). Recall, as we described in the main text, that Fe(II) production rates were measured in the absence of Cr(VI) or 1,1,1,2-TeCA, and that Fe(II) was not measurable during reaction between aged NZVI particles and Cr(VI). We also note that aqueous Fe(II) concentrations were below our limit of detection (~ 1 mM) in 25 mM nitrate and nitrate suspensions at pH 8.

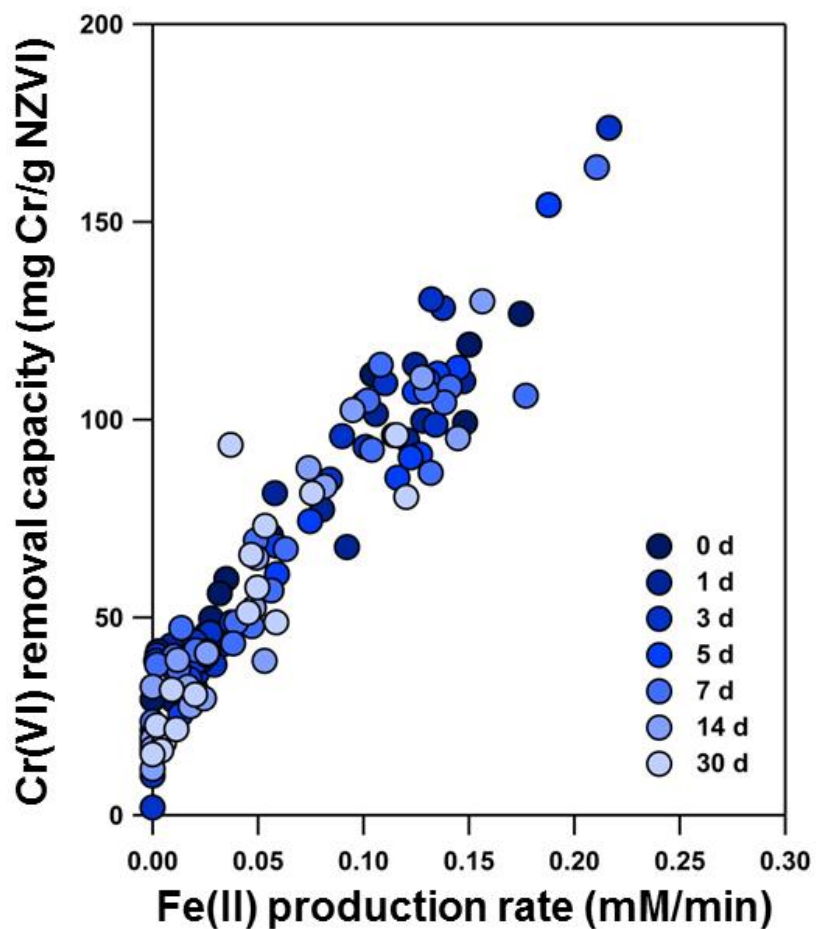


Figure 2-15. Correlation between total Cr(VI) removal capacity and Fe(II) production rate when data from all anion systems is categorized based on the extent of suspension aging. This plot is analogous to Figure 2-13 in the main text, in which the same data set is shown for scenarios in which data are sorted by anion identity and concentration (Figure 2-13a) and suspensions pH (Figure 2-13b). No clear influence of aging time is observed, as Cr(VI) removal capacities and Fe(II) production rates from all durations of aging are randomly distributed along the linear relationship shown for these variables.

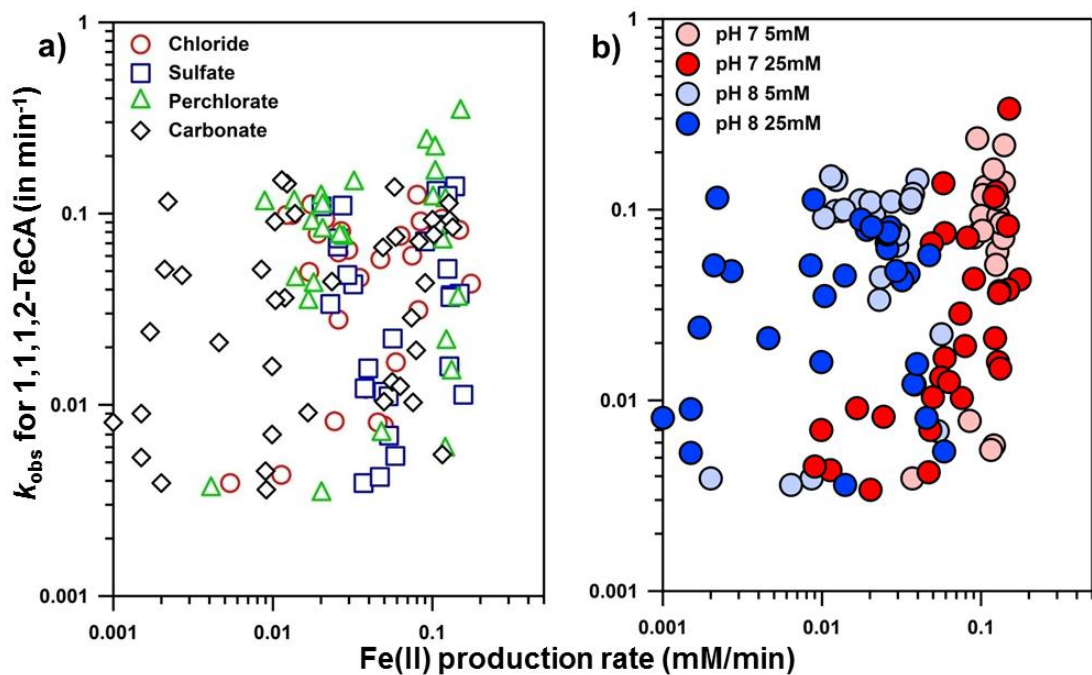


Figure 2-16. Plot of k_{obs} values for 1,1,1,2-TeCA reduction as a function of Fe(II) production rate when data is categorized based upon (a) anion identity and (b) pH condition and anion concentration. Data for nitrate-containing suspensions are not shown due to the lack of measurable Fe(II) production rates. In contrast to results with Cr(VI) removal capacities, no clear correlation between k_{obs} values for 1,1,1,2-TeCA and Fe(II) production rates. The lack of such a relationship, as well as the differences in the rates of reactivity loss toward 1,1,1,2-TeCA and Cr(VI), indicate a difference in the entities primarily responsible for their reduction of in NZVI systems.

2.5. Environmental Implications

Unlike previous studies conducted under more idealized conditions, results herein show that NZVI reactivity toward chlorinated solvents such as 1,1,1,2-TeCA is likely to be exhausted over one month in circumneutral pH environments, and potentially far shorter timescales in environments impacted by NO_3^- and HCO_3^- . Fundamentally, several lines of evidence presented herein also suggest that 1,1,1,2-TeCA (solution accessible Fe(0)) and Cr(VI) (surface-associated ferrous iron) are reduced primarily by different reactive entities in NZVI suspensions, and that these reductants species display different timescales and mechanisms of passivation during aging. Consequently, the impact of anions and anion concentrations on NZVI longevity is difficult to generalize broadly across contaminant classes, as is the influence of solution pH, which also was markedly different for 1,1,1,2-TeCA and Cr(VI). The impact of specific corrosion products on NZVI longevity is also difficult to predict; the onset of ICH formation ultimately killed NZVI activity toward 1,1,1,2-TeCA, but exerted little influence on Cr(VI) removal capacity. Perhaps the only generalization safely made is largely intuitive; co-solutes that accept reducing equivalents from Fe(0) (e.g., NO_3^-) dampen reactivity and shorten longevity more so than species that only alter the rate and products of NZVI corrosion.

Given concerns over materials cost and potential negative consequences of engineered nanomaterials in the environment, NZVI should only be used when it holds a clear and obvious advantage over more traditional granular iron technologies. Given its notably higher rate of corrosion, NZVI is by far the best choice for pollutants susceptible to reduction not only by Fe(0) but also by Fe(II). This point is clearly demonstrated with

Cr(VI), which appears to be primarily reduced by ferrous iron species in our experimental systems. A notable limitation of our study, however, is that we have largely ignored that role played by Cr(III)-Fe(III) phases generated via Cr(VI) reduction in limiting NZVI longevity during application. Our work, which focuses on NZVI reactivity loss arising from corrosion (i.e., water reduction), is not meant to imply that treatment zones will stay active toward Cr(VI) over several months; in actuality, their lifetime will be heavily influenced by the available Cr(VI) concentration. Thus, ideal treatment applications for NZVI are those pollutant targets such as nitroaromatic compounds, which are readily reducible by ferrous iron but only yield soluble reduction products.

A notable finding of this work is the correlation illustrating the strong link between Fe(II) production rate and Cr(VI) removal (Figure 2-13), suggesting that Cr(VI) removal is primarily driven by Fe(II) species rather than Fe(0) in NZVI systems. This relationship needs to be further explored for other commercially available forms of nanoscale and granular zero-valent iron. If the relationship is also observed for other types of zero-valent iron, it should prove useful for identifying materials with optimal Cr(VI) removal capacities and best suited for application at Cr(VI) contaminated sites. The ability to predict zero-valent iron treatment efficiency from a relatively easily measurable property such as Fe(II) production or corrosion rate should also guide the development of more reactive iron-based reductants that improve upon current commercially available formulations.

2.6. Acknowledgements

The authors acknowledge the Central Facility for Advanced Microscopy and Microanalysis (CFAM) at UC Riverside for assistance with TEM images and Dr. Pingyung Feng for assistance with XRD analysis.

2.7. Literature cited

1. Li, L.; Fan, M.; Brown, R.C.; Van Leeuwen, J.; Wang, J.; Wang, W.; Song, Y.; Zhang, P., Synthesis, properties, and environmental applications of nanoscale iron-based materials: a review. *Crit. Rev. Environ. Sci. Technol.* 2006, *36*, 405-431.
2. Li, X.; Elliot, D.W.; Zhang, W.-X., Zero-valent iron nanoparticles for abatement of environmental pollutants: materials and engineering aspects. *Crit. Rev. Solid State Mater. Sci.* 2006, *31*, 111-122.
3. Tratnyek, P.G.; Johnson, R.L., Nanotechnologies for environmental cleanup. *Nano Today* 2006, *1*, 44-48.
4. Zhang, W.-X., Nanoscale iron particles for environmental remediation: an overview. *J. Nanopart. Res.* 2003, *5*, 323-332.
5. Elliot, D.W.; Zhang, W.-X., Field assessment of nanoscale bimetallic particles for groundwater treatment. *Environ. Sci. Technol.* 2001, *35*, 4922-4926.
6. Henn, K.W.; Waddill, D.W., Utilization of nanoscale zero-valent iron for source remediation- A case study. *Remediation Journal* 2006, *16*, 57-77.
7. Wei, Y.-T.; Wu, S.-C.; Chou, C.-M.; Che, C.-H.; Tsai, S.-M.; Lien, H.-L., Influence of nanoscale zero-valent iron on geochemical properties of groundwater and vinyl chloride degradation: a field case study. *Water Res.* 2010, *44*, 131-140.
8. He, F.; Zhao, D.; Paul, C., Field assessment of carboxymethyl cellulose stabilized iron nanoparticles for in situ destruction of chlorinated solvents in source zones. *Water Res.* 2010, *44*, 2360-2370.
9. Liu, Y.; Lowry, G.V., Effect of particle age (Fe^0 content) and solution pH on NZVI reactivity: H_2 evolution and TCE dechlorination. *Environ. Sci. Technol.* 2006, *40*, 6085-6090.

10. Sarathy, V.; Tratnyek, P.G.; Nurmi, J.T.; Baer, D.R.; Amonette, J.E.; Chun, C.L.; Penn, R.L.; Reardon, E.J., Aging of iron nanoparticles in aqueous solution: effects on structure and reactivity. *J. Phys. Chem. C* 2008, *112*, 2286-2293.
11. Xie, Y.; Cwiertny, D.M., Use of dithionite to extend the reactive lifetime of nanoscale zero-valent iron treatment systems. *Environ. Sci. Technol.* 2010, *44*, 8649-8655.
12. Henderson, A.D.; Demond, A.H., Long-term performance of zero-valent iron permeable reactive barriers: a critical review. *Environ. Eng. Sci.* 2007, *24*, 401-423.
13. Devlin, J.F.; Allin, K.O., Major Anion Effects on the Kinetics and Reactivity of Granular Iron in Glass-Encased Magnet Batch Reactor Experiments. *Environ. Sci. Technol.* 2005, *39*, 1868-1874.
14. Cheng, I.F.; Muftikian, R.; Fernando, Q.; Korte, N., Reduction of nitrate to ammonia by zero-valent iron. *Chemosphere* 1997, *35*, 2689-2695.
15. Gotpagar, J.; Lyuksyutov, S.; Cohn, R.; Grulke, E.; Bhattacharyya, D., Reductive Dehalogenation of Trichloroethylene with Zero-Valent Iron: Surface Profiling Microscopy and Rate Enhancement Studies. *Langmuir* 1999, *15*, 8412-8420.
16. Hao, Z.-W.; Xu, X.-H.; Jin, J.; He, P.; Liu, Y.; Wang, D.-H., Simultaneous removal of nitrate and heavy metals by iron metal. *Journal of Zhejiang University Science* 2005, *6*, 307-310.
17. Ritter, K.; Odziemkowski, M.S.; Simpgraga, R.; Gillham, R.W.; Irish, D.E., An in situ study of the effect of nitrate on the reduction of trichloroethylene by granular iron. *J. Contam. Hydrol.* 2003, *65*, 121-136.
18. Schlicker, O.; Ebert, M.; Fruth, M.; Weidner, M.; Wilst, W.; Dahmke, A., Degradation of TCE with iron: The role of competing chromate and nitrate reduction. *Ground Water* 2000, *38*, 403-409.
19. Klausen, J.; Ranke, J.; Schwarzenbach, R.P., Influence of solution composition and column aging on the reduction of nitroaromatic compounds by zerovalent iron. *Chemosphere* 2001, *44*, 511-517.
20. Lipczynskakochany, E.; Harms, S.; Milburn, R.; Sprah, G.; Nadarajah, N., Degradation of carbon-tetrachloride in the presence of iron and sulfur-containing compounds. *Chemosphere* 1994, *29*, 1477-1489.

21. MacDougall, B.; Graham, M.J., In *Corrosion Mechanisms in Theory and Practice*, Marcus, P.; Oudar, J., Eds. Marcel Dekker: 1995; pp 143-173.
22. Agrawal, A.; Tratnyek, P.G., Reduction of Nitro Aromatic Compounds by Zero-Valent Iron Metal. *Environ. Sci. Technol.* 1995, *30*, 153-160.
23. Mackenzie, P.D.; Horney, D.P.; Sivavec, T.M., Mineral precipitation and porosity losses in granular iron columns. *J. Haz. Mater.* 1999, *68*, 1-17.
24. Roh, Y.; Lee, S.Y.; Elless, M.P., Characterization of corrosion products in the permeable reactive barriers *Environ. Geol.* 2000, *40*, 184-194.
25. Phillips, D.H.; Gu, B.; Watson, D.B.; Roh, Y.; Liang, L.; Lee, S.Y., Performance evaluation of a zerovalent iron reactive barrier: mineralogical characteristics. *Environ. Sci. Technol.* 2000, *34*, 4169-4176.
26. Agrawal, A.; Ferguson, W.J.; Gardner, B.O.; Christ, J.A.; Bandstra, J.Z.; Tratnyek, P.G., Effects of carbonate species on the kinetics of dechlorination of 1,1,1-trichloroethane by zero-valent iron. *Environ. Sci. Technol.* 2002, *36*, 4326-4333.
27. Klausen, J.; Vikesland, P.J.; Kohn, T.; Burris, D.R.; Ball, W.P.; Roberts, A.L., Longevity of Granular Iron in Groundwater Treatment Processes: Solution Composition Effects on Reduction of Organohalides and Nitroaromatic Compounds. *Environ. Sci. Technol.* 2003, *37*, 1208-1218.
28. Jeen, S.W.; Gillham, R.W.; Blowes, D.W., Effects of carbonate precipitates on long-term performance of granular iron for reductive dechlorination of TCE. *Environ. Sci. Technol.* 2006, *40*, 6432-6437.
29. Jeen, S.-W.; Jambor, J.L.; Blowes, D.W.; Gillham, R.W., Precipitates on granular iron in solutions containing calcium carbonate with trichloroethene and hexavalent chromium. *Environ. Sci. Technol.* 2007, *41*, 1989-1994.
30. Bi, E.; Bowen, I.; Devlin, J.F., Effect of Mixed Anions (HCO_3^- , SO_4^{2-} , ClO_4^-) on Granular Iron (Fe0) Reactivity. *Environ. Sci. Technol.* 2009, *43*, 5975-5981.
31. Kohn, T.; Livi, K.J.T.; Roberts, A.L.; Vikesland, P.J., Longevity of Granular Iron in Groundwater Treatment Processes: Corrosion Product Development. *Environ Sci & Tec* 2005, *39*, 2867-2879.
32. Alowitz, M.J.; Scherer, M.M., Kinetics of nitrate, nitrite and Cr(VI) reduction by iron metal. *Environ. Sci. Technol.* 2002, *36*, 299-306.

33. Westerhoff, P., Reduction of nitrate, bromate, and chlorate by zerovalent iron (Fe⁰). *J. Environ. Eng.* 2003, *129*, 10-16.
34. Reardon, E.J.; Fagan, R.; Vogan, J.L.; Przepiora, A., Anaerobic corrosion reaction kinetics of nanosized iron. *Environ. Sci. Technol* 2008, *42*, 2420-2424.
35. Reardon, E.J., Zerovalent Irons: Styles of Corrosion and Inorganic Control on Hydrogen Pressure Buildup. *Environ. Sci. Technol.* 2005, *39*, 7311-7317.
36. Reardon, E.J., Anaerobic Corrosion of Granular Iron: Measurement and Interpretation of Hydrogen Evolution Rates. *Environ. Sci. Technol.* 1995, *29*, 2936-2945.
37. Nurmi, J.T.; Tratnyek, P.G.; Sarathy, V.; Baer, D.R.; Amonette, J.E.; Pecher, K.; Wang, C.; Linehan, J.C.; Matson, D.W.; Penn, R.L.; Driessen, M.D., Characterization and properties of metallic iron nanoparticles: Spectroscopy, electrochemistry, and kinetics. *Environ. Sci. Technol.* 2005, *39*, 1221-1230.
38. Yan, W.; Herzing, A.A.; Kiely, C.J.; Zhang, W.-X., Nanoscale zero-valent iron (nZVI): aspects of the core-shell structure and reactions with inorganic species in water. *J. Contam. Hydrol.* 2010, *118*, 96-104.
39. Liu, Y.; Phenrat, T.; Lowry, G.V., Effect of TCE concentration and dissolved groundwater solutes on NZVI-promoted TCE dechlorination and H₂ evolution. *Environ. Sci. Technol.* 2007, *41*, 7881-7887.
40. Reinsch, B.C.; Forsberg, B.; Penn, R.L.; Kim, C.S.; Lowry, G.V., Chemical Transformations during Aging of Zerovalent Iron Nanoparticles in the Presence of Common Groundwater Dissolved Constituents. *Environ. Sci. Technol.* 2010, *44*, 3455-3461.
41. Cao, J.; Elliott, D.W.; Zhang, W.-X., Perchlorate reduction by nanoscale iron particles. *J. Nanopart. Res.* 2005, *7*, 499-506.
42. Moore, A.M.; De Leon, C.H.; Young, T.M., Rate and Extent of Aqueous Perchlorate Removal by Iron Surfaces. *Environ. Sci. Technol.* 2003, *37*, 3189-3198.
43. Stucki, J.W., The quantitative assay of minerals for Fe²⁺ and Fe³⁺ using 1,10-phenanthroline. II. A photochemical method. *Soil Sci. Soc. Am. J.* 1981, *45*, 638-641.

44. Stucki, J.W.; Anderson, W.L., The quantitative assay of minerals for Fe²⁺ and Fe³⁺ using 1,10-phenanthroline. I. Sources of variability. *Soil Sci. Soc. Am. J.* 1981, *45*, 633-637.
45. Bose, M., Mechanism of the reaction between dichromate and diphenylcarbazide *Nature* 1952, *170*, 213.
46. Cwiertny, D.M.; Roberts, A.L., On the nonlinear relationship between k_{obs} and reductant mass loading in iron batch systems. *Environ. Sci. Technol.* 2005, *39*, 8948-8957.
47. Cornell, R.M.; Schwertmann, U., *The Iron Oxides: Structure, Properties, Reactions, Occurrences and Uses* 2nd ed.; Wiley-VCH: Weinheim, Germany, 2003; p 664.
48. Wilkin, R.T.; Puls, R.W. *Capstone Report on the Application, Monitoring and Performance of Permeable Reactive Barriers for Ground Water Remediation*; U.S. Environmental Protection Agency, Office of Research and Development: Cincinnati, OH, 2003.
49. Shi, Z.; Nurmi, J.T.; Tratnyek, P.G., Effects of nano zero-valent iron on oxidation-reduction potential. *Environ. Sci. Technol.* 2011, *45*, 1586-1592.

3. Use of Dithionite to Extend the Reactive Lifetime of Nanoscale Zero-Valent Iron Treatment Systems²

3.1. Abstract

Nanoscale zero-valent iron (NZVI) represents a promising approach for source zone control, but concerns over its reactive lifetime may limit application. Here, we demonstrate that dithionite ($S_2O_4^{2-}$), a reducing agent for *in situ* redox manipulation, can restore the reducing capacity of passivated NZVI. Slurries of NZVI were aged in the presence (3 days) and absence (60 days) of dissolved oxygen over a range of pH (6-10). Upon loss of reactivity toward model pollutants (1,1,1,2-tetrachloroethane, hexavalent chromium (Cr(VI)), nitrobenzene), aged suspensions were reacted with dithionite, and the composition and reactivity of the dithionite-treated materials were determined. Products of aging generally depended on pH and the presence of oxygen, while the amount of dithionite influenced the identity and reducing capacity of products generated from reaction with aged NZVI suspensions. Notably, air oxidation at $pH \geq 8$ quickly exhausted NZVI reactivity despite preservation of significant Fe(0) in the particle core. Under these conditions, formation of a passive surface layer hindered the complete transformation of NZVI particles into Fe(III) oxides, which occurred at lower pH. Reduction of this passive layer by low dithionite concentrations (< 1 g/g NZVI) restored suspension reactivity to levels equal to, and occasionally greater than, that of unaged NZVI. Multiple dithionite additions further improved pollutant removal, allowing at

² An abbreviated version of this chapter has been published in *Environmental Science and Technology*. Y. Xie and D.M. Cwiertny, Use of Dithionite to Extend the Reactive Lifetime of Nanoscale Zero-Valent Iron Treatment Systems. *Environ. Sci. Technol.* **2010**, *44*, 8649-8655.

least a 15-fold increase in Cr(VI) removal (~300 mg of Cr(VI)/g NZVI) relative to fresh NZVI (~20 mg of Cr(VI)/g NZVI).

3.2. Introduction

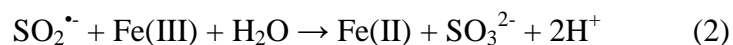
Although subsurface delivery of nanoscale zero-valent iron (NZVI) is an emerging treatment technique for pollutant source zones and deep pollutant plumes [1-3], concerns over the reactive lifetime or longevity of NZVI may hinder its growth into a reliable technology. Because of its high reactivity, NZVI exhibits low selectivity, also reacting with non-target dissolved oxygen and water during application [2]. These side reactions consume zero-valent iron (Fe(0)) and its reducing equivalents, hasten the formation of passive ferric iron (Fe(III)) oxides, and ultimately cause complete loss of reducing capacity [4].

Indeed, growing field- and laboratory scale evidence suggests that the longevity of NZVI is rather limited when compared to lifetimes associated with granular iron permeable reactive barriers (PRBs), for which several examples exist with reported or estimated longevity of several years to decades [5]. In an early NZVI demonstration, Elliott and Zhang [6] observed a 50% decrease in trichloroethene (TCE) removal efficiency over 22 d. More recently, Henn and Waddill [7] observed reductive dehalogenation of TCE and 1,1,1-trichloroethane (1,1,1-TCA) attributable to NZVI for 6-9 months, but removal over longer timescales was attributed to biotic processes stimulated by favorable redox conditions post-NZVI delivery. Using experimentally measured rates of anaerobic iron corrosion, Reardon *et al.* [8] estimated NZVI half-lives

around 80 d in water, although greater longevity was reported in slurries with sand due to silica's role as a corrosion inhibitor. In a noteworthy study by Liu and Lowry [9], pseudo-first-order rate constants (k_{obs} values) for TCE reduction decreased by roughly a factor of 6 over 10 days. Although reactivity was essentially stable over the next 8 months in their deoxygenated, unbuffered (pH 6.9-8.9) experimental systems, the authors concluded that the reactivity of NZVI at neutral pH would be consumed over a few weeks. Similarly, Sarathy *et al.* [4] found that reactivity towards carbon tetrachloride in unbuffered, deoxygenated systems was gradually lost over a few hundred days due to the formation of a passivating, mixed-valent Fe(II)-Fe(III) surface film.

To increase application and improve long-term performance, strategies for sustaining the reactivity of NZVI treatment zones must be developed. Conventional wisdoms call for the delivery of additional NZVI upon reactivity loss, but this may be prohibitive depending on material costs and also will increase the likelihood of aquifer clogging. Alternatively, chemical regeneration, an approach widely utilized in catalysis [10], represents a promising yet largely unexplored route for sustaining treatment zone activity. For example, strong acid has been used to destabilize passive Fe(III) oxides on Fe(0), thereby restoring reactivity to once exhausted granular iron [11]. Others have attempted regeneration with sodium borohydride [12], a strong reductant capable of returning oxidized iron to a zero-valent state. Although likely impractical due to the impact these aggressive reagents will exert on subsurface environments, such approaches demonstrate that chemical agents capable of altering the surface composition of passivated iron particles may provide a route to sustaining NZVI longevity.

A logical candidate for chemical regeneration of passivated NZVI is dithionite ($\text{S}_2\text{O}_4^{2-}$). Previously used in groundwater remediation via *in situ* redox manipulation (ISRM) [13], dithionite is a potent reductant in alkaline solutions ($E_o^{1/2} = -1.12 \text{ V}$ [14]) in which it reversibly dissociates to form highly reactive sulfoxyl radicals (eq 1) that can reduce Fe(III) to ferrous iron (Fe(II)) (eq 2) [15].



Some have also suggested that at very basic pH (> 10), dithionite reduces Fe(II) to Fe(0), yielding a highly reactive form of NZVI comparable to material generated from reduction with borohydride [16].

Based upon observations during ISRM [13, 15, 17], it can be anticipated that dithionite will reduce passive products of NZVI oxidation to yield various forms of aqueous, solid-phase or surface-associated Fe(II), many of which are capable reductants for common groundwater pollutants [18]. In addition to generating new Fe(II)-based reductants from Fe(III) corrosion products, dithionite may also restore NZVI reactivity by re-exposing Fe(0) trapped underneath passive Fe(III) oxide surface coatings. Other practical advantages of dithionite stem from its use for treatment of hexavalent chromium (Cr(VI)) via ISRM at the DOE Hanford Site [19], as many of the logistical and regulatory aspects of its subsurface application already have been addressed.

In the current study, we demonstrate the feasibility of dithionite as a chemical regenerant for the reducing capacity of passivated NZVI systems. Slurries of a commercially available NZVI were aged in the presence (3 days) and absence (60 days)

of dissolved oxygen over a range of pH (pH 6-10) in buffered systems. Notably, most previous aging studies have utilized strict oxygen-free conditions and have rarely controlled suspension pH during aging. The latter is particularly important because the amount of NZVI typically delivered into the subsurface will likely be too low to alter pH values poised by the high buffering capacities of most soils [9]. Thus, the systems employed herein are intended to more accurately reflect the range of subsurface conditions likely to be encountered at treatment sites.

Upon loss of reactivity toward a range of different model pollutants including Cr(VI), nitrobenzene, and 1,1,1,2-tetrachloroethane (1,1,1,2-TeCA), passivated NZVI suspensions were characterized by an array of techniques to identify products of aging and subsequently reacted with dithionite solutions. The products from the reaction between dithionite and aged NZVI were then identified through further materials characterization, and their reactivity was measured in additional batch experiments with our model pollutant suite.

The specific goals of this study were to establish the timescales of NZVI longevity and the products of particle aging at different pH values for redox conditions favorable (anaerobic) and potentially unfavorable (aerobic) for NZVI application. Another aim was to determine whether the repeated use of dithionite represents a viable step toward sustainable and long-term *in situ* groundwater treatment with NZVI. This entailed identifying the optimal operational parameters for restoring reducing capacity with dithionite and linking changes in reactivity resulting from the reaction of aged NZVI with dithionite to changes in suspension composition and mineralogy.

3.3. Experimental Methods

Reagents

NZVI was purchased from Nanostructured and Amorphous Materials, Inc. (Houston, TX). This material is a dry powder packaged under N₂ that is synthesized from the reduction of iron oxides by H₂ and stabilized via partial oxidation under 10% O₂. The material was highly reactive, igniting upon exposure to air. The vendor reports an average particle size of 25 nm and a BET surface area of 40-60 m²/g. Additional characterization suggests the particles consist of roughly 80% Fe(0) and 20% magnetite (Figure 3-1).

Sodium dithionite (Na₂S₂O₄; ~85%; Sigma-Aldrich) solutions were prepared in either 50 mM sodium carbonate (NaHCO₃; HPLC Grade; Fisher) at pH 11, 0.001 N sodium hydroxide (NaOH; 97+%; ACS reagent grade), or DI water. Reactivity studies were conducted with 1,1,1,2-tetrachloroethane (1,1,1,2-TeCA; ~99%; Aldrich), nitrobenzene (reagent grade; Sigma-Aldrich), and hexavalent chromium (Cr (VI)) prepared from potassium chromate (K₂CrO₄; reagent grade, Fisher). The buffers use to maintain system pH in aging and reactivity studies were either Trizma hydrochloride (Reagent Grade, > 99% redox titration), MES hydrate (99%, for biochemistry), or HEPES (minimum 99.5% titration) and NaCl (ACS reagent, ≥99.0%) was used to poise ionic strength. All solutions were prepared in deionized water (Millipore, Q-Grad 2) and were deoxygenated by sparging with N₂ (at least 1 h/L). NZVI and all solutions were stored within an anaerobic glovebox (95% N₂, 5% H₂, Coy Laboratory Products) until use.

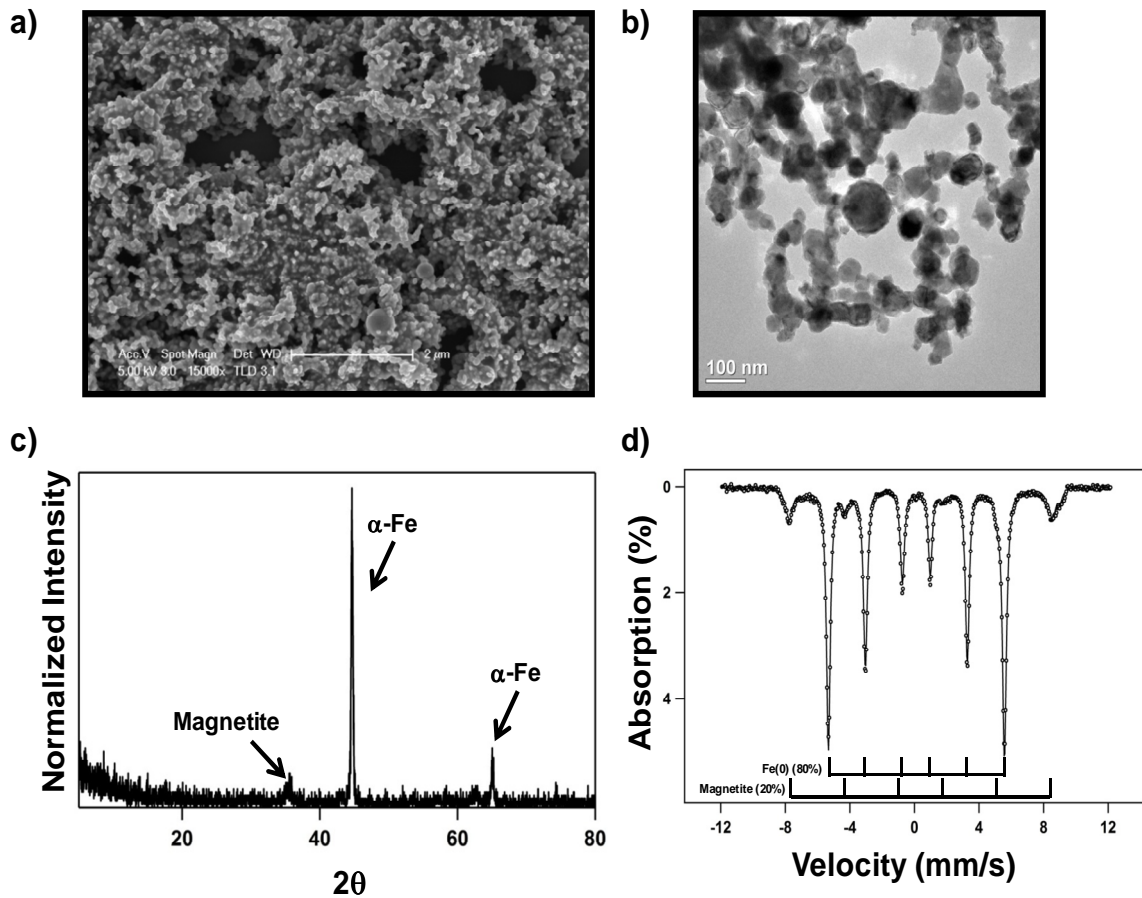


Figure 3-1: (a) Scanning electron microscopy, (b) transmission electron microscopy, (c) powder X-ray diffraction and (d) ⁵⁷Fe Mössbauer spectroscopy analysis of NZVI from Nanostructured and Amorphous Materials. Mössbauer spectrum was collected at 13K. The data collected during Mössbauer analysis are shown as open circles, whereas the solid line represents the model fit to the experimental data (see details below). Key features associated with the different phases present in the material are indicated in the XRD pattern and Mössbauer spectra.

Aging of NZVI Suspensions

Within an anaerobic chamber, 2 g/L suspensions of NZVI were prepared in 125 mL Erlenmeyer flasks using deoxygenated buffers at pH 6 (MES), 7 (HEPES) and 8 (HEPES or Tris). The buffer concentration was 50 mM, and ionic strength was poised with NaCl. Experiments found no impact on aging and reactivity for NaCl concentrations ranging between 5 to 100 mM NaCl. Aging studies were also conducted with unbuffered, higher pH (pH 10-12) suspensions adjusted to the desired value with 0.5 M NaOH. Suspensions were removed from the glovebox, briefly sonicated (~10 s) to disperse the NZVI, and allowed to oxidize in air for 3 d on an incubator shaker at 25 °C, assuming a dissolved oxygen concentration of 0.26 mM from atmospheric equilibration. Periodically, the suspension pH was measured and, if necessary, adjusted to its original value with either 5 N NaOH or 5 N HCl.

NZVI was also aged in the absence of oxygen. Suspensions (2 g/L) were prepared as described previously and transferred to 250 mL bottles. Bottles were screw-capped, wrapped in Parafilm and removed from the glovebox for brief (~ 10 s) sonication, after which the suspensions were returned to the chamber. Suspensions were aged up to 60 d, during which they were gently mixed by hand once a day.

Periodically, the pH was measured and adjusted as needed. Suspensions were allowed to oxidize in air for three days while agitated on an incubator shaker (New Brunswick Scientific), which mixed the flasks at 200 RPM. During this time, the suspension pH was measured periodically and, if necessary, adjusted to its original value with either 5 N NaOH or 5 N HCl. Typically, the pH of NZVI suspensions aged at pH 6

and 7 were relatively constant over the 3 days of air aging, while 1-2 drops (~ 10 μL) of 5 N NaOH were added to the pH 8 suspensions after approximately 5 h to return the pH to its original value. After this pH adjustment, the suspensions remained relatively stable at pH 8.0 for the remainder of the aging time.

While open to the atmosphere, evaporation caused the total suspension volume to decrease over time, in turn slightly concentrating the NZVI suspension. The exact volume of solution lost to evaporation was determined from the difference in suspension mass measured over time, thereby allowing the exact concentration of NZVI to be calculated at the conclusion of air oxidation.

For anaerobic systems aged up to 60 d, evaporation was not an issue as the aging vessels were sealed over this time period. Some pH drift was observed in a few systems. While suspensions at pH 8 system were relatively stable over this period, 1-2 drops (~10 μL) of 5 N HCl was added to pH 7 suspensions over the first few hours of aging to maintain pH around 7.0-7.2, after which the pH was essentially constant for the remainder of the aging.

Reaction of Dithionite with Aged NZVI Suspensions

Dithionite solutions for ISRM were prepared in alkaline 0.4 M carbonate buffer to slow disproportionation [19]. The majority of our experiments used sodium dithionite in a 50 mM sodium carbonate buffer adjusted to pH 11. Because high carbonate concentrations could promote siderite (FeCO_3) formation, solutions also were prepared in either 0.001 N (pH 11) sodium hydroxide or DI water. These alternative solutions yielded

identical results to solutions prepared in 50 mM sodium carbonate, suggesting siderite did not play an important role in our systems.

Because dithionite reacts quickly with dissolved oxygen, air-aged NZVI suspensions were first degassed via N₂-sparging and transferred into the anaerobic chamber prior to reaction. This limited the amount of dithionite necessary for reaction; in the presence of oxygen, greater concentrations could be used to scavenge O₂. Suspensions aged inside the anaerobic chamber were reacted directly with dithionite.

Reaction with dithionite was initiated by adding 2 mL of various dithionite stock solutions to 15 mL of aged NZVI suspension, producing concentrations ranging from 0.5-80 mM (or 0.02 – 3.6 g dithionite/g NZVI) in the reactor. The reaction proceeded for 24 h with mixing, during which the reaction rate was determined from the change in dithionite concentration over time. The rate of reaction between dithionite and aged NZVI was determined by measuring the change in dithionite concentration and the production of dissolved Fe(II) over time. Suspensions samples were removed periodically from the reactor using a 1 mL disposable syringe, passed through a 0.2 μm PTFE filter and analyzed as described below. Control experiments were also conducted with dithionite in solutions free of oxidized NZVI, as well as in systems with as received NZVI particles. In all instances, solution pH was monitored with time after the addition of the dithionite solution to the aged suspension, with minimal change being observed in all instances. Thus, for suspensions aged at pH 6, 7 and 8, the reaction with dithionite could be assumed to occur at the same pH at which the suspension was aged.

To avoid the contribution of residual dithionite in subsequent reactivity studies, suspensions were centrifuged (8000 RPM for 5 minutes) at the conclusion of reaction, and the supernatant was decanted. The reduced solids were then washed two times with deoxygenated, deionized water, and finally re-suspended in the appropriate buffer for reactivity studies.

Reactivity Studies with Model Pollutants

The reactivity of as received NZVI, aged NZVI, and aged NZVI after reaction with dithionite was determined via experiments with Cr(VI), nitrobenzene, and 1,1,1,2-TeCA. As the rate of Cr(VI) reduction was too fast to furnish a rate coefficient, we report Cr(VI) removal capacities determined from experiments in which 0.5 mM Cr(VI) was added repeatedly to the reactor until removal was no longer observed. Nitrobenzene and 1,1,1,2-TeCA exhibited exponential decay during reaction, thus reactivity toward these compounds is described with k_{obs} values.

Reactors were constructed inside the anaerobic chamber by adding the appropriate mass of as received NZVI particles, or an appropriate volume of either aged NZVI or water-washed, dithionite-reacted NZVI suspensions to a 20 mL reactor. All dithionite-treated materials were resuspended in fresh, deoxygenated buffer of the same pH used for aging. A reductant loading equivalent to 2 g/L of NZVI was used in all experiments with 1,1,1,2-TeCA and nitrobenzene, while a reductant loading equivalent to 2.8 g/L of NZVI was used in reactions with Cr(VI).

More details about sample collection are referred to chapter 2, for nitrobenzene, 70 μL from a 30 mM solution of nitrobenzene in methanol was injected into prepared reactors (resulting in an initial concentration of 100 μM).

Materials Characterization

The composition of NZVI, aged NZVI, and aged NZVI after reaction with dithionite was investigated with X-ray diffraction (XRD). Changes in particle morphology were examined with scanning electron microscopy (SEM) and transmission electron microscopy (TEM). The iron phases present in all samples were also explored via ^{57}Fe Mössbauer spectroscopy. Surface chemical composition for dithionite-treated samples was obtained via X-ray photoelectron spectroscopy (XPS).

The morphology of materials was examined using scanning electron microscopy (SEM; FEI/Philips XL30-FEG) operated at acceleration voltage of 10 kV. For SEM, samples were prepared by placing a drop of suspension on a SEM pin stub. The methanol was allowed to evaporate, and the sample was then sputtered with a thin Pt/Pd film prior to analysis. The sample preparation protocol and XRD, TEM system employed for this study are identical to those described in chapter 2.

Mössbauer spectroscopy was performed in the laboratory of Dr. Michelle Scherer at the University of Iowa. Aqueous suspensions of fresh NZVI, as well as NZVI suspensions aged in air for 3 d at pH 6 and 8, were shipped overnight to the University of Iowa in air tight containers under a nitrogen atmosphere, and were analyzed upon arrival. The samples were opened within an anaerobic chamber (95% N_2 , 5% H_2) and particles

were collected on 13 mm filter discs and mounted as a wet paste between two layers of Kapton tape for analysis. Mössbauer spectra were collected at 13 and 77 K using methods described in Larese-Casanova and Scherer [20]. All spectra are reported in reference to α -Fe foil calibration spectrum taken at room temperature. To obtain estimates as to the relative concentration of the phases present in each sample, spectra were fit using Recoil software package (University of Ottawa, Ottawa, Canada) with a Lorentzian model. Parameters were set initially to reference values for solid phases anticipated in each sample based on XRD analysis, and then allowed to vary using a least-squares optimization.

All XPS analyses were conducted in the laboratory of Dr. Howard Fairbrother at Johns Hopkins University. Aqueous slurries of samples were shipped overnight to Johns Hopkins University in air tight containers with a nitrogen atmosphere. All samples were analyzed immediately upon arrival so as to minimize the possibility of changes introduced during transport, storage and handling. Samples were opened in air, mounted onto stainless steel sample stubs using double-sided adhesive copper conducting tape (3M[®] Code 1182), and then transferred to a fast load lock introduction chamber prior to entry into the XPS analysis chamber. XPS analysis was conducted using a PHI 5400 system ($P_{\text{base}} < 3 \times 10^{-9}$ Torr). Spectra were acquired using Mg K_{α} X-rays (1253.6 eV) from a PHI 04-500 Dual Anode X-ray Source operated at 15 kV and 300 W. All XP spectra were acquired at 15 kV and 300 W. Full surveys (1100-0 eV) were carried out with a pass energy of 178.95 eV and a step size of 1 eV. Elemental scans were acquired with a pass energy of 44.75 eV and a step size of 0.125 eV. Ejected photoelectrons were analyzed

with a PHI 10-360 Precision Energy Analyzer operated at a pass-energy of 178.95 eV and a 45° takeoff angle. Atomic concentrations were determined by photoelectron peak integration. The position of adventitious carbon (284.8 eV in the C(1s) region) was used to calibrate the XPS binding energy scale for all substrates [21].

Analytical Methods

Dithionite concentrations were quantified using direct UV/visible absorbance ($\epsilon=6900 \text{ mol}^{-1}\text{cm}^{-1}$ at $\lambda= 315 \text{ nm}$ [15]). Dissolved Fe(II) and Cr(VI) concentrations were quantified colorimetrically using 1,10-phenanthroline and diphenylcarbazide, respectively. The concentration of 1,1,1,2-TeCA and its sole reduction product 1,1-dichloroethylene were determined via gas chromatography with electron capture detection (GC/ECD). Nitrobenzene was quantified using HPLC with diode array detection.

Dithionite concentrations were quantified using direct UV/visible absorbance ($\epsilon=6900 \text{ mol}^{-1}\text{cm}^{-1}$ at $\lambda= 315\text{nm}$ [15]). Samples were prepared within an anaerobic chamber, and cuvettes were capped with parafilm and analyzed via UV/vis. Experiments revealed that the rate of dithionite oxidation in these capped cuvettes was slow compared to the timescales necessary for UV/vis analysis (< 1 min). Dithionite standards from sodium dithionite were prepared in carbonate buffer (pH=11) and analyzed in a manner identical to the experimental samples.

Analysis of nitrobenzene and its reduction products were performed via HPLC with diode array detection (Agilent 1200 series) using a Zorbax C-18 column. Details

regarding the system and conditions used for nitrobenzene analysis can be found elsewhere [22]. Other measurements for dissolved Fe(II) concentration and aqueous Cr(VI) concentration were according to the procedure outlined in chapter 2. The concentration of 1,1,1,2-TeCA and its sole reduction product 1,1-dichloroethylene (1,1-DCE) were determined via gas chromatography with electron capture detection (GC/ECD). The analytical methods and GC/ECD used for this study are identical to those presented in chapter 2.

3.4. Results and Discussion

Characterization and Reactivity Loss of NZVI Suspensions Aged in Air

At pH 6 and 7, air oxidation caused the color of suspensions to change from black to brown over 3 days (Figure 3-2a). Results from XRD (Figure 3-3a), Mössbauer spectroscopy (Figure 3-4a), and TEM (Figure 3-4b) support the near complete conversion of NZVI into the ferric oxide lepidocrocite, with traces of magnetite also detected. In contrast, suspensions aged in air at $\text{pH} \geq 8$ maintained their initial appearance (Figure 3-5a), and characterization indicated a considerable fraction of Fe(0) remaining in the particles after 3 d of air exposure. The primary phase identifiable with XRD was α -Fe (Figure 3-5a), and estimates from Mössbauer spectroscopy suggest the aged materials consisted of ~30% Fe(0) (Figure 3-4a). Both XRD and Mössbauer spectroscopy also revealed the presence of magnetite. Furthermore, although no additional phases were detectable via XRD, Mössbauer spectra were consistent with the formation of a poorly

ordered Fe(III) phase resembling lepidocrocite. Despite these compositional changes, the morphology of the aged materials (Figure 3-4c) was comparable to that of fresh NZVI (Figure 3-1b).

Batch studies with 1,1,1,2-TeCA conducted as a function of exposure time to air showed rapid reactivity loss for all suspensions in a matter of hours (Figure 3-6). Reactivity loss toward Cr(VI) and nitrobenzene occurred over a similar timescale. While reactivity loss was expected for low pH suspensions consisting primarily of passive ferric oxides, it was unexpected for NZVI aged at $\text{pH} \geq 8$; despite the persistence of Fe(0) in these suspensions for 3 d, reduction of 1,1,1,2-TeCA ceased after 3 h. At or above pH 8, therefore, exposure to air must have produced a passive surface coating that slowed or altogether inhibited further oxidation of the Fe(0) particle core. Notably, the formation of such a passivating oxide layer that protects the underlying metal from further oxidation is commonly observed during the corrosion of iron and steel in basic aqueous media [23].

Our observation of atmospherically stable NZVI particles in suspension at $\text{pH} \geq 8$ is similar to the recent report by Kim *et al.* [24], who produced atmospherically stable NZVI via the controlled exposure of dried nanoparticles to air. Here, we show that an alternate route to atmospherically stable NZVI is air oxidation in basic media. This behavior has negative implications for NZVI performance, however, because high pH, partially oxidizing environments will likely cause a significant fraction of reducing equivalents in NZVI to go unutilized, trapped as Fe(0) in the particle core by an unreactive oxide shell.

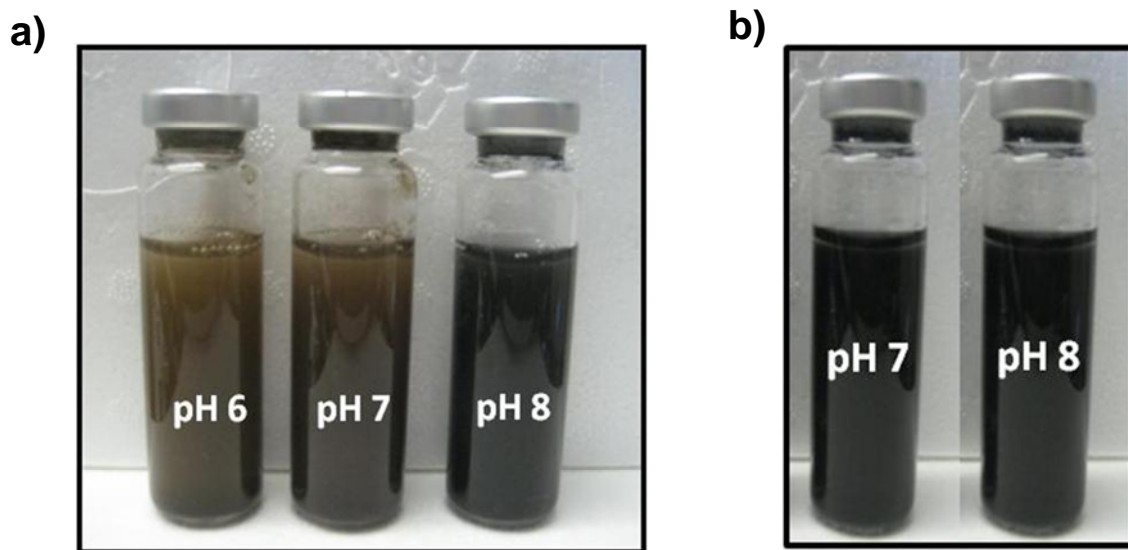


Figure 3-2. Appearance of NZVI suspensions (a) aged for 3 days in air at pH 6, 7 and 8 or (b) aged for 60 days at pH 7 and 8 within an anaerobic chamber (95% N₂ and 5% H₂).

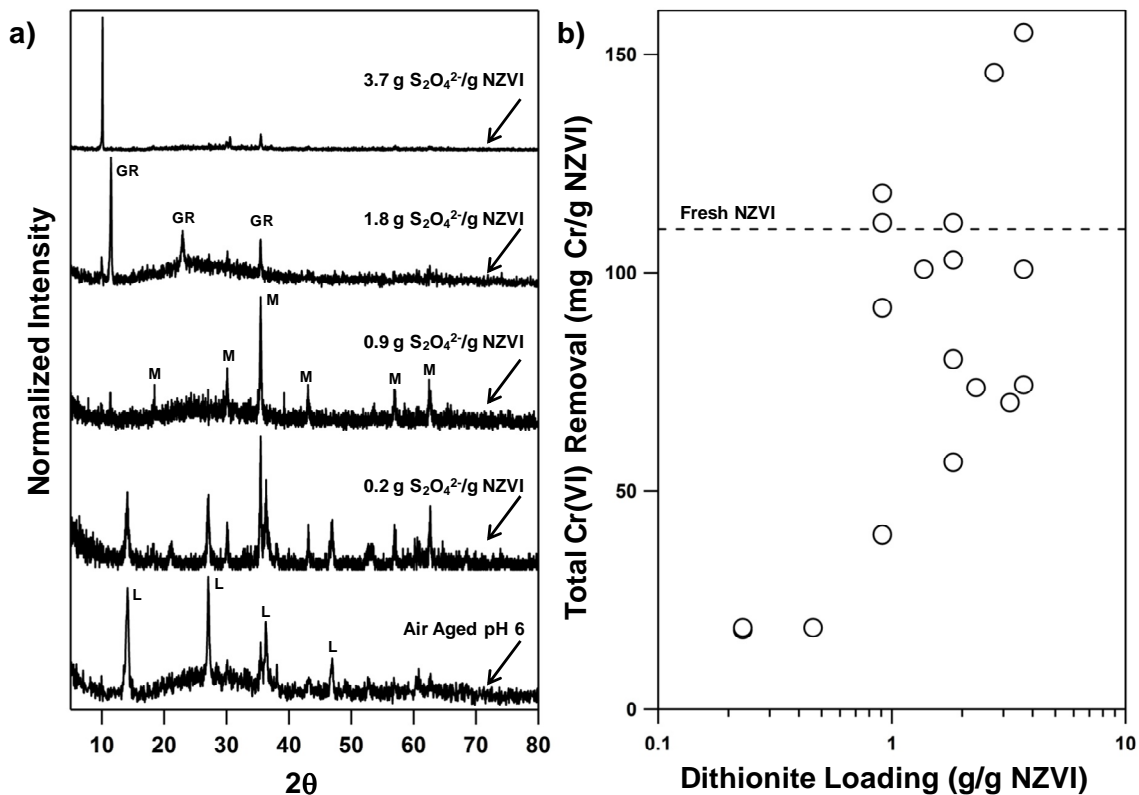


Figure 3-3. (a) X-ray diffraction patterns for NZVI suspensions aged in air for 3 days at pH 6 before and after reaction with various dithionite solutions. Values of dithionite are reported per unit mass of NZVI initially present in suspension. Identifiable mineral phases are indicated, where L represents lepidocrocite based on reference powder diffraction file ICDD 9-88 [25] and M and GR represent magnetite and green rust, respectively, based upon previously reported d-spacings for these species [26]. (b) Total Cr(VI) removal exhibited by products of the reaction between dithionite and NZVI suspensions aged in air for 3 d at pH 6. The total amount of Cr(VI) removed at pH 6 is reported per unit mass equivalents of NZVI present in the system (2.8 g/L). Also indicated (dashed horizontal line) is the removal of Cr(VI) exhibited by fresh NZVI at the same mass loading and pH. Passivated NZVI showed no measurable removal of Cr(VI).

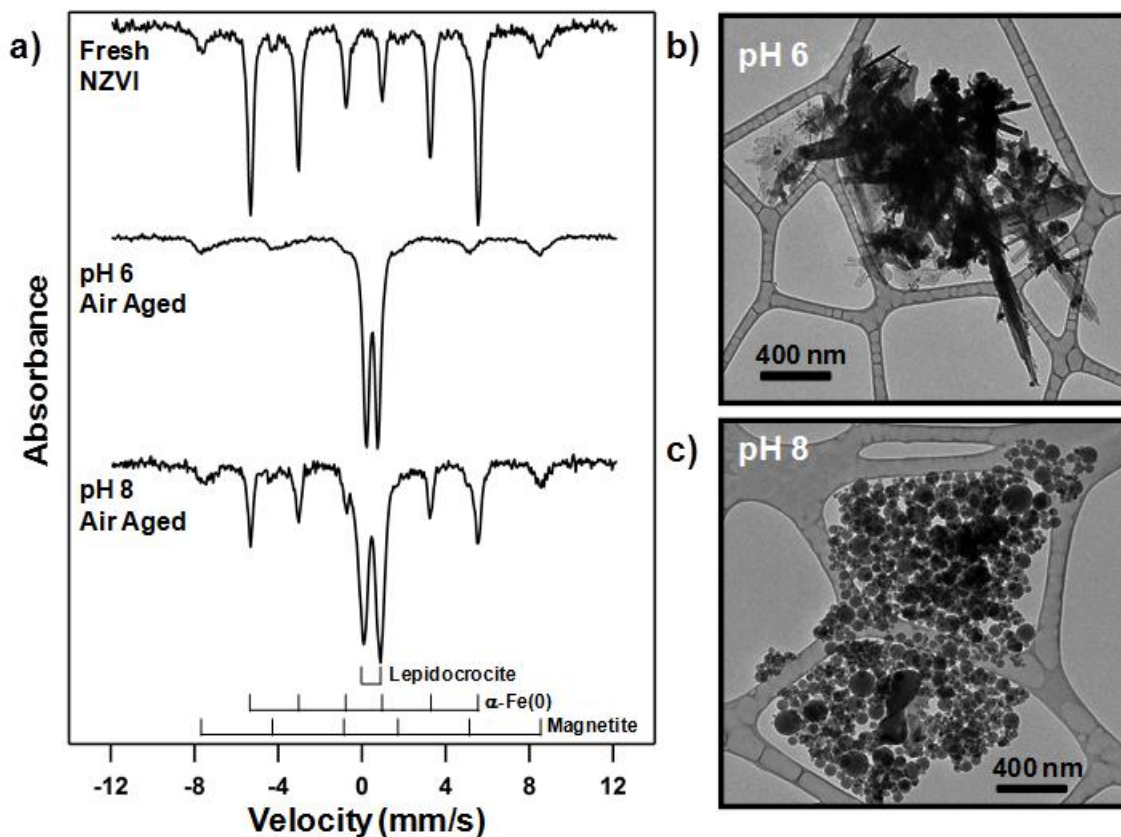


Figure 3-4. (a) ^{57}Fe Mössbauer spectra for fresh (as received) NZVI, and NZVI aged in a suspension exposed to air for 3 d at pH 6 and 8. Corresponding TEM images of the products of NZVI aging at (b) pH 6 and (c) pH 8 are also shown. Mössbauer spectra were collected at 77 K, and spectral features associated with specific iron phases that were detected are noted. Identification of different iron species was based upon results of Lorentzian model fits used to describe raw data, in complement with results from XRD. At pH 6, TEM images revealed that the originally spherical NZVI particles transformed into a mixture of nanoscale phases, one of which exhibited the lath-like morphology characteristic of lepidocrocite [26]. At pH 8, the morphology of the aged NZVI largely resembled that of the as received material (see Figure 3-1)

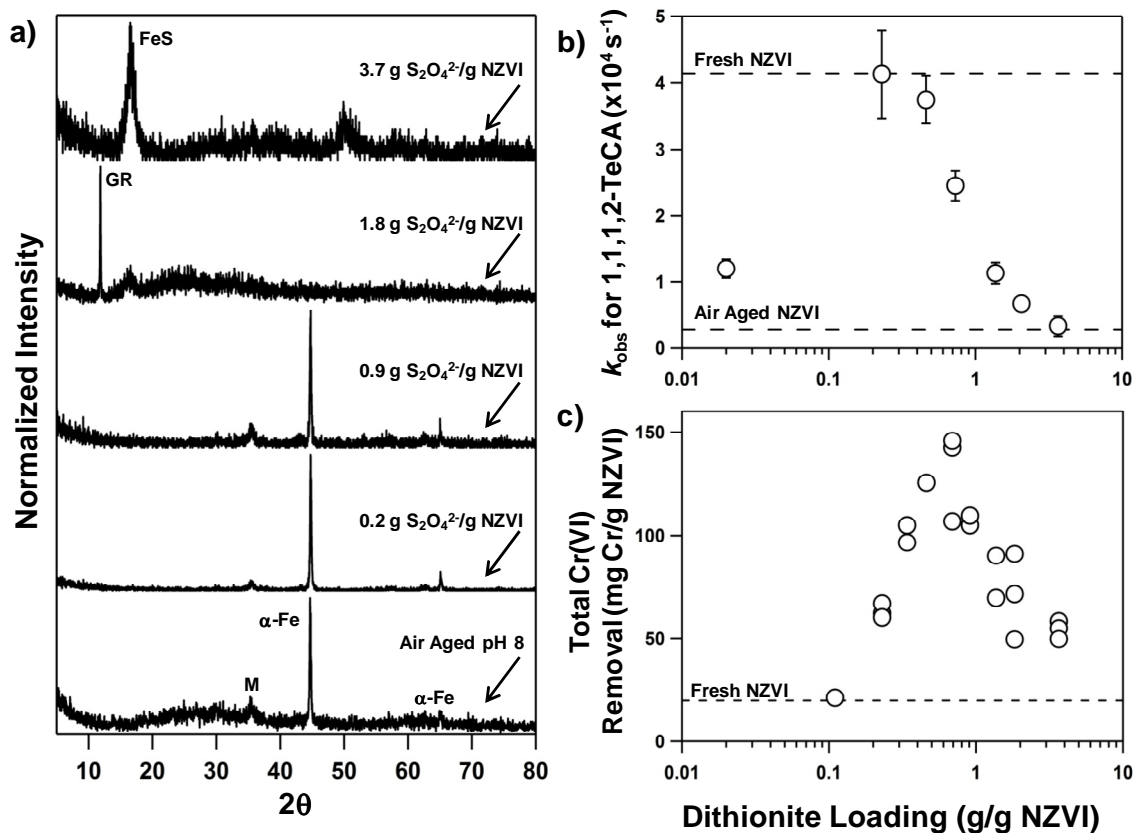


Figure 3-5. (a) X-ray diffraction patterns for NZVI suspensions aged in air for 3 days at pH 8 before and after reaction with various dithionite solutions. Values of dithionite are reported per unit mass of NZVI initially in suspension. Diffraction lines attributable to α -Fe are noted. Identifiable mineral phases are also indicated, where M, GR and FeS are the diffraction lines we attribute to magnetite, green rust and iron sulfide, respectively. Measured reactivity of the products of the reaction between dithionite and NZVI suspensions aged in air for 3 d at pH 8 shown (b) as values of k_{obs} for 1,1,1,2-TeCA reduction and (c) as values of total Cr(VI) removal. Both reactivity metrics are shown as a function of dithionite concentration, and the total amount of Cr(VI) reduced is reported per unit mass equivalents of NZVI in the systems (2.0 g/L and 2.8 g/L for 1,1,1,2-TeCA and Cr(VI) reduction, respectively). Also indicated, where appropriate, is the reactivity exhibited toward these species by fresh and air-aged NZVI. All reactivity studies were conducted at pH 8 in 50 mM Tris.

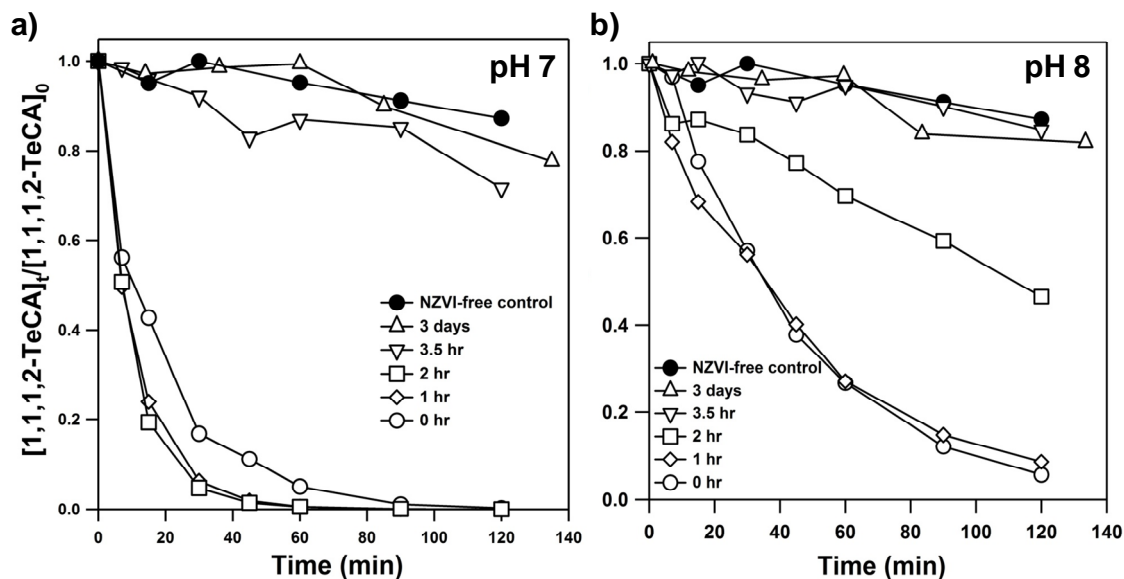


Figure 3-6. Concentration profiles for 1,1,1,2-TeCA in NZVI suspensions (2 g/L) aged in air (a) at pH 7 and (b) at pH 8. Kinetic data are shown as a function of suspension exposure time to air. Also provided are 1,1,1,2-TeCA concentration data obtained in NZVI-free controls, in which a small amount of loss was observed as a result of sorption to septa used to seal the reactors. When concentration profiles in NZVI-containing systems were equivalent to those measured in the NZVI-free controls, it was assumed that NZVI reactivity toward 1,1,1,2-TeCA was lost due to passivation promoted via reaction with dissolved oxygen. NZVI suspensions showed comparable longevity at pH 7 and 8 when aged in the presence of air, with complete reactivity loss after 3.5 h in each system.

Solution pH is the critical variable governing the formation of this passive coating. We propose that the different aging products observed as a function of pH reflect the fate of Fe(II) produced via Fe(0) corrosion. At pH 8 and above, the rapid oxygenation of Fe(II) before it can diffuse away from the particle surface produces the protective surface film. In contrast, slower rates Fe(II) oxygenation at lower pH allow for its release into bulk solution and the subsequent homogeneous oxidation to yield new Fe(III) phases.

Characterization and Reactivity Loss of NZVI Suspensions Aged in the Absence of Oxygen.

NZVI suspensions aged under the N₂/H₂ atmosphere of an anaerobic chamber lost reactivity much more slowly than air-aged materials. At all pH values investigated, no visible color changes were discerned, with suspensions maintaining their initial black appearance through 60 d of aging (Figure 3-2b).

To avoid contributions in reactivity from aqueous Fe(II) generated during aging, only the reactivity toward 1,1,1,2-TeCA was examined for suspensions aged within an anaerobic chamber. In pH 7 suspensions, reactivity toward 1,1,1,2-TeCA decreased steadily over time until little reducing capacity remained after 60 d (Figure 3-7). After 30 d at pH 7, XRD analysis lacked a clear diffraction line for α -Fe (Figure 3-8a), suggesting that water reduction consumed the majority, if not all, of the Fe(0) initially present in the system. Beyond 30 d, only a relatively weak diffraction pattern indicative of magnetite could be discerned, with TEM images (Figure 3-8b) of 60 d aged materials bearing little resemblance to fresh NZVI.

At pH 8, reactivity loss was more immediate initially, with nearly a 6-fold loss in activity over 0.5 d (Figure 3-7). Reactivity loss ultimately slowed, however, and measurable reduction of 1,1,1,2-TeCA was still observed after 60 d. Unlike pH 7, XRD analysis of NZVI aged for 30 and 60 d at pH 8 indicate the persistence of Fe(0) (Figure 3-8a). TEM images also clearly indicate the formation of a new surface phase on the nanoparticles (Figure 3-8b). Although not identifiable via XRD, this surface phase is probably redox active (e.g., Fe(II)-containing) due to the reactivity toward 1,1,1,2-TeCA measured in these samples.

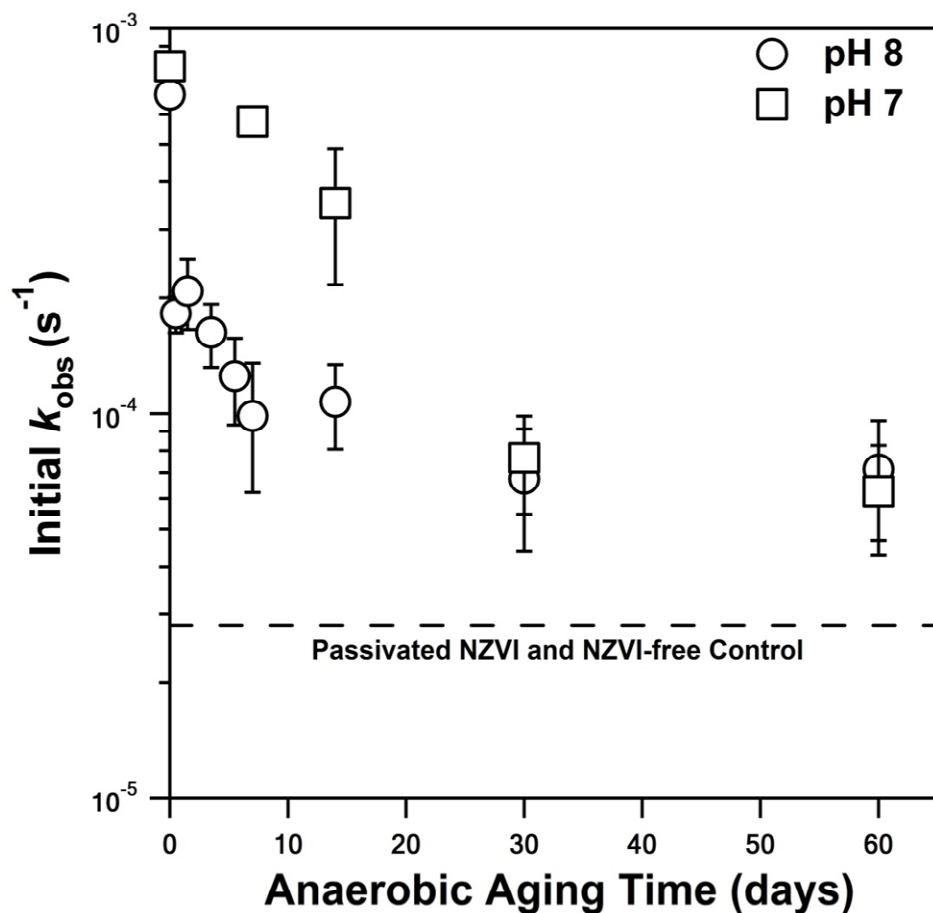


Figure 3-7. Change in initial k_{obs} values for the reduction of 1,1,1,2-TeCA with respect to the aging time of NZVI suspensions within an anaerobic chamber. NZVI suspensions (2 g/L) were aged at pH 7 (50 mM HEPES) and pH 8 (50 mM Tris) for up to 60 days. Uncertainties represent 95% confidence limits on at least triplicate experiments. Also indicated as a dotted line is the k_{obs} value obtained in both passivated and NZVI free control studies; loss of 1,1,1,2-TeCA in control systems is attributable to a sorption of 1,1,1,2-TeCA to septa used to seal the reactors, which resulted in approximately 10-15% loss of 1,1,1,2-TeCA over a typical experiment (~2 h).

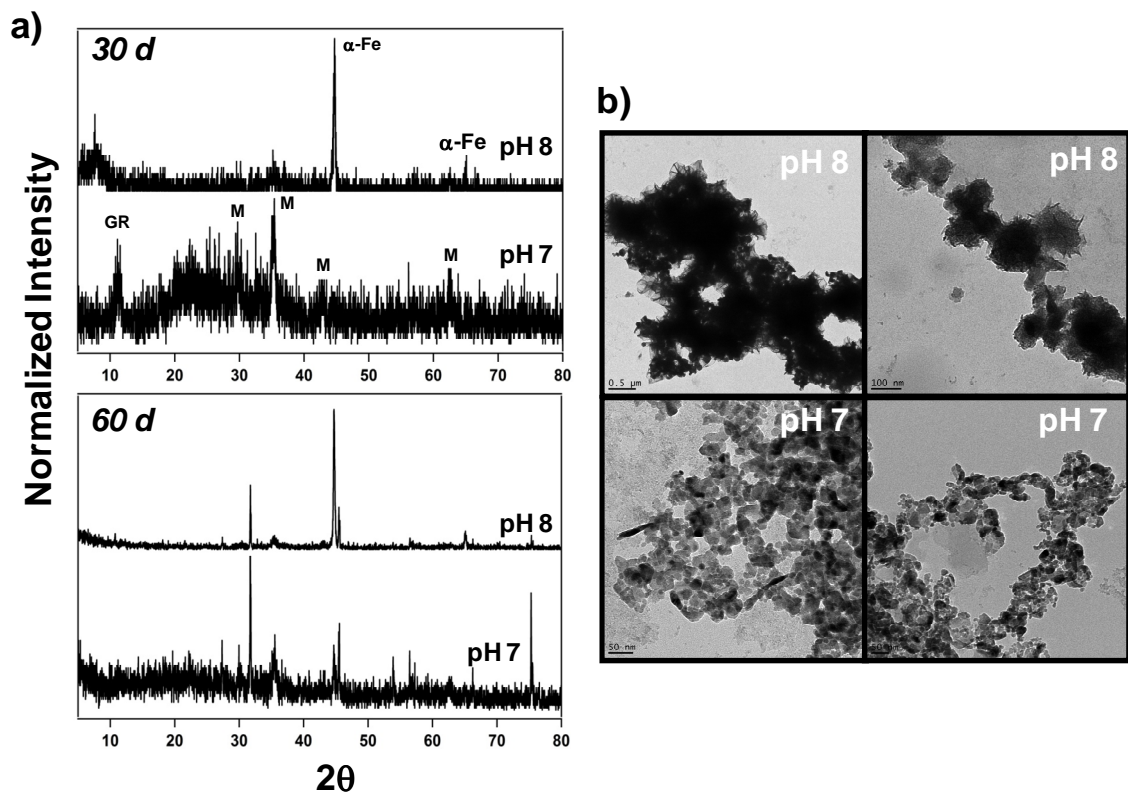


Figure 3-8. (a) X-ray diffraction patterns for NZVI suspensions (2 g/L) aged inside an anaerobic chamber (95% N₂, 5% H₂) for 30 and 60 days at pH 7 (50 mM HEPES) and pH 8 (50 mM Tris). (b) Corresponding TEM images of NZVI aged for 60 days in aqueous suspensions at pH 7 and pH 8. In XRD patterns, the only detectable iron-containing phases were α-Fe, magnetite, and green rust, as indicated. Notably, the α-Fe signal was considerably greater in the pH 8 suspensions both at 30 and 60 d of aging. For the 60 d samples, diffraction lines observed near 2θ values of 32°, 44° and 76° are indicative of NaCl, which was present in our systems to poise ionic strength and was not sufficiently removed from these particular samples via washing with DI water prior to analysis. For TEM images at pH 8, a new yet unidentified phase was observed on the surface of the aged NZVI particles. At pH 7, on the other hand, particles showed little resemblance to as received NZVI particles, and appear considerably smaller than the unaged material (Figure 3-1b).

Characterization and Reactivity of NZVI Aged in Air at pH 6 and 7 after Reaction with Dithionite.

Dithionite reacted quickly with pH 6 and 7 air-aged suspensions, with decreases in dithionite concentration over time accompanied by Fe(II) production (Figure 3-9a). The reaction also produced Fe(II)-containing mineral phases (Figure 3-3a), as expected from established trends in dithionite reactivity with ferric iron oxides [13]. The identity of these Fe(II) phases depended strongly on the concentration of dithionite. X-ray diffraction patterns were consistent with low concentrations of dithionite (< 1 g/g NZVI) transforming lepidocrocite, the primary NZVI oxidation product, into magnetite. Higher concentrations (2.5 g/g NZVI) yielded diffraction patterns consistent with hydroxycarbonate green rust formation, presumably from the carbonate present in the dithionite solution. The highest dithionite loading investigated (3.7 g/g NZVI) yielded a similar, but not identical, diffraction pattern to that of hydroxycarbonate green rust, perhaps indicating differences in anion substitution. For example, sulfate green rust may be generated from products of dithionite oxidation. In support of this scenario, XPS analysis (Figure 3-10) indicated the presence of oxidized forms of sulfur (e.g., sulfate or sulfite) on the surface of these dithionite-treated solids.

Products of the reaction with dithionite at pH 6 and 7 were unreactive toward 1,1,1,2-TeCA over the timescales for reduction by fresh NZVI, consistent with most Fe(II)-containing solids representing weaker reductants for chlorinated solvents than Fe(0). In contrast, these phases exhibited considerable reactivity toward nitrobenzene [27] and Cr(VI) [28], species known to be reducible by Fe(II). Nitrobenzene (Figure 3-11) and

Cr(VI) (Figure 3-3b) were quickly degraded with dithionite-treated suspensions, and the extent of pollutant removal increased with increasing dithionite loading. Notably, Cr(VI) removal capacity (in mg of Cr(VI)/g of NZVI initially present in suspension) at higher dithionite concentrations approached and in some cases exceeded the removal capacity measured for fresh NZVI. Magnetite [29] and green rust [30] have both been shown to reduce Cr(VI) in laboratory studies, and we reiterate that any residual dithionite was removed via washing of the reduced materials prior to reaction with Cr(VI). Thus, even though Fe(0) is no longer present in these systems, reducing equivalents provided by dithionite generate Fe(II)-phases of sufficiently high reactivity so as to exhibit efficiencies comparable to fresh NZVI.

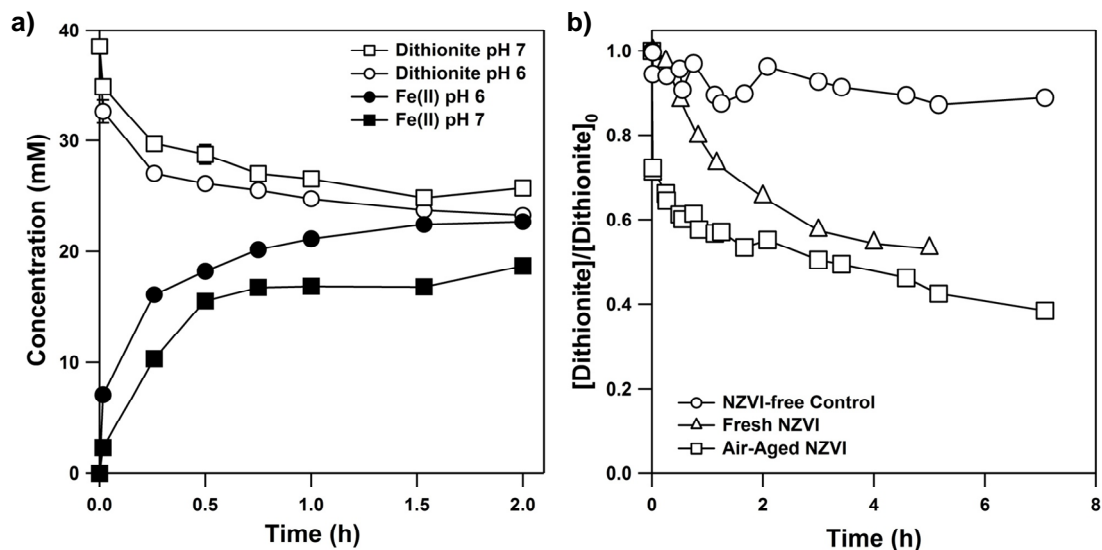


Figure 3-9. Change in dithionite concentration over time during reaction with air-aged NZVI (a) at pH 6 and 7 and (b) at pH 8. At all pH values, there was a nearly instantaneous drop in dithionite concentration upon its addition to the aged NZVI suspension. As shown in panel (a), this dithionite decay was accompanied by the concurrent production of dissolved Fe(II). Because dithionite concentration was relatively stable over 24 h in NZVI-free controls (see panel b), the initial drop in concentration is attributed to a rapid reaction with the Fe(III) produced via air-oxidation of the NZVI suspension. In (b), the more gradual rate of dithionite decay over longer timescales is likely indicative of dithionite reaction with the underlying Fe(0) trapped in the core of the particles air-aged at pH 8 to yield iron sulfides. This scenario is supported by experiments with fresh NZVI in which dithionite was consumed at a rate similar to that observed over longer timescales in the aged NZVI systems.

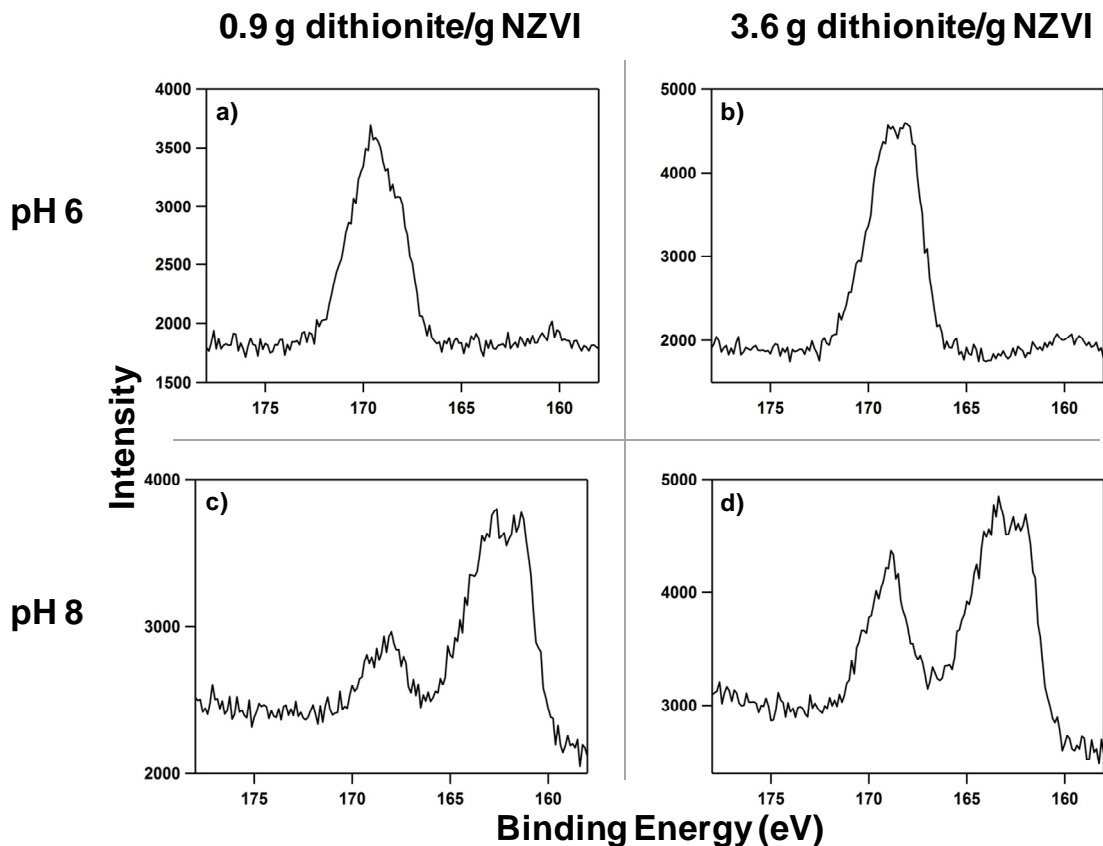


Figure 3-10. X-ray photoelectron spectra of air-aged NZVI suspensions (2 g/L) after reaction with dithionite. Shown are spectra for NZVI suspensions aged in air at pH 6 (a, b) and pH 8 (c,d) after reaction with 0.9 and 3.6 g dithionite/g NZVI. As detailed in the manuscript, air-aging of NZVI suspensions at pH 6 yielded mostly lepidocrocite, which upon reaction with dithionite yields Fe(II)-containing phases and higher valence sulfur species (e.g., sulfite and sulfate) arising from dithionite oxidation. In support of this scenario, only higher binding energies (166-173 eV) in the range previously reported for sulfite and sulfate in iron systems [31, 32] were observed in spectra of these materials (a and b). In contrast, a significant fraction of Fe(0) was preserved in NZVI suspensions aged in air at pH 8. As a result, reduction of dithionite by Fe(0) produced reduced forms of sulfur, as indicated by the broad peak at lower binding energy (160-165 eV), which was only observed for aging and reaction at pH 8. These lower binding energies are consistent with those reported for species such as monosulfide and disulfide in iron systems [33]. We also cannot rule out the possibility of elemental sulfur on the surface of dithionite-treated materials. The relative amounts of these reduced sulfur forms were not quantified.

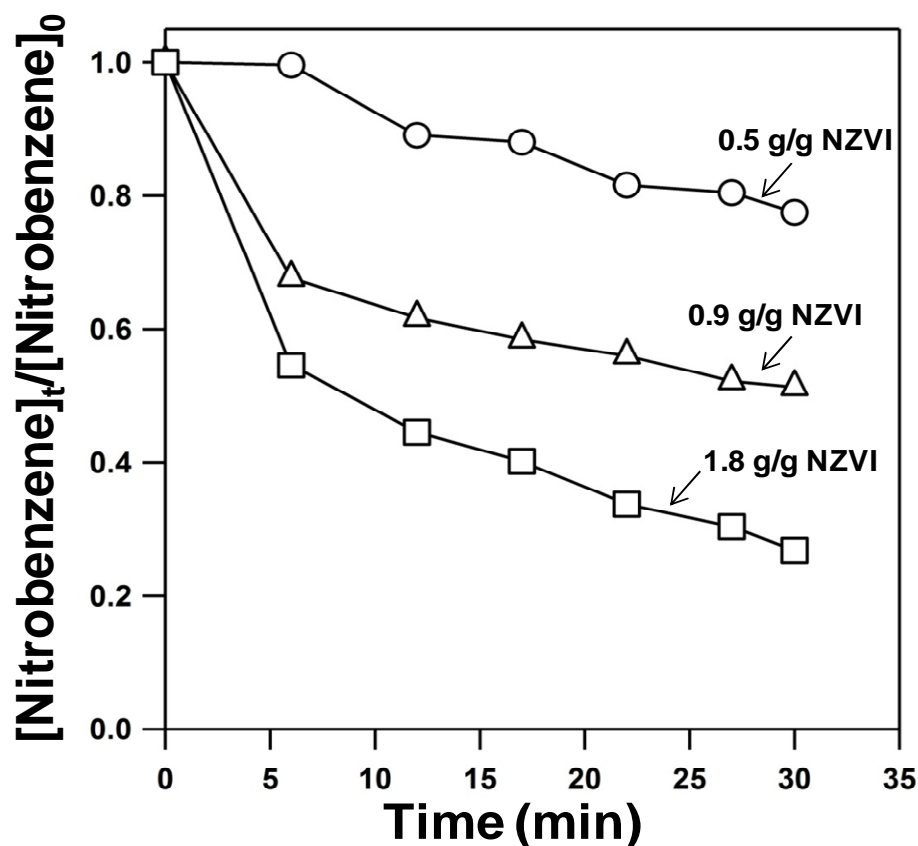


Figure 3-11. Change in nitrobenzene concentration over time in suspensions of air-aged NZVI particles after reaction with the concentrations of dithionite noted. For the purpose of comparison, concentration data are normalized to the initial reactor concentration in each case. Suspensions (2 g/L) were aged for 3 d in air at pH 6 (50 mM MES). Experiments with nitrobenzene were also conducted at pH 6 with an initial nitrobenzene concentration of 100 μM . Although not shown, aniline was detected as the primary reduction product, and mass balances were typically greater than 90%. Air-aging of NZVI at pH 6 primarily yielded the ferric oxide lepidocrocite, and aged suspensions showed no reactivity toward nitrobenzene. Reduction of the aged suspension with dithionite produced Fe(II)-containing phases such as magnetite and green rust. As shown, the rate and extent of nitrobenzene reduction increased with respect to the amount of dithionite reacted with the air-aged NZVI, suggesting Fe(II) species generated from the reduction of lepidocrocite by dithionite are responsible for nitrobenzene reduction. Notably, all residual dithionite was removed via centrifugation and washing of the solid phase prior to the addition of nitrobenzene to the reactor. Although not shown in the figure, the reactivity of the dithionite-treated materials was considerably less than fresh NZVI, which resulted in the near complete decay of nitrobenzene in a few minutes.

Characterization and Reactivity of NZVI Aged in Air at pH 8 after Reaction with Dithionite.

Suspensions of NZVI aged in air at pH 8 also reacted nearly instantaneously with dithionite (Figure 3-9b). Again, the dithionite loading was critical in determining the identity and reactivity of the reaction products. Diffraction patterns indicated that α -Fe remained the dominant identifiable phase after reaction with low concentrations of dithionite (< 1 g/g NZVI) (Figure 2a). At higher concentrations, however, evidence suggests that excess dithionite oxidizes the residual Fe(0) in the aged particles to produce new phases. Intermediate dithionite loadings (1.8 g/g NZVI) generated a product with a large d-spacing (7.44 Å) indicative of green rust [26]. The highest concentration investigated (3.7 g/g NZVI) yielded a poorly crystalline phase with a dominant diffraction line at a d-spacing of 5.4 Å (Figure 2a), which is approximate to the highest intensity d-spacing previously reported for a synthetic nanocrystalline iron sulfide [34] and for substituted iron sulfides such as tochilinite [25]. XPS confirmed the presence of reduced sulfur in these samples, with low binding energy peaks in the S(2p) region consistent with the presence of poly-, di- or monosulfide, and potentially elemental sulfur (see Figure 3-10).

Not surprisingly, the dithionite concentration also had considerable implications for the reactivity of the treated suspensions. For 1,1,1,2-TeCA, 0.2-0.4 g dithionite/g NZVI produced k_{obs} values that were statistically equivalent to that of fresh NZVI (Figure 3-5b). Below these concentrations, degradation of 1,1,1,2-TeCA was enhanced relative to passivated NZVI, but it remained less reactive than fresh NZVI. Above this optimal

dithionite dose k_{obs} values decreased with increasing dithionite concentration. Ultimately, at the highest concentration of dithionite investigated (3.7 g/g NZVI), no removal of 1,1,1,2-TeCA was observed relative to minor losses measured in reductant-free controls arising from sorption to the septa.

Slightly different behavior was observed for Cr(VI) reduction at pH 8 (Figure 3-5c). The lowest dithionite concentration considered (0.11 g/g NZVI) produced materials with a removal capacity identical to fresh NZVI. A steady increase in Cr(VI) removal was observed with increasing dithionite concentration, culminating in a maximum removal capacity of nearly 150 mg Cr(VI)/g NZVI at a dithionite load of 0.7 g/g NZVI. Above this concentration, Cr(VI) removal in the regenerated systems decreased with increasing dithionite, but all removal capacities remained greater than that for fresh NZVI.

Reactivity trends toward 1,1,1,2-TeCA and Cr(VI) at pH 8 correlate to the products of the reaction between dithionite and air-oxidized NZVI suspensions. For 1,1,1,2-TeCA reduction, we interpret the optimal dithionite load around 0.2-0.4 g/g NZVI as the amount necessary to thin the passive layer generated by air oxidation, thereby exposing Fe(0) at or close to the particle surface so as to facilitate reduction. At higher dithionite concentrations, the oxidation of available Fe(0) by dithionite to yield sulfides is likely responsible for the decreased activity. Hansson *et al.* [35] found that the formation of iron sulfide films on Fe(0) surfaces inhibits charge transfer, resulting in lower rates of chlorinated solvent reduction. Moreover, while iron sulfides are capable of reducing halogenated solvents [36], they will do so at a much slower rate than Fe(0).

For Cr(VI) reduction, all dithionite concentrations yielded greater removal

capacities than fresh NZVI. Removal capacities even exceeded previous reports for other forms of NZVI, such as borohydride generated nanoparticles [37]. In Figure 3-5 the maximum Cr(VI) removal capacity occurs at a dithionite loading of 0.7 g/g Fe, which is nearly two times greater than the dose producing the maximum k_{obs} value for 1,1,1,2-TeCA reduction. Notably, Fe(0) is the dominant phase identified via XRD for conditions yielding maximum reactivity toward both species. We hypothesize that while sulfide formation on Fe(0) surfaces inhibits chlorinated solvent reduction, it promotes Cr(VI) removal by enhancing Fe(0) corrosion. Hansson *et al.* [35] observed that the corrosion rate of high purity iron increased with increasing exposure to NaS₂. As aqueous forms of Fe(II) [28] and the observed Fe(II)-containing solid phases [38, 39] represent suitable reductants for Cr(VI), this enhanced rate of corrosion would ultimately promote Cr(VI) removal relative to systems with slower Fe(II) production rates.

Reactivity of NZVI Aged in the Absence of Oxygen after Reaction with Dithionite.

For NZVI suspensions aged at pH 7 for 7, 14, and 30 d within an anaerobic chamber, products of the reaction with dithionite (≥ 0.02 g/g NZVI) were less reactive toward 1,1,1,2-TeCA than the aged material (Figure 3-12). The inhibitory role of dithionite in 1,1,1,2-TeCA reduction can be inferred from trends established for air-oxidized NZVI; oxidation of Fe(0) by dithionite consumes reducing equivalents while the formation of surface iron sulfides accelerates passivation.

In contrast, the reactivity toward 1,1,1,2-TeCA of NZVI suspensions aged in the

absence of oxygen at pH 8 could be restored via reaction with dilute solutions of dithionite (Figure 3-13). Reaction of NZVI aged 30 d at pH 8 with 0.02 g dithionite/g NZVI resulted in a rate of 1,1,1,2-TeCA reduction equal to that measured for fresh NZVI. Notably, higher dithionite concentrations resulted in reactivity loss, as observed at pH 7. Because appreciable Fe(0) was identified via XRD for the aged particles, low dithionite concentrations must promote reactivity by destabilizing the oxide layer on the particle surface, in turn increasing the amount of Fe(0) at or near the solution interface. We propose this behavior only occurs at higher pH values where the surface oxide layer is sufficiently thick due to Fe(II) solubility limitations; consumption of dithionite via reaction with the oxide layer prevents extensive passivation of the underlying Fe(0).

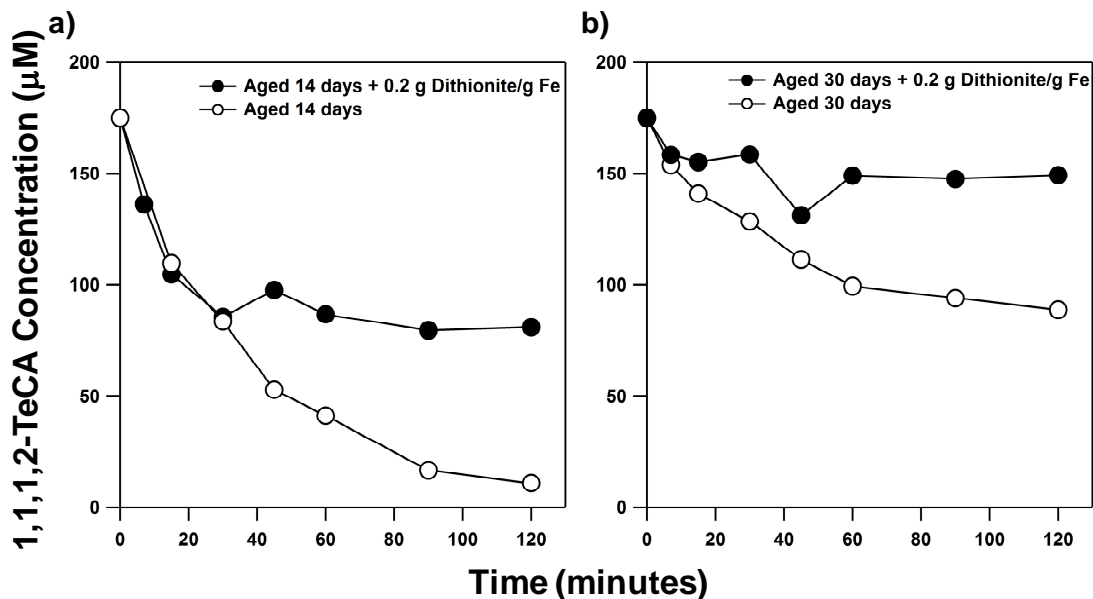


Figure 3-12. Inhibitory influence of dithionite on the reactivity toward 1,1,1,2-TeCA of NZVI suspensions (2 g/L) aged at pH 7 (50 mM HEPES) within an anaerobic chamber for (a) 14 d and (b) 30 d. Open circles correspond to the change in 1,1,1,2-TeCA concentration over time resulting from reaction with the aged NZVI suspension. Solid circles show 1,1,1,2-TeCA decay after the aged NZVI suspensions were reacted with 0.2 g dithionite/g NZVI. Generally, the reaction with dithionite inhibited the rate of 1,1,1,2-TeCA reduction. In panel (a), the dithionite-treated materials exhibited comparable reactivity to the aged suspension, at least initially. The loss in reactivity after approximately 30 minutes for the dithionite-treated material is consistent with surface passivation, presumably from iron sulfides generated via the reduction of dithionite by Fe(0) that inhibit further 1,1,1,2-TeCA reduction.

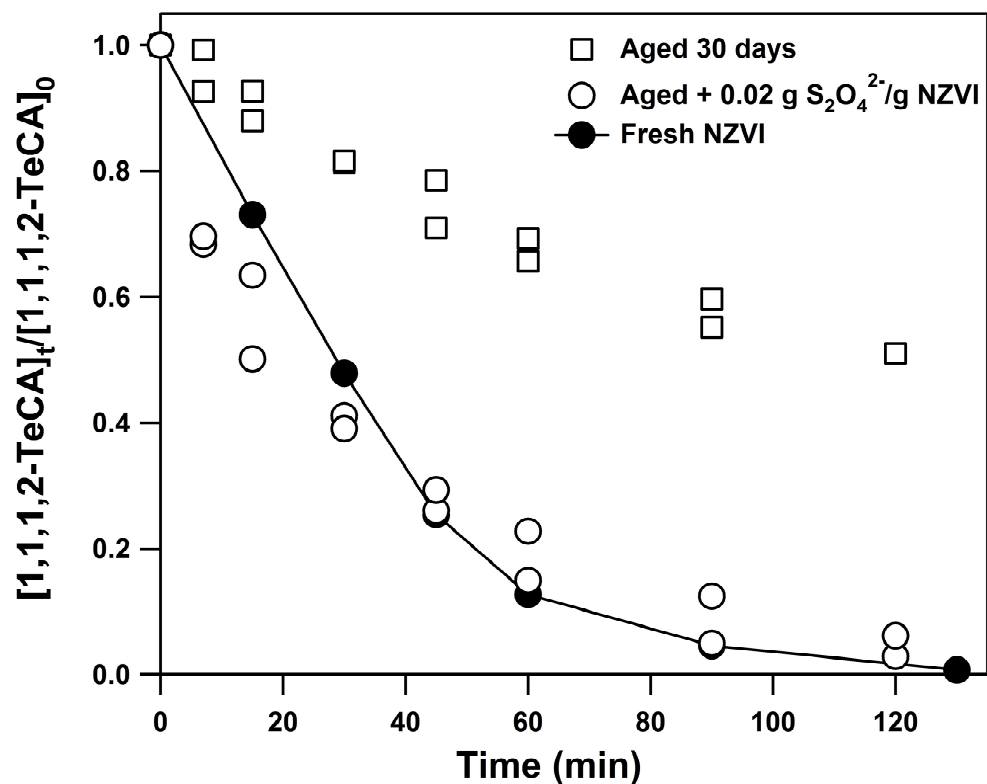


Figure 3-13. Change in 1,1,1,2-TeCA concentration as a function of time in fresh NZVI suspensions (solid circles), NZVI suspensions aged 30 d inside an anaerobic chamber (open squares), and products of the reaction between 0.02 g dithionite/g NZVI and the 30 d aged NZVI suspension (open circles). For the purpose of comparison, the concentration of 1,1,1,2-TeCA measured over time was normalized to the initial reactor concentration (~170 μ M). All experiments were conducted at a reductant mass loading of 2 g/L at pH 8 in 50 mM Tris.

Sustained Suspension Reactivity via Multiple Reactions with Dithionite.

A final set of experiments examined the reactivity of an NZVI suspension toward Cr(VI) over the course of sequential reaction cycles with dithionite (Figure 3-14). NZVI oxidized in air at pH 8 was reduced with 0.7 g dithionite/g NZVI and subsequently reacted with Cr(VI) until exhaustion, at which time the reaction with dithionite was repeated. After 5 instances of reaction with dithionite, the total Cr(VI) removal was approximately 300 mg of Cr(VI)/g NZVI, a 15-fold increase relative to fresh NZVI at pH 8. For comparison, this sequential regeneration procedure was also explored for oxygen-free NZVI suspensions that were passivated via reaction with Cr(VI) at pH 8. This scenario assumes that for treatment systems with high Cr(VI) concentration, reduction of Cr(VI) to a passivating Cr(III)-Fe(III) solid phase [37] is the primary mechanism responsible for NZVI reactivity loss. Again, the repeated reaction of the Cr-passivated NZVI with 0.7 g dithionite/g NZVI increased the total removal of Cr(VI) by roughly a factor of 3 relative to the fresh NZVI. Thus, Cr(VI) removal efficiency per gram of NZVI can be considerably enhanced through the use of dithionite to restore system reducing capacity. Further work is needed, however, to confirm that repeated dithionite addition does not extensively mobilize Cr(III) produced from Cr(VI) reduction.

Interestingly, Figure 3-14 shows that dithionite enhanced the reactivity of NZVI passivated via air oxidation to a far greater extent than NZVI passivated via reaction with Cr(VI). This suggests that differences in the nature of the passive layer generated via reaction with O₂ and Cr(VI) in turn affect the passivated materials' subsequent reactivity toward dithionite. While suspension aging in air produces a particle with an Fe(0) core

surrounded by magnetite and a passive ferric oxide shell, XRD characterization of Cr(VI) passivated materials also indicates the presence of largely Fe(0) and a phase with d-spacings comparable to magnetite [26] (Figure 3-15). Others have shown that reduction of Cr(VI) by NZVI produces a stable, alloy-like Cr(III)-Fe(III) hydroxide shell on NZVI particles [37]. Accordingly, the nature of the passivating layer on Fe(0) surfaces must be viewed as an important variable in the efficiency of dithionite as a regenerant for treatment system reactivity.

3.5. Environmental Implications

Depending upon geochemical conditions, our results suggest NZVI reactivity ranges anywhere from several hours to a couple of months, and thus concerns over its longevity during application may be warranted. To counteract the effects of aging, we show that dithionite can be used to restore the reactivity of passivated NZVI treatment systems, and that its repeated use can sustain the system's reducing capacity far beyond timescales achievable with NZVI alone. Optimal performance of dithionite requires, however, an understanding of the mechanism responsible for NZVI reactivity loss; dissolved oxygen concentrations, solution pH, and likely the presence of other co-solutes will not only influence the reactive lifetime of NZVI but also the products of aging and the reactivity of species formed via reaction with dithionite. Identifying the major products of NZVI passivation will be critical for process efficiency, therefore, because it will dictate the amount of dithionite necessary to optimize performance of the regenerated treatment system. The pH-dependent aging and products of dithionite

reaction proposed for aerobically and anaerobically aged materials are summarized in Schematic 3-1 and 3-2, respectively.

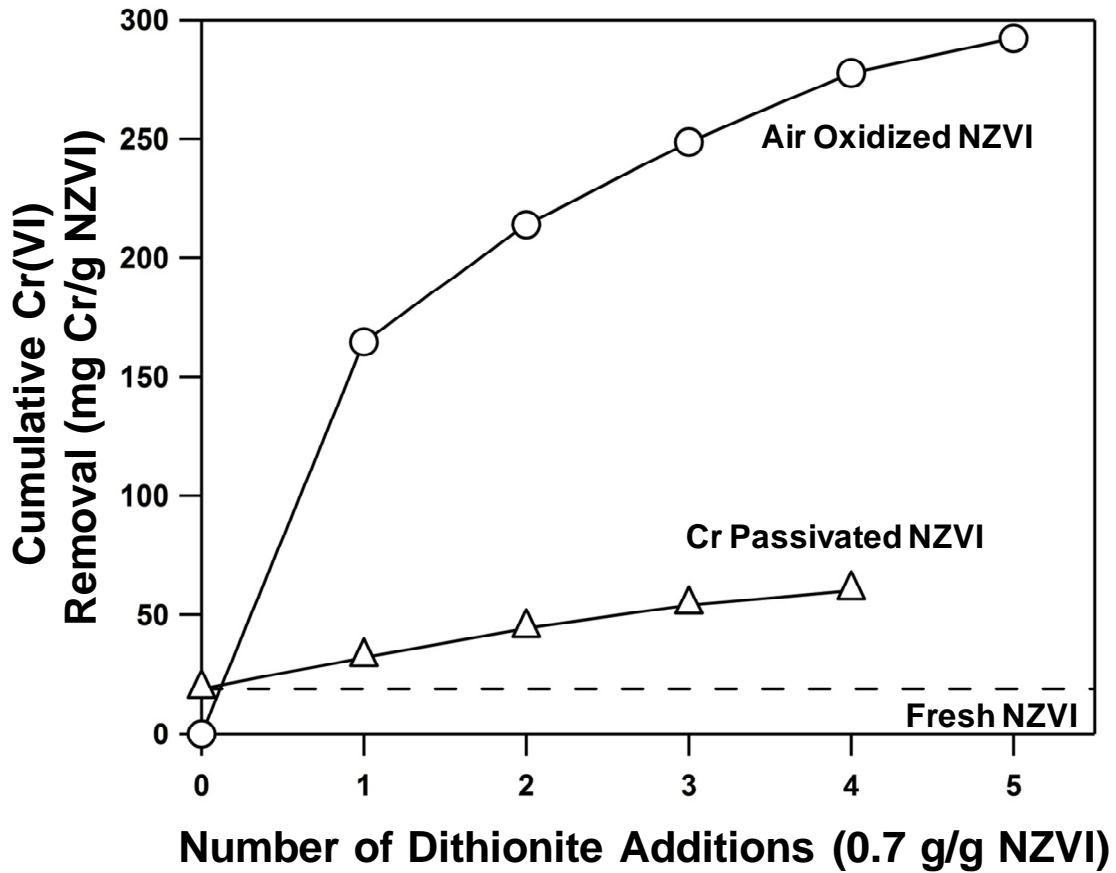


Figure 3-14. Cumulative Cr(VI) removal as a result of multiple, sequential reactions of passivated NZVI suspensions with 0.7 g dithionite/g NZVI. Cumulative Cr(VI) removal is reported on a per mass basis with respect to the mass equivalents of NZVI initially present in suspension. Removal capacities are shown for NZVI suspensions aged in air for 3 d at pH 8 and for fresh NZVI passivated through reaction with excess Cr(VI). Also shown is the removal capacity determined for fresh NZVI. All experiments were conducted at a reductant mass loading of 2.8 g/L at pH 8 in 50 mM Tris.

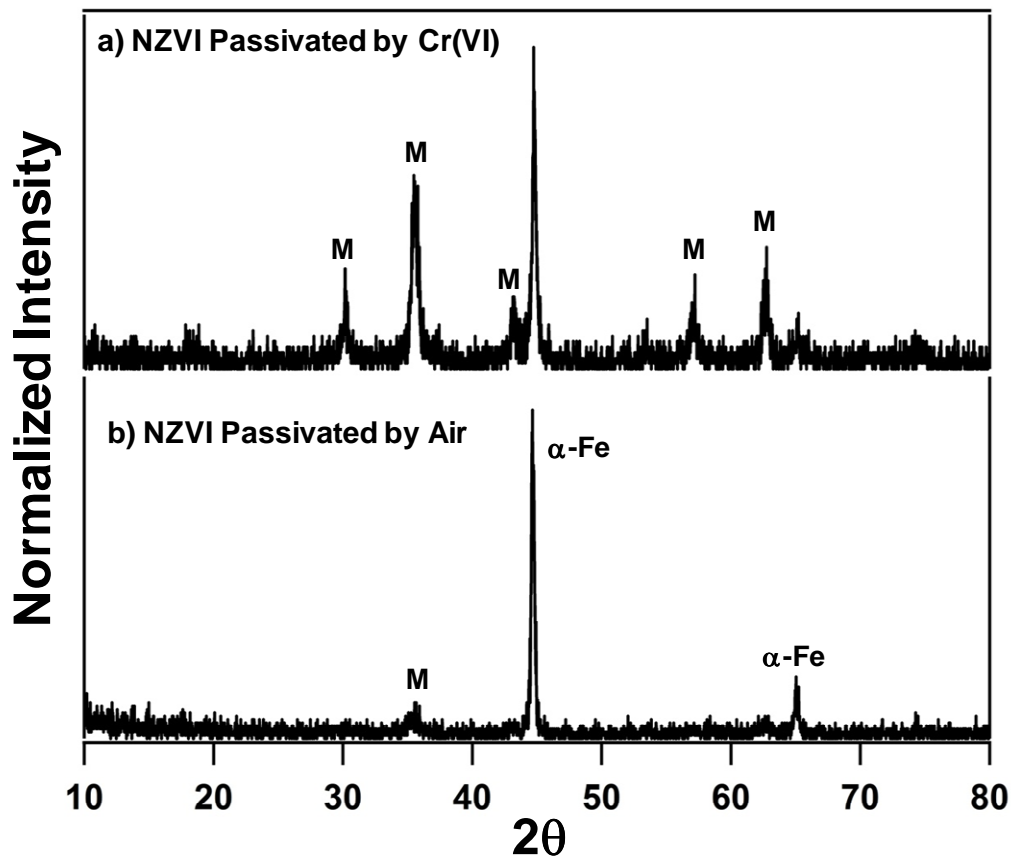
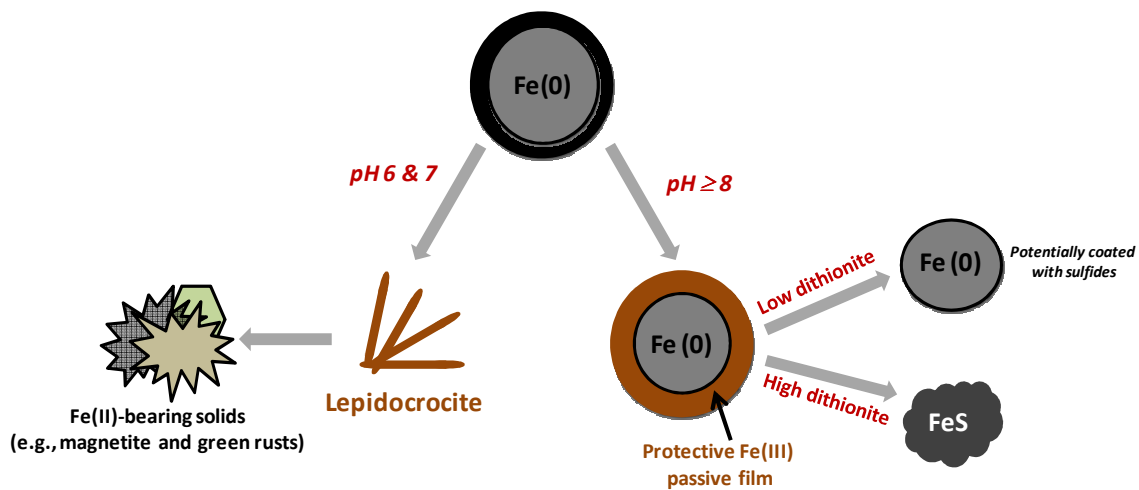
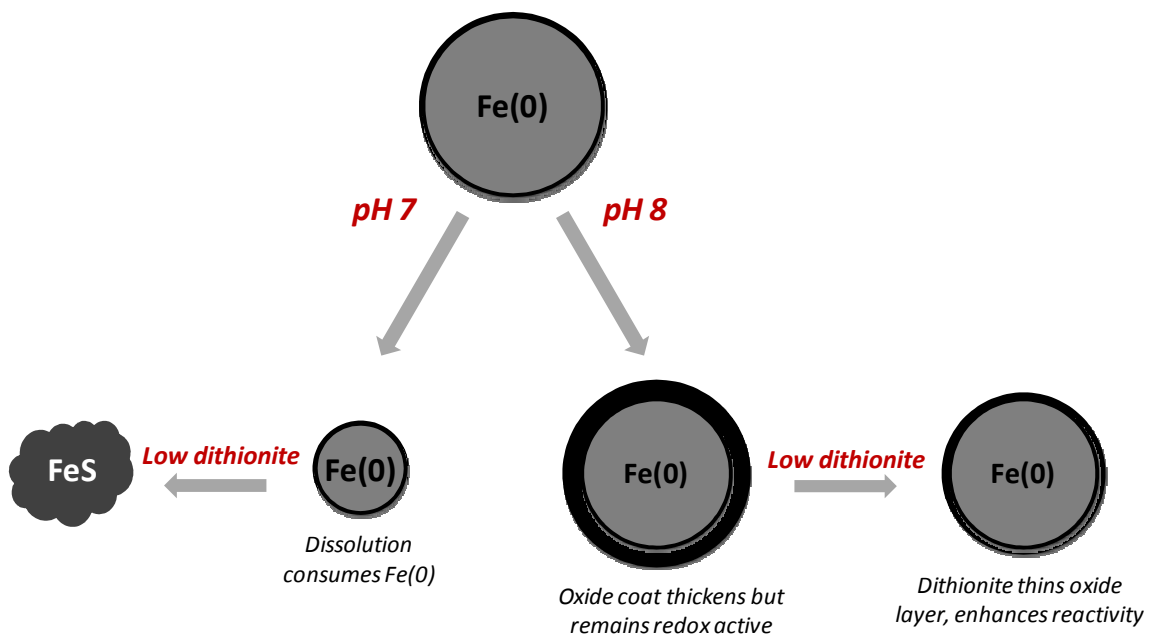


Figure 3-15. X-ray diffraction (XRD) patterns for NZVI suspensions (a) passivated by reaction with excess Cr(VI) in the absence of oxygen and (b) passivated by exposure to air for 3d. Suspensions (2 g/L) were prepared at pH 8 (50 mM Tris). For panel (a), solutions of Cr(VI) were added repeatedly to a deoxygenated 2 g/L NZVI suspension until no further loss in aqueous Cr(VI) was measured. The solids were then separated from the supernatant via centrifugation and washed several times with deoxygenated deionized water before drying the wet slurry on a microscope slide for XRD analysis. After passivation by Cr(VI), the only phases detected via XRD were magnetite (diffraction lines noted with M), and α -Fe. Thus, NZVI passivation induced by reduction of Cr(VI) preserved a considerable portion of Fe(0) in the particle core. For panel (b), results are the same as those shown in Figure 3-5 of the manuscript text. NZVI passivation via suspension exposure to air also resulted in a considerable portion of Fe(0) preserved in the particle core, although no secondary phases resulting from oxygenation were detectable via XRD.



Schematic 3-1. Product summary proposed for the aging of NZVI suspensions in equilibrium with air (i.e., in the presence of dissolved oxygen) and the subsequent reaction with variable loadings of dithionite.



Schematic 3-2. Product summary proposed for the aging of NZVI suspensions in the absence of dissolved oxygen and the subsequent reaction with low (< 0.1 g/g NZVI) dithionite loadings. At both pH values, more concentrated dithionite solutions would primarily generate iron sulfides.

The most promising use of this approach appears to be for sites contaminated with pollutants prone to facile reduction not only by Fe(0), but also by various forms of Fe(II). For example, we show that nitroaromatic compounds and Cr(VI) are readily reducible by nearly all of the products generated from the reaction of aged NZVI suspensions with dithionite, regardless of whether Fe(0) is present in the passivated particle core. Furthermore, the amount of dithionite can be tailored to control the reactive phases generated and tune the reducing capacity of the system.

Other potential benefits of dithionite as a regenerant of iron-based treatment systems merit further exploration. First, it may be feasible to couple dithionite application with stimulated biogeochemical processes that promote pollutant natural attenuation. In iron-rich environments, microbiological respiration of sulfate results in precipitation of FeS, a process previously exploited for treatment of groundwater contaminated by vinyl halides [40]. In a similar fashion, stimulation of sulfate-reducing bacteria could be used to sequester dithionite oxidation products as FeS, thereby further increasing the size of the reducing zone in the subsurface.

Our results also have potential implications for the storage and handling of highly reactive NZVI materials prior to application. This work and others [24] have shown that atmospherically stable NZVI particles can be prepared as a powder or wet suspension via controlled exposure to oxygen. Kim et al. [24] found, however, that stabilization leads to less reactive materials. One way to help alleviate concerns associated with NZVI reactivity loss during storage, handling, subsurface delivery and transport may be the application of these atmospherically stable NZVI particles in tandem with dithionite.

After particle delivery, subsequent application of dithionite could be used to restore their reactivity to levels comparable to fresh NZVI.

Finally, the outcomes from this work should be directly applicable to larger scale iron particles, including micron and millimeter-sized particles commonly used in PRBs. There is potential, therefore, for dithionite to serve as a mechanism for restoring reactivity to exhausted PRBs whose treatment efficiency has been compromised by buildup of passive oxidation products on the reductant particle surface.

3.6. Acknowledgements

The authors would like to acknowledge Drs. Michelle M. Scherer and Christopher Gorski of the University of Iowa for their assistance with Mossbauer analysis, Mr. Matthew Theriault for his assistance with nitrobenzene experiments, Dr. D. Howard Fairbrother and Kevin Wepasnick for their assistance with XPS analysis, which was conducted in the surface analysis laboratory at Johns Hopkins University as part of the Materials Research Science and Engineering Center funded by the NSF, and Dr. Stephen McDaniel of the U.C. Riverside Central Facility for Advanced Microscopy and Microanalysis for assistance with SEM and TEM.

3.7. Literature Cited

1. Zhang, W.-X., Nanoscale Iron Particles for Environmental Remediation: An Overview. *J. Nanopart. Res.* **2003**, *5*, 323-332.
2. Tratnyek, P.G.; Johnson, R.L., Nanotechnologies for Environmental Cleanup. *Nano Today* **2006**, *1*, 44-48.

3. Li, X.; Elliot, D.W.; Zhang, W.-X., Zero-Valent Iron Nanoparticles for Abatement of Environmental Pollutants: Materials and Engineering Aspects. *Crit. Rev. Solid State Mater. Sci.* **2006**, *31*, 111-122.
4. Sarathy, V.; Tratnyek, P.G.; Nurmi, J.T.; Baer, D.R.; Amonette, J.E.; Chun, C.L.; Penn, R.L.; Reardon, E.J., Aging of Iron Nanoparticles in Aqueous Solution: Effects on Structure and Reactivity. *J. Phys. Chem. C* **2008**, *112*, 2286-2293.
5. Henderson, A.D.; Demond, A.H., Long-Term Performance of Zero-Valent Iron Permeable Reactive Barriers: A Critical Review. *Environ. Eng. Sci.* **2007**, *24*, 401-423.
6. Elliot, D.W.; Zhang, W.-X., Field Assessment of Nanoscale Bimetallic Particles for Groundwater Treatment. *Environ. Sci. Technol.* **2001**, *35*, 4922-4926.
7. Henn, K.W.; Waddill, D.W., Utilization of Nanoscale Zero-Valent Iron for Source Remediation- A Case Study. *Remediation Journal* **2006**, *16*, 57-77.
8. Reardon, E.J.; Fagan, R.; Vogan, J.L.; Przepiora, A., Anaerobic Corrosion Reaction Kinetics of Nanosized Iron. *Environ. Sci. Technol.* **2008**, *42*, 2420-2424.
9. Liu, Y.; Lowry, G.V., Effect of Particle Age (Fe⁰ Content) and Solution pH on NZVI Reactivity: H₂ Evolution and TCE Dechlorination. *Environ. Sci. Technol.* **2006**, *40*, 6085-6090.
10. Somorjai, G.A.; Li, Y., *Introduction to Surface Chemistry and Catalysis*. 2nd ed.; John Wiley and Sons: New York, NY, 2010.
11. Grenier, A.C.; McGuire, M.M.; Fairbrother, D.H.; Roberts, A.L., Treatment of Vapor-Phase Organohalides with Zerovalent Iron and Ni/Fe Reductants. *Environ. Eng. Sci.* **2004**, *21*, 421-435.
12. Zhu, B.-W.; Lim, T.-T., Catalytic Reduction of Chlorobenzenes with Pd/Fe Nanoparticles: Reactive Sites, Catalyst Stability, Particle Aging and Regeneration. *Environ. Sci. Technol.* **2007**, *41*, 7523-7529.
13. Szecsody, J.E.; Fruchter, J.S.; Williams, M.D.; Vermeul, V.R.; Sklarew, D., *In Situ* Chemical Reduction of Aquifer Sediments: Enhancement of Reactive Iron Phases and TCE Dechlorination. *Environ. Sci. Technol.* **2004**, *38*, 4656-4663.
14. Cotton, F.A.; Wilkinson, G., *Advanced Inorganic Chemistry*. John Wiley and Sons: 1962; p 959.

15. Amonette, J.E.; Szecsody, J.E.; Schaef, H.T.; Templeton, J.C.; Gorby, Y.A.; Fruchter, J.S., Abiotic Reduction of Aquifer Materials by Dithionite: A Promising in-Situ Remediation Technology. In *In Situ Remediation: Scientific Basis for Current and Future Technologies*, Gee, G. W.; Wing, N. R., Eds. Battelle Press: Columbus, OH, 1994; pp 851-881.
16. Sun, Q.; Feitz, A.J.; Guan, J.; Waite, T.D., Comparison of the Reactivity of Nanosized Zero-Valent Iron (NZVI) Particles Produced by Borohydride and Dithionite Reduction of Iron Salts. *Nano* **2008**, *3*, 341-349.
17. Ludwig, R.D.; Su, C.; Lee, T.R.; Wilkin, R.T.; Acree, S.D.; Ross, R.R.; Keeley, A., *In Situ* Chemical Reduction of Cr(VI) in Groundwater Using a Combination of Ferrous Sulfate and Sodium Dithionite: A Field Investigation *Environ. Sci. Technol.* **2007**, *41*, 5299-5305.
18. Elsner, M.; Schwarzenbach, R.P.; Haderlein, S., Reactivity of Fe(II)-Bearing Minerals toward Reductive Transformation of Organic Contaminants. *Environ. Sci. Technol.* **2004**, *38*, 799-807.
19. Williams, M.D.; Vermeul, V.R.; Szecsody, J.E.; Fruchter, J.S. *100-D Area in Situ Redox Treatability Test for Chromate-Contaminated Groundwater* PNNL-13349; Pacific Northwest National Laboratory: Richland Washington, 2000.
20. Larese-Casanova, P.; Scherer, M.M., Fe(II) Sorption on Hematite: New Insights Based on Spectroscopic Measurements. *Environ. Sci. Technol.* **2007**, *41*, 471-477.
21. Moulder, J.F.; Stickle, W.F.; Sobol, P.E.; Bomben, K.D., *Handbook of X-Ray Photoelectron Spectroscopy: A Reference Book of Standard Spectra for Identification and Interpretation of XPS Data*. Perkin-Elmer Corp.: Eden Prairie, MN, 1992.
22. Cwiertny, D.M.; Handler, R.M.; Schaefer, M.V.; Grassian, V.H.; Scherer, M.M., Interpreting Nanoscale Size-Effects in Aggregated Fe-Oxide Suspensions: Reaction of Fe(II) with Goethite. *Geochim. Cosmochim. Ac.* **2008**, *72*, 1365-1380.
23. Tamura, H., The Role of Rusts in Corrosion and Corrosion Protection of Iron and Steel. *Corros. Sci.* **2008**, *50*, 1872-1883.
24. Kim, H.-S.; Ahn, J.-Y.; Hwang, K.-Y.; Kim, I.-K.; Hwang, I., Atmospherically Stable Nanoscale Zero-Valent Iron Particles Formed under Controlled Air Contact: Characteristics and Reactivity. *Environ. Sci. Technol.* **2010**, *44*, 1760-1766.

25. Anthony, J.W.; Bideaux, R.A.; Bladh, K.W.; Nichols, M.C., *Handbook of Mineralogy*. Mineralogical Society of America: Chantilly, VA, 2003; Vol. Vols. I-V.
26. Cornell, R.M.; Schwertmann, U., *The Iron Oxides: Structure, Properties, Reactions, Occurrences and Uses* 2nd ed.; Wiley-VCH: Weinheim, Germany, 2003; p 664.
27. Hofstetter, T.B.; Heijman, C.G.; Haderlein, S.B.; Holliger, C.; Schwarzenbach, R.P., Complete Reduction of TNT and Other (Poly)Nitroaromatic Compounds under Iron-Reducing Subsurface Conditions. *Environ. Sci. Technol.* **1999**, *33*, 1479-1487.
28. Sedlak, D.L.; Chan, P.G., Reduction of Hexavalent Chromium by Ferrous Iron. *Geochim. Cosmochim. Acta* **1997**, *61*, 2185-2192.
29. Peterson, M.L.; Brown, J., G.E.; Parks, G.A., Direct XAFS Evidence for Heterogeneous Redox Reaction at the Aqueous Chromium/Magnetite Interface. *Colloids Surf., A* **1996**, *107*, 77-88.
30. Skovbjer, L.L.; Stipp, S.L.S.; Utsunomiya, S.; Ewing, R.C., The Mechanism of Reduction of Hexavalent Chromium by Green Rust Sodium Sulphate: Formation of Cr-Goethite. *Geochim. Cosmochim. Acta* **2006**, *70*, 3582-3592.
31. Eggleston, C.M.; Ehrhardt, J.-J.; Stumm, W., Surface Structural Controls on Pyrite Oxidation Kinetics: An XPS-UPS, STM, and Modeling Studies. *American Mineralogist* **1996**, *81*, 1036-1056.
32. Baltrusaitis, J.; Cwiertny, D.M.; Grassian, V.H., Adsorption of Sulfur Dioxide on Hematite and Goethite Particle Surfaces *Phys. Chem. Chem. Phys.* **2007**, *9*, 5542-5554.
33. Herbert, J., R.B.; Benner, S.G.; Pratt, A.R.; Blowes, D.W., Surface Chemistry and Morphology of Poorly Crystalline Iron Sulfides in Media Containing Sulfate-Reducing Bacteria. *Chemical Geology* **1998**, *144*, 87-97.
34. Jeong, H.Y.; Klaue, B.; Blum, J.D.; Hayes, K.F., Sorption of Mercuric Ion by Synthetic Nanocrystalline Mackinawite (FeS). *Environ. Sci. Technol.* **2007**, *41*, 7699-7705.
35. Hansson, E.B.; Odziemkowski, M.S.; Gillham, R.W., Influence of Na₂S on the Degradation Kinetics of CCl₄ in the Presence of Very Pure Iron. *J. Contam. Hydrol.* **2008**, *98*, 128-134.

36. Butler, E.C.; Hayes, K.F., Kinetics of the Transformation of Halogenated Aliphatic Compounds by Iron Sulfide. *Environ. Sci. Technol.* **2000**, *34*, 422-429.
37. Li, X.-Q.; Cao, J.; Zhang, W.-X., Stoichiometry of Cr(VI) Immobilization Using Nanoscale Zerovalent Iron (NZVI): A Study with High-Resolution X-Ray Photoelectron Spectroscopy (Hr-XPS). *Ind. Eng. Chem. Res.* **2008**, *47*, 2131-2139.
38. Patterson, R.R.; Fendorf, S., Reduction of Hexavalent Chromium by Amorphous Iron Sulfide. *Environ. Sci. Technol.* **1997**, *31*, 2039-2044.
39. Williams, A.G.B.; Scherer, M.M., Kinetics of Cr(VI) Reduction by Carbonate Green Rust. *Environ. Sci. Technol.* **2001**, *35*, 3488-3494.
40. Kennedy, L.G.; Everett, J.W.; Becvar, E.; DeFeo, D., Field-Scale Demonstration of Induced Biogeochemical Reductive Dechlorination at Dover Air Force Base, Dover, Delaware. *J. Contam. Hydrol.* **2006**, *88*, 119-136.

4. Chlorinated Solvent Transformation in Palladized Zero-Valent Iron Systems: New Insights from Rate Dependence on Reductant Loading and Solvent Kinetic Isotope Effects

4.1. Abstract

Palladized nanoscale zero-valent iron (Pd/NZVI) has grown in popularity for source zone control, yet the entities responsible for pollutant transformation in these systems and the optimal conditions for their subsurface application are poorly understood. Here, trends in Pd/Fe reactivity toward 1,1,1,2-tetrachloroethane (1,1,1,2-TeCA) and *cis*-dichloroethene (*cis*-DCE) were examined as a function of pH, chlorinated solvent concentration, Pd loading and reductant mass loading (ρ_m values) for bimetals prepared from both nanoscale and micron-sized Fe(0). Mechanistic insights were obtained through measurement of solvent kinetic isotope effects (SKIEs) via parallel experiments in H₂O and D₂O. Collectively, our data support two pathways for chlorinated solvent reduction in Pd/NZVI batch systems. Most notably, SKIEs for 1,1,1,2-TeCA and *cis*-DCE reduction by Pd/NZVI [$k_{\text{obs}}(\text{H}_2\text{O})/k_{\text{obs}}(\text{D}_2\text{O})$] increase substantially with Pd loading and Pd/NZVI concentration. At low Pd loadings and Pd/NZVI concentrations, modest reactivity enhancements occur via galvanic couple formation. In contrast, the magnitude of SKIEs (up to 100) in the most reactive Pd/NZVI systems suggests the involvement of atomic hydrogen. However, evidence of atomic hydrogen participation was not observed for Pd/Fe prepared from larger Fe(0) particles, nor for any size of non-palladized Fe(0). SKIEs for 1,1,1,2-TeCA reduction decrease during anaerobic aging of Pd/NZVI particles,

revealing that atomic hydrogen is likely to persist only over one to two weeks during Pd/NZVI application.

4.2. Introduction

Since its inception [1], application [2-4] of palladized nanoscale zero-valent iron (Pd/NZVI) for source zone control has grown rapidly. Pd/Fe is typically the most reactive of iron-based bimetallic reductants [5-7], achieving greater rates of pollutant removal [1, 5, 8] and more fully dehalogenated products [5, 9] than zero-valent iron [Fe(0)]. Despite growth in its application, the wealth of literature on Pd/Fe reductants reveals relatively divergent performance. Specifically, a common metric for Pd/Fe reactivity is the extent to which it enhances pollutant transformation relative to Fe(0), a value typically obtained by normalizing the pseudo-first-order rate constant (k_{obs} values) for pollutant reduction by Pd/Fe [$k_{\text{obs}}(\text{Pd/Fe})$] to the corresponding k_{obs} value from an identical system with Fe(0) [$k_{\text{obs}}(\text{Fe})$]. For Pd/Fe, reported rate enhancement factors (hereafter referred to as REFs) range between 2 [5] and 1000 [10]. To date, the source of such variation is not entirely understood, although during application it is clearly desirable to optimize Pd/Fe characteristics and treatment zone conditions to yield the largest REF achievable.

It is tempting to attribute variations in performance to differences in the Pd/Fe particles prepared in different studies. For example, increasing the amount and surface coverage of Pd on Fe(0) particles increases Pd/Fe reactivity [5, 8, 11], supporting a scenario in which pollutant transformation is suggested to occur on the Pd surface [12-14]. However, several studies have systematically varied Pd loading and surface coverage

while holding other system variables constant [5, 8, 15], observing maxima in Pd/Fe reactivity that typically limit REFs toward the lower end of the aforementioned spectrum. Other currently unrecognized factors must, therefore, contribute to the observed range in Pd/Fe performance.

One possible explanation is that the mechanism of pollutant transformation, specifically the nature of the reductant, differs between Fe(0) and Pd/Fe systems. Two pathways for rate enhancement by Pd/Fe have gained popular acceptance. One hypothesis [2, 16, 17] involves the formation of a galvanic couple between Fe(0) and Pd, in which iron functions as the anode where oxidation of Fe(0) to Fe(II) occurs while Pd serves as the cathode at which pollutant reduction takes place. In the couple, Fe(0) becomes more easily oxidized, in turn increasing the rate of electron transfer to the pollutant at the Pd surface. Others have postulated [5, 6, 17-19] that Pd functions as a hydrogenation catalyst, such that adsorbed or absorbed atomic hydrogen species associated with the Pd surface are the responsible entities for pollutant transformation. Evidence for both pathways exists, although it remains unclear as to which is dominant in Pd/Fe systems or how their relative importance changes in response to reductant characteristics, solution chemistry, or the evolving Pd/Fe surface during particle aging.

Mounting evidence suggests that the chemical processes controlling pollutant transformation in Pd/Fe systems is distinct from Fe(0). For example, Cwiertny *et al.* [10] observed that the same Pd/Fe formulation that enhanced 1,1,1-trichloroethane (1,1,1-TCA) reduction 10-fold also enhanced *cis*-dichloroethylene (*cis*-DCE) reduction by more than 1000, indicating a strong dependence of Pd/Fe reactivity on the target oxidant. *cis*-

DCE also exhibited a far greater increase in k_{obs} values per unit of deposited Pd on the Fe(0) surface. Because $k_{\text{obs}}(\text{Pd/Fe})$ and $k_{\text{obs}}(\text{Fe})$ used to determine REFs are measured in identical experimental systems, it is often assumed that REFs do not reflect system variables such as reductant loading (ρ_{m} in g/L), target pollutant concentration, and pH. However, such assumptions are rarely tested and, most importantly, are likely to fail if different mechanisms exist in Fe(0) and Pd/Fe systems, and in turn would introduce large variations in reported REFs for Pd/Fe systems.

In this study, we explore REFs achieved in Pd/Fe reductant systems over a range of experimental conditions. Pd/Fe reductants were prepared via a displacement plating method using a commercially available NZVI powder (referred to as Pd/NZVI). In subsequent reactivity experiments with 1,1,1,2-tetrachloroethane (1,1,1,2-TeCA) and *cis*-dichloroethene (*cis*-DCE), we examined how REFs for Pd/NZVI changed over a broad range of Pd additive loadings (0.05-0.35% Pd by mass), solution pH (6-8), reductant mass loadings (ρ_{m} values of 0.03-5.68 g/L), target pollutant concentrations (3 – 2000 μM), and suspension aging time (0-30 days). Additional studies were performed with several Pd/Fe reductants prepared from micron-sized Fisher electrolytic iron (hereafter referred to as Pd/ZVI), allowing the influence of Fe(0) particle size on bimetal reactivity also to be assessed directly for the first time. Collectively, our approach not only helps to identify the optimal reductant characteristics and application conditions for Pd/Fe performance, but changes in REFs in response to these variables would provide indirect evidence that different pollutant transformation mechanisms are at play in Fe(0) and Pd/Fe systems.

In complementary experiments, new insights into the mechanism of pollutant transformation in Fe(0) and Pd/Fe systems were obtained through measurement of solvent kinetics isotope effects (SKIEs) via parallel reactions with 1,1,1,2-TeCA and *cis*-DCE conducted in D₂O- and H₂O-based buffer systems. When a solvent is replaced with an isotopically substituted analogue, SKIEs occur when the solvent is a reactant or when there are significant interactions between the solvent and transition structures generated via reaction [20]. SKIE values are quantified by normalizing k_{obs} values measured in H₂O [$k_{\text{obs}}(\text{H}_2\text{O})$] to the k_{obs} value measured in an identical system with D₂O [$k_{\text{obs}}(\text{D}_2\text{O})$], with larger values indicating a role for solvent molecules in the reaction.

As a mechanistic tool, SKIE values have rarely been explored for bimetallic systems, with two reports producing conflicting results. Schrick *et al.* [17] observed a large SKIE of 14 for trichloroethene (TCE) reduction by Ni/NZVI, which was interpreted as evidence for the involvement of atomic hydrogen. In a later examination of SKIE values for 1,1,1-TCA reduction with Cu/Fe prepared from Fisher electrolytic iron [21], relatively small SKIE values (1.62 ± 0.08 and 1.34 ± 0.08) were observed at two different Cu loadings (5 and 125 μmole of Cu/g Fe, respectively), suggesting a minimal role for atomic hydrogen in these systems. In this work, SKIE values were measured for Fe(0) and Pd/Fe systems with 1,1,1,2-TeCA and *cis*-DCE over the range of aforementioned reductant and system variables (e.g., Pd coverage, pH, ρ_{m} values, Fe(0) particle size) to explore conditions that may promote atomic hydrogen involvement during pollutant reduction.

4.3. Experimental Section

Reagents

NZVI was acquired from Nanostructured and Amorphous Materials, Inc. (Houston, TX). Characterization of this material has been previously described [22]. Fisher electrolytic iron powder (100 mesh; hereafter abbreviated as ZVI) was used as a representative granular iron. Reactivity studies were conducted in buffers of HEPES (Sigma-Aldrich; 99.5%) or MES (Sigma-Aldrich; 99.7%) with sodium chloride (NaCl, Aldrich, $\geq 99.0\%$). Buffer pH was adjusted with hydrochloric acid (Fisher, trace metal grade) and sodium hydroxide (NaOH; 97+%; ACS reagent grade). Potassium hexachloropalladate (IV) ($\text{Cl}_6\text{K}_2\text{Pd}$, Aldrich, 99%) was used to generate Pd/Fe reductants. Aqueous solutions were prepared using deionized water (Milipore, Q-Grad 2), while SKIEs were measured in systems with deuterium oxide (D_2O , Aldrich, 99.9 atom % D). All solutions were deoxygenated prior to use by sparging with compressed N_2 for at least 1 hr/L. Reactivity studies used 1,1,1,2-tetrachloroethane (1,1,1,2-TeCA; $\sim 99\%$, Aldrich) and *cis*-1,2-dichloroethene (*cis*-DCE; 97%, Aldrich), with stock solutions prepared in methanol (certified ACS, Fisher Scientific). Aqueous samples from experiments were extracted and diluted in n-hexane (GC-Resolv, Fisher Scientific). Reagents used in colorimetric analysis of aqueous Fe(II) include 1,10-phenanthroline (Aldrich, 99+%), ammonium acetate (Sigma-Aldrich, $\geq 98\%$), and glacial acetic acid (Fisher, certified ACS plus).

Pd/Fe synthesis

Pd/Fe reductants were prepared via displacement plating within an anaerobic chamber based on procedures modified from previous work [5]. For plating of NZVI particles, NZVI suspensions (2 g/L) were prepared in deoxygenated, DI water and sonicated for 30 seconds. Displacement plating was accomplished by adding a specific volume (between 100 – 700 μ L) of 0.5 mM K_2PdCl_6 stock solution prepared in 0.01 N HCl to 5 mL of the dispersed NZVI suspension. For plating of ZVI particles, between 5-50 mg of ZVI were weighed into 20 ml serum bottles (Wheaton) and washed with ~0.1-1 mL of 1 M HCl (keeping a constant ratio of ZVI to acid volume) for 10 minutes while stirring by hand, followed by two washes with deoxygenated, deionized water. Displacement plating was accomplished by adding an appropriate volume (1-10 mL; again keeping a constant ratio of ZVI to plating solution volume) of 0.5 mM K_2PdCl_6 stock solution prepared in 0.01 N HCl to the acid-washed and water-rinsed iron. Stock solutions of Pd were prepared fresh daily.

After addition of Pd, slurries of NZVI or ZVI were mixed vigorously by hand for 5 min, over which time the initially orange supernatant became clear, indicating Pd loss from solution. Mass ratios of Pd to Fe(0) (either as ZVI or NZVI) were chosen based upon previous work [5, 10] to coincide with complete deposition of Pd from solution to the Fe(0) particle surface over this timescale. A magnetic stir plate was then used to collect the Pd/Fe particles on the reactor bottom, the supernatant was decanted by pipet so as to minimize loss of Pd/Fe, and a small fraction of the supernatant was collected for ICP-MS analysis to confirm complete Pd deposition during plating. Freshly prepared Pd/Fe particles were then rinsed twice with deoxygenated, DI water. After washing,

Pd/Fe particles were resuspended in an appropriate buffer solution for use in reactivity studies. As a control for reactivity studies, ZVI and NZVI samples were processed in a similar manner, including the addition of the appropriate volume of 0.01 N HCl free of Pd, although these simulated plating and washing processes had no observable effect on their reactivity.

Reactivity toward Chlorinated Solvents

The reactivity of NZVI, 0.05% Pd/NZVI and 0.35% Pd/NZVI, as well as ZVI and 1% Pd/ZVI was examined toward 1,1,1,2-TeCA and *cis*-DCE. For Pd/NZVI, a specific volume of a 2 g/L suspension of freshly prepared particles was added to a nominal 10 mL vial (Wheaton), the vial was filled with an appropriate buffer until free of headspace, and the vial was then crimp-sealed with a PTFE-lined butyl rubber septa. By varying the amount of Pd/NZVI stock suspension initially added to the reactor, diluting with buffer to a final total volume of 10 mL allowed us to conduct reactivity studies over a range of reductant solid loadings (or ρ_m values) from 0.03-0.6 g/L. For Pd/ZVI, we varied the mass of ZVI plated with Pd and then diluting freshly prepared Pd/ZVI particles to a final volume of ~9 mL to result in ρ_m values ranging from 0.6 – 5.7 g/L. For both Pd/NZVI and Pd/ZVI, experiments with variable ρ_m were conducted at a fixed initial concentration of 175 μ M. To examine the influence of the initial 1,1,1,2-TeCA concentration on Pd/NZVI reactivity, a constant volume (70 μ L) of a 1,1,1,2-TeCA methanolic stock solution with concentration ranging from 0.45 – 22.1 mM 1,1,1,2-TeCA was added to reactors with 0.05 g/L Pd/NZVI, producing initial concentrations in the reactor from 3 –

2000 μM . HEPES buffer was utilized for experiments within the pH range of 7 to 8, whereas MES was utilized in a few studies conducted between pH 5 and 6.5. The buffer concentration was 25 mM, and 25 mM sodium chloride was used in all solutions to provide ionic strength.

After construction, all reactors were removed from the glovebox and placed on a rotator (Cole-Parmer) that mixed the vials end-over-end at 60 RPM. Reactions with 1,1,1,2-TeCA and *cis*-DCE were initiated immediately via addition of methanolic spike to achieve the initial reactor concentrations listed above. Reactors were sampled periodically over time according to the procedures described in chapter 2.

Measurement of Solvent Kinetics Isotope Effects

To measure SKIEs, reactivity studies were conducted in parallel with H_2O and D_2O . Solutions of 25 mM HEPES/NaCl were prepared in D_2O , using the following correction [23] to pH meter measurements to account for differences in the pH and pD scales.

$$\text{pD} = \text{pH meter reading} + 0.40 \quad (4-1)$$

D_2O solutions were adjusted to the appropriate pD value using concentrated NaOH solution, which also was prepared in D_2O . SKIEs were measured as a function of pD loading on NZVI and ZVI and over a range of ρ_m values. In systems with variable ρ_m values, initial concentrations of 1,1,1,2-TeCA or *cis*-DCE were chosen so that a constant molar ratio of 0.02 of organohalide oxidant to iron-based reductant was employed in all systems to avoid any surface site limitations or competition effects that may occur at

elevated chlorinated solvent concentrations. The magnitude of SKIEs were calculated from the reactivity disparity between these two sets of reactors (i.e., $k_{\text{obs}}(\text{H}_2\text{O})/k_{\text{obs}}(\text{D}_2\text{O})$) that were prepared under otherwise identical conditions (e.g. Pd loading, Pd/Fe reductant concentration, pH and chlorinated solvent initial concentration).

Pd/NZVI Aging Studies.

Within an anaerobic chamber (97% N₂, 3% H₂), 2 g/L NZVI and 0.35% Pd/NZVI were prepared in 25 mM HEPES/NaCl solution at pH 8 and placed in a sealed 10 mL (Wheaton) vials with 5 mL of headspace. These suspensions were allowed to age for 30 days, mixing each by hand once a day. Periodically during aging, a portion of the suspension was withdrawn and diluted with fresh buffer prepared in H₂O to a final concentration of 0.22 g/L. In parallel, another sample of suspension was diluted to the same ρ_m value with buffer prepared in D₂O, such that analysis of 1,1,1,2-TeCA decay rates in both systems would allow the magnitude of SKIE to be evaluated as a function of reductant particle aging. To avoid any contribution from the H₂O present in the sample of the aged stock suspensions used in D₂O systems, care was taken to remove residual H₂O was removed via pipette prior to addition of D₂O. Reactivity studies with 1,1,1,2-TeCA were then conducted with aged particles of NZVI and 0.35% Pd/NZVI according to the aforementioned procedures. We note that in complement to reactivity studies, transmission electron microscopy (TEM) images were also collected for Pd/Fe reductants during aging.

Measurement of Fe(II) Production

For iron-based reductants, aqueous Fe(II) production was measured as an indicator of corrosion rate. Freshly prepared and washed reductant particles were suspended in fresh 25 mM HEPES/NaCl solution at pH 8 to achieve a total reductant concentration of 1 g/L. As Fe(II) production commenced upon buffer addition, reactors were placed immediately on a rotator that mixed the vials end-over-end at 60 RPM and samples were withdrawn over 15 min via a plastic syringes to measure the initial rate of Fe(II) production. More experimental details are referred in chapter 2.

Analytical Methods

Concentrations of 1,1,1,2-TeCA and *cis*-DCE in samples were determined via gas chromatography with electron capture detection (GC/ECD). The analytical methods for 1,1,1,2-TeCA and *cis*-DCE shared the same column and temperature program, and all details were presented in chapter 2. Reduction products for 1,1,1,2-TeCA (1,1,1-dichloroethene) and *cis*-DCE (primarily ethane and ethane) were identified and quantified via headspace analysis and gas chromatography with flame ionization detection (GC/FID). Headspace analysis used an HP-Plot Q column (30m × 0.32 mm × 20 μm; J & W Scientific) and a temperature program beginning at 50 °C, then increasing at 30 °C/min to 240 °C before holding for 10 minutes. For product analysis, 2 mL of aqueous sample was withdrawn from the reactor and stored in 20 mL headspace autosampler vial with magnetic screw cap. Samples were incubated at 60 °C for 5 min

(longer incubation times produced little difference in response), while mixing to promote gas-water partitioning prior to injection of 300 μL gas phase onto the column.

Measurements for dissolved Fe(II) concentration were according to the procedure outlined in chapter 2. The morphology of aged NZVI and 0.35% Pd/NZVI was examined using transmission electron microscopy. Further details of our TEM analysis and sample preparation are provided in chapter 2.

4.4. Results and Discussion

Influence of Solid Loading on Pd/Fe Reactivity toward 1,1,1,2-TeCA

In all reductant systems, 1,1,1,2-TeCA was transformed to 1,1-DCE, consistent with reductive β -elimination as the only loss pathway. Loss of 1,1,1,2-TeCA exhibited exponential decay, with k_{obs} values obtained from the slopes of semi-log plots of 1,1,1,2-TeCA concentration versus time. Values of k_{obs} for 1,1,1,2-TeCA reduction as a function of reductant solid loading (ρ_{m} values) are shown in Figure 4-1 for reductants prepared with Fisher electrolytic iron (hereafter referred to as ZVI) and iron nanoparticles from Nanostructured and Amorphous Materials (hereafter referred to as NZVI). Values of k_{obs} are shown for both unamended iron (hereafter referred to as Fe(0)) and palladized iron (hereafter referred to as Pd/Fe) systems, with 1% Pd (by mass) on ZVI and 0.05% or 0.35% Pd (by mass) on NZVI.

As expected from previous reports for ZVI [5] and NZVI [8, 24], Pd/Fe was more reactive than Fe(0) and reactivity increased with Pd loading. However, the magnitude of REF in Pd/Fe systems varied not only between ZVI and NZVI, but also as a function of

ρ_m values. In ZVI systems (Figure 4-1a), k_{obs} values exhibited a non-linear dependence on ρ_m ($k_{\text{obs}} \propto \rho_m^{0.4 \pm 0.1}$) as determined from the slope of $\log k_{\text{obs}}$ versus $\log \rho_m$ plots, similar to behavior previously observed with this ZVI batch [21]. Addition of 1% Pd, however, alters this functional relationship, with k_{obs} values exhibiting a nearly first-order dependence on ρ_m ($k_{\text{obs}} \propto \rho_m^{0.9 \pm 0.2}$), as expected for surface reactions.

Unexpectedly in NZVI systems, k_{obs} values were essentially independent of solid loading ($k_{\text{obs}} \propto \rho_m^{0.1 \pm 0.1}$; see also Figure 4-2), whereas addition of 0.05% Pd produced a dependence ($k_{\text{obs}} \propto \rho_m^{1.2 \pm 0.2}$) that was statistically equivalent to first-order. Interestingly, for 0.35% Pd/NZVI, the rate of change for k_{obs} increased with reductant loading, yielding a reaction order in ρ_m of 1.6 (± 0.2), significantly greater from unity.

As a practical consequence of these relationships, the REFs provided by Pd/Fe depend strongly on the experimental ρ_m value. For example, REF for Pd/ZVI relative to ZVI ranges from 3 to 10-fold over the ρ_m values investigated (up to 5.68 g/L), whereas with Pd/NZVI REFs span from 2- to 300-fold (up to 0.56 g/L). The observed dependence of REF on ρ_m values likely explains the majority of scatter that exists in reported REFs for Pd/Fe.

From a fundamental perspective, the non-linear dependence of k_{obs} on ρ_m in Fe(0) systems suggests some system variable limits reactive surface area to a greater extent at high ρ_m . In contrast, the near first-order dependence of k_{obs} on ρ_m values for 1% Pd/ZVI and 0.05% Pd/NZVI suggest that Pd deposition overcomes this limitation of Fe(0) systems and makes the reductant surface more uniformly active. Such behavior is

consistent with Pd deposition producing new sites for 1,1,1,2-TeCA reduction. For 0.35% Pd/NZVI, the unique parabolic dependence between k_{obs} and ρ_m is consistent with multiple mechanisms for 1,1,1,2-TeCA reduction, with the relative importance of these pathways depending on Pd and Pd/NZVI loadings.

Trends in mass-normalized rate constants for 1,1,1,2-TeCA reduction by NZVI

For Fe(0)-based reductant systems, mass-normalized rate constants (k_m values), as defined in equations 4-2 and 4-3, are frequently reported.

$$-\frac{d[C]}{dt} = k_m \rho_m [C] = k_{\text{obs}} [C] \quad (4-2)$$

$$k_m = \frac{k_{\text{obs}}}{\rho_m} \quad (4-3)$$

Values of k_m for 1,1,1,2-TeCA reduction [$k_m(1,1,1,2\text{-TeCA})$] are shown for NZVI, 0.05% Pd/NZVI and 0.35% Pd/NZVI in Figure 4-3 as a function of the molar ratio of 1,1,1,2-TeCA to NZVI-based reductant (i.e., $[1,1,1,2\text{-TeCA}]/[\text{Reductant}]$). Values of $k_m(1,1,1,2\text{-TeCA})$ in Figure 4-3 were calculated using data in Figure 4-1, where k_{obs} values in equation 2 were measured experimentally by varying ρ_m (0.03 – 0.56 g/L) and holding the initial concentration of 1,1,1,2-TeCA constant (176 μM) (data shown as solid symbols in Figure 4-3). Alternatively, values of k_m were also calculated using k_{obs} values

measured in experimental systems where the initial 1,1,1,2-TeCA concentration was varied (3.5 – 2000 μM) at a constant ρ_m (0.05 g/L) (data shown as open symbols in Figure 4-3).

For NZVI, as a consequence of the non-linear dependence of $k_{\text{obs}}(1,1,1,2\text{-TeCA})$ on ρ_m shown in Figure 4-1, $k_m(1,1,1,2\text{-TeCA})$ values differed depending on the approach used to measure k_{obs} values. For experiments varying ρ_m but using a constant initial 1,1,1,2-TeCA concentration, $k_m(1,1,1,2\text{-TeCA})$ decreased as the molar ratio of 1,1,1,2-TeCA to NZVI decreased (i.e., $k_m(1,1,1,2\text{-TeCA})$ decreased with increasing ρ_m). In contrast, $k_m(1,1,1,2\text{-TeCA})$ values from experimental systems with varying 1,1,1,2-TeCA concentration and constant ρ_m were nearly constant over the molar ratios explored. Consequently, at low 1,1,1,2-TeCA to NZVI molar ratios, $k_m(1,1,1,2\text{-TeCA})$ values varied by a factor of 20 depending on the experimental approach for measuring $k_{\text{obs}}(1,1,1,2\text{-TeCA})$ values.

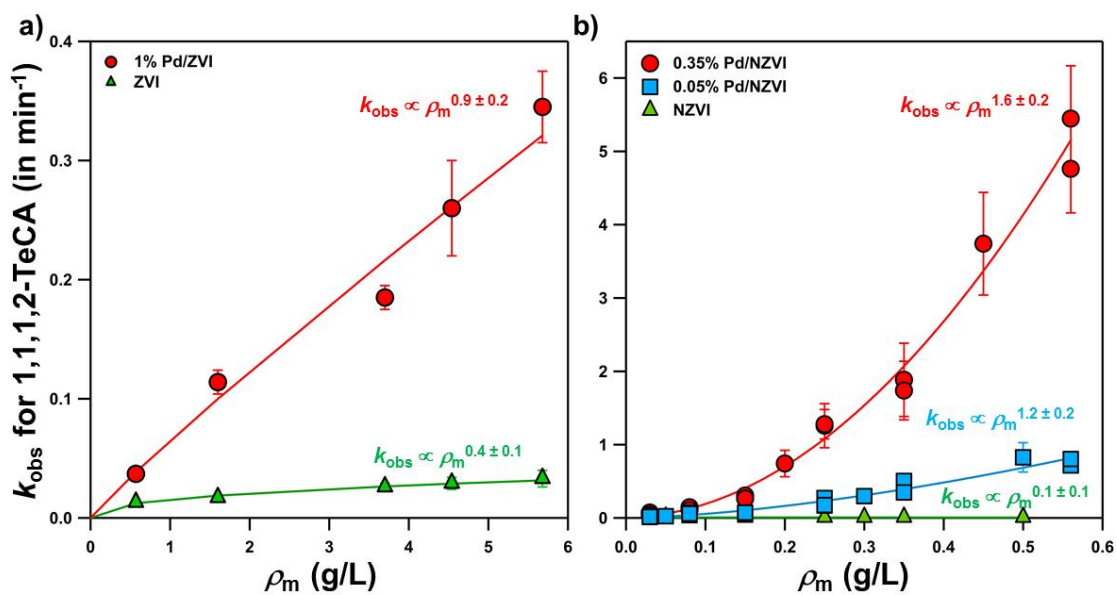


Figure 4-1. Change in the k_{obs} values for 1,1,1,2-TeCA reduction as a function of solid loading (ρ_m values) in systems with (a) ZVI and 1% Pd/ZVI and (b) NZVI, 0.05% Pd/NZVI and 0.35% Pd/NZVI. Reactions were at pH 8 in 25 mM HEPES buffer with 25 mM NaCl. Uncertainties represent 95% confidence intervals from regression analyses performed on semi-log plots of 1,1,1,2-TeCA concentration as a function of time, the slopes of which were used to obtain the k_{obs} values shown. Typical reactor-to-reactor variability is shown for NZVI, for which data represents k_{obs} values from duplicate experiments.

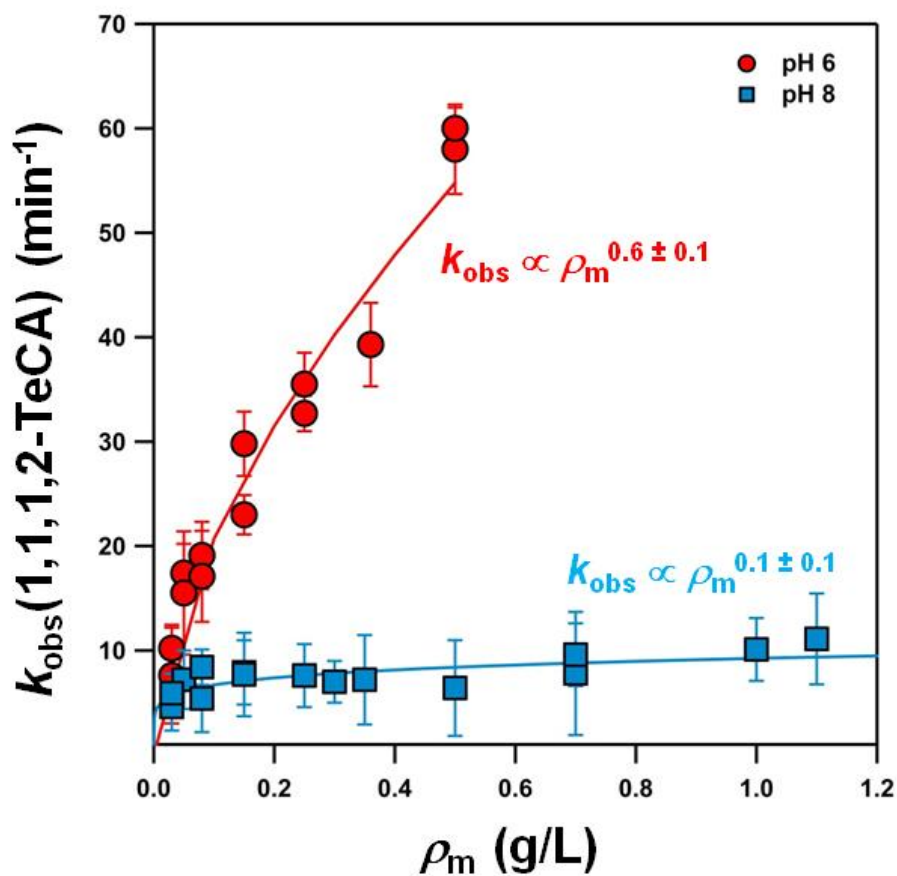


Figure 4-2. Change in the $k_{obs}(1,1,1,2\text{-TeCA})$ values over time for NZVI at pH 6 and 8. The functional relationship between $k_{obs}(1,1,1,2\text{-TeCA})$ and ρ_m is shown, obtained from best fit linear regression of $\log(k_{obs})$ versus $\log(\rho_m)$ plots. A decrease from pH 8 to pH 6 not only increases the rate constant for 1,1,1,2-TeCA transformation, it also increases the linearity of the relationship between $k_{obs}(1,1,1,2\text{-TeCA})$ values and ρ_m , consistent with a more uniformly reactive NZVI surface at lower pH values.

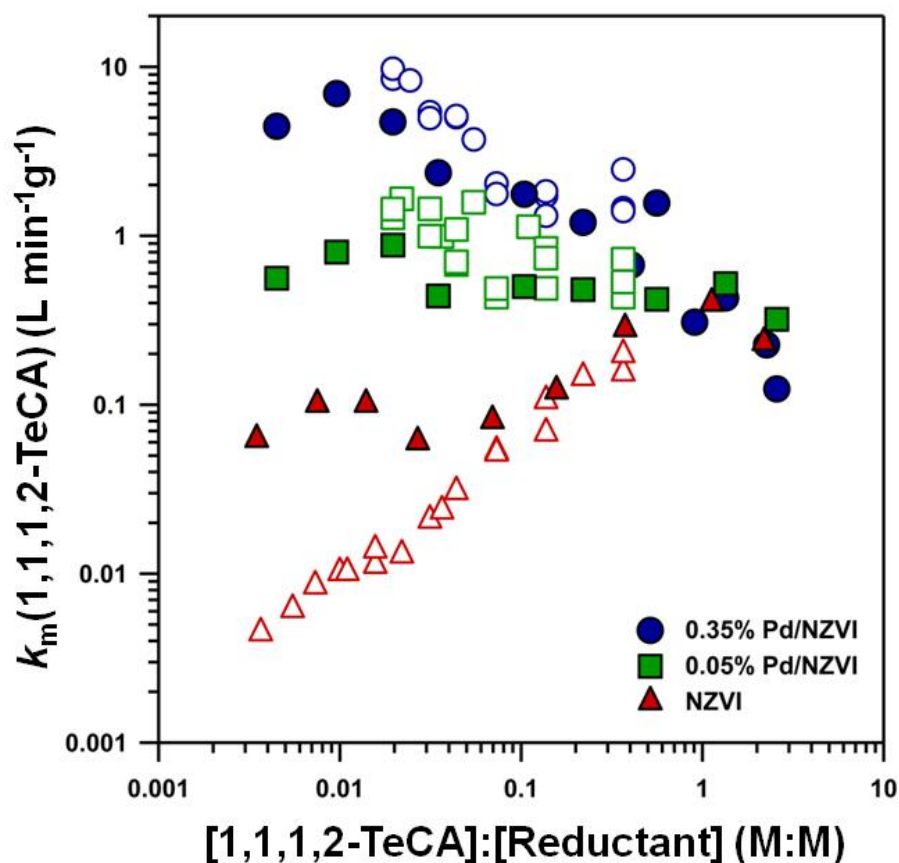


Figure 4-3. Change in mass-normalized rate constants for 1,1,1,2-TeCA reduction [$k_m(1,1,1,2\text{-TeCA})$ values] as a function of the molar ratio of the initial 1,1,1,2-TeCA concentration and iron-based reductant in NZVI (red symbols), 0.05% Pd/NZVI (green symbols) and 0.35% Pd/NZVI (blue symbols) systems. Open symbols represent $k_m(1,1,1,2\text{-TeCA})$ values calculated from $k_{\text{obs}}(1,1,2\text{-TeCA})$ values measured experimentally by holding the initial concentration of 1,1,1,2-TeCA constant at 175 μM while varying the reductant mass loading (or ρ_m value) between 0.03-0.6 g/L. Solid symbols represent $k_m(1,1,1,2\text{-TeCA})$ values calculated from $k_{\text{obs}}(1,1,2\text{-TeCA})$ values measured experimentally by holding the ρ_m value constant at 0.05 g/L and varying the initial 1,1,1,2-TeCA concentration from 3-2000 μM . All experiments were conducted at pH 8 in 25 mM HEPES buffer.

This difference in $k_m(1,1,1,2\text{-TeCA})$ values indicates that conditions unique to experimental systems with high ρ_m must limit NZVI reactivity. We attribute the diminished reactivity at high ρ_m to the disproportionate formation of inhibitory corrosion products in such systems. In closed systems with high NZVI concentrations, solubility limits for ferrous (Fe(II)) and ferric (Fe(III)) iron corrosion products will be achieved quickly, in turn causing greater accumulation of passive corrosion products on the NZVI particle surface. This scenario is also likely responsible for the non-linear relationship between ρ_m and k_{obs} in granular ZVI systems observed herein (Figure 4-1a) and elsewhere [25]. In fact, the greater independence of k_{obs} values on ρ_m in NZVI systems is likely due to the orders of magnitude greater corrosion rates reported for these materials relative to larger Fe(0) particles [26-28].

Evidence supporting greater NZVI passivation in systems with high ρ_m was obtained by examining the influence of pH on the relationship between k_{obs} and ρ_m . Figure 4-2 shows that k_{obs} values exhibit a greater, albeit still non-linear, dependence on NZVI loading at pH 6, at which the solubility of Fe(II) is orders of magnitudes greater than pH 8. This behavior agrees with reports for Fisher electrolytic iron [25] in which the relationship between k_{obs} for 1,1,1-trichloroethane reduction and ρ_m became essentially first-order at low pH. Thus, as pH decreases, the constraint of Fe(II) solubility at high ρ_m values is relieved, slowing corrosion production accumulation on the NZVI surface and in turn producing a more linear, near-first-order dependence of k_{obs} on ρ_m .

**Trends in mass-normalized rate constants for 1,1,1,2-TeCA reduction
by Pd/NZVI**

For 0.05% Pd/NZVI, relatively constant $k_m(1,1,1,2\text{-TeCA})$ values were measured over the entire range of molar ratios investigated. Moreover, $k_m(1,1,1,2\text{-TeCA})$ values in 0.05% Pd/NZVI systems were essentially equivalent whether data were collected by experimentally varying ρ_m or initial 1,1,1,2-TeCA concentration. Notably, the agreement in $k_m(1,1,1,2\text{-TeCA})$ values holds even at low [1,1,1,2-TeCA] to [0.05% Pd/NZVI] ratios where $k_m(1,1,1,2\text{-TeCA})$ values from NZVI systems diverged considerably [e.g., compare $k_m(1,1,1,2\text{-TeCA})$ values for NZVI and 0.05% Pd/NZVI at a molar ratio of 0.02-0.03].

The consistency of $k_m(1,1,1,2\text{-TeCA})$ values measured in 0.05% Pd/NZVI systems suggests that addition of Pd makes the reductant surface less susceptible to the passivation mechanisms occurring in high ρ_m NZVI systems. Because rates of Fe(II) production were equivalent in the NZVI and Pd/NZVI systems explored herein (Figure 4-4), the extent of insoluble corrosion product formation should be comparable in both systems. However, the corrosion products appear less effective at passivating the 0.05% Pd/NZVI surface relative to NZVI, at least over the timescales of our experiments exploring the influence of ρ_m .

Finally, because k_{obs} values increase in a parabolic fashion with respect to ρ_m in 0.35% Pd/NZVI systems, values of $k_m(1,1,1,2\text{-TeCA})$ decrease as the molar ratio of [1,1,1,2-TeCA] to [Pd/NZVI] increases. Values of $k_m(1,1,1,2\text{-TeCA})$ were in agreement regardless of whether initial values of [1,1,1,2-TeCA] or ρ_m was varied experimentally.

Consequently, the reactivity of 0.35% Pd/NZVI is greatest with excess Pd/NZVI and diminished in systems with excess 1,1,1,2-TeCA.

From a practical perspective, Figure 4-3 shows that in systems with roughly equimolar concentrations of 1,1,1,2-TeCA and NZVI-based reductant, $k_m(1,1,1,2\text{-TeCA})$ values are roughly equivalent for all reductants. We acknowledge that under such conditions, assumptions of the pseudo-first order model used to obtain $k_{\text{obs}}(1,1,1,2\text{-TeCA})$ values from which $k_m(1,1,1,2\text{-TeCA})$ fail, but comparison of 1,1,1,2-TeCA concentration loss over time (Figure 4-5) clearly reveals equivalent reactivity of Pd/NZVI and NZVI as the molar ratio of 1,1,1,2-TeCA to reductant approaches unity. Thus, little, if any, reactivity enhancement is provided by Pd/NZVI when it is not present in excess. Possible explanations for the equivalent reactivity of Pd/NZVI and NZVI could be surface site limitation resulting at such high solvent concentrations, or that Pd/NZVI reductants are more susceptible to surface passivation in the presence of such high concentrations of 1,1,1,2-TeCA, which represents a relatively strong oxidant.

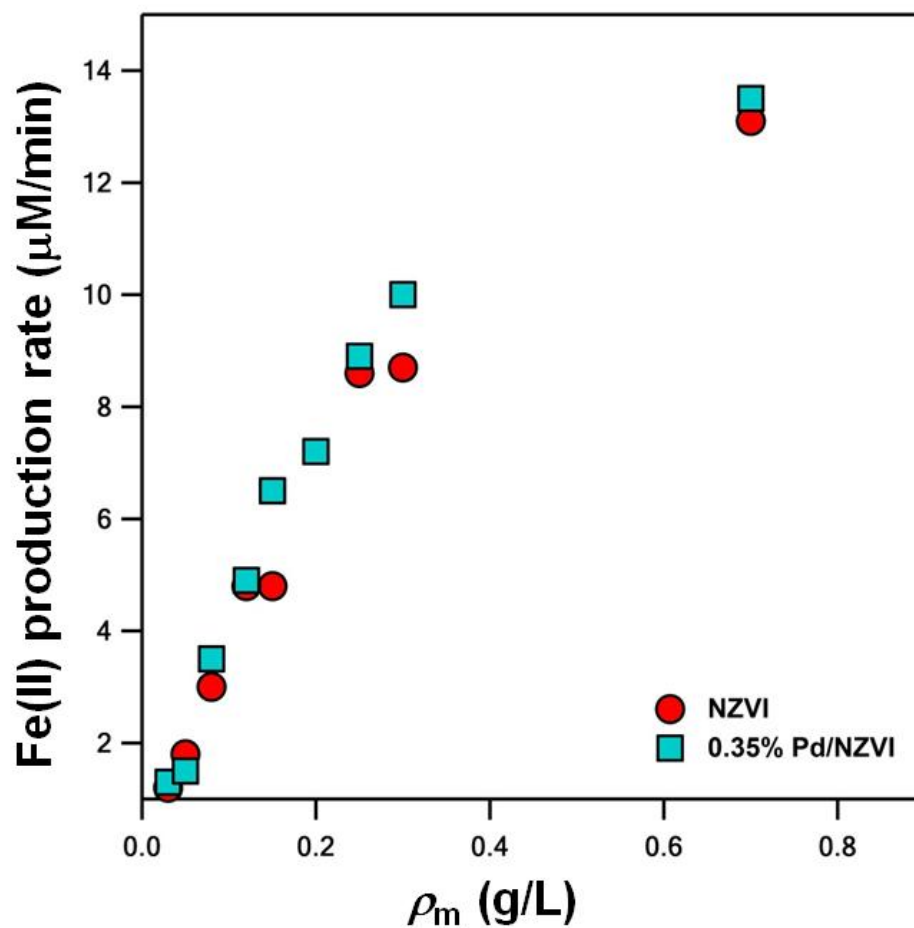


Figure 4-4. Change in Fe(II) production rate for NZVI and 0.35% Pd/NZVI as a function of ρ_m value. Fe(II) production rates were determined from the slopes of best-fit linear regression analyses of Fe(II) concentration over time in 1 g/L suspensions of each material at pH 8. Fe(II) concentration data were collected over the first 15 minutes of NZVI-based reductant dissolution, such that rates reflect initial rates of Fe(II) production. Regression analyses typically resulted in best-fit linear relationships with R^2 values greater than 0.95. Essentially no difference in Fe(II) production rate was observed for any of the NZVI-based reductants explored in this work.

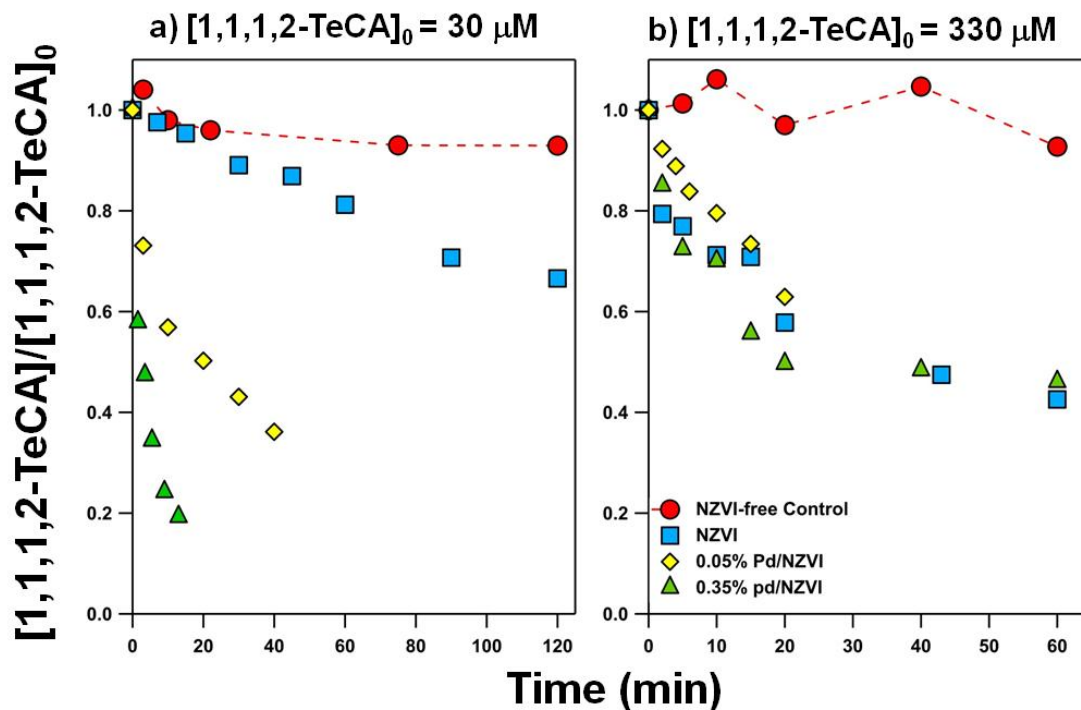


Figure 4-5. Change in normalized 1,1,1,2-TeCA concentration as a function of time in NZVI, 0.05% Pd/NZVI, and 0.35% Pd/NZVI suspensions. Data are shown for an initial 1,1,1,2-TeCA concentration of (a) 30 μM and (b) 330 μM . All experiments were conducted at a ρ_m value of 0.05 g/L and at pH 8 in 25 mM HEPES/25 mM NaCl solution. Data are also shown for NZVI-free control reactors, in which small amounts of 1,1,1,2-TeCA loss were observed due to sorption to the septa used to seal reactors. Where a clear influence of Pd loading on 1,1,1,2-TeCA decay rate is observed in reactors with initially 30 mM 1,1,1,2-TeCA, the reactors with a higher initial concentration exhibit no clear influence of Pd on the reactivity of NZVI-based reductants toward 1,1,1,2-TeCA.

Solvent Kinetic Isotope Effects for 1,1,1,2-TeCA Reduction by NZVI and Pd/NZVI

Figure 4-6 shows plots of $\ln[1,1,1,2\text{-TeCA}]$ versus time in NZVI, 0.05% Pd/NZVI and 0.35% Pd/NZVI systems in H_2O and D_2O at pH 8. Semi-log concentration versus time plots are shown for two different ρ_m values (0.03 and 0.6 g/L) for each reductant. No significant SKIE was observed in unamended NZVI systems at the ρ_m values explored, with essentially equivalent loss of 1,1,1,2-TeCA over time in H_2O and D_2O solutions. For 0.05% Pd/NZVI, systems at a ρ_m value of 0.03 g/L also did not exhibit an appreciable SKIE, although at the higher reductant loading of 0.6 g/L a clear reactivity differences was observed between H_2O and D_2O systems, resulting in a measured SKIE [$k_{\text{obs}}(\text{H}_2\text{O})/k_{\text{obs}}(\text{D}_2\text{O})$] of 4. For 0.35% Pd/NZVI, both low and high ρ_m values produced obvious SKIEs, but the magnitude of the effect was considerably greater (SKIE of ~20) at 0.6 g/L relative to 0.03 g/L (SKIE of 2.3).

These SKIE measurements clearly indicate that different processes govern 1,1,1,2-TeCA reduction in NZVI and Pd/NZVI systems. Moreover, the range in magnitude of SKIEs observed for Pd/NZVI systems as a function of Pd loading and ρ_m value support a scenario in which multiple mechanisms or reactive entities are likely responsible for 1,1,1,2-TeCA reduction by Pd/NZVI, and that system conditions appear to influence the relative contribution of these parallel reduction pathways.

Figure 4-7 presents measured values of SKIEs as a function of the corresponding REF observed in different Pd/NZVI systems. Data are shown for 0.05% and 0.35% Pd/NZVI reacted over a range of ρ_m values at pH 8. In Figure 4-7, two distinct regimes

for SKIEs as a function of REF are observed. The first regime is characterized by a relatively slight rate of increase in SKIE for REFs up to ~100, while the second regime displays a much steeper rate of increase in SKIE as REFs exceed 100.

We believe the regime of large magnitude of SKIEs (≥ 4) corresponds to conditions where some form of atomic hydrogen (i.e., adsorbed or absorbed H) is primarily involved in 1,1,1,2-TeCA reduction. As in Figure 4-5, the largest SKIEs were observed at high Pd loadings and high ρ_m values. In closed batch systems, these conditions promote the formation and accumulation of atomic hydrogen, a product of iron corrosion and intermediate in H₂ production, at the reductant particle surface. Indeed, the much smaller to non-existent SKIE values observed at REFs up to almost two orders of magnitude suggests that some other mechanism must also be able to enhance rates of 1,1,1,2-TeCA reduction by Pd/NZVI under conditions when accumulation of H on the reductant surface is less favorable (i.e., at low Pd loading and low ρ_m values).

We propose that rate enhancement in the lower SKIE regime arises from the formation of a galvanic couple between deposited Pd and the underlying metallic NZVI particle core. As shown in Figure 4-8, displacement plating produces numerous 3-4 nm Pd nanoparticles widely distributed on NZVI particles at both 0.5 and 0.35% Pd concentration. On freshly prepared Pd/NZVI, these Pd nanodeposits represent more ideal sites for electron transfer to 1,1,1,2-TeCA than surface oxides, which will predominate on NZVI particles at pH 8. Thus, their addition to the NZVI surface should enhance 1,1,1,2-TeCA reduction without the involvement of atomic hydrogen species. A line of evidence in support of such a scenario is a relatively strong, first-order correlation between

$k_{\text{obs}}(1,1,1,2\text{-TeCA})$ values and measured Fe(II) production rates for Pd/Fe systems within the low SKIE value regime (Figure 4-9), behavior that was not observed for NZVI.

This scenario is also analogous to the rate enhancement typically observed in Fe(0) systems pretreated via acid-washing or in response to a decrease in suspension pH, both of which will thin the surface oxide layer so as to enhance electron transfer from the metallic Fe(0) core. For several ρ_m values of NZVI at pH 6, we examined SKIEs as a function of the rate increase achieved from a decrease in suspension pH from pH 8 to pH 6 (defined as $\text{REF}_{\text{pH}} = k_{\text{obs}}(\text{pH } 6)/k_{\text{obs}}(\text{pH } 8)$). Over the ρ_m values investigated, a decrease from pH 8 to 6 produced as much as a 6-fold increase in reactivity. Notably, however, SKIEs did not increase significantly above 1, indicated as the dashed line in Figure 4-7, which is comparable to those values observed for Pd/NZVI systems with low Pd and low ρ_m values.

The shift in 1,1,1,2-TeCA reduction from primarily a galvanic couple promoted pathway to a reaction with atomic H likely depends on the available mass of Pd to serve as a reservoir for atomic H. The average size of Pd deposits (determined by TEM) was identical for 0.05% and 0.35% Pd/NZVI (Figure 4-8), although the Pd distribution on 0.05% Pd/NZVI was generally more heterogeneous (see white arrows in Figure 4-8b where little to no Pd islands were observed for 0.05% Pd/NZVI) relative to more uniformly coated 0.35% Pd/NZVI particles. Collectively, TEM analysis suggests that the total of mass of Pd in the system and not the size of individual Pd islands dictates accumulation of H in Pd/NZVI systems.

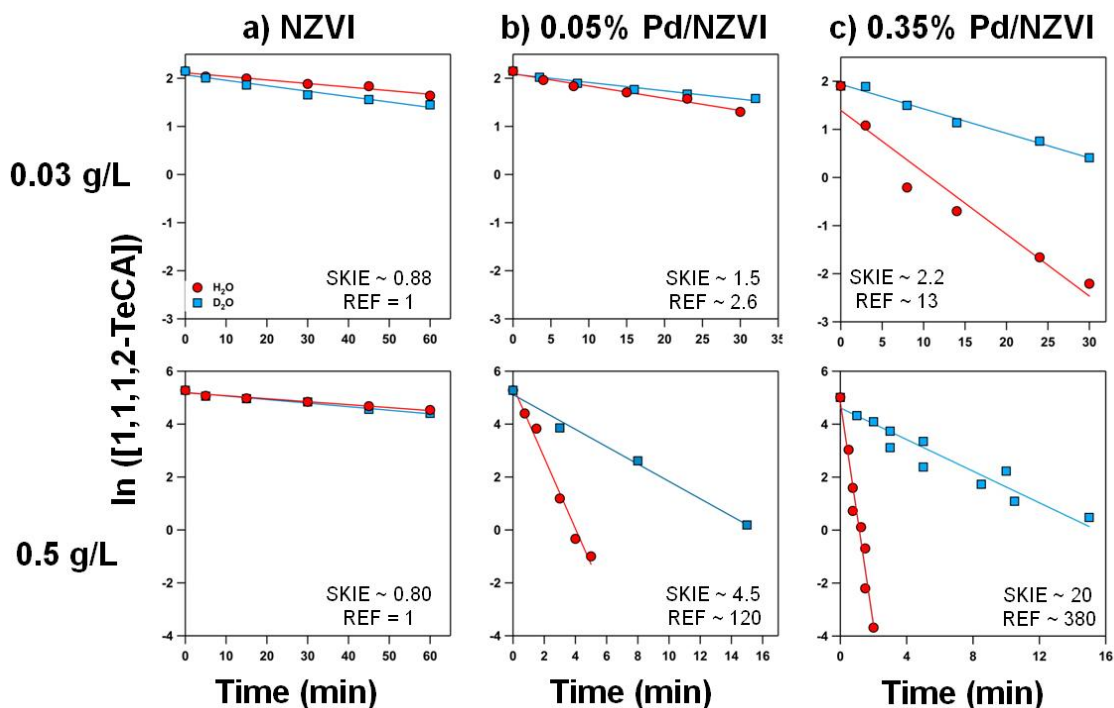


Figure 4-6. Semi-log plots of 1,1,1,2-TeCA concentration versus time for (a) NZVI, (b) 0.05% Pd/NZVI, and (c) 0.35% Pd/NZVI. Data are shown for experiments conducted in H₂O and D₂O solutions, as well as for two ρ_m values (0.03 and 0.5 g/L). All experiments were conducted at pH 8 using the same molar ratio (0.019 M:M) of initial 1,1,1,2-TeCA to NZVI-based reductant. Data at each ρ_m value are shown on the same y-axis scale for ease of comparison. Measured SKIEs and REFs are provided for each system, clearly illustrating the lack of solvent isotope effects in NZVI systems and their increase in magnitude with increasing Pd loading and ρ_m value.

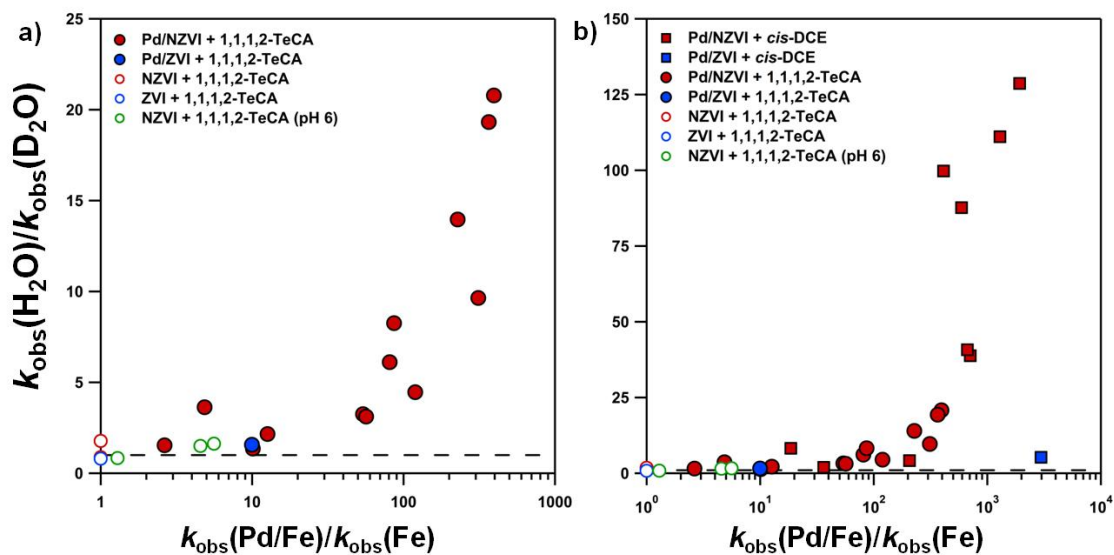


Figure 4-7. Correlation between solvent kinetics isotope effect [$k_{\text{obs}}(\text{H}_2\text{O})/k_{\text{obs}}(\text{D}_2\text{O})$] and reactivity enhancement factor [$k_{\text{obs}}(\text{Pd}/\text{Fe})/k_{\text{obs}}(\text{Fe})$] for (a) the reduction of 1,1,1,2-TeCA and (b) the reduction of *cis*-DCE (note that data for 1,1,1,2-TeCA are also shown for comparison). Data presented were collected at different ρ_m values in a variety of Fe(0) and Pd/Fe based reductant systems, as indicated in the key. The majority of data were collected at pH 8, although in panel (a) data for NZVI are also presented to illustrate the SKIE achieved with a the rate increase associated with a change from pH 8 to pH 6 (open circles in green). For this data collected at pH 6, the magnitude of rate enhancement (shown on the x-axis) was by normalizing the $k_{\text{obs}}(1,1,1,2\text{-TeCA})$ value at pH 6 to the corresponding value measured in an otherwise identical pH 8 suspension.

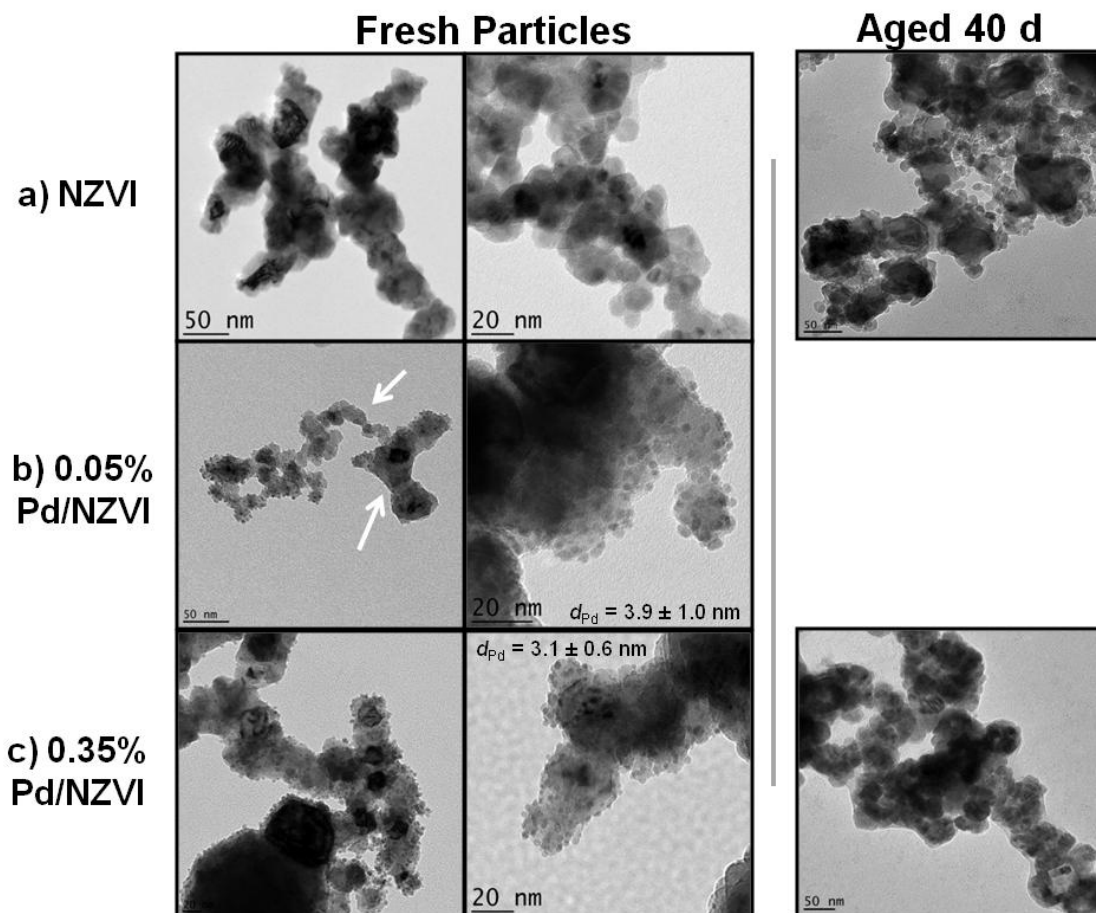


Figure 4-8. Representative TEM images of (a) NZVI, (b) 0.05% Pd/NZVI, and (c) 0.35% Pd/NZVI. Images are shown for freshly prepared NZVI and Pd/NZVI reductants (left panel) as well as after 40 days of aging in 2 g/L suspensions at pH 8. The pH of aged suspensions was maintained with 25 mM HEPES buffer prepared in 25 mM NaCl. Arrows for freshly prepared 0.05% Pd/NZVI indicate regions on the particle surface where surface deposits of Pd were not evident, supporting a more heterogeneous distribution at lower Pd loadings. Notably, the diameter of Pd deposits (d_{Pd} , determined from sizing of at least 100 particles with TEM) was equivalent for both 0.05 and 0.35% Pd/NZVI particles.

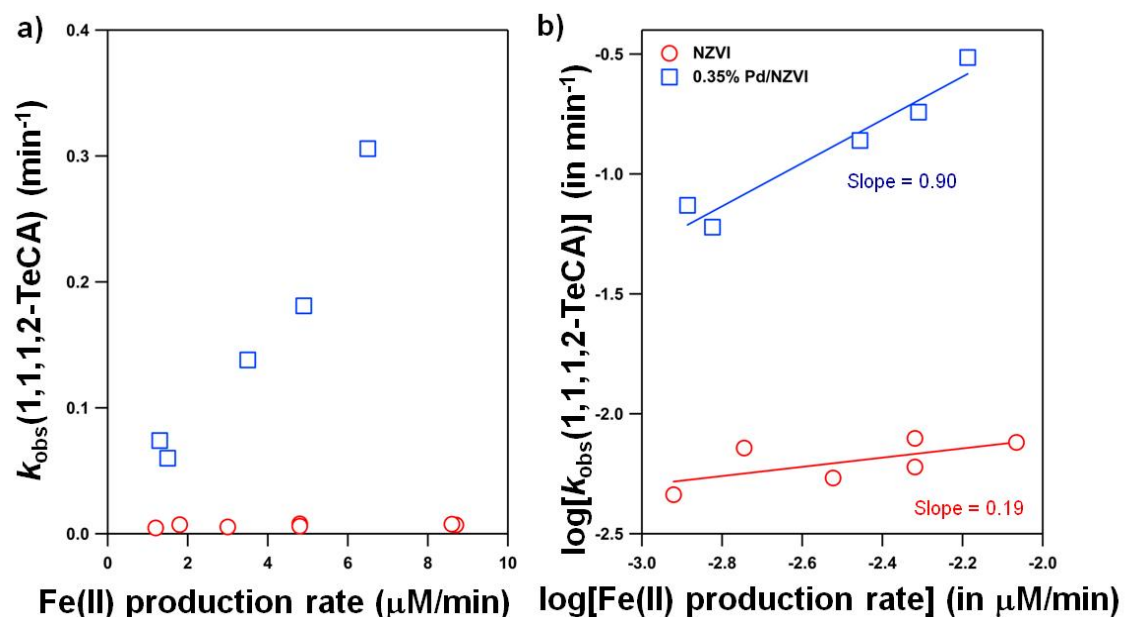


Figure 4-9. Plot of $k_{\text{obs}}(1,1,1,2\text{-TeCA})$ as a function of Fe(II) production rate for NZVI and 0.35% Pd/NZVI shown on (a) linear and (b) logarithmic scales. Values of $k_{\text{obs}}(1,1,1,2\text{-TeCA})$ and Fe(II) production rate were measured at pH 8 over a range of ρ_{m} values from 0.03-0.7 g/L, for which only the subset of data (from 0.03-0.15 g/L) producing a linear, first-order relationship between these variables for Pd/NZVI are shown. The correlation between $k_{\text{obs}}(1,1,1,2\text{-TeCA})$ and Fe(II) production rate at low ρ_{m} values is consistent with a mechanism for rate enhancement of 1,1,1,2-TeCA reduction involving formation of a galvanic cell between deposited Pd and Fe(0) in the NZVI particle core.

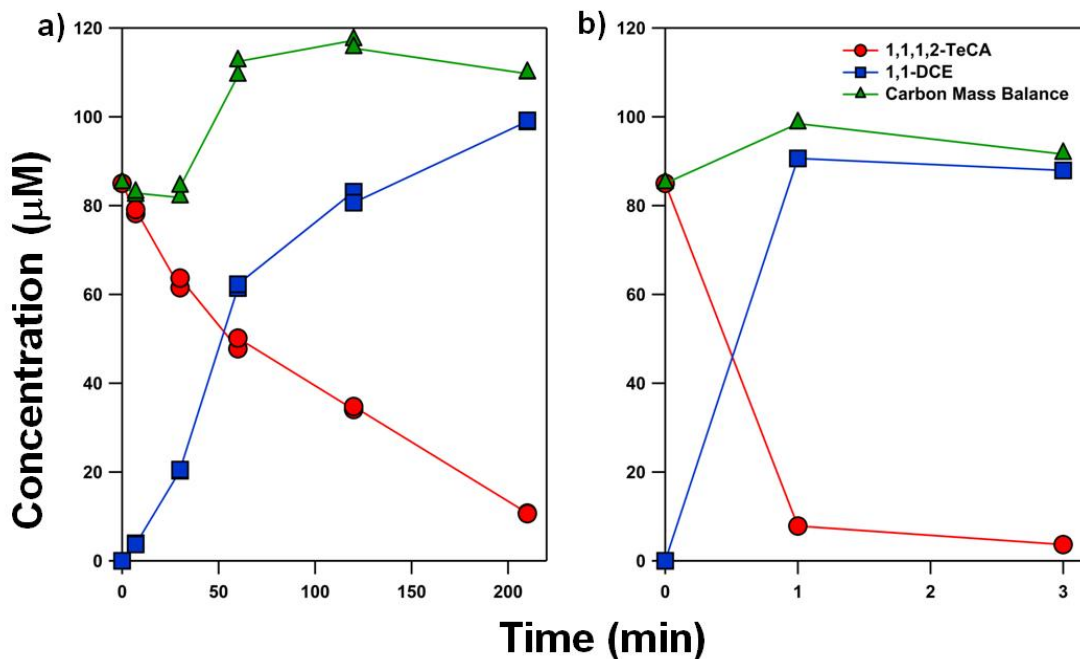


Figure 4-10. Concentration profiles for 1,1,1,2-TeCA decay and formation of 1,1-dichloroethylene (1,1-DCE), the only reduction production observed from 1,1,1,2-TeCA transformation in both Fe(0) and Pd/Fe systems. Concentration data for 1,1,1,2-TeCA and 1,1-DCE are shown for (a) NZVI and (b) 0.35% Pd/NZVI at pH 8 and a ρ_m value of 0.22 g/L. Also shown are carbon mass balances over time in these systems, which were generally greater than 95% for experiments conducted herein. Thus, 1,1,1,2-TeCA transformation occurred entirely by reductive β -elimination in all reductant systems, regardless of the presence of Pd on the Fe(0) particle surface.

Finally, we note that despite strong evidence for multiple mechanism for 1,1,1,2-TeCA reduction in Pd/NZVI systems, there was no observable change in reduction product formation. Reduction of 1,1,1,2-TeCA yielded 1,1-dichloroethene via reductive β -elimination in NZVI and all Pd/NZVI systems (Figure 4-10). The only difference for Pd/NZVI was that 1,1-DCE was then rapidly degraded to ethane and ethylene, which was not observed in unamended NZVI systems.

Solvent Kinetic Isotope Effects for cis-DCE Reduction by NZVI and Pd/NZVI

For *cis*-DCE reduction by NZVI, a solvent isotope was observed but was not quantifiable. As shown in Figure 4-11 for a 0.6 g/L NZVI suspension, *cis*-DCE decay was observed in H₂O, but the *cis*-DCE loss in D₂O was equivalent to that observed in NZVI-free controls, in which modest loss of *cis*-DCE (~ 1% per h) occurred via sorption onto septa used to seal our reactors (Figure 4-11). This observation is in contrast to 1,1,1,2-TeCA, for which SKIEs were not observed during reduction by NZVI.

In Pd/NZVI systems, significant SKIEs were observed for *cis*-DCE reduction. As with 1,1,1,2-TeCA, SKIEs were not constant, but rather increased with increasing Pd loading and Pd/NZVI concentration (Figure 4-12). Using initial $k_{\text{obs}}(\textit{cis}\text{-DCE})$ values measured in NZVI systems (the first 60 minutes of decay as shown in Figure 4-11), measured SKIE values for *cis*-DCE reduction by Pd/NZVI were also evaluated as a function of the REF achieved with Pd/NZVI relative to unamended NZVI. Figure 4-7b shows that SKIE values for *cis*-DCE as a function of REF agree well with the trends

observed for 1,1,1,2-TeCA, with low SKIEs corresponding to relatively low REFs and SKIE values increasing rapidly as REFs exceed 100.

The general agreement in SKIE data as a function of REF for 1,1,1,2-TeCA and *cis*-DCE suggests that the same reduction mechanisms are operative for both compounds; as previously hypothesized, low SKIEs likely correspond to *cis*-DCE reduction primarily via galvanic electron transfer through Pd from Fe(0), whereas larger SKIEs are consistent with atomic hydrogen as the primary reductant for *cis*-DCE. However, measured SKIE values at a specific Pd loading and ρ_m value were consistently considerably greater for *cis*-DCE than 1,1,1,2-TeCA. For example, in 0.5 g/L suspensions of 0.35% Pd/NZVI, SKIE values for 1,1,1,2-TeCA and *cis*-DCE are 20 and 400 respectively. Thus, in otherwise identical experimental systems, in which we assume equal concentrations of surface associated atomic hydrogen are available, *cis*-DCE appears most prone to reduction. This could simply reflect a greater affinity for atomic hydrogen reaction at a sp^2 hybridized carbon center arising from the π -bond of *cis*-DCE relative to the fully saturated sp^3 hybridized carbon center on 1,1,1,2-TeCA.

Solvent Kinetic Isotope Effects in ZVI Systems

For comparison to NZVI-based reductants, a limited number of experiments explored SKIEs for 1,1,1,2-TeCA and *cis*-DCE reduction in ZVI and Pd/ZVI systems. For 1,1,1,2-TeCA reduction by ZVI, equivalent rates of 1,1,1,2-TeCA decay were observed in H₂O and D₂O systems (Figure 4-13a), consistent with results for NZVI. Values of SKIE were also measured for 1% Pd/ZVI, which enhanced 1,1,1,2-TeCA

reduction by roughly 10-fold (an REF comparable to that reported by Cwiertny *et al.* [10] for Pd/ZVI toward 1,1,1-TCA, also an alkyl polyhalide). In 1% Pd/ZVI systems (Figure 4-13b), an essentially negligible SKIE of 1.6 was observed, in good agreement with trends in SKIE as a function of REF developed for Pd/NZVI systems (Figure 4-7a). Unlike Pd/NZVI suspensions, however, Cwiertny *et al.* [10] showed that this 10-fold REF for alkyl polyhalide reduction represents a maximum for this particular Pd/ZVI formulation. Thus, Pd/ZVI reactivity toward 1,1,1,2-TeCA appears constrained to the low SKIE regime in Figure 4-7a, consistent with atomic hydrogen playing a less important role in ZVI suspensions relative to NZVI systems.

As reported previously [10], the rate of *cis*-DCE reduction by this lot of Fisher electrolytic iron was too slow to furnish a measurable rate constant, thus SKIEs were not measurable in ZVI suspensions. However, in systems with 1% Pd/ZVI, *cis*-DCE was rapidly degraded, exhibiting a half-life of 6 minutes. Using estimates of the rate constant for *cis*-DCE reduction by ZVI described by Cwiertny *et al.* [10], this corresponds to a REF of at least 3000, a value far exceeding the REF for 1% Pd/ZVI reduction of 1,1,1,2-TeCA and any REFs previously reported herein for 1,1,1,2-TeCA or *cis*-DCE reduction by Pd/NZVI. Despite this large REF, a relatively small SKIE of 5.3 was measured via comparison of *cis*-DCE decay in H₂O and D₂O suspensions (Figure 4-14). In Figure 4-7b, this SKIE and REF value deviate considerably from the trend developed for NZVI-based reductants, suggesting different molecular-level processes govern *cis*-DCE reduction in NZVI- and ZVI-based reductant systems, although the same reduction products (ethane and ethane) were observed in each case. Based on trends in SKIE values, it appears that

reduction of *cis*-DCE by Pd/ZVI proceeds primarily via appears via a pathway that does not include atomic hydrogen. Although the mechanistic details for *cis*-DCE in Pd/ZVI and Pd/NZVI suspensions are not yet entirely clear, distinct rate-determining steps must govern *cis*-DCE reduction in each system.

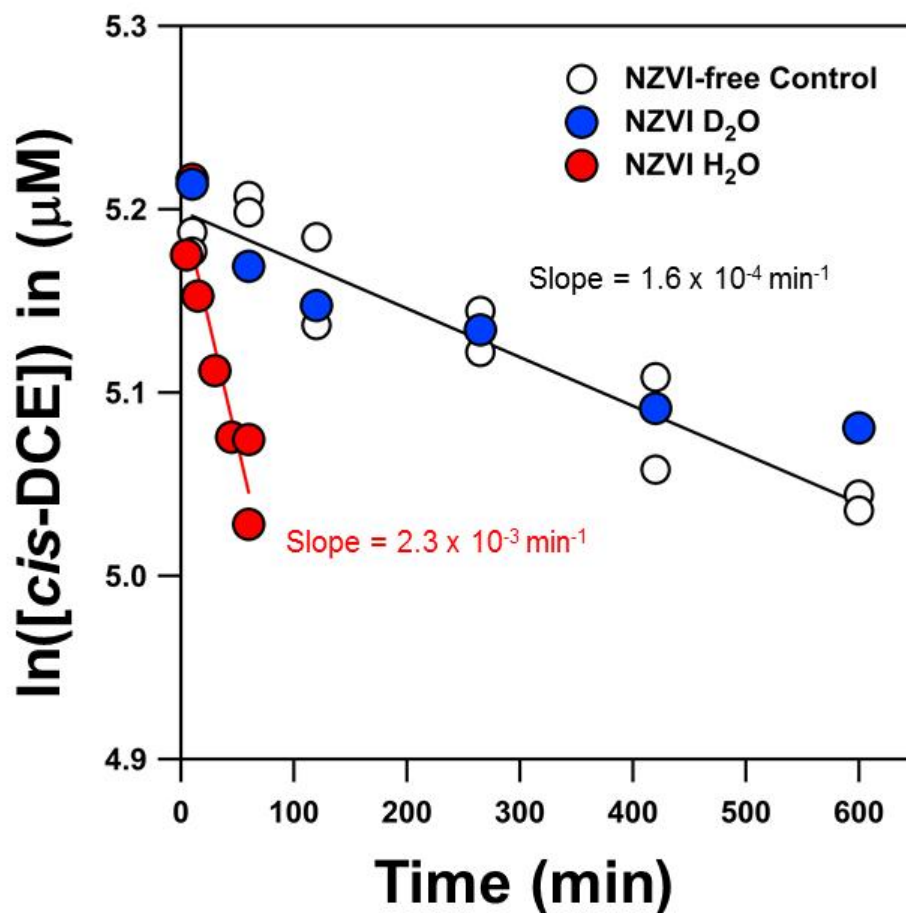


Figure 4-11. Plots of \ln *cis*-DCE concentration as a function of time in NZVI suspensions of H₂O and D₂O. Experiments were conducted at 0.6 g/L NZVI with initial *cis*-DCE concentration of 176 μ M in 25 mM HEPES/25 mM NaCl solutions at pH 8. Data are also shown for a NZVI-free control system, in which a modest amount of loss (~1% by mass per h) was observed due to sorption to septa. Loss of *cis*-DCE in NZVI H₂O systems was significant (an order of magnitude greater than loss in controls based on slopes obtained from linear regression analyses). However, loss of *cis*-DCE in NZVI D₂O systems was equivalent to controls. The observation of a solvent kinetic isotope effect for *cis*-DCE reduction by NZVI is in contrast to results for 1,1,1,2-TeCA, for which a lack of SKIE was observed via reduction by NZVI in identical experimental systems.

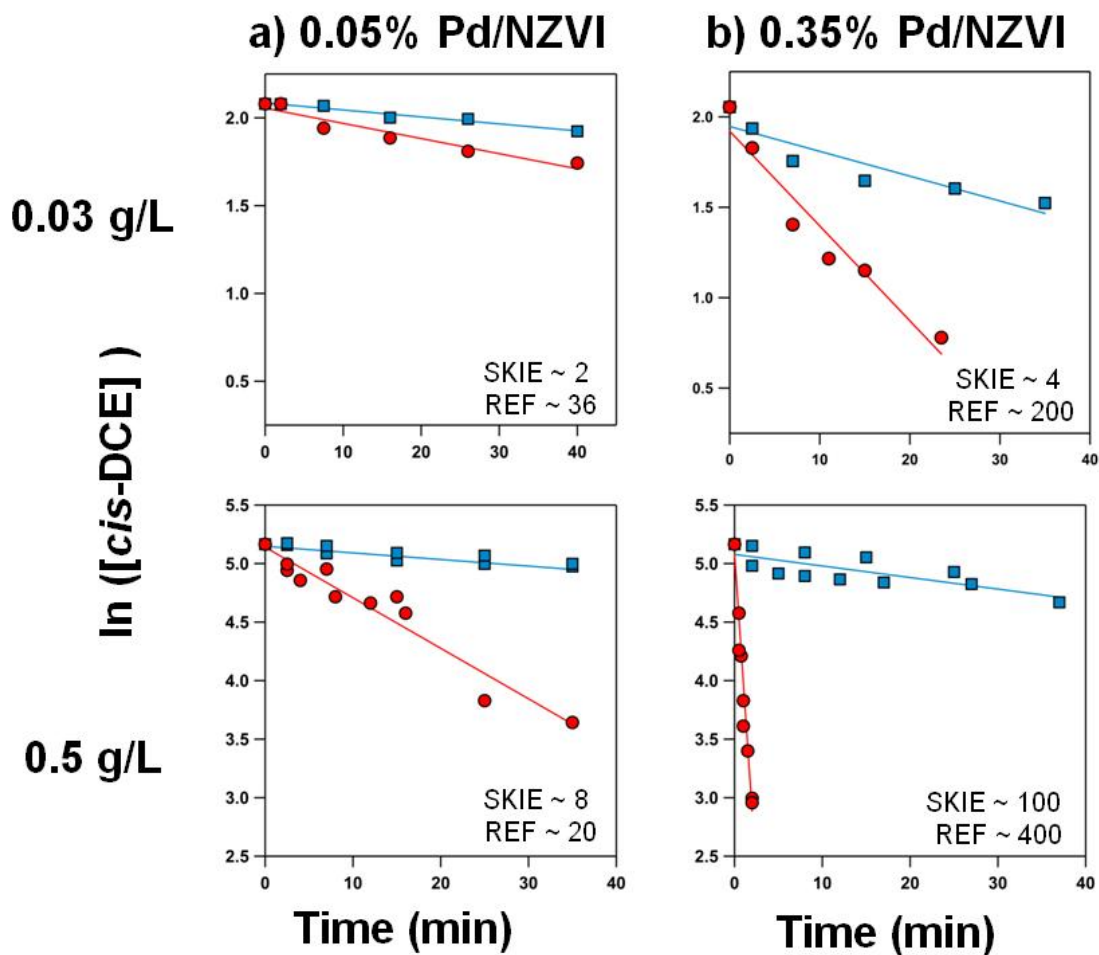


Figure 4-12. Semi-log plots of *cis*-DCE concentration versus time for (a) 0.05% Pd/NZVI and (b) 0.35% Pd/NZVI. Data are shown for experiments conducted in H₂O and D₂O solutions, as well as for two ρ_m values (0.03 and 0.5 g/L). All experiments were conducted at pH 8 using the same molar ratio (0.018 M : M) of initial *cis*-DCE to NZVI-based reductant. Data at each ρ_m value are shown on the same y-axis scale for ease of comparison. Measured SKIEs and REFs are provided for each system, clearly illustrating the increase in SKIE magnitude with increasing Pd loading and ρ_m value.

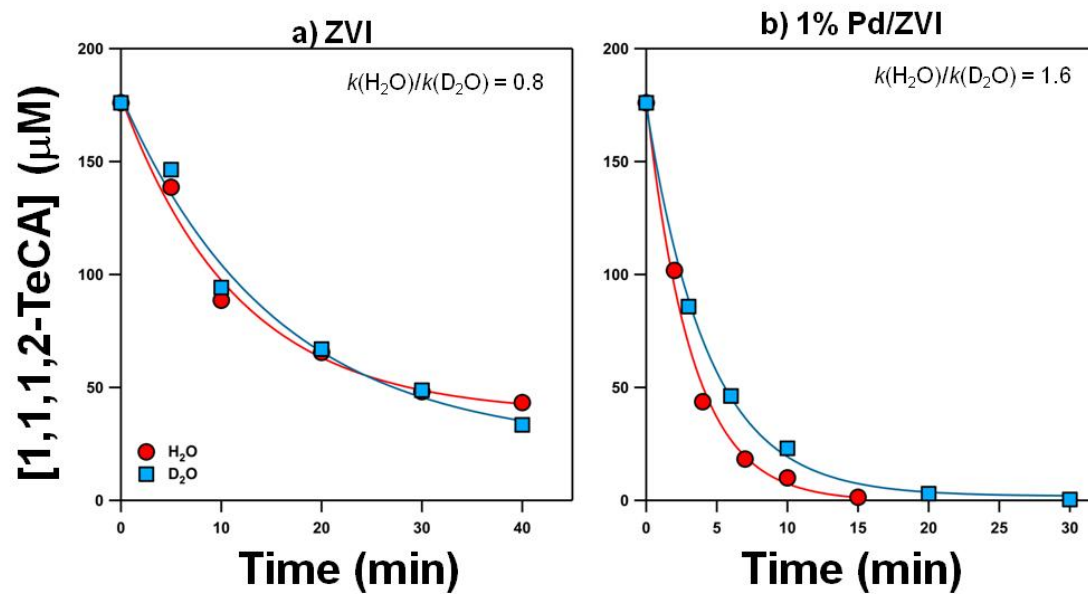


Figure 4-13. Change in 1,1,1,2-TeCA concentration as a function of time in suspensions of (a) ZVI and (b) 1% Pd/ZVI. Reactions were conducted in 5.7 g/L suspensions prepared at pH 8 in H₂O and D₂O. Experiments used an initial 1,1,1,2-TeCA concentration of 176 μM.

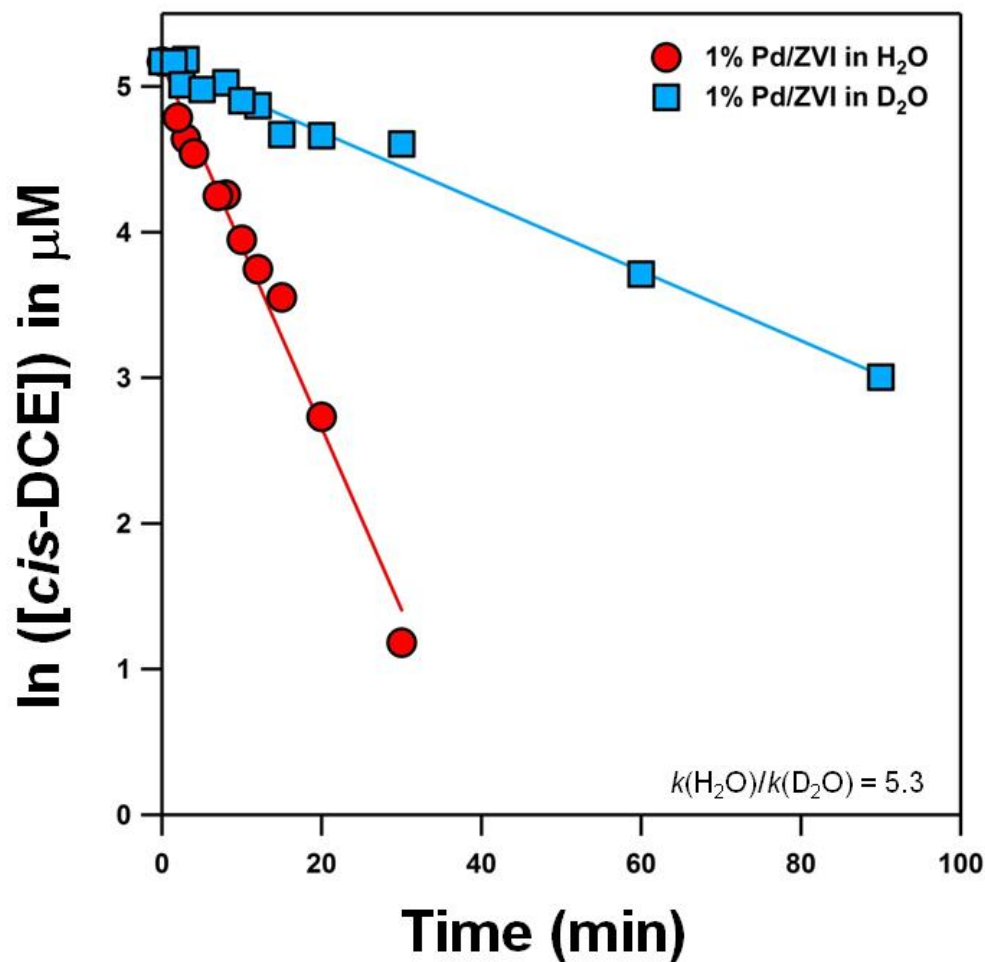


Figure 4-14. Natural log of *cis*-DCE concentration as a function of time for 1% Pd/ZVI prepared in H₂O and D₂O suspensions of 5.7 g/L. Experiments used an initial concentration of *cis*-DCE at 175 μM at pH 8 (25 mM HEPES/25 mM NaCl).

4. 5. Implications for Pd/NZVI Applications

Our results support multiple mechanisms for chlorinated solvent reduction, either involving direct electron transfer or via reaction with atomic hydrogen, occurring in Pd/NZVI systems. To evaluate if the relative importance of these mechanisms evolves over time during Pd/NZVI application, we measured SKIEs for NZVI and 0.35% Pd/NZVI particles aged for up to one month at pH 8. As shown in Figure 4-15, the reactivity of 0.35% Pd/NZVI, measured in both H₂O and D₂O solutions, decreased nearly 50-fold over two weeks and then remained essentially constant for the remainder of the month long aging study. In contrast, the reactivity of bare NZVI, while initially far less than 0.35% Pd/NZVI, exhibited only modest amounts of reactivity loss over 30 days.

As anticipated from earlier results, negligible SKIEs were observed in NZVI systems over the duration of aging. In contrast, significant SKIEs were measured in 0.35% Pd/NZVI systems during the first 10 days of aging, but the magnitude of SKIE decreased over time, ultimately approaching the magnitude of SKIEs observed in NZVI systems. Notably, the decrease in SKIE for Pd/NZVI coincides with the timescales of greatest reactivity loss.

If we use measured SKIEs to assess the dominant mechanism of 1,1,1,2-TeCA transformation, atomic hydrogen species only appear to be active in Pd/NZVI systems on the order of one or two weeks. The concomitant decrease in reactivity and SKIEs over this time likely arises from the growth of surface oxides on the reductant surface that bury deposited Pd and in turn limit the production, accumulation and access to solution of atomic hydrogen at the Pd surface. Such a scenario is supported by TEM images (Figure

4-8); although aged 0.35% Pd/NZVI maintained greater reactivity than aged NZVI, the Pd deposits initially visible on the NZVI surface were no longer apparent after 40 days of aging, coated by oxides that accumulated on the reductant surface over time. Accordingly, the long-term reactivity of 0.35% Pd/NZVI is likely derived from an enhanced rate of electron transfer from the underlying metallic iron core to the oxide-solution interface of the aged particles. Electron transfer from Fe(0) through a conductive surface oxide is also the most probable mechanism responsible for 1,1,1,2-TeCA reduction in aged NZVI systems, consistent with the negligible SKIE measured over the duration of NZVI aging. A schematic of the proposed mechanism and aging pathways as a function of Pd loading is shown in Figure 4-16.

Consequently, during application of Pd/NZVI, multiple mechanisms for chlorinated solvent transformation in are potentially at play, and the nature of the reductant particle (e.g., Pd loading), the type of pollutant target (e.g., alkyl versus vinyl polyhalide) and characteristics of the subsurface treatment system (Pd/NZVI concentration) will dictate the relative importance of each mechanism. From a practical perspective, the mechanism involving atomic H is most desirable, as it coincides with the greatest rates of pollutant transformation. Participation of atomic hydrogen will be favored at early timescales in treatment systems utilizing reductants with high Pd loadings and very high Pd/NZVI subsurface concentrations such that excess reductant is present within the treatment zone. All indications herein also support atomic H formation only occurs extensively in NZVI-based Pd/Fe systems and not for unpalladized NZVI or larger ZVI particle sizes. The role of atomic H is prominent in NZVI systems presumably

due to the enhanced rates of corrosion exhibited by these materials relative to larger commercially available iron particles.

However, many of our results raise questions as to the value of Pd/Fe applications. It is noteworthy that in order to achieve the best performance of Pd/NZVI, systems attributes long thought to be disadvantageous from the standpoint of economics (e.g., high Pd loading and high ρ_m values will produce high material costs) must be embraced. Further, our results show that at high solvent to reductant ratios, which would be typical of most saturated contaminant plumes, there is little reactivity difference between Pd/NZVI and NZVI, potentially indicating surface site limitation in Pd/NZVI systems that may negate any benefit of their use. A final point of concern relates to conditions required for atomic H formation. All results presented herein were conducted in closed batch systems, which allow Fe(0) corrosion products such as atomic or molecular hydrogen to accumulate. During field scale applications, it remains to be seen if levels of atomic hydrogen needed to attain optimal reactivity can be achieved in more dynamic, flow-through, open systems that might alter the driving force for H accumulation on or within Pd. Thus, while the results herein shed new light on the mechanisms driving contaminant transformation at palladized-iron surfaces, future efforts must demonstrate that the favorable Pd/Fe reactivity achievable in the laboratory is also attainable in the field. To date, the limited availability of data from Pd/NZVI field-scale installations precludes such an analysis.

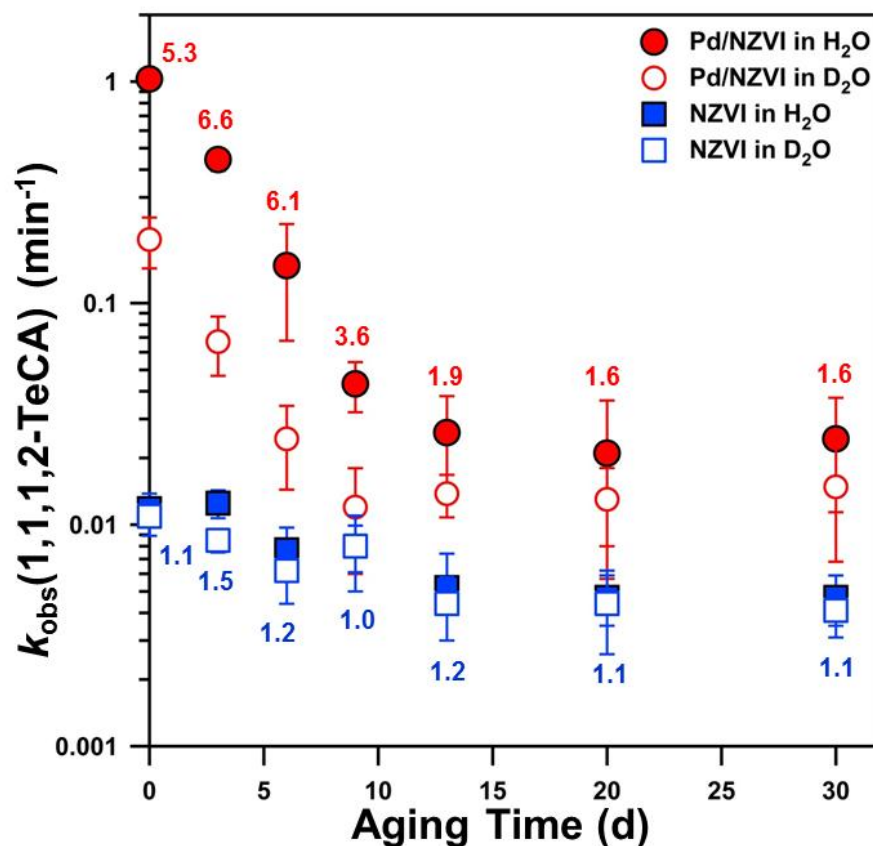


Figure 4-15. Change in the k_{obs} values for 1,1,1,2-TeCA reduction over time for bare NZVI (blue data) and 0.35% Pd/NZVI (red data) in the presence of H₂O (solid symbols) and D₂O (open symbols) during anaerobic aging. Measured solvent kinetic isotope effects as a function of time are provided for Pd/NZVI (red numbers) and NZVI (blue numbers). Suspensions of 2 g/L were aged over one month in pH 8 solution. The reactivity of aged NZVI-based reductants was measured periodically at a ρ_m value of 0.22 g/L and an initial 1,1,1,2,-TeCA concentration of 77 μ M at pH 8. All solutions were prepared in 25 mM HEPES and 25 mM NaCl.

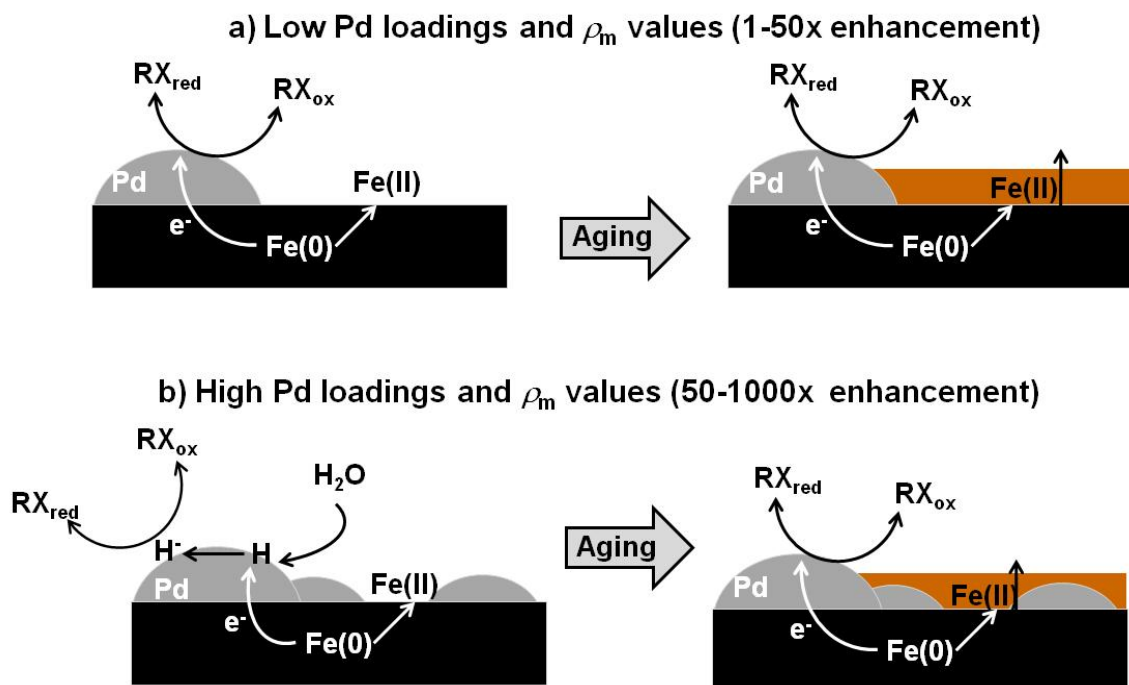


Figure 4-16. Schematic of the dominant reaction pathway responsible for organohalide (RX) reduction in Pd/NZVI systems. (a) At relatively low Pd loadings and low ρ_m values, deposits of Pd represent more favorable sites for electron transfer relative to the passive iron oxide film typically coating the NZVI particle surface, thereby promoting RX reduction via the galvanic flow of electrons from the underlying Fe(0) to the Pd/solution interface. Over time, growth of passive iron oxide covers the Pd islands, ultimately inhibiting RX reduction. (b) At high Pd loadings and high ρ_m values, sufficient Pd exists to serve as a reservoir for accumulation of atomic hydrogen, which represents the primary reactive entity under these conditions. During aging, growth of the passive iron oxide begins to limit the accessibility of Pd to the solution interface, in turn slowing the production and storage of atomic hydrogen. Aging studies revealed that reactivity of Pd/NZVI was greater than NZVI over the entire duration of aging. We attribute the enhanced reactivity of Pd/NZVI over longer timescales (i.e., > 2 weeks) to the galvanic corrosion mechanism postulated in (a), where the small amounts of Pd left exposed to solution represent more ideal sites for electron transfer than the surface of the thickening iron oxide film.

4.6. Literature Cited

1. Wang, C.-B.; Zhang, W.-X., Synthesizing Nanoscale Iron Particles for Rapid and Complete Dechlorination of TCE and PCBs. *Environ. Sci. Technol.* **1997**, *31*, 2154-2156.
2. Elliott, D.W.; Zhang, W.-X., Field Assessment of Nanoscale Bimetallic Particles for Groundwater Treatment. *Environ. Sci. Technol.* **2001**, *35*, 4922-4926.
3. Korte, N.E.; Zutman, J.L.; Schlosser, R.M.; Liang, L.; Gu, B.; Fernando, Q., Field Application of Palladized Iron for the Dechlorination of Trichloroethene. *Waste Management* **2000**, *20*, 687-694.
4. *U.S. Environmental Protection Agency, Selected Sites Using or Testing Nanoparticles for Remediation (www.clu-in.org/download/remed/nano-site-list.pdf). Office of Solid Waste and Emergency Response, 2008.*
5. Cwiertny, D.M.; Bransfield, S.J.; Livi, K.J.T.; Fairbrother, D.H.; Roberts, A.L., Exploring the Influence of Granular Iron Additives on 1,1,1-Trichloroethane Reduction. *Environ. Sci. Technol.* **2006**, *40*, 6837-6843.
6. Lin, C.J.; Lo, S.L.; Liou, Y.H., Dechlorination of Trichloroethylene in Aqueous Solution by Noble Metal-Modified Iron. *J. Haz. Mater.* **2004**, *116*, 219-228.
7. Kim, Y.-H.; Carraway, E.R., Reductive Dechlorination of TCE by Zero Valent Bimetals. *Environ. Technol.* **2003**, *24*, 69-75.
8. Lien, H.-L.; Zhang, W.-X., Nanoscale Pd/Fe Bimetallic Particles: Catalytic Effects of Palladium on Hydrodechlorination. *Appl. Catal. B. Environ.* **2007**, *77*, 110-116.
9. Lien, H.-L.; Zhang, W.-X., Nanoscale Iron Particles for Complete Reduction of Chlorinated Ethenes. *Coll. Surf. A* **2001**, *191*, 97-105.
10. Cwiertny, D.M.; Bransfield, S.J.; Roberts, A.L., Influence of the Oxidizing Species on the Reactivity of Iron-Based Bimetallic Reductants. *Environ. Sci. Technol.* **2007**, *41*, 3734-3740.
11. Chun, C.L.; Baer, D.R.; Matson, D.W.; Amonette, J.E.; Penn, R.L., Characterization and Reactivity of Iron Nanoparticles Prepared with Added Cu, Pd, and Ni. *Environ. Sci. Technol.* **2010**, *44*, 5079-5085.
12. Fang, Y.; Al-Abed, S.R., Dechlorination Kinetics of Monochlorobiphenyls by Fe/Pd: Effects of Solvent, Temperature, and PCB Concentration. *Appl. Catal. B. Environ.* **2008**, *78*, 371-380.

13. Yan, W.; Herzing, A.A.; Li, X.-q.; Kiely, C.J.; Zhang, W.-X., Structural Evolution of Pd-Doped Nanoscale Zero-Valent Iron (NZVI) in Aqueous Media and Implications for Particle Aging and Reactivity. *Environ. Sci. Technol.* **2010**, *44*, 4288-4294.
14. Zhu, B.-W.; Lim, T.-T., Catalytic Reduction of Chlorobenzenes with Pd/Fe Nanoparticles: Reactive Sites, Catalyst Stability, Particle Aging, and Regeneration. *Environ. Sci. Technol.* **2007**, *41*, 7523-7529.
15. Bransfield, S.J.; Cwiertny, D.M.; Roberts, A.L.; Fairbrother, D.H., Influence of Copper Loading and Surface Coverage on the Reactivity of Granular Iron toward 1,1,1-Trichloroethane. *Environ. Sci. Technol.* **2006**, *40*, 1485-1490.
16. Xu, Y.; Zhang, W.-X., Subcolloidal Fe/Ag Particles for Reductive Dehalogenation of Chlorinated Benzenes. *Ind. Eng. Chem. Res.* **2000**, *39*, 2238-2244.
17. Schrick, B.; Blough, J.L.; Jones, A.D.; Mallouk, T.E., Hydrodechlorination of Trichloroethylene to Hydrocarbons Using Bimetallic Nickel Iron Nanoparticles. *Chem. Mater.* **2002**, *14*, 5140-5147.
18. Cheng, I.F.; Fernando, Q.; Korte, N., Electrochemical Dechlorination of 4-Chlorophenol to Phenol. *Environ. Sci. Technol.* **1997**, *31*, 2443-2443.
19. Bryden, K.J.; Ying, J.Y., Pulsed Electrodeposition Synthesis and Hydrogen Absorption Properties of Nanostructured Palladium-Iron Alloy Films. *J. Electrochem. Soc.* **1998**, *145*, 3339-3346.
20. Carroll, F.A., *Perspectives on Structure and Mechanism in Organic Chemistry*. Brooks Cole: New York, 1998.
21. Cwiertny, D.M., Mechanistic Investigations of Granular Iron and Iron-Based Bimetallic Reductants for Treatment of Organohalide Pollutants. Ph.D. Thesis. Johns Hopkins University, Baltimore, MD, 2005.
22. Xie, Y.; Cwiertny, D.M., Use of Dithionite to Extend the Reactive Lifetime of Nanoscale Zero-Valent Iron Treatment Systems. *Environ. Sci. Technol.* **2010**, *44*, 8649-8655.
23. Perrin, D.D.; Dempsey, B., *Buffers for Ph and Metal Ion Control*. John Wiley and Sons: New York, 1974.
24. Wei, J.; Xu, X.; Liu, Y.; Wang, D., Catalytic Hydrodechlorination of 2,4-Dichlorophenol over Nanoscale Pd/Fe: Reaction Pathway and Some Experimental Parameters. *Water Res.* **2006**, *40*, 348-354.

25. Cwiertny, D.M.; Roberts, A.L., On the Nonlinear Relationship between Kobs and Reductant Mass Loading in Iron Batch Systems. *Environ. Sci. Technol.* **2005**, *39*, 8948-8957.
26. Reardon, E.J.; Fagan, R.; Vogan, J.L.; Przepiora, A., Anaerobic Corrosion Reaction Kinetics of Nanosized Iron. *Environ. Sci. Technol.* **2008**, *42*, 2420-2425.
27. Reardon, E.J., Anaerobic Corrosion of Granular Iron: Measurement and Interpretation of Hydrogen Evolution Rates. *Environ. Sci. Technol.* **1995**, *29*, 2936-2945.
28. Reardon, E.J., Zerovalent Irons: Styles of Corrosion and Inorganic Control on Hydrogen Pressure Buildup. *Environ. Sci. Technol.* **2005**, *39*, 7311-7317.

5. Hybrid hematite/multi-walled carbon nanotube (α - Fe_2O_3 /MWCNT) nanostructures as sorbents for Cu(II) and Cr(VI)

5.1. Abstract

Major hurdles in the application of nanomaterials for water treatment include loss of reactive surface area from particle aggregation and the development of application platforms that limit the potential release of nanomaterials into the treated water supply. Here, we develop a novel class of hybrid nanostructures through the growth of hematite (α - Fe_2O_3) nanoparticles, which are recognized sorbents for heavy metals, on multi-walled carbon nanotubes (MWCNTs). The hybrid nanostructures were synthesized via the hydrolysis of ferric nitrate in the presence of carboxylated MWCNTs, and their activity as sorbents toward Cu(II) and chromate (CrO_4^{2-}) was examined as a function of pH (i.e., pH edge experiments) and initial metal concentration (i.e., adsorption isotherms). Characterization of α - Fe_2O_3 /MWCNT nanostructures revealed that the amount (0.07 and 0.5 g/g α - Fe_2O_3 /MWCNT) and size [$5.9 (\pm 1.1)$ and $8.9 (\pm 1.5)$ nm, respectively] of hematite nanoparticles immobilized on MWCNT surfaces were tunable during synthesis. Generally, mass normalized concentrations of adsorbed Cu(II) and CrO_4^{2-} were greatest for α - Fe_2O_3 /MWCNT relative to adsorption on either MWCNTs or freely suspended α - Fe_2O_3 nanoparticles. The enhanced sorption capacity of the hybrid nanostructures is due, at least in part, to their greater available surface area of MWCNT-immobilized α - Fe_2O_3 when compared to extensively aggregated α - Fe_2O_3 nanoparticles in suspension.

Differences in the pH-dependent trends of Cu(II) and CrO_4^{2-} uptake on $\alpha\text{-Fe}_2\text{O}_3/\text{MWCNT}$ nanostructures also suggest that the immobilized $\alpha\text{-Fe}_2\text{O}_3$ nanoparticles exhibit unique and enhanced surface reactivity relative to their freely suspended nanoparticle analogues.

5.2. Introduction

Since their discovery by Iijima [1], carbon nanotubes (CNTs) have received considerable research focus because of their unique properties including their high mechanical strength [2], large external specific surface area [3], and electrical and thermal superconductivity [4]. CNTs consist of one or more graphene sheets rolled into a cylinder with a nanoscale diameter that is several microns in length [5]. They can exist as single-wall (SWNT), double-wall or multi-wall (MWNT) varieties depending on their number of graphene layers. Their unique morphological, mechanical, physicochemical and electrical properties have led to their extensive industrial application as sorbents [6-8], catalyst supports [9], construction materials [10], and in drug delivery [11] and sensor development [12].

As sorbents, CNTs are gaining popularity. Previous bench-scale experiments have demonstrated their superior sorption capacity toward gases (e.g., hydrogen [13], methane [14], argon [14] and xenon [14], NO_2 [15] and CO [15]) and aqueous phase organohalides (e.g., trihalomethane [16] and dioxin [17]) and metals (e.g., Pb(II) [18], Cd(II) [8], Am(III) [19], Ni(II) [20], Zn(II) [21] and Cu(II) [6]). For metals, in particular, CNTs represent promising sorbents because oxygen-containing surface functionalities added to

promote their aqueous solubility and dispersivity also represent sites for metal complexation. However, their application is likely limited to cationic metal species only, as most of these oxygen containing surface moieties will be negatively charged over the range of environmentally relevant pH values [22, 23], and thus adsorption of anionic species will be limited by unfavorable electrostatic interactions.

Iron oxides are recognized sorbents for both cationic and anionic metal species, and they too are growing in popularity as nanoscale adsorbents [24-29]. Nanoparticles of iron oxides such as hematite ($\alpha\text{-Fe}_2\text{O}_3$) and goethite ($\alpha\text{-FeOOH}$) are ideal sorbents because they possess large surface area-to-volume ratios, are relatively easy and inexpensive to synthesize, and, as earth abundant materials [30], pose little threat of adverse environmental impacts. The application of iron oxide nanoparticles as sorbents may be hindered, however, by their limited stability in suspension [31], which results in extensive aggregation that consumes reactive surface area [32, 33]. One approach to overcome the limitations of nanoparticle aggregation is to immobilize the iron oxide nanoparticles on a support structure, thereby preventing nanoparticle-nanoparticle interactions. Examples of support materials previously employed for various sizes of iron oxides include activated carbon [34], clay particles [35] and sand [29].

Multi-walled carbon nanotubes (MWCNTs) represent a promising new support material for iron oxide nanoparticle sorbents. CNTs have been successfully applied as nanoparticle supports in catalysis [36-39] and numerous methods are available for the synthesis of CNTs decorated with metal and metal oxide nanoparticles [40-47], most of which are tunable for systematic variation of the distribution and size of the nanoparticles

deposited on the CNT surface. To date, the most common iron oxide immobilized on CNT surfaces is magnetite (Fe_3O_4) [48-51] because of its magnetic nature, which may enable CNT recovery via collection in a magnetic field. Notably, some studies have focused on the application of Fe_3O_4 /CNT hybrid nanostructures as sorbents [48, 52, 53], although these studies have failed to establish if CNT-immobilized Fe_3O_4 nanoparticles hold any clear advantage as sorbents relative to the individual components from which they are constructed. Further, Fe_3O_4 may be a poor choice of sorbent material for water treatment, as it is also redox active and therefore unstable in the presence of oxygen. Nevertheless, hybrid CNTs prepared with more traditional iron oxide sorbents such as hematite or goethite have not been investigated.

In this study, we prepare MWCNTs decorated with hematite ($\alpha\text{-Fe}_2\text{O}_3$) nanoparticles and demonstrate the application of these hybrid nanostructures as sorbents for metals in water. Hybrid $\alpha\text{-Fe}_2\text{O}_3$ /MWCNT nanostructures were prepared via the forced hydrolysis of a ferric nitrate precursor solution in the presence of oxidized (i.e., carboxylated) MWCNTs. The synthesis products were extensively characterized to examine how the amount and size of $\alpha\text{-Fe}_2\text{O}_3$ nanoparticles on the MWCNT surface could be tuned during synthesis. Subsequently, the activity of these hybrid nanostructures as sorbents for Cu(II) and chromate (CrO_4^{2-}) was examined as a function of suspension pH (i.e., pH edge) and metal concentration (i.e., adsorption isotherm). A key objective of this work was to determine if the $\alpha\text{-Fe}_2\text{O}_3$ /MWCNT hybrid nanostructures exhibited unique and different reactivity from the sum of their individual nanomaterial components (i.e., suspensions of MWCNT and $\alpha\text{-Fe}_2\text{O}_3$ nanoparticles).

5.3. Experimental Section

Reagents

MWCNTs synthesized by chemical vapor deposition (CVD) were acquired from CheapTubes.com. These MWCNTs have a vendor-reported purity of >95%, with an outer diameter (OD) of less than 8 nm, an inner diameter (ID) of 2-5 nm, a length of 10-30 μm , and a specific surface area of 500 m^2/g . Ferric nitrate nonahydrate (Fisher; 100%) was used as an iron precursor in the synthesis of hematite nanoparticles and hematite-coated MWCNTs. Adsorption experiments were conducted with hexavalent chromium [Cr(VI)] prepared from potassium chromate (K_2CrO_4 ; Fisher; reagent grade) and copper(II) chloride dihydrate ($\text{CuCl}_2 \cdot 2\text{H}_2\text{O}$; Acros Organics; 98%). Reagents used for CrO_4^{2-} colorimetric analysis included diphenyl carbazide (Fisher; Certified ACS grade) and sulfuric acid (H_2SO_4 , Acros Organics; 95-98%). Zincon monosodium salt (Fluka Analytical) was utilized for measurement of aqueous Cu(II) concentration. Colorimetric analysis of aqueous Fe(III) utilized 1,10-phenanthroline (Aldrich, 99+%), ammonium acetate (Sigma-Aldrich; >98%), hydroxylamine hydrochloride (Sigma-Aldrich; 99%) and glacial acetic acid (Fisher; ACS grade). Sodium chloride (NaCl ; ACS reagent; $\geq 99.0\%$) was used to poise ionic strength and all solutions were prepared in deionized water (Milipore, Q-Grad 2). Solution pH was adjusted via hydrochloric acid (Fisher, trace metal grade) and sodium hydroxide (NaOH ; 97+%; ACS reagent grade).

Oxidation of MWCNTs

As received MWCNTs were treated prior to use with concentrated (70%) HNO₃ according to established protocols [54, 55]. Briefly, 100 mg of as received MWCNTs was dispersed in 250 mL of 70% HNO₃ and sonicated for 1 h. The dispersed suspension was then refluxed for 1.5 h at 140° C in a temperature controlled oil bath while stirring. After cooling overnight, the acid-treated tubes were then collected on a 0.2 μm nitrocellulose filter and washed extensively with deionized water until the wash solution reached pH 5. Washed MWCNTs were then dried at 80 °C overnight and ground via mortar and pestle prior to suspending in DI water at a final concentration of 1 g/L. Suspensions were then sonicated for 20 h to promote oxidized MWCNT dispersion prior to use in synthesis.

Preparation of hematite nanoparticles

Hematite nanoparticles were synthesized according to “Method 4” in Schwertmann and Cornell [56]. Adapted from the work of Sorum [57], this approach is known to produce unidimensional crystals with diameters between 7-10 nm. Briefly, 60 mL of 1 M ferric nitrate solution was added drop-wise via peristaltic pump (rate of 0.5 mL/min) into 750 mL of boiling water that was well-mixed with a magnetic stirrer. At early stages of ferric nitrate addition, the boiling water was red in color but transparent. Eventually the solution thickened to form a suspension with red particles. After the drop-wise addition was completed, the nanoparticle suspension was removed from the hot plate and allowed to cool overnight. Once cool, the suspension was loaded into dialysis tubing (MWCO of 3500) and dialyzed against DI water, with the DI water being exchanged 3-4 times a day over a period of 4 days. After dialysis, the suspension was

dried in air via partitioning suspension aliquots into several plastic weight boats. After drying, the particles were ground with mortar and pestle and passed through a 53 μm sieve.

Synthesis of MWCNTs decorated with hematite nanoparticles

2 mL of 1 g/L oxidized MWNTs were added to 40 mL of boiling water that was well mixed with a magnetic stir bar and stir plate. After stirring for 5 minutes, either 0.8 or 3.2 mL of 0.016 M $\text{Fe}(\text{NO}_3)_3$ was added drop wise to the boiling mixture. These volumes of ferric nitrate were selected based upon their mass relative to the starting mass of MWCNTs; assuming complete conversion to $\alpha\text{-Fe}_2\text{O}_3$, these conditions would produce final mass ratios of $\alpha\text{-Fe}_2\text{O}_3$ to MWCNT of 0.5:1 and 2:1, respectively. The mixture was stirred for an additional 10 min. The mixture was allowed to sit overnight prior to separation of the solids via centrifugation, followed by several washes with deionized water to remove any residual aqueous Fe(III) or Fe(III) oxide particles not associated with the MWCNT surface. Finally, the washed material was resuspended in 2 mL of DI water to produce a 1 g/L suspension based on the available MWCNT mass, which was used as concentrated stock suspension in subsequent adsorption experiments.

Quantifying total iron mass deposited on MWNTs

The total mass of iron deposited on MWCNTs was determined via acid digestion of $\alpha\text{-Fe}_2\text{O}_3$ -MWCNT hybrid nanostructures. For acid digestion, 1 mL of a 0.5 g/L suspension (based on available MWCNT mass) of hybrid nanostructures was transferred

to a 2 mL microcentrifuge tube, centrifuged at 10000 RPM for 10 min, and the supernatant was removed via pipette and discarded. To the solids residual in the centrifuge tube, 1 mL of 5 N HCl was added and the acidified tubes were allowed to sit for 24 hr, over which time the deposited oxide was solubilized. Longer dissolution times (e.g., 48 h) produced identical results. After 24 h, centrifugation was used to separate the MWCNTs from the acidified solution containing dissolved ferric iron. An aliquot of 40 μ L was taken and diluted into 1 mL of DI water and immediately analyzed for total dissolved iron via the colorimetric methods described below.

Adsorption experiments

Adsorption experiments with nanomaterials were conducted with a model metal cation, Cu(II), and an model metal anion, Cr(VI) as chromate (CrO_4^{2-}), both of which are regulated by EPA in drinking water [58]. For all nanomaterials, Cu(II) and CrO_4^{2-} sorption was examined as a function of initial metal concentration (i.e., sorption isotherm) and as a function of the suspension pH (i.e., pH edge experiment).

For sorption experiments with Cu(II), sorption isotherms and pH edge experiments with freely suspended hematite nanoparticles used a solid loading of either 0.05 or 0.1 g/L. For MWCNT-based sorbents (i.e., oxidized MWCNT and hybrid α - Fe_2O_3 -MWCNT nanostructures), sorption experiments used a solid loading of 0.05 or 0.1 g/L based upon available MWCNT mass.

For Cu(II), pH edge experiments were collected over the range from pH 3 to 7 with an initial Cu(II) concentration of 80 μ M (5.1 mg/L). This concentration of Cu(II)

represented the maximum value that was stable at pH 7 in homogeneous controls conducted in the absence of nanomaterial sorbents; at higher concentrations and pH values, loss of Cu(II) over time was observed in sorbent-free controls consistent with the precipitation of copper hydroxide. Sorption isotherm experiments were conducted at pH 6 with initial Cu(II) concentrations ranging from 5 to 100 μM (0.3-6.4 mg/L), with all sorbent-free controls exhibiting stable Cu(II) concentration over time.

Sorption experiments were conducted in solutions of 25 mM NaCl and without any pH buffer, with all pH control achieved through the addition of weak acid (HCl) or base (NaOH) to achieve and maintain the desired pH value. For experiments with Cu(II), a small volume (between 5-200 μL) of a 10 mM CuCl_2 stock solution prepared in pH 3 DI water was delivered via pipet to 10 mL of pH-adjusted 25 mM NaCl to produce the desired initial Cu(II) concentration. The initial Cu(II) concentration was then measured and an aliquot of sorbent stock suspension was added subsequently to the Cu(II) solution to initiate the sorption experiment. After sorbent delivery, the suspension pH was measured again, and, if necessary, adjusted immediately to the desired value (i.e., initial $\text{pH} \pm 0.1$ unit). The pH value was also measured at the end of the sorption experiment (1 h). Typically, the pH was relatively constant over the duration of the sorption experiment (within ± 0.2 pH units of the initial value). On a few occasions, larger pH drifts were observed. In these instances, reported pH values represent the average of the pH values measured at the start and end of the adsorption experiment, and the standard deviation is presented as a measure of the uncertainty associated with the system pH.

Sorption experiments were conducted in 20 mL vials that were crimp-sealed with grey butyl rubber septum coated with PTFE. Once assembled, these vials were placed on an apparatus that mixed the reactors end-over-end at 60 RPM for 1 h, which was sufficient for sorption equilibrium to be achieved. After 1 h, the vials were removed from the rotator and 1 mL of suspension was withdrawn for analysis. To remove the solid phase, samples were passed through 0.2 μM syringe-driven filters (PTFE). All samples were analyzed via the colorimetric methods described below, and the amount of adsorbed metal was determined via mass balance from the difference between the initially measured metal concentration and the dissolved phase concentration measured at equilibrium.

Sorption experiments with CrO_4^{2-} were conducted in a similar fashion, using the same sorbent loadings as in experiments with Cu(II). These experiments used a stock solution of 10 mM of Cr(VI) prepared from potassium chromate in DI water. pH edge experiments were collected over the pH range from 2 to 10 at an initial CrO_4^{2-} concentration at 15 μM (1.7 mg/L). Sorption isotherms were collected at pH 2 and pH 6 at initial CrO_4^{2-} concentrations ranging from 5 to 200 μM (0.6-23 mg/L). Other experimental details are as previously described for sorption experiments with Cu(II).

Materials characterization

Nitric acid treated MWCNTs were characterized with X-ray photoelectron spectroscopy [54, 55] to determine total surface oxygen content and the fraction of total oxygen content attributable to specific oxygen-containing surface functionalities. The

morphology of MWCNTs, α -Fe₂O₃ nanoparticles, and hybrid α -Fe₂O₃/MWCNT nanostructures was examined via transmission electron microscopy (TEM; FEI Tecnai 12 G2 equipped with a LaB6 electron gun) operated at 120 kV. Prior to characterization, aqueous samples of nanomaterial suspensions were centrifuged to separate the solids from the supernatant and then resuspended in methanol. This procedure limited interference from NaCl originally present in suspension during TEM imaging. For sample preparation, a drop of diluted nanomaterial suspension was dried on a carbon-coated Cu grid (300 mesh). Higher resolution TEM images with electron energy loss spectroscopy were conducted using a JEOL JEM-2100F field emission microscope operating at 200 kV. High contrast imaging was performed using a HAADF detector and a 0.2 nm electron probe operating in scanning mode (STEM). Images were acquired using commercially available Digital Micrograph software.

Nanomaterial suspensions were characterized via measurements of zeta potential collected over pH values ranging from 2 to 9. Suspensions of each nanomaterial (i.e., hematite, MWCNT and hybrid hematite-MWCNT nanostructures with different loadings of deposited iron) were prepared via dilution to produce an absorbance at $\lambda=546$ nm between 0.3 to 0.35. These suspensions were allowed to equilibrate overnight prior to zeta potential analysis so as to produce steady-state conditions in the suspension. Approximately 1.5 mL of well-mixed suspension was then transferred to a 3 mL microcuvette for analysis using a ZetaPals zeta potential analyzer (Brookhaven Instruments Corporation, Holtsville, NY).

Nanomaterial suspension stability was also examined via measurement of sedimentation rates. Suspensions of each nanomaterial were prepared at pH 6.0 in 25 mM NaCl. A portion of the suspensions was transferred to a quartz microcuvette with 1 cm pathlength, and the change in suspension absorbance at λ of 510 nm was measured over one hour. For suspensions of hematite nanoparticles, a 20 mg/L solid loading was employed. For MWCNT-based sorbents (i.e., oxidized MWCNT and hybrid α -Fe₂O₃-MWCNT nanostructures), sedimentation experiments used a solid loading of 20 mg/L based upon available MWCNT mass.

Analytical methods

Total dissolved iron was quantified using the 1,10-phenanthroline method [59, 60]. Briefly, 40 μ L of acidified supernatant from digestion of hematite-MWCNT nanostructures was diluted with 1 mL of DI water. For colorimetric analysis, 20 μ L of a 10 g/L hydroxylamine solution was first added to the diluted sample to reduce all Fe(III) to Fe(II). Then, 200 μ L of a 1 g/L solution of 1,10-phenanthroline, which complexes Fe(II), and 200 μ L of a 100 g/L ammonium acetate buffer were added to the sample. The mixture was allowed to sit in the dark for ~30 min prior to analysis. Absorbance measurements were then performed on a Shimadzu UV-visible spectrophotometer at λ =510 nm. Standards for Fe(II) were prepared from anhydrous beads of ferrous chloride (FeCl₂, 99.9%, Sigma-Aldrich).

Dissolved concentrations of Cr(VI) were determined colorimetrically with the reagent diphenylcarbazide [61]. Briefly, 80 μ L of filtered sample was diluted with 1 mL

of deionized water and then combined with 40 μL of 5N sulfuric acid and 40 μL of a solution prepared by dissolving 250 mg of diphenylcarbazide in 50 mL acetone. The mixture was allowed to react for 30 min in the dark, over which time a pink color developed if Cr(VI) was present above the detection limits ($\sim 36 \mu\text{g/L}$). The solutions were analyzed on a Shimadzu UV/visible spectrophotometer at $\lambda = 540 \text{ nm}$. Standards of Cr(VI) were made from potassium chromate and were prepared for analysis in a manner identical to the experimental samples.

Dissolved concentrations of Cu(II) were measured colorimetrically with 2-carboxy-2'-hydroxy-5'-sulfoformazylbenzene (also known as Zincon [62]). The procedure called for 0.130 g of Zincon powder to be dissolved in 2 mL of 1 M sodium hydroxide and subsequently diluted to a final volume of 100 mL with DI water, yielding a final Zincon concentration of 0.002 M. The solution was deep red in color and tests showed it to be stable for one week. A 60 μL aliquot of the Zincon solution was added to 940 μL of filtered sample, and the mixture was allowed to react for 40 min in the dark, over which time color developed if Cu(II) was present above the method detection limit ($\sim 0.1 \text{ mg/L}$). The color of the sample changed from red to dark brown with increasing dissolved Cu(II) concentrations. The samples were analyzed on a Shimadzu UV/visible spectrophotometer at $\lambda = 600 \text{ nm}$. Standards of Cu(II) from copper(II) chloride dihydrate ($\text{CuCl}_2 \cdot 2\text{H}_2\text{O}$) were prepared for UV/vis analysis in a fashion identical to the experimental samples.

5.4. Results and Discussion

Morphology and Size Characteristics of $\alpha\text{-Fe}_2\text{O}_3/\text{MWCNT}$ Nanostructures

TEM images of nitric acid oxidized MWCNTs and α -Fe₂O₃ nanoparticles synthesized via hydrolysis of ferric nitrate in the absence of MWCNTs are shown in Figure 5-1. Products of the hydrolysis of ferric nitrate in the presence of MWCNTs are shown in Figure 5-2 for two total masses of iron utilized during synthesis. For the MWCNTs and α -Fe₂O₃ nanoparticles, details of their characterization are provided elsewhere [63, 64]. Briefly for oxidized MWCNTs [64], reaction of as-received MWCNTs with concentrated nitric acid increased the total surface oxygen content of the MWCNTs from 1.9 to 8.25 atomic percent, with the majority of oxygen resulting from the formation of carboxylic acid (-COOH), hydroxyl (-OH) and carbonyl (-C=O) groups on the CNT surface. Briefly for hematite nanoparticles [63], X-ray diffraction analysis confirmed the nanoparticles to be hematite (α -Fe₂O₃) based on comparison to a reference diffraction pattern and corresponding *d*-spacings [29]. Particle sizing via TEM revealed roughly spherical particle geometry with a primary particle size of 7.5 (\pm 1.3) nm (determined from TEM sizing of at least 100 particles) and a specific surface area from N₂ BET of 80 m²/g. However, as observed in Figure 5-1b, and explored at length elsewhere [63], the α -Fe₂O₃ nanoparticles tend to be extensively and densely aggregated in most aqueous suspensions.

Comparison of Figures 5-1 and 5-2 shows clear differences between the individual α -Fe₂O₃ and MWCNT nanomaterials and the synthesis products generated from hydrolysis of ferric nitrate in the presence of MWCNTs. TEM images in Figure 5-2 are consistent with the deposition and growth of iron oxide nanoparticles on the surface of MWCNTs during synthesis. Selected area electron diffraction (SAED) conducted with

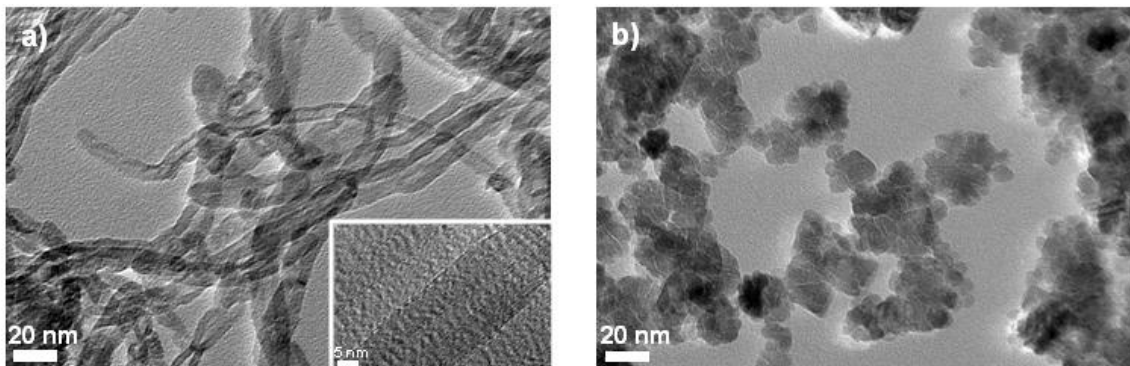


Figure 5-1. TEM images of (a) oxidized MWCNTs (with inset of a single MWCNT at high magnification) and (b) aggregated hematite (α -Fe₂O₃) nanoparticles synthesized from the hydrolysis of ferric nitrate.

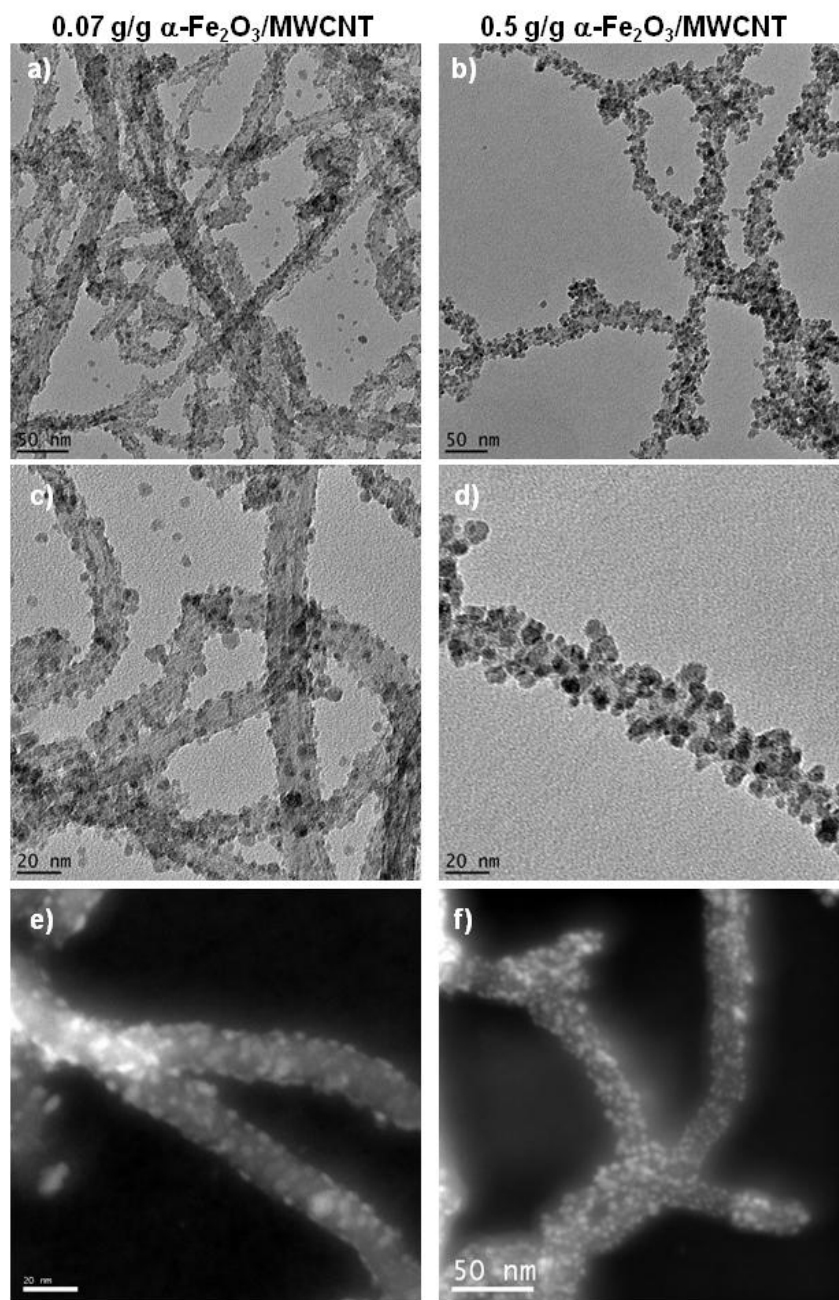


Figure 5-2. TEM images for 0.07 and 0.5 g/g α -Fe₂O₃/MWCNT at low (a and b, respectively) and high (c and d, respectively) magnifications. Also shown for each material (e and f, respectively) are dark field TEM images, in which contrast indicates differences in elemental mass. In dark field images, heavier elements are brighter, consistent with the bright regions on the CNT surface representing α -Fe₂O₃ nanoparticles. Electron energy loss spectroscopy (EELS; not shown) confirmed that the bright regions in the dark field images are iron.

TEM indicated the iron oxide particles were crystalline with *d*-spacings representative of hematite.

From acid digestion, the amount of iron deposited on the MWCNT surface was determined to be tunable during synthesis. The synthesis route involving the addition of 3.2 mL of 0.016 M Fe(NO₃)₃ resulted in the deposition of 0.49 ± 0.04 g of α-Fe₂O₃ per g MWCNT (which we hereafter refer to as 0.5 g/g α-Fe₂O₃/MWNT). This value represents the average and standard deviation of nine measurements of total iron concentration obtained via acid digestion of four different synthesis batches at these conditions. The low standard deviation across four different synthesis batches suggests our synthesis approach and final product were highly reproducible. For comparison, the synthesis route utilizing only 0.8 mL of 0.016 M Fe(NO₃)₃ yielded 0.068 ± 0.005 g of α-Fe₂O₃ per g of MWCNT (hereafter referred to as 0.07 g/g α-Fe₂O₃/MWNT). Notably, the theoretical maximum yields, assuming complete conversion and deposition of Fe(NO₃)₃ to α-Fe₂O₃, are 0.5 and 2 g/g, respectively, for the addition of 0.8 and 3.2 mL of 0.016 M Fe(NO₃)₃ during the synthesis. Thus, only 13% and 24% of the total available Fe(III) was deposited on the MWCNTs during synthesis.

Based on TEM particle sizing, α-Fe₂O₃ nanoparticles deposited on MWCNTs were roughly hemispherical, but their diameter increased with the total mass of iron deposited on the MWCNT surface. For 0.07 g/g α-Fe₂O₃/MWCNT, an α-Fe₂O₃ particle size of 5.9 (± 1.1) nm was observed (value represents the mean and standard deviation of TEM sizing of at least 50 surface deposited α-Fe₂O₃ particles), whereas similar analysis of 0.5 g/g α-Fe₂O₃/MWCNT produces an average particles size of 8.9 (± 1.5) nm.

Notably, for this larger mass of deposited α -Fe₂O₃, the particles are nominally greater than that observed for the hematite nanoparticles synthesized in the absence of MWCNTs.

Characteristics of α -Fe₂O₃/MWCNT Suspensions

Zeta potential values measured as a function of pH are shown in Figure 5-3 for suspensions of α -Fe₂O₃ nanoparticles, oxidized MWCNTs, and both iron loadings of α -Fe₂O₃/MWCNT nanostructures. As expected from previously reported behavior [22, 23], oxidized MWNTs were negatively charged over the entire pH range, dropping slightly from -25 to -40 mV as pH increased from pH 2 to pH 9. Such behavior is consistent with the surface carboxyl and hydroxyl groups added during oxidation with nitric acid being predominantly deprotonated over the environmentally relevant range of pH values.

Suspensions of α -Fe₂O₃ nanoparticles displayed behavior typically expected from established trends in the acid-base surface character of hematite. For hematite suspensions, pH values of zero point of charge ranging from 7.5-9.5 and isoelectric points ranging from 7.0-9.3 have been reported previously [29], whereas suspensions of the aggregated α -Fe₂O₃ nanoparticles transition from a positive to negative zeta potential between pH 6.5-8.0. Thus, the pH-dependent surface charge of the synthesized α -Fe₂O₃ nanoparticles is within the typical range displayed by other synthetic forms of hematite.

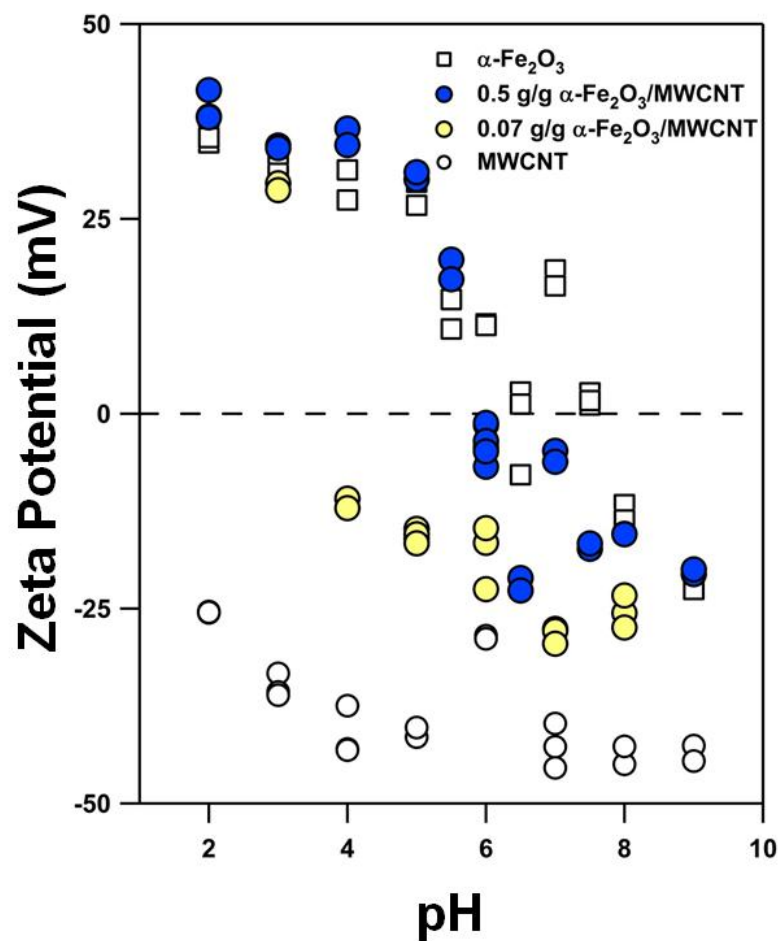


Figure 5-3. Zeta potential values measured as a function of pH for suspensions of $\alpha\text{-Fe}_2\text{O}_3$ nanoparticles, 0.07 and 0.5 g/g $\alpha\text{-Fe}_2\text{O}_3$ /MWCNT and oxidized MWCNTs. Suspension preparation for zeta potential analysis is described in the text. Notably, all zeta potential values were measured in 25 mM NaCl without pH buffer, which is identical to the conditions used in adsorption studies.

In α -Fe₂O₃/MWCNT nanostructures, values of zeta potential were dependent on the total amount of iron deposited on the MWCNT surface. For suspensions of 0.5 g/g α -Fe₂O₃/MWCNT, trends in zeta potential as a function of pH were roughly equivalent to values measured in suspensions of α -Fe₂O₃ nanoparticles. Notably, from pH 6.0 to 7.5, values of zeta potential for 0.5 g/g α -Fe₂O₃/MWCNT were consistently and repeatedly more negative than values measured in α -Fe₂O₃ suspensions, although this behavior is slightly obscured from the scatter in zeta potential values from one pH value to the next.

The pH-dependent trends in zeta potential for the lower iron loading on MWCNTs (i.e., 0.07 g/g α -Fe₂O₃/MWCNT) varied markedly from the nanostructures with higher iron loading. While the zeta potential at pH 3 was equivalent to that observed for α -Fe₂O₃ suspensions (and, therefore, 0.5 g/g α -Fe₂O₃/MWCNT), the zeta potential at all other pH values fell in between the range of values measured for suspensions of α -Fe₂O₃ and oxidized MWCNTs. Thus, 0.07 g/g α -Fe₂O₃/MWCNT nanostructures appear to exhibit surface chemistry that is unique from their building blocks. Notably, the zeta potentials for suspensions of 0.07 g/g α -Fe₂O₃/MWCNT are not mass weighted averages of the zeta potential values measured for α -Fe₂O₃ and MWCNT suspensions; such a small mass of α -Fe₂O₃ relative to MWCNTs would be expected to produce negligible deviation from the behavior of pure MWCNT suspensions.

In addition to zeta potential measurements, the stability of α -Fe₂O₃/MWCNT suspensions relative to suspensions of oxidized MWCNTs and α -Fe₂O₃ was explored via sedimentation experiments conducted at pH 6 (Figure 5-4). MWCNTs exhibited high

suspension stability, as anticipated from established behavior for the aqueous stability of oxidized carbon nanotubes. Their high stability is derived from the deprotonated surface oxide groups added via functionalization with nitric acid. The stability is also expected from the relatively large, negative zeta potential measured for these materials at pH 6, which results in strong electrical double layer repulsive forces between particles.

Surprisingly, the extensive deposition of α -Fe₂O₃ nanoparticles on the MWCNT surface exerted little effect on suspension stability. MWCNTs coated with 0.5 g/g of α -Fe₂O₃ exhibited stability in suspension that was nearly equivalent to that observed for MWCNTs (7% and 3% loss in initial absorbance after one hour, respectively). Notably, suspensions of α -Fe₂O₃ nanoparticles at pH 6 exhibited the least stability of all nanomaterials considered, with absorbance decreasing by roughly 40% over one hour.

Adsorption of Cu(II) as a function of suspension pH

Trends in the pH-dependent adsorption of Cu(II) on each nanomaterial are shown in Figure 5-5. Over the pH range investigated (pH 3-7), Cu(II) adsorption occurred to some extent on all nanomaterial substrates. For the purpose of comparing Cu(II) adsorption on hybrid nanostructures to sorption in suspensions of each individual nanomaterial, adsorbed Cu(II) concentrations as a function of pH are presented after normalization by the mass concentration of MWCNT (Figure 5-5a with units of mg Cu(II)/g MWCNT) and α -Fe₂O₃ (Figure 5-5b with units of mg Cu(II)/g α -Fe₂O₃).

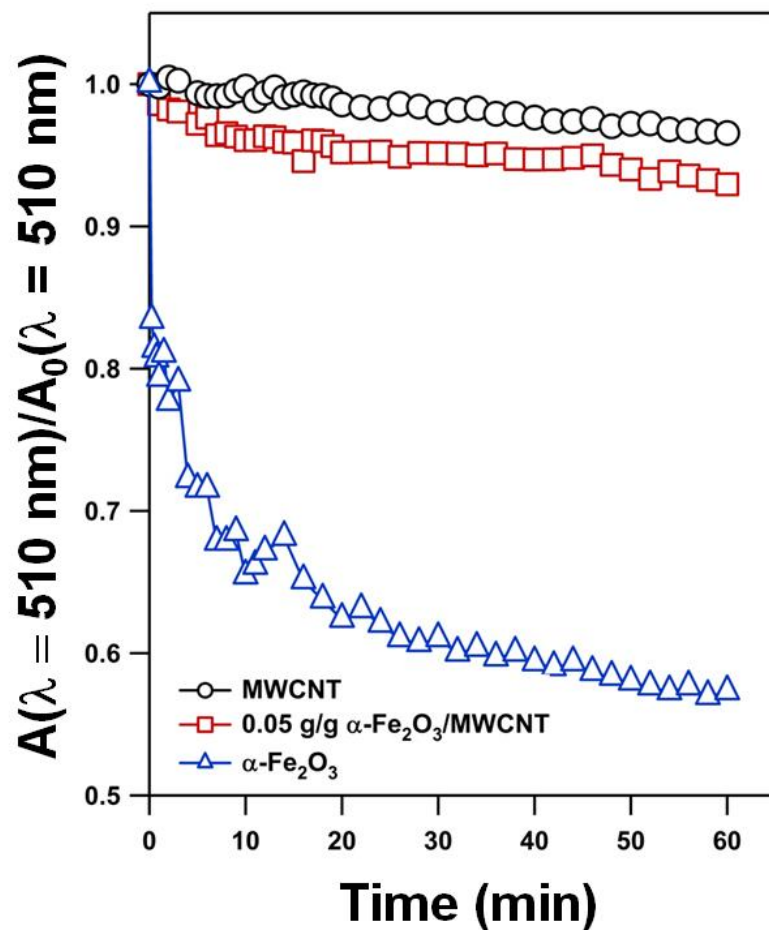


Figure 5-4. Sedimentation results for suspensions of oxidized MWCNTs, 0.5 g/g α -Fe₂O₃/MWCNT and α -Fe₂O₃ nanoparticles. The nanomaterial concentration of each suspension was 0.02 g/L (for MWCNT-based sorbents, this mass reflects the total available MWCNT mass in suspension). All suspensions were prepared at pH 6 in 25 mM NaCl. Data represent the change in normalized absorbance (A measured at 510 nm) over time due to particle settling in a 1 cm path length quartz microcuvette.

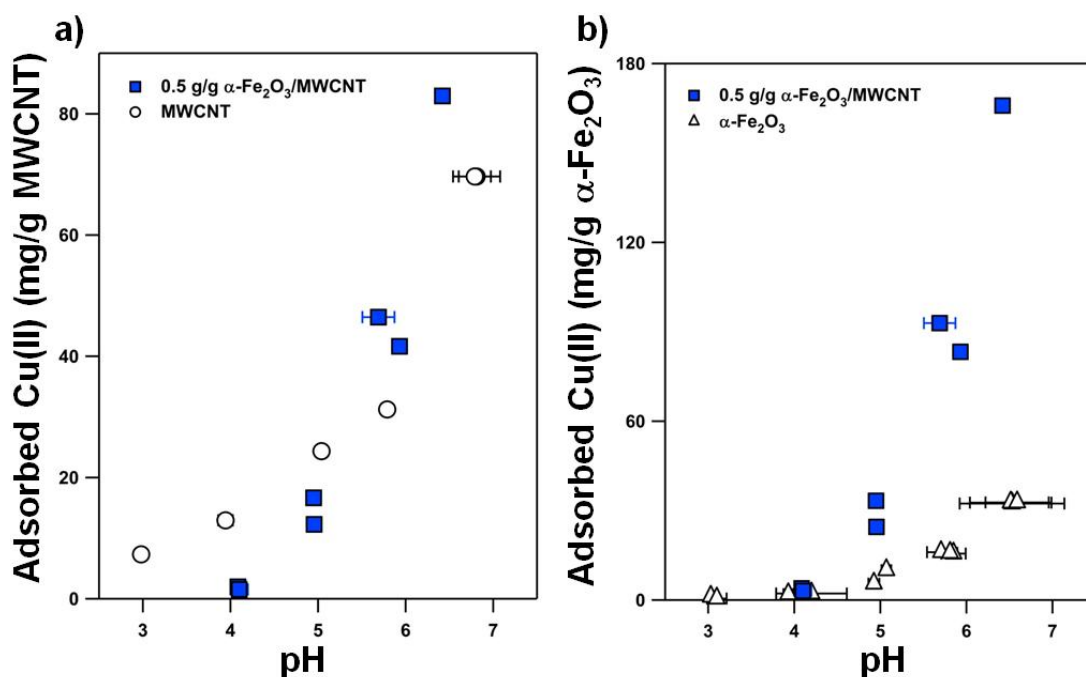


Figure 5-5. Adsorption of Cu(II) as a function of pH in suspensions of oxidized MWCNTs, α -Fe₂O₃ nanoparticles and 0.5 g/g α -Fe₂O₃ /MWCNT hybrid nanostructures. Adsorbed concentrations of Cu(II) are presented after normalization by the total mass of (a) MWCNT and (b) α -Fe₂O₃ in suspension. Experiments were conducted in 25 mM NaCl without pH buffer. pH values represent the average over the duration of the adsorption experiment based upon measurements at the start and end of the sorption experiment (with duration of 1 h). The uncertainties associated with these average pH values represent the standard deviation associated with the initial and final pH measured in the adsorption experiment. Experiments used an initial Cu(II) concentration of 80 μ M (5.1 mg/L), and suspension concentrations of 0.05 g/L for MWCNT and α -Fe₂O₃ /MWCNT (based on total MWCNT mass) and 0.05 and 0.1 g/L for α -Fe₂O₃ nanoparticles.

For oxidized MWCNTs (Figure 5-5a), the amount of Cu(II) adsorbed on the MWCNT surface increased steadily with increasing pH. At lower pH values (e.g., pH 3 and 4), Cu(II) uptake was measurable, albeit slight, in MWCNT suspensions only, whereas adsorption in the 0.5 g/g α -Fe₂O₃/MWCNT system was essentially negligible at pH values below 4. As the pH increased, the concentration of adsorbed Cu(II) increased more rapidly in the 0.5 g/g α -Fe₂O₃/MWCNT suspensions, with the mass of adsorbed Cu(II) in hybrid nanostructure systems surpassing that measured in MWCNT suspension when normalized to the total mass of MWCNT in suspension.

Because the zeta potential of the 0.5 g/g α -Fe₂O₃/MWCNT closely resembles that of the freely suspended hematite nanoparticles, a more appropriate comparison of sorbent activity is the amount of Cu(II) adsorbed per gram of α -Fe₂O₃ available in suspension. For both freely suspended α -Fe₂O₃ nanoparticles and 0.5 g/g α -Fe₂O₃/MWCNT nanostructures, adsorbed Cu(II) increased with increasing pH. This is typical behavior for the pH-dependent adsorption of cations on iron oxide surfaces, consistent with electrostatics as the primary driver for Cu(II) uptake [29]. Over the range of pH values investigated (Figure 5-5b), α -Fe₂O₃ nanoparticles grown on MWCNTs exhibited a far greater capacity for Cu(II) than α -Fe₂O₃ nanoparticles suspended freely. For example, at pH 5.9 Cu(II) uptake per gram of hematite was roughly 6-fold greater on 0.5 g/g α -Fe₂O₃/MWCNT relative to suspended α -Fe₂O₃ nanoparticles. Thus, on a per mass basis, α -Fe₂O₃ nanoparticles grown on MWCNTs are considerably more reactive toward Cu(II) than their suspended nanoparticle analogues.

This improved Cu(II) sorption capacity per gram of α -Fe₂O₃ exhibited by the hybrid nanostructures is at least partially attributable to the increase in reactive surface area arising from dispersion of the α -Fe₂O₃ nanoparticles on the MWCNT substrate. Nanoparticles of α -Fe₂O₃ appear extensively aggregated in suspension (see Figure 5-1b), which will limit the amount of reactive surface area available per gram of α -Fe₂O₃. Deposition and growth of α -Fe₂O₃ nanoparticles on the MWCNTs, while consuming some reactive surface area via contact with the underlying substrate, appears to limit extensive interaction between α -Fe₂O₃ nanoparticles (see Figure 5-2), in turn increasing the amount of surface area per gram of α -Fe₂O₃ available to Cu(II) at the particle-water interface.

Evidence also supports, however, unique surface chemistry of the hybrid nanomaterials relative to their building blocks. Figure 5-6 examines the functional relationship between adsorbed Cu(II) (in mg/g of either MWCNT or α -Fe₂O₃) and solution pH. Data from the pH edge experiments (shown in Figure 5-5) are now presented on a log-log scale, more clearly illustrating the unique pH dependence exhibited by 0.5 g/g α -Fe₂O₃/MWCNT relative to the relationships observed for MWCNTs and α -Fe₂O₃. Notably, based on the slopes of best-fit regression lines shown in Figure 5-6, uptake of Cu(II) on 0.5 g/g α -Fe₂O₃/MWCNT is most sensitive to increasing pH relative to adsorption on oxidized MWCNTs and α -Fe₂O₃ nanoparticles. We contend that if the increased activity of hybrid nanomaterial sorbents was entirely the

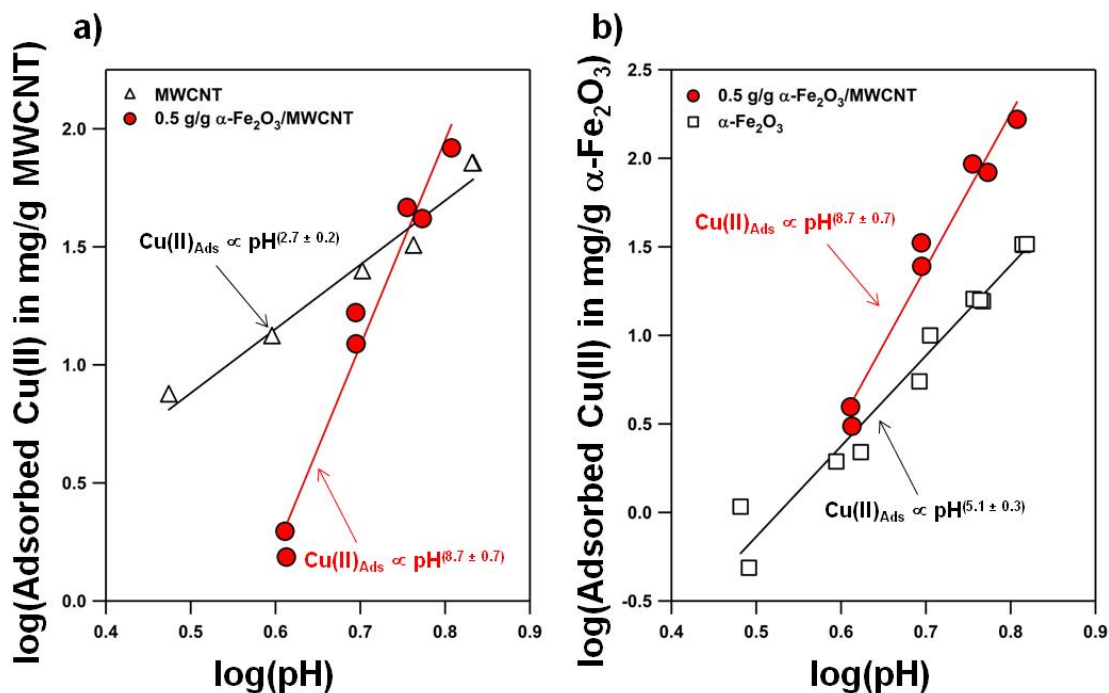


Figure 5-6. Data from pH edge adsorption experiments presented on a log-log scale for adsorbed concentrations of Cu(II) normalized by the total mass of (a) MWCNT and (b) $\alpha\text{-Fe}_2\text{O}_3$ in suspension. Lines represent best-fits from linear regression analyses. The equations provided show the slope of these best fit regression lines for each sorbent material, revealing that 0.5 g/g $\alpha\text{-Fe}_2\text{O}_3$ /MWCNT is the sorbent most sensitive with respect to changes in suspension pH.

result of increases in available α -Fe₂O₃ surface area, then similar pH dependencies between MWCNT-immobilized and suspended α -Fe₂O₃ particles would be observed. Rather, evidence suggests that α -Fe₂O₃ grown on MWCNTs exhibit unique reactivity that is distinct from that of either oxidized MWCNTs or α -Fe₂O₃ nanoparticles.

Adsorption Isotherms for Cu(II)

Trends in Cu(II) adsorption examined over a range of initial aqueous Cu(II) concentrations at pH 6 are shown in Figure 5-7. As with pH edge data, the amount of adsorbed Cu(II) is presented after normalization by the mass concentration of MWCNT (Figure 5-7a with units of mg Cu(II)/g MWCNT) and α -Fe₂O₃ (Figure 5-7b with units of mg Cu(II)/g α -Fe₂O₃) available in suspension. Sorption isotherms are presented for oxidized MWCNTs, α -Fe₂O₃ nanoparticles and 0.07 and 0.5 g/g α -Fe₂O₃/MWCNT. For all sorbents, isotherms followed Langmuir-type adsorption, and Langmuir model fits obtained from non-linear regression analyses are also shown in Figure 5-7, along with best-fit values for model parameters including the Langmuir coefficient (K) and the maximum adsorption capacity (Γ_{\max}) for each material.

As expected from pH edge experiments, 0.5 g/g α -Fe₂O₃/MWCNT considerably outperformed MWCNTs and α -Fe₂O₃ on a per mass basis. Most notable, however, are the isotherm results obtained for the hybrid nanostructures with a lower loading of α -Fe₂O₃ (0.07 g/g) on MWCNTs. When normalized to MWCNT mass (Figure 5-7a), 0.07 g/g α -Fe₂O₃/MWCNT exhibited comparable performance relative to oxidized MWCNTs at pH 6. While it may be tempting to attribute the uptake of Cu(II) on 0.07 g/g α -Fe₂O₃/

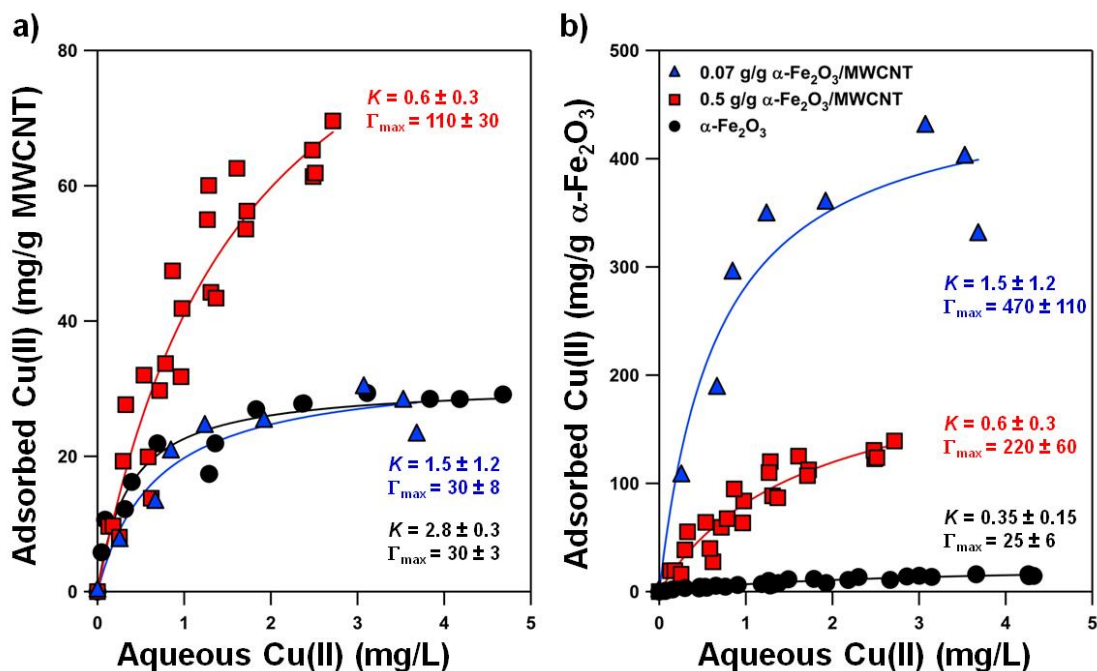


Figure 5-7. Cu(II) adsorption isotherms at pH 6.0 in suspensions of oxidized MWCNTs, $\alpha\text{-Fe}_2\text{O}_3$ nanoparticles and 0.07 and 0.5 g/g $\alpha\text{-Fe}_2\text{O}_3$ /MWCNT hybrid nanostructures. Adsorbed concentrations of Cu(II) are presented after normalization by the total mass of (a) MWCNT and (b) $\alpha\text{-Fe}_2\text{O}_3$ in suspension. Experiments were conducted in 25 mM NaCl without pH buffer at suspensions concentrations of 0.05 g/L for MWCNT and $\alpha\text{-Fe}_2\text{O}_3$ /MWCNTs hybrid nanomaterials and 0.05 and 0.1 g/L for $\alpha\text{-Fe}_2\text{O}_3$ nanoparticles. Lines represent Langmuir model fits obtained from non-linear regression analysis. Best fit Langmuir isotherm parameters (i.e., the Langmuir isotherm coefficient, K , and the maximum adsorbed Cu(II) concentration, Γ_{\max} for the units shown) are presented for each sorbent material.

MWCNT entirely to interactions of Cu(II) with the underlying MWCNT substrate, we note that appreciable uptake in these low iron hybrid systems was not observed below pH 6. Because pH edge experiments with oxidized MWCNTs (see Figure 5-5a) revealed measureable uptake of Cu(II) at pH 4 and 5, similar pH-dependent behavior would also be expected for 0.07 g/g α -Fe₂O₃/MWCNT if Cu(II) uptake was driven entirely by the underlying MWCNT substrate in these systems. Thus, we conclude that the deposited hematite nanoparticles must contribute to, if not dominate, the Cu(II) uptake observed in isotherm experiments at pH 6 with 0.07 g/g α -Fe₂O₃/MWCNT.

If Cu(II) adsorption on 0.07 g/g α -Fe₂O₃/MWCNT is driven primarily by the deposited hematite nanoparticles, then these α -Fe₂O₃ particles are highly reactive on a per mass basis relative to the α -Fe₂O₃ nanoparticles in other sorbent systems. Normalization of adsorbed Cu(II) concentrations by available α -Fe₂O₃ mass in suspension (Figure 5-7b) suggests hematite on the 0.07 g/g α -Fe₂O₃/MWCNT exhibits an extraordinary capacity for Cu(II) uptake that is roughly an order of magnitude (200-fold) greater than the α -Fe₂O₃ nanoparticles in suspension.

As with 0.5 g/g α -Fe₂O₃/MWCNTs, the superior reactivity per mass of α -Fe₂O₃ likely arises, in part, from the greater degree of available hematite surface area in 0.07 g/g α -Fe₂O₃/MWCNT suspensions. We also propose it reflects the unique surface chemistry inherent to the 0.07 g/g α -Fe₂O₃/MWCNT nanostructures. Zeta potential measurements at pH 6 (see Figure 5-3) revealed the surface charge on 0.07 g/g α -Fe₂O₃/MWCNT to be more negative than other hematite-containing adsorbents, presumably due to the large

negative charge associated with the MWCNT substrate used to immobilize the hematite nanoparticles. This negatively charged surface should be more ideal for Cu(II) sorption; favorable electrostatics will promote interaction between negatively charged surface sites and positively charged Cu(II) ions. Note that complexation with hydroxide ions (OH^-) yields equimolar concentrations of Cu^{2+} and $\text{Cu}(\text{OH})^+$ at pH 6.3 [65]. Thus, for freely suspended hematite nanoparticles or hematite nanoparticles on the 0.5 g/g α - Fe_2O_3 /MWCNT surface, both of which are more positively charged at pH 6.0, electrostatic interactions between dissolved Cu complexes and the sorbent surface will be weaker. Finally, we must not discount the potential for unique size-dependent reactivity for hematite on the surface of 0.07 g/g α - Fe_2O_3 /MWCNT. Recall the size of hematite particles grown on MWCNT surfaces are roughly 6 and 9 nm in diameter for 0.07 and 0.5 g/g α - Fe_2O_3 /MWCNT nanostructures, respectively. Notably, most size-dependent properties (so-called “nanoeffects”) are observed below a size threshold of 10 nm [66], and this may also explain the superior mass normalized reactivity of 0.07 g/g α - Fe_2O_3 /MWCNT nanostructures.

Adsorption of Chromate (CrO_4^{2-})

The pH-dependent sorption of chromate (CrO_4^{2-}) on freely suspended α - Fe_2O_3 nanoparticles and 0.5 g/g α - Fe_2O_3 /MWCNT hybrid nanostructures is shown in Figure 5-8. Notably, CrO_4^{2-} sorption on MWCNTs was not observed over the entire pH range, as was anticipated from the unfavorable electrostatic interactions between the negatively charged MWCNT surface and CrO_4^{2-} . For hematite-containing sorbents, the amount of adsorbed

CrO_4^{2-} decreased with increasing pH, as is the expected behavior for anionic uptake on iron oxides [29]. When normalized to the available mass of hematite for each sorbent system, 0.5 g/g $\alpha\text{-Fe}_2\text{O}_3/\text{MWCNT}$ hybrid nanostructures are once again superior adsorbents. This is particularly evident at low pH values ($\text{pH} < 6$), whereas the difference in CrO_4^{2-} uptake between sorbent systems narrowed slightly with increasing pH increases.

Sorption isotherms with CrO_4^{2-} were also conducted at pH 2 and pH 6 (Figure 5-9). Isotherms were modeled assuming a Langmuir-type sorption process (note that adsorption reversibility, a key assumption of the Langmuir isotherm, was not tested). Consistent with the trends observed in pH edge experiments, the 0.5 g/g $\alpha\text{-Fe}_2\text{O}_3/\text{MWCNT}$ hybrid nanostructures exhibit roughly a 3-fold greater sorption capacity than freely suspended hematite nanoparticles at pH 2 based upon Γ_{max} values obtained from Langmuir model fits. At pH 6, on the other hand, mass normalized concentrations of adsorbed CrO_4^{2-} were roughly two-fold greater for 0.5 g/g $\alpha\text{-Fe}_2\text{O}_3/\text{MWCNT}$ relative to freely suspended hematite nanoparticles.

As with Cu(II) sorption, the enhanced sorption activity of 0.5 g/g $\alpha\text{-Fe}_2\text{O}_3/\text{MWCNT}$ toward CrO_4^{2-} may be partially attributed to an increase in available hematite surface area in hybrid nanostructure suspensions relative to freely suspended, and extensively aggregated, hematite nanoparticles. Once again, however, there is evidence to support a scenario in which hematite nanoparticles grown on MWCNT possess reactivity that is fundamentally different from their suspended analogues. Specifically, pH-dependent sorption data for CrO_4^{2-} reveal that uptake is essentially independent below pH 5 in suspensions of hematite nanoparticles. However, mass-

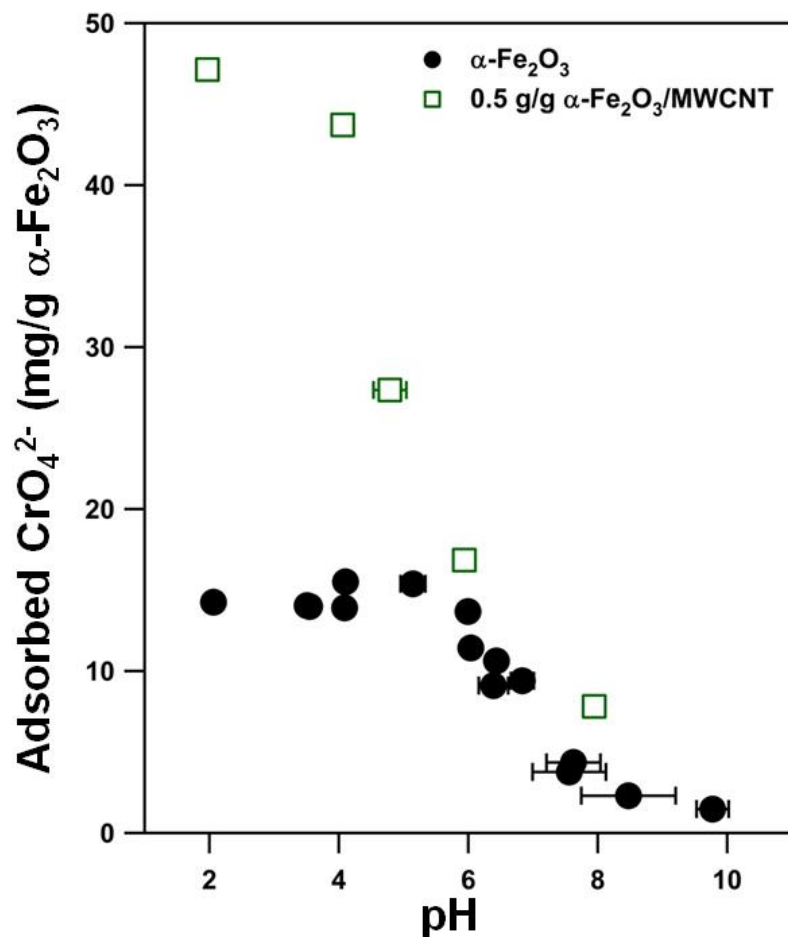


Figure 5-8. Adsorption of CrO_4^{2-} as a function of pH in suspensions of $\alpha\text{-Fe}_2\text{O}_3$ nanoparticles and 0.5 g/g $\alpha\text{-Fe}_2\text{O}_3/\text{MWCNT}$ hybrid nanostructures. Adsorbed concentrations of CrO_4^{2-} are presented after normalization by the total mass of hematite in suspension. Experiments were conducted in 25 mM NaCl without pH buffer, where pH values represent the average value over the duration of the adsorption experiment (1 h) based upon measurements at the start and end of reaction. The uncertainties associated with these average pH value represent the standard deviation associated with the initial and final pH value measured in the adsorption experiment. Experiments used an initial CrO_4^{2-} concentration of 15 μM (1.7 mg/L), and suspensions concentrations of 0.05 g/L for $\alpha\text{-Fe}_2\text{O}_3/\text{MWCNT}$ (based on total MWCNT mass) and 0.05 and 0.1 g/L for $\alpha\text{-Fe}_2\text{O}_3$ nanoparticles. No adsorption was observed on the surface of oxidized MWCNTs, as would be expected from the unfavorable electrostatic interactions between anionic CrO_4^{2-} and the negatively charged MWCNT surface.

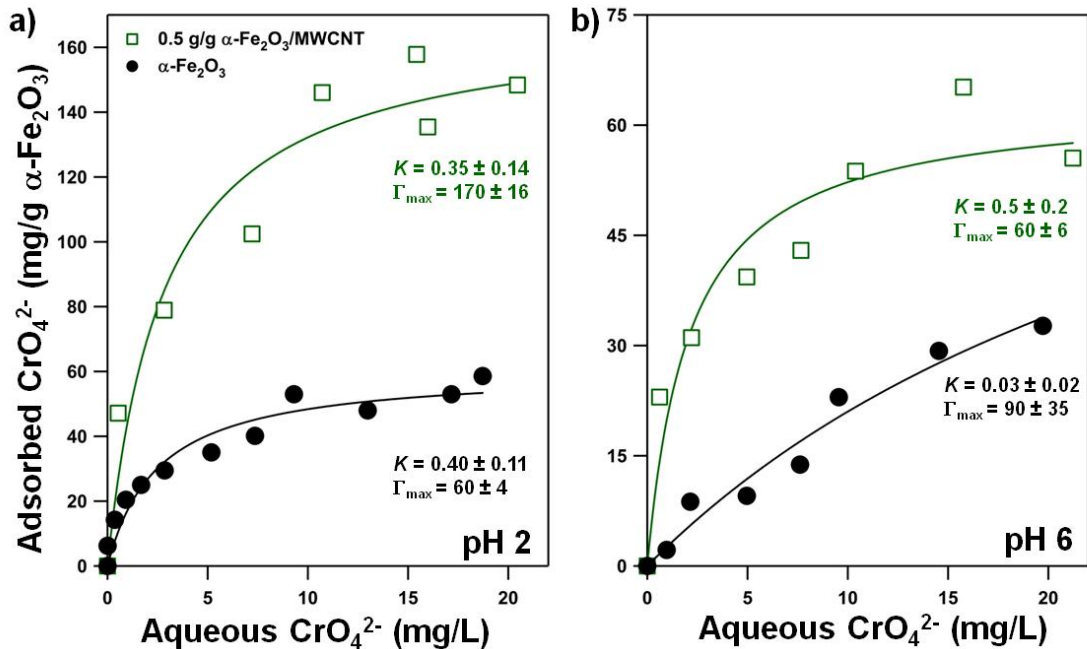


Figure 5-9. CrO_4^{2-} adsorption isotherms at (a) pH 2.0 and (b) pH 6.0 in suspensions of $\alpha\text{-Fe}_2\text{O}_3$ nanoparticles and 0.5 g/g $\alpha\text{-Fe}_2\text{O}_3/\text{MWCNT}$ hybrid nanostructures. Adsorbed concentrations of CrO_4^{2-} are presented after normalization by the total hematite mass in each suspension. Experiments were conducted in 25 mM NaCl without pH buffer at suspension concentrations of 0.05 g/L for $\alpha\text{-Fe}_2\text{O}_3/\text{MWCNT}$ s hybrid nanomaterials (based on total MWCNT mass) and 0.05 and 0.1 g/L for $\alpha\text{-Fe}_2\text{O}_3$ nanoparticles. Lines represent Langmuir model fits obtained from non-linear regression analysis. Best fit Langmuir isotherm parameters (i.e., the Langmuir isotherm coefficient, K , and the maximum adsorbed CrO_4^{2-} concentration, Γ_{max} for the units shown) are presented for each sorbent material.

normalized concentrations of adsorbed CrO_4^{2-} nearly doubled from pH 5 to pH 2 in hybrid nanostructure suspensions. The different dependence exhibited by 0.5 g/g α - Fe_2O_3 /MWCNT at low pH values suggests that the surface sites present on the hematite deposited on MWCNTs exhibit unique reactivity relative to hematite nanoparticles suspended in solution

5.5. Environmental Significance

Advanced materials will play a prominent role in society's progress toward more sustainable water supplies. Here, we show that a novel class of hybrid nanomaterial can considerably outperform both traditional (i.e., α - Fe_2O_3 particles) and emerging (i.e., oxidized MWCNTs) sorbent materials. From a practical perspective, the value of these hybrid nanostructures is not limited to simply their superior capacity for Cu(II) and CrO_4^{2-} . Notably, the deposition and growth of α - Fe_2O_3 on MWCNT does not significantly change suspension stability. Thus, aggregation of these α - Fe_2O_3 /MWCNT nanostructures will be limited over environmentally relevant pH values, and potentially over a broad range of water chemistries, in turn maximizing their reactive surface area during treatment applications.

The results with 0.07 g/g α - Fe_2O_3 /MWCNT are most promising because these materials provide the clearest example of a hybrid nanostructure exhibiting unique physicochemical properties relative to the individual nanomaterials from which it was constructed. Specifically, the zeta potential values measured for these materials are

different from values measured independently for α -Fe₂O₃ nanoparticles and MWCNTs. The key variable in governing surface chemical activity appears to be the amount of α -Fe₂O₃ deposited. Accordingly, the surface chemistry of these hybrid nanostructures is highly tunable. While this work was limited to only two loadings of α -Fe₂O₃ on MWCNT, there is the potential that other synthetic formulations can be developed that will further optimize reactivity toward Cu(II) and CrO₄²⁻. It is also likely that the surface chemistry of α -Fe₂O₃/MWCNT nanomaterials can be tailored to optimize treatment efficiency of alternative targets of concern in water and wastewater.

5.6. Acknowledgements

The authors would like to acknowledge the Central Facility for Advanced Microscopy (CFAMM) at U.C. Riverside for assistance with TEM imaging, Dr. Jonas Baltrusaitis of the Central Microscopy Research Facility (CMRF) at the University of Iowa for assistance with HR-TEM/EELS and SAED analysis, and Dr. Yan Lin for assistance on the synthesis, characterization and adsorption studies with each sorbent material.

5.7. Literature Cited

1. Iijima, S., Helical Microtubules of Graphitic Carbon. *Nature* **1991**, *354*, 56-58.
2. Schadler, L.S.; Giannaris, S.C.; Ajayan, P.M., Load Transfer in Carbon Nanotube Epoxy Composites. *Appl. Phys. Lett.* **1998**, *73*, 3842-3844.
3. Dillon, A.C.; Jones, K.M.; Bekkedahl, T.A.; Kiang, C.H.; Bethune, D.S.; Heben, M.J., Storage of Hydrogen in Single-Walled Carbon Nanotubes. *Nature* **1997**, *386*, 377-379.
4. Tang, Z.K.; Zhang, L.; Wang, N.; Zhang, X.X.; Wen, G.H.; Li, G.D.; Wang, J.N.; Chan, C.T.; Sheng, P., Superconductivity in 4 Angstrom Single-Walled Carbon Nanotubes. *Science* **2001**, *292*, 2462-2465.
5. Mauter, M.S.; Elimelech, M., Environmental Applications of Carbon-Based Nanomaterials. *Environ. Sci. Technol.* **2008**, *42*, 5843-5859.
6. Li, Y.-H.; Ding, J.; Luan, Z.; Di, Z.; Zhu, Y.; Xu, C.; Wu, D.; Wei, B., Competitive Adsorption of Pb^{2+} , Cu^{2+} and Cd^{2+} Ions from Aqueous Solutions by Multiwalled Carbon Nanotubes. *Carbon* **2003**, *41*, 2787-2792.
7. Li, Y.-H.; Luan, Z.; Xiao, X.; Zhou, X.; Xu, C.; Wu, D.; Wei, B., Removal of Cu^{2+} Ions from Aqueous Solutions by Carbon Nanotubes. *Ads. Sci. Technol.* **2003**, *21*, 475-485.
8. Li, Y.-H.; Wang, S.; Luan, Z.; Ding, J.; Xu, C.; Wu, D., Adsorption of Cadmium(II) from Aqueous Solution by Surface Oxidized Carbon Nanotubes. *Carbon* **2003**, *41*, 1057-1062.
9. Anna, M.; et al., The Role of Metal Nanoparticles in the Catalytic Production of Single-Walled Carbon Nanotubes: Review. *J. Phys. Condensed Matter* **2003**, *15*, S3011.
10. Makar, J.M.; Beaudoin, J.J., Carbon Nanotubes and Their Application in the Construction Industry. *1st International Symposium on Nanotechnology in Construction* **2010**, 11.
11. Bianco, A.; Kostarelos, K.; Prato, M., Applications of Carbon Nanotubes in Drug Delivery. *Current Opinion in Chemical Biology* **2005**, *9*, 674-679.
12. Tang, X.; Bansaruntip, S.; Nakayama, N.; Yenilmez, E.; Chang, Y.-l.; Wang, Q., Carbon Nanotube DNA Sensor and Sensing Mechanism. *Nano Lett.* **2006**, *6*, 1632-1636.

13. Ning, G.Q.; Wei, F.; Luo, G.H.; Wang, Q.X.; Wu, Y.L.; Yu, H., Hydrogen Storage in Multi-Wall Carbon Nanotubes Using Samples up to 85 G. *Appl. Phys. A. Mater. Sci. Process.* **2004**, *78*, 955-959.
14. Shi, W.; Johnson, J.K., Gas Adsorption on Heterogeneous Single-Walled Carbon Nanotube Bundles. *Phys. Rev. Lett.* **2003**, *91*, 015504.
15. Santucci, S.; Picozzi, S.; Di Gregoria, F.; Lozzi, L.; Cantalini, C.; Velentini, L.; Kenny, J.M.; Delley, B., NO₂ and CO Gas Adsorption on Carbon Nanotubes: Experiment and Theory. *J. Chem. Phys.* **2003**, *119*, 7.
16. Lu, C.; Chung, Y.-L.; Chang, K.-F., Adsorption of Trihalomethanes from Water with Carbon Nanotubes. *Water Res.* **2005**, *39*, 1183-1189.
17. Long, R.Q.; Yang, R.T., Carbon Nanotubes as Superior Sorbent for Dioxin Removal. *J. Am. Chem. Soc.* **2001**, *123*, 2058-2059.
18. Li, Y.-H.; Wang, S.; Wei, J.; Zhang, X.; Xu, C.; Luan, Z.; Wu, D.; Wei, B., Lead Adsorption on Carbon Nanotubes. *Chem. Phys. Lett.* **2002**, *357*, 263-266.
19. Wang, X.; Chen, C.; Hu, W.; Ding, A.; Xu, D.; Zhou, X., Sorption of ²⁴³Am(III) to Multiwall Carbon Nanotubes. *Environ. Sci. Technol.* **2005**, *39*, 2856-2860.
20. Chen, C.; Wang, X., Adsorption of Ni(II) from Aqueous Solution Using Oxidized Multiwall Carbon Nanotubes. *Ind. Eng. Chem. Res.* **2006**, *45*, 9144-9149.
21. Lu, C.; Chiu, H., Adsorption of Zinc(II) from Water with Purified Carbon Nanotubes. *Chem. Eng. Sci.* **2006**, *61*, 1138-1145.
22. Smith, B.; Wepasnick, K.; Schrote, K.E.; Bertele, A.R.; Ball, W.P.; O'Melia, C.; Fairbrother, D.H., Colloidal Properties of Aqueous Suspensions of Acid-Treated, Multi-Walled Carbon Nanotubes. *Environ. Sci. Technol.* **2008**, *43*, 819-825.
23. Smith, B.; Wepasnick, K.; Schrote, K.E.; Cho, H.-H.; Ball, W.P.; Fairbrother, D.H., Influence of Surface Oxides on the Colloidal Stability of Multi-Walled Carbon Nanotubes: A Structure-Property Relationship. *Langmuir* **2009**, *25*, 9767-9776.
24. Hu, J.; Chen, G.; Lo, I.M.C., Removal and Recovery of Cr(VI) from Wastewater by Maghemite Nanoparticles. *Water Res.* **2005**, *39*, 4528-4536.
25. Hu, J.; Lo, M.C.; Chen, G.H., Adsorption of Cr(VI) by Magnetite Nanoparticles. *Water Sci. Technol* **2004**, *50*, 139-146.

26. Wang, P.; Lo, I.M.C., Synthesis of Mesoporous Magnetic γ -Fe₂O₃ and Its Application to Cr(VI) Removal from Contaminated Water. *Water Res.* **2009**, *43*, 3727-3734.
27. Mayo, J.T.; Yavuz, C.; Yean, S.; Cong, L.; Shipley, H.; Yu, W.; Falkner, J.; Kan, A.; Tomson, M.; Colvin, V.L., The Effect of Nanocrystalline Magnetite Size on Arsenic Removal. *Sci. Technol. Adv. Mater.* **2007**, *8*, 71-75.
28. Shipley, H.J.; Yean, S.; Kan, A.T.; Tomson, M.B., Adsorption of Arsenic to Magnetite Nanoparticles: Effect of Particle Concentration, pH, Ionic Strength, and Temperature. *Environ. Toxicol. Chem.* **2009**, *28*, 509-515.
29. Cornell, R.M.; Schwertmann, U., *The Iron Oxides: Structure, Properties, Reactions, Occurrences and Uses* 2nd ed.; Wiley-VCH: Weinheim, Germany, 2003; p 664.
30. Waychunas, G.A.; Kim, C.S.; Banfield, J.F., Nanoparticulate Iron Oxide Minerals in Soils and Sediments: Unique Properties and Contaminant Scavenging Mechanisms. *J. Nanopart. Res.* **2005**, *7*, 409-433.
31. He, Y.T.; Wan, J.; Tokunaga, T., Kinetic Stability of Hematite Nanoparticles: The Effect of Particle Sizes. *J. Nanopart. Res.* **2008**, *10*, 12.
32. Yean, S.; Cong, L., Effect of Magnetite Particle Size on Adsorption and Desorption of Arsenite and Arsenate. *J. Mater. Res.* **2005**, *20*, 3255-3264.
33. Vikesland, P.J.; Heathcock, A.M.; Rebodos, R.L.; Makus, K.E., Particle Size and Aggregation Effects on Magnetite Reactivity toward Carbon Tetrachloride. *Environ. Sci. Technol.* **2007**, *41*, 5277-5283.
34. Oliveira, L.C.A.; Rios, R.V.R.A.; Fabris, J.D.; Garg, V.; Sapag, K.; Lago, R.M., Activated Carbon/Iron Oxide Magnetic Composites for the Adsorption of Contaminants in Water. *Carbon* **2002**, *40*, 2177-2183.
35. Oliveira, L.C.A.; Rios, R.V.R.A.; Fabris, J.D.; Sapag, K.; Garg, V.K.; Lago, R.M., Clay Iron Oxide Magnetic Composites for the Adsorption of Contaminants in Water. *Appl. Clay Sci.* **2003**, *22*, 169-177.
36. Wang, Y.; Wu, M.; Jiao, Z.; Lee, J.Y., Sn@CNT and Sn@C@CNT Nanostructures for Superior Reversible Lithium Ion Storage. *Chem. Mater.* **2009**, *21*, 3210-3215.
37. Velamakanni, A.; Magnuson, C.W.; Ganesh, K.J.; Zhu, Y.; An, J.; Ferreira, P.J.; Ruoff, R.S., Site-Specific Deposition of Au Nanoparticles in CNT Films by Chemical Bonding. *ACS Nano* **2010**, *4*, 4962-4962.

38. Xu, L.; Zhu, Y.; Tang, L.; Yang, X.; Li, C., Biosensor Based on Self-Assembling Glucose Oxidase and Dendrimer-Encapsulated Pt Nanoparticles on Carbon Nanotubes for Glucose Detection. *Electroanalysis* **2007**, *19*, 717-722.
39. Jung, J.H.; Hwang, G.B.; Lee, J.E.; Bae, G.N., Preparation of Airborne Ag/Cnt Hybrid Nanoparticles Using an Aerosol Process and Their Application to Antimicrobial Air Filtration. *Langmuir* **2010**, *27*, 10256-10264.
40. Kim, H.-S.; Lee, H.; Han, K.-S.; Kim, J.-H.; Song, M.-S.; Park, M.-S.; Lee, J.-Y.; Kang, J.-K., Hydrogen Storage in Ni Nanoparticle-Dispersed Multiwalled Carbon Nanotubes. *J. Phys. Chem. B* **2005**, *109*, 8983-8986.
41. Yoon, B.; Wai, C.M., Microemulsion-Templated Synthesis of Carbon Nanotube-Supported Pd and Rh Nanoparticles for Catalytic Applications. *J. Am. Chem. Soc.* **2005**, *127*, 17174-17175.
42. Zhu, Y.; Elim, H.I.; Foo, Y.L.; Yu, T.; Liu, Y.; Ji, W.; Lee, J.Y.; Shen, Z.; Wee, A.T.S.; Thong, J.T.L.; Sow, C.H., Multiwalled Carbon Nanotubes Beaded with ZnO Nanoparticles for Ultrafast Nonlinear Optical Switching. *Adv. Mater.* **2006**, *18*, 587-592.
43. An, J.W.; You, D.H.; Lim, D.S., Tribological Properties of Hot-Pressed Alumina-Cnt Composites. *Wear* **2003**, *255*, 677-681.
44. Zhang, Y.; Franklin, N.W.; Chen, R.J.; Dai, H., Metal Coating on Suspended Carbon Nanotubes and Its Implication to Metal-Tube Interaction. *Chem. Phys. Lett.* **2000**, *331*, 35-41.
45. Peng, X.; Chen, J.; Misewich, J.A.; Wong, S., Carbon Nanotube-Nanocrystal Heterostructures. *Chem. Soc. Rev.* **2009**, *38*, 1076-1098.
46. Georgakilas, V.; Gournis, D.; Tzitzios, V.; Pasquato, L.; Guldi, D.M.; Prato, M., Decorating Carbon Nanotubes with Metal or Semiconductor Nanoparticles. *J. Mater. Chem.* **2007**, *17*, 2679-2694.
47. Hu, X.; Dong, S., Metal Nanomaterials and Carbon Nanotubes-Synthesis, Functionalization and Potential Applications Towards Electrochemistry. *J. Mater. Chem.* **2008**, *18*, 1279-1295.
48. Mishra, A.K.; Ramaprabhu, S., Magnetite Decorated Multiwalled Carbon Nanotube Based Supercapacitor for Arsenic Removal and Desalination of Seawater. *J. Phys. Chem. C.* **2010**, *114*, 2583-2590.

49. Qu, S.; Wang, J.; Kong, J.; Yang, P.; Chen, G., Magnetic Loading of Carbon Nanotube/Nano-Fe₃O₄ Composite for Electrochemical Sensing. *Talanta* **2007**, *71*, 1096-1102.
50. Huang, Z.; Li, J.; Chen, Q.; Wang, H., A Facile Carboxylation of CNT/Fe₃O₄ Composite Nanofibers for Biomedical Applications. *Mater. Chem. Phys.* **2009**, *114*, 33-36.
51. Wan, J.; Cai, W.; Feng, J.; Meng, X.; Liu, E., In Situ Decoration of Carbon Nanotubes with Nearly Monodisperse Magnetite Nanoparticles in Liquid Polyols. *J. Mater. Chem.* **2007**, *17*, 1188-1192.
52. Chen, C.; Hu, J.; Shao, D.; Li, J.; Wang, X., Adsorption Behavior of Multiwall Carbon Nanotube/Iron Oxide Magnetic Composites for Ni(II) and Sr(II). *J. Haz. Mater.* **2009**, *164*, 923-928.
53. Gong, J.-L.; Wang, B.; Zeng, G.-M.; Yang, C.-P.; Niu, C.-G.; Niu, Q.-Y.; Zhou, W.-J.; Liang, Y., Removal of Cationic Dyes from Aqueous Solution Using Magnetic Multi-Wall Carbon Nanotube Nanocomposite as Adsorbent. *J. Haz. Mater.* **2009**, *164*, 1517-1522.
54. Wepasnick, K.; Smith, B.A.; Bitter, J.L.; Fairbrother, D.H., Chemical and Structural Characterization of Carbon Nanotube Surfaces. *Anal. Bioanal. Chem.* **2010**, *396*, 1003-1014.
55. Wepasnik, K.A.; Smith, B.A.; Schrote, K.E.; Wilson, H.K.; Diegelmann, S.R.; Fairbrother, D.H., Surface and Structural Characterization of Multi-Walled Carbon Nanotubes Following Different Oxidated Treatments. *Carbon* **2011**, *49*, 24-36.
56. Schwertmann, U.; Cornell, R.M., *Iron Oxides in the Laboratory: Preparation and Characterization*. 2nd ed.; Wiley-VCH: New York, 2000.
57. Sorum, C.H., The Preparation of Chloride Free Colloidal Ferric Oxide from Ferric Chloride. *J. Am. Chem. Soc.* **1928**, *50*, 1263-1267.
58. United States Environmental Protection Agency. *Ground Water and Drinking Water. National Primary Drinking Water Standards*; EPA-816-F-03-016; U.S. Environmental Protection Agency, Office of Water: Washington, D.C., 2003.
59. Stucki, J.W., The Quantitative Assay of Minerals for Fe²⁺ and Fe³⁺ Using 1,10-Phenanthroline. II. A Photochemical Method. *Soil Sci. Soc. Am. J.* **1981**, *45*, 638-641.

60. Stucki, J.W.; Anderson, W.L., The Quantitative Assay of Minerals for Fe²⁺ and Fe³⁺ Using 1,10-Phenanthroline. I. Sources of Variability. *Soil Sci. Soc. Am. J.* **1981**, *45*, 633-637.
61. Bose, M., Mechanism of the Reaction between Dichromate and Diphenylcarbazide. *Nature* **1952**, *170*.
62. Rush, R.M.; Yoe, J.H., Colorimetric Determination of Zinc and Copper with 2-Carboxy-2'-Hydroxy-5'-Sulfoformazylbenzene. *Anal. Chem.* **1954**, *26*, 1345-1347.
63. Lanzl, C.A.; Baltrusaitis, J.; Cwiertny, D.M., Influence of Primary Particle Size on the Dissolution of Hematite Nanoparticle Aggregates. *in preparation for submission to J. Phys. Chem. C*.
64. Oulton, R.L.; Nalbandian, M.J.; Cwiertny, D.M., Multi-Walled Carbon Nanotubes Increase OH Radical Production During Ozonation. *in preparation for submission to Environ. Sci. Technol.*
65. Morel, F.M.M.; Hering, J.G., *Principles and Applications of Aquatic Chemistry*. Wiley-Interscience: New York, 1993.
66. Auffan, M.; Rose, J.; Bottero, J.-Y.; Lowry, G.V.; Jolivet, J.-P.; Wiesner, M.R., Towards a Definition of Inorganic Nanoparticles from an Environmental Health and Safety Perspective. *Nature Nanotechnology* **2009**, *4*, 634-641.

6. Conclusions

6.1. Predicting nanoscale zero-valent iron longevity in complex geochemical environments

Prior to this work, limited information was available regarding the timescales over which nanoscale zero-valent iron (NZVI) remained redox active. Most prior work had considered reactivity loss in relatively idealized systems, in which no attempts were made to control suspension pH or to examine the influence that common co-solutes in groundwater exert on NZVI reactive lifetime or longevity. Both pH control and co-solute effects merit consideration during such studies to better simulate groundwater geochemical conditions. Mass loadings of NZVI delivered to the subsurface (typically 1.9-30 g/L) [1] may not be high enough to overcome the buffering capacity typically encountered in most groundwater and soil systems. While co-solute effects for larger-scale, micron-to-millimeter sized granular iron are relatively well understood [2-4], the enhanced rates of corrosion reported for NZVI make it difficult to predict *a priori* the timescales and magnitude over which co-solutes influence NZVI corrosion product formation, and in turn, system reducing capacity.

Work in Chapter 2 quantifies NZVI lifetime over a range of geochemical conditions, in which experimental variables include co-solute anion identity and concentration, environmentally relevant pH values, and different pollutant (oxidant) classes. Experiments aged 2 g/L suspensions of NZVI in oxygen-free systems in the absence of a pollutant, modeling a system in which reaction with water (i.e., corrosion)

represents the dominant mode of NZVI reactivity loss (i.e., passivation). Collectively, batch experiments monitored the reactivity change of NZVI towards model pollutants 1,1,1,2-tetrachloroethane (1,1,1,2-TeCA) and hexavalent chromium [Cr(VI)] over one month during this aging protocol. Reactive lifetime or longevity of NZVI towards 1,1,1,2-TeCA in the presence of Cl^- , SO_4^{2-} and ClO_4^- lasted approximately 30 days, over which reactivity loss was on the order of 95%. This reactive lifetime is considerably shorter than those reported previously when NZVI was aged under more idealized conditions. For 1,1,1,2-TeCA reduction, the longevity of NZVI was relatively insensitive to the concentration of these three anions, nor did it vary significantly over the range of pH values considered (pH 7 and 8). For chlorinated solvent reduction, therefore, sites impacted by these particular anions (i.e., Cl^- , SO_4^{2-} and ClO_4^-) appear to be most ideal with respect to minimizing the impact of co-solute anions on NZVI longevity.

The lifetime of NZVI was considerably shorter in the presence of HCO_3^- and NO_3^- , with reactivity toward 1,1,1,2-TeCA lasting anywhere between 1 and 14 days depending on the anion concentration at both pH 7 and 8. Specifically, NZVI suspensions containing low HCO_3^- concentration (5 mM) exhibited comparable longevity to Cl^- , SO_4^{2-} and ClO_4^- , with measurable reactivity toward 1,1,1,2-TeCA over 30 days. In contrast, an increase to 25 mM concentration shortened NZVI longevity to 14 days. Similar concentration-dependent behavior for nitrate-containing NZVI suspensions produced a lifetime toward 1,1,1,2-TeCA lasting anywhere from 1 day (at 25 mM) to 30 days (at 5 mM).

Interestingly, the longevity of NZVI toward Cr(VI), the other model groundwater pollutant considered, exhibited vastly different trends than those observed for 1,1,1,2-TeCA. For instance, pH exerted a far more significant influence on NZVI longevity toward Cr(VI), whereas the anion concentration had little impact. Specifically, in the presence of Cl^- , SO_4^{2-} , ClO_4^- and HCO_3^- , Cr(VI) removal capacity at pH 7 was approximately 2-3 times greater than that at pH 8, and, most notably, activity toward Cr(VI) was sustained over entire duration of aging (30 d) in nearly all systems including nitrate.

The primary conclusion drawn from all reactivity data collected over time is that different entities are responsible for reduction of 1,1,1,2-TeCA and Cr(VI) in aged NZVI suspensions. Available Fe(0) content governed 1,1,1,2-TeCA transformation. Thus, co-solutes that compete for reducing equivalents or that form passive surface oxides that limit the access of Fe(0) in the particle core to the solution interface both dampen reactivity and dramatically shorten longevity. In contrast, reduction of Cr(VI) was controlled by the amount of Fe(II) generated during Fe(0) corrosion, as supported by a clear linear relationship between the Fe(II) production rate and extent of Cr(VI) removal in aged suspensions.

The practical implication to be drawn from results in Chapter 2 is that knowledge of groundwater characteristics will be imperative in assessing whether NZVI application is suitable at a particular contaminant site. Clearly, those groundwaters that are low in alkalinity and do not have nitrate as a co-contaminant are most ideally suited for NZVI performance toward chlorinated solvents. At sites with high alkalinity or background

nitrate, as is the case for the chlorinated solvent plume present at 100D Area of the Hanford Site in Washington [5], alternative treatment strategies will merit consideration.

Another clear implication of the work in Chapter 2 is that not only NZVI reactivity but also longevity should be viewed as target compound (i.e., oxidant) specific. Prior research has tried extensively to establish generalizable trends in Fe(0) reactivity that can be broadly applied to various pollutants over a range of solution chemistries [3, 4, 6]. However, as is exemplified by the contrasting results with 1,1,1,2-TeCA and Cr(VI) in Chapter 2, trends in longevity and co-solutes effects are compound-specific because different reactive entities are responsible for the transformation of 1,1,1,2-TeCA and Cr(VI) in aged NZVI suspensions.

Based on such considerations, work herein shows that the most effective and efficient use of NZVI is to plumes and source zones of contaminants susceptible to reduction by ferrous iron [Fe(II)]. It is well established that NZVI is a greater source of Fe(II) relative to granular Fe(0), which tends to exhibit corrosion rates that are several orders of magnitude less than those reported for NZVI. Further, during application to Fe(II)-reducible compounds, evidence herein suggests that NZVI suspensions exhibit slower rates of reactivity loss, are less influenced by co-solute anion identity and concentration, are effective over environmentally relevant pH values, and the extent of pollutant removal can likely be predicted from metrics of Fe(0) corrosion. These findings should be of interest to engineers and regulators attempting to identify whether NZVI treatment systems, which are rapidly growing in popularity, are an appropriate technology at a particular contaminant site.

6.2. Extending nanoscale zero-valent iron longevity via chemical regeneration

A major hurdle in the widespread application of nanoscale zero-valent iron for treatment of contaminated groundwater and source zone control will be the limited timescales over which reductant particles maintain their reducing capacity. Indeed, work in Chapter 2 revealed that in some groundwater systems and for specific pollutant targets, NZVI longevity may be limited to only a few days due to the formation of corrosion products on the reductant particle surface, which will limit the availability of electrons from the metallic Fe(0) particle core.

Work in Chapter 3 demonstrated that a promising approach for extending the practical lifetime of NZVI treatment zones is through the use of a chemical regenerant. In particular, dithionite, a sulfur-based reductant previously used for *in situ* redox manipulation [5, 7], represents a suitable reductant for transforming passive ferric iron corrosion products generated via air oxidation of NZVI into redox-active solid phases capable of reducing several common groundwater contaminants including Cr(VI). A noteworthy result was found during air aging of NZVI suspensions at pH 8; rapid oxidation of NZVI produced a passive shell that trapped a considerable portion of Fe(0) in the particle core, thereby suppressing the transfer of reducing equivalents to the particle-solution interface. For this scenario, relatively low levels of dithionite were used to reduce this passive surface coating and expose the underlying Fe(0) particle core, in

turn restoring reactivity of the once passivated particles toward both a chlorinated solvent (1,1,1,2-TeCA) and hexavalent chromium (Cr(VI)).

For the use of dithionite as a chemical regenerant of passivated NZVI, the key operational parameters were found to be the solution pH at which the NZVI particles underwent air oxidation, which influenced the identity of the Fe(III) oxide phases generated via oxidation, and the amount of dithionite used for regeneration, which influenced the products of its reaction with NZVI oxidation products. In particular, in systems where residual Fe(0) remained in the passivated NZVI particle core, it was critical to limit the amount of dithionite used for regeneration because excess dithionite was able to oxidize Fe(0) to produce iron sulfides that exhibited less reactivity toward 1,1,1,2-TeCA than Fe(0).

Overall, the use of dithionite as a regenerant for passivated NZVI treatment zones is very promising because the process can be repeated multiple times to sustain the long-term reactivity of the treatment zone. This in turn will increase the amount of pollutants that can be removed per gram of NZVI applied in the field. For example, experiments in Chapter 3 revealed that multiple, sequential reactions of passivated NZVI with dithionite could be used to enhance the removal capacity of Cr(VI) by roughly a factor of 15. Given concerns over the material costs associated with commercially available forms of NZVI, the ability to increase and sustain the reducing capacity of NZVI treatment zones should be attractive to engineers intending to use this technology for treatment of pollutant source zones or deep contaminant plumes in the subsurface.

6.3. Enhancing zero-valent iron reactivity through the use of noble metal surface additives

The use of palladium surface deposits to enhance Fe(0) reactivity has gained considerable popularity, resulting in numerous instances of field-scale applications of palladized iron (Pd/Fe) for treatment of contaminated groundwater plumes and pollutant source zones [8, 9]. Despite the extensive laboratory scale research and now numerous field scale applications of these so-called bimetallic reductants, relatively little remains known about the practical and theoretical considerations impacting their performance. Prior to this work, few studies attempted to identify the optimal conditions for their application, nor has any consensus regarding the mechanism of pollutant transformation in Pd/Fe systems been achieved. This is evident from the broad range of rate enhancements reported in the literature for Pd/Fe reductants relative to traditional unamended iron systems, as well as the limited amount of information regarding the influence of variables such as iron particle size (e.g., NZVI relative to micron-sized or granular zero valent iron) and oxidant concentration on Pd/Fe reactivity.

In Chapter 4, both practical and fundamental insights into the performance of Pd/Fe reductants are provided. Experiments explored the relationship between reactivity metrics for Pd/Fe reductants (e.g., pseudo-first-order rate constants for 1,1,1,2-TeCA reduction or k_{obs} values) and reductant loading (ρ_{m} values) in both unamended Fe(0) and Pd/Fe systems for commercially available granular iron (i.e., Fisher electrolytic iron) and NZVI. Notably, a more linear, first-order relationship between k_{obs} and ρ_{m} values was

observed for Pd/Fe reductants regardless of Fe(0) particle size, whereas k_{obs} values in unamended Fe(0) systems exhibited a weaker, non-linear dependence on reductant loading. Consequently, the degree of rate enhancement afforded by Pd/Fe varied considerably as a function of reductant loading in experimental systems, which likely helps to explain, at least in part, the range of rate enhancement factors reported in the literature for Pd/Fe reductants.

Another finding with practical consequence is that in Pd/NZVI systems with high chlorinated solvent concentrations, reactivity toward 1,1,1,2-TeCA was comparable to that observed in unamended NZVI systems. The similarity in reactivity between Pd/NZVI and NZVI systems is noteworthy, as it calls into question the benefit of using Pd/NZVI at sites characterized by high or near saturated concentrations of chlorinated solvent, which is typical of many groundwater plumes and pollutant source zones. The root cause of the similar reactivity between Pd/NZVI and NZVI under such conditions is not entirely understood and merits further investigation. It may reflect surface site limitations in Pd/Fe systems, where the amount of deposited Pd dictates the number of sites available for chlorinated solvent reduction. It may also reflect the ability of such high concentrations of chlorinated solvent to oxidize the reductant surface, which would work to bury Pd islands with passive Fe(III) oxides and thereby negate their rate-enhancing effect.

Fundamental insights in Chapter 4 shed new light on the mechanism of chlorinated solvent reduction in Pd/Fe and Fe(0) systems using measurements of solvent kinetic isotope effects [SKIEs; defined as $k_{\text{obs}}(\text{H}_2\text{O})/k_{\text{obs}}(\text{D}_2\text{O})$]. Notably, in Pd/Fe

systems, SKIEs change as a function of the rate enhancement provided by Pd, with the largest SKIEs occurring in systems with high Pd loading and large values of ρ_m . This observation indicates that multiple rate-determining steps for solvent reduction are available in Pd/Fe systems, and that the relative contribution of these mechanisms changes as a function of Pd and reductant loading.

Because two distinct regimes of SKIEs were observed as a function of rate enhancement, we propose that two mechanisms for chlorinated solvent reduction occur in Pd/Fe systems. One pathway involves direct electron transfer from the metallic Fe(0) core to the chlorinated solvent at the particle-solution interface via formation of a galvanic couple between Pd and Fe(0). The second mechanism, which predominates at high Pd loadings and high ρ_m values in our closed experimental systems, involves some form of reactive atomic hydrogen (e.g., adsorbed or absorbed atomic hydrogen), which is generated as an intermediate during H₂ evolution, associated with the Pd surface. Notably, evidence for atomic hydrogen formation was only observed in NZVI systems, presumably due to their far greater rate of corrosion (i.e., H₂ evolution) relative to larger scale Fe(0) particles.

These two mechanisms appear to be relevant both for saturated alkyl polyhalides (e.g., 1,1,1,2-TeCA) and π -bond containing vinyl polyhalides (e.g., *cis*-DCE). However, evidence suggests that vinyl halides are more susceptible to reduction by atomic hydrogen, as indicated by the much higher values of SKIEs measured for *cis*-DCE relative to 1,1,1,2-TeCA in otherwise identical experimental Pd/Fe systems. The largest rate enhancements were also observed for vinyl polyhalides. From a practical perspective,

therefore, Pd/Fe reductants will be best suited for the treatment of vinyl polyhalides such as *cis*-DCE and TCE, and their application should likely be limited to such plumes.

Other practical insights for Pd/NZVI reactivity were obtained through aging studies. Aging studies revealed that large SKIEs indicative of atomic hydrogen involvement only persisted on the order of two weeks in Pd/NZVI systems. Beyond two weeks, Pd/NZVI reactivity diminished and SKIEs values were relatively low, suggesting that long term reactivity in Pd/NZVI systems is attributable primarily to galvanic electron transfer. Collectively, the practical and fundamental results presented in Chapter 4 should guide the development of Pd/Fe reductants with optimal activity while also establishing the field-scale conditions and pollutant targets most ideal for their application.

6.4. Improving performance of iron-based nanomaterial sorbents through immobilization on carbon nanotube supports

Despite growing interest in the application of engineered nanomaterials in water and wastewater treatment, a major application challenge is their extensive aggregation, which consumes reactive surface area and limits their treatment capacity. Concerns also exist about the safe application of engineered nanomaterials, particularly given rising concerns over adverse human and ecological health impacts in the event of their incidental release into the environment. In this regard, application of engineered

nanomaterials as slurries is impractical, given the complications associated with separating and recovering the reactive materials from the treated product water.

In Chapter 5, hematite ($\alpha\text{-Fe}_2\text{O}_3$) nanoparticles on the order of 7 nm in diameter were grown on the surface of carboxylated multi-walled carbon nanotubes (MWCNTs) via a forced hydrolysis mechanism, and the resulting hematite decorated MWCNTs were utilized as high surface area sorbents for Cu(II) and Cr(VI). We observed several benefits of using $\alpha\text{-Fe}_2\text{O}_3$ decorated MWCNTs as sorbents relative to the more conventional application of $\alpha\text{-Fe}_2\text{O}_3$ nanoparticle sorbents in slurries or suspensions. Immobilization of $\alpha\text{-Fe}_2\text{O}_3$ on MWCNTs limited nanoparticle aggregation, thereby increasing the available surface area for metal uptake. Indeed, on a per mass basis at pH 6, a much greater degree of Cu(II) uptake was observed for $\alpha\text{-Fe}_2\text{O}_3$ -MWCNTs hybrid nanostructures relative to $\alpha\text{-Fe}_2\text{O}_3$ nanoparticles suspended as aggregates in solution. Notably, heterogeneous deposition and growth of $\alpha\text{-Fe}_2\text{O}_3$ on MWCNTs allows for a high degree of control of sorbent properties, with both the total amount of $\alpha\text{-Fe}_2\text{O}_3$ deposited and the average size of deposited $\alpha\text{-Fe}_2\text{O}_3$ nanoparticles representing tunable variables during material synthesis.

Another benefit of using hybrid $\alpha\text{-Fe}_2\text{O}_3$ -MWCNT nanostructures is that they allow for potential synergistic reactive properties in which the new material exhibits properties different from the sum of its individual parts. For example, the amount of Cu(II) sorption observed for $\alpha\text{-Fe}_2\text{O}_3$ -MWCNT hybrid nanostructures at pH 6 was greater than that predicted from the sum of Cu(II) uptake in suspensions of each

component. While this result is in part due to the greater availability of α -Fe₂O₃ surface area when grown on MWCNTs, it may also reflect unique surface chemical properties of the hybrid nanostructures. Notably, zeta potentials of the hybrid nanostructures were dependent on total α -Fe₂O₃ loading, providing a route to tune nanostructure surface chemistry to yield characteristics distinct from either pure α -Fe₂O₃ or MWCNT suspensions. Similarly, pH-dependent trends in Cu(II) and Cr(VI) adsorption on hybrid nanostructures were distinct from those trend observed with the other sorbent materials, suggesting that α -Fe₂O₃-MWCNT possess new and unique surface chemistry relative to their individual nanomaterial building blocks.

6.5. Future work

Predicting the Reactivity and Longevity of NZVI in Diverse Aquatic

Chemical Systems

The impact of a broader range of groundwater conditions on NZVI reactivity needs to be investigated. For instance, work in Chapter 3 only considered aging of NZVI in O₂-saturated water, which is unlikely for most groundwaters, and there remains the need to explore the influence of prolonged exposure to trace levels of oxygen, particularly given the large number of contaminated groundwater sites with low levels of dissolved oxygen (DO). Also, the aging mechanism considered focused primarily on reaction with water (i.e., corrosion). There remains a need to consider how NZVI longevity changes in response to continuous exposure to relatively concentrated solutions

of pollutants (e.g., chlorinated solvents or reducible metals). In most field scale applications with high concentrations of target pollutants, reactions with water, oxygen and the target oxidant will all contribute to NZVI passivation. The relative importance of these aging pathways, as well as potential differences in their impact on the nature of NZVI corrosion products, requires future investigation. It would be optimal to conduct the aforementioned experiments in flow-through column studies, which better reflect the dynamic nature of NZVI *in situ* treatment zones.

From results in Chapter 2, another focus for future investigation is the relationship observed herein between Cr(VI) removal capacity and Fe(II) production rate for NZVI. The generality of this trend must be extended to other commercially available forms of Fe(0), as well as to other Fe(II) reducible contaminants (e.g., nitroaromatics). This correlation may represent a key diagnostic for predicting Fe(0) reactivity toward Fe(II) reducible contaminants, which would be incredibly valuable in attempting to identify *a priori* the most reactive material for deployment at a contaminated site.

Chemical Regeneration Mechanisms for NZVI Treatment Zone Reactivity

Future efforts should explore other potential reductants that could be used as regenerants for the reducing capacity of NZVI *in situ* treatment zones. In particular, several organics including ascorbic acid, hydroquinone and hydroxylamine are known reductants for Fe(III) and could potentially function in a role similar to dithionite. Given that dithionite can oxidize residual Fe(0) to yield less active iron sulfides, it would be

desirable to identify other chemical regenerants that would not interact with any Fe(0) persisting in passivated NZVI particles.

The use of dithionite or similar chemical regenerant also needs to be extended into practical application. As NZVI installation sites increase in number, there will be opportunities for demonstrating *in situ* treatment zone regeneration at the field scale once the initial reducing capacity for the treatment system is lost. Of course, it will be necessary to further optimize the regeneration process in a more dynamic flow through laboratory or pilot-scale system (e.g., columns) prior to implementation at the field-scale.

Finally, the implications for chemical regeneration on improving the storage and handling of highly reactive NZVI particles merit examination. For example, the high reactivity and limited selectivity of NZVI makes preserving reactivity during storage, handling and delivery challenging. With chemical regeneration, it may be possible to manipulate NZVI surface chemistry to make storage and handling less problematic. Specifically, the controlled oxidation of NZVI by O₂ could be used to produce a passive surface layer that protects and preserves the Fe(0) in the particle core. This “passive” NZVI could be delivered to the treatment zone, followed by application of a suitable regenerant to restore its reducing capacity once in the subsurface, thereby limiting loss of reducing equivalents during storage, handling, delivery and subsurface transport. It may even be possible to tailor the nature of the surface oxide generated during the controlled oxidation so as to promote NZVI subsurface transport; passive layers should limit the role that magnetism plays in promoting aggregation [10].

Enhancing NZVI Reactivity through the Use of Noble-Metal Additives

As noted in Chapter 4, there is a need to examine further the production and activity of atomic hydrogen under conditions more representative of open, field-scale systems to address questions as to whether atomic hydrogen can be generated in sufficient quantities outside of closed batch systems. Also, other lines of evidence need to be collected to confirm the presence and involvement for atomic hydrogen in Pd/Fe systems. Potential routes for validation include the use of probe compounds that exhibit specific activity toward forms of atomic hydrogen. For example, Miehr *et al.* [11] utilized 2-chloroacetophenone as a probe for distinguishing reduction by electron-transfer and hydride transfer mechanisms.

It would also be worthwhile to extend the experimental findings, especially the relationship between rate enhancement and solvent kinetic isotope effects, to other bimetallic systems. Cwiertny *et al.* observed a relationship between metrics for hydrogen solubility in metals (Pd, Ni, Co, Cu, Au and Pt) and k_{obs} values for 1,1,1-TCA reduction in bimetallic systems of these metal additives on granular Fe(0) [12]. If forms of atomic hydrogen are involved in other bimetallic systems, a similar trend in SKIEs and atomic hydrogen solubility might also be anticipated as well.

A particularly interesting bimetal worthy of future investigation is Pt/Fe. In preliminary studies conducted in complement to Chapter 4, we found Pt/NZVI enhanced reactivity toward 1,1,1,2-TeCA relative to NZVI. However, Cwiertny *et al.* observed that deposition of Pt onto Fisher electrolytic iron actually inhibited Fe(0) reactivity toward 1,1,1-TCA [12], a trend also observed herein toward 1,1,1,2-TeCA via preliminary work

not shown in Chapter 4. The source of the disparate influence of Pt on NZVI and granular iron reactivity merits additional exploration.

Improving Iron Nanomaterial Performance via Production of High Surface Area Hybrid Nanostructures

Many fruitful areas of future research exist in the development and application of hybrid nanostructures for environmental quality control. Work in Chapter 5 focused solely on iron oxide nanoparticles immobilized on multi-walled carbon nanotubes. To increase the range of application of such hybrid nanostructures, synthesis methods for the immobilization of other nanoparticles on CNTs need to be developed. In the context of this work, metallic Fe(0) nanostructures could be immobilized on CNTs for application as reductants. Opportunities also exist to expand beyond iron-based nanostructures. There are also more opportunities to tune the reactivity of hybrid nanostructures through the use of other carbonaceous nanomaterial substrates. Commercially available options that could serve as novel supports for nanoparticle immobilization include single-walled CNTs, graphene, and electrospun carbon nanofibers. Once the reactivity of these hybrid nanostructures is optimized, future efforts should shift toward establishing innovative application platforms for these advanced materials, particularly identifying ways to immobilize the hybrid nanostructures for application in flow-through, filtration type systems.

6.6. Literature Cited

1. U.S. Environmental Protection Agency, Selected Sites Using or Testing Nanoparticles for Remediation (www.clu-in.org/download/remed/nano-site-list.pdf) Office of Solid Waste and Emergency Response, 2008.
2. Agrawal, A.; Ferguson, W.J.; Gardner, B.O.; Christ, J.A.; Bandstra, J.Z.; Tratnyek, P.G., Effects of Carbonate Species on the Kinetics of Dechlorination of 1,1,1-Trichloroethane by Zero-Valent Iron. *Environ. Sci. Technol.* **2002**, *36*, 4326-4333.
3. Bi, E.; Bowen, I.; Devlin, J.F., Effect of Mixed Anions (HCO_3^- , SO_4^{2-} , ClO_4^-) on Granular Iron (Fe(0)) Reactivity. *Environ. Sci. Technol.* **2009**, *43*, 5975-5981.
4. Devlin, J.F.; Allin, K.O., Major Anion Effects on the Kinetics and Reactivity of Granular Iron in Glass-Encased Magnet Batch Reactor Experiments. *Environ. Sci. Technol.* **2005**, *39*, 1868-1874.
5. Williams, M.D.; Vermeul, V.R.; Szecsody, J.E.; Fruchter, J.S. *100-D Area in Situ Redox Treatability Test for Chromate-Contaminated Groundwater* PNNL-13349; Pacific Northwest National Laboratory: Richland Washington, 2000.
6. Liu, Y.; Phenrat, T.; Lowry, G.V., Effect of TCE Concentration and Dissolved Groundwater Solutes on NZVI-Promoted TCE Dechlorination and H_2 Evolution. *Environ. Sci. Technol.* **2007**, *41*, 7881-7887.
7. Amonette, J.E.; Szecsody, J.E.; Schaef, H.T.; Templeton, J.C.; Gorby, Y.A.; Fruchter, J.S., Abiotic Reduction of Aquifer Materials by Dithionite: A Promising in-Situ Remediation Technology. In *In Situ Remediation: Scientific Basis for Current and Future Technologies*, Gee, G. W.; Wing, N. R., Eds. Battelle Press: Columbus, OH, 1994; pp 851-881.
8. Elliott, D.W.; Zhang, W.-X., Field Assessment of Nanoscale Bimetallic Particles for Groundwater Treatment. *Environ. Sci. Technol.* **2001**, *35*, 4922-4926.
9. Korte, N.E.; Zutman, J.L.; Schlosser, R.M.; Liang, L.; Gu, B.; Fernando, Q., Field Application of Palladized Iron for the Dechlorination of Trichloroethene. *Waste Management* **2000**, *20*, 687-694.
10. Phenrat, T.; Saleh, N.; Sirk, K.; Tilton, R.D.; Lowry, G.V., Aggregation and Sedimentation of Aqueous Nanoscale Zerovalent Iron Dispersions. *Environ. Sci. Technol.* **2006**, *41*, 284-290.
11. Miehr, R.; Tratnyek, P.G.; Bandstra, J.Z.; Scherer, M.M.; Alowitz, M.J.; Bylaska, E.J., Diversity of Contaminant Reduction Reactions by Zerovalent Iron: Role of the Reductate. *Environ. Sci. Technol.* **2004**, *38*, 139-147.

12. Cwiertny, D.M.; Bransfield, S.J.; Livi, K.J.T.; Fairbrother, D.H.; Roberts, A.L., Exploring the Influence of Granular Iron Additives on 1,1,1-Trichloroethane Reduction. *Environ. Sci. Technol.* **2006**, *40*, 6837-6843.

Curriculum Vitae

Yang Xie was born on December 24th 1984 and raised in Wuhan, Hubei, China. In 2003, she graduated from No. 1 Middle School Affiliated to Central China Normal School and enrolled in Environmental Engineering program in University of Wuhan. She studied the phosphate and nitrate adsorption performance on activated carbon (powder vs. granular) as her senior design. She achieved second scholarship in 2003 and 2005, third scholarship in 2004.

In September of 2007, she then joined the Chemical and Environmental Engineering program in University of California, Riverside with Dean's Distinguished Fellowship. Her PhD studies investigated the routes to optimize the performance of metallic iron and iron oxide nanomaterials for treatment of impaired water supplies.